Optimization of Endwall Cooling for High-Pressure Nozzle Guide Vanes



Francesco Guido Ornano

University College

University of Oxford

A thesis submitted for the degree of

Doctor of Philosophy

Michaelmas 2018

Abstract

Optimization of Endwall Cooling for High-Pressure Nozzle Guide Vanes

Francesco Guido Ornano, University College, *DPhil* in Engineering Science, Michaelmas term 2019

This thesis reports a combined experimental, numerical, and analytical work aimed to develop and optimize platform cooling for high-pressure nozzle guide vanes. The work is divided into a number of sections, each aimed to tackle different challenges in designing endwall cooling systems.

In the first section, a fundamental work on the scaling of film cooling is presented and discussed. This work aims to give insights into the use of the correct parameters when scaling film effectiveness data. With the aid of extensive RANS and LES predictions, a number of non-dimensional groups are independently varied whilst keeping the remaining groups constant. This enabled the independent effect of each group to be studied. An important observation that departs from previous literature is that there is a strong region dependence of the sensitivity of the film effectiveness to each of these parameters.

The second section involves an experimental investigation of the effect of the aerodynamic field on the adiabatic film effectiveness distribution on an engine-realistic endwall geometry. The study is carried out in aerodynamic similarity of the films between engine and laboratory conditions. It is shown that for relatively low values of momentum flux ratios (i.e. representative of the low portion of the engine range) jet lift-off is observed, with inefficient use of coolant. This suggests that—for a given coolant mass flow rate—endwall film cooling systems may be optimized by increasing internal pressure loss and therefore reducing the momentum flux ratio.

The third section focuses on the optimization of external film cooling. The aim is to develop a rapid optimization routine based on the scalar

tracking model and multi-objective genetic algorithms. The individual contribution of each film cooling hole is evaluated in CFD by solving an independent passive-scalar equation, and film effectiveness sensitivity to coolant mass flow rate is dealt with linear superposition techniques. The latter is used as a proxy for the CFD and it is computationally inexpensive. The approach can be therefore used in standard optimization techniques—such as genetic algorithms—to perform rapid system optimizations. An optimization routine involving the film cooling of a flat plate with external flow acceleration is performed by minimizing the temperature difference from a target distribution whilst minimizing mixing loss. Limitations of the proposed strategy are also reported and discussed in detail.

The fourth section involves the design of a HP-NGV endwall cooling system based on the reverse-pass scheme. That is, a system in which the internal coolant flows substantially in the opposite direction to the mainstream flow. The HP-NGV platforms are designed and assessd by using bespoke conjugate heat transfer and aerodynamic models. The proposed designs are shown to outperform the baseline configuration by reducing the metal temperature peak and flattening the temperature distribution. Three designs are down-selected for manufacturing by laser-sintering using titanium alloy and tested at high speed conditions.

The final section includes the aero-thermal characterization of novel HP-NGV platform designs based on the reverse-pass scheme and manufactured by laser-sintering. Tests are performed at engine-matched Reynolds number, Mach number, Biot number, and coolant-to-mainstream pressure ratio, on a full-annulus test section. Detailed film effectiveness distributions on vane platforms are measured by means of infrared thermography. Engine baseline and reverse-pass-based designs are compared in back-to-back experimental tests at engine-representative conditions over a range of coolant-to-mainstream pressure ratios.

To the memory of my grandparents Anna Rosa and Giuseppe.

Acknowledgements

I will always be grateful to my supervisor Prof. Thomas Povey for giving me the opportunity—a once-in-a-lifetime opportunity—to become part of his group, and collaborate in such a prestigious environment. His guidance and support have been invaluable for any aspect of my PhD. His outstanding expertise and intuition were always inspiring to me. I feel hugely privileged to have worked with him.

I would like to thank Rolls Royce plc for funding the project. My gratitude also goes to Ed Romero and Anton Rawlinson for their valuable inputs.

I am indebted to all the workshop staff, and in particular to Dominic Harris for his help during my days working in the *Blow-down* area.

I would like to thank Ben Kirollos for the valuable inputs on the reverse-pass design philosophy and infra-red thermography.

Thanks must go to all Osney mates for the amazing time spent together. Good luck for the future guys! A big thank goes to Mathias and Nafiz, for the technical discussions and their help during the experimental campaign on the ECAT facility.

And most of all, my deepest gratitude goes to my family, and in particular to Mum, Dad, and Giancarlo for being by my side, every step I take. Finally, my very special thank goes to you, Tea. Thank you for your love, and for every moment together.

Contents

1 Introduction **1**

1.1 Flow in turbine passages 1
1.2 Cooling requirements 3
1.3 Endwall cooling 4
1.4 Film cooling 6
1.5 Research contribution 7

2 Theory of Non-dimensional Groups in Film Effectiveness Studies **10**

2.1 Introduction 11
2.1.1 Dimensional analysis of film cooling: literature review 12
2.1.2 Practice in experiments 12
2.2 Dimensional Analysis 15
2.3 Region-specific scaling parameters 20
2.4 Test matrix 22
2.5 Numerical methods for RANS simulations 23
2.5.1 Solver settings 23
2.5.2 Mesh and boundary conditions 23
2.5.3 Grid independency study 25
2.6 Numerical methods for LES 25
2.6.1 Solver settings 26
2.6.2 Mesh resolution for LES study 27
2.6.3 Choice of time step 28
2.6.4 Frequency analysis 29
2.7 Results and discussion 30
2.7.1 Momentum flux ratio 30
2.7.2 Specific heat capacity flux ratio 33
2.7.3 Blowing ratio – main physical processes 37
2.7.4 Blowing ratio – structural changes caused by shear 48

2.7.5 Temperature ratio 51
2.8 Conclusions 60

3 Effect of Momentum-Flux Ratio on HP-NGV Platform Cooling 66
3.1 Introduction 67
3.2 Experimental methods 70
3.2.1 Infrared thermography 74
3.2.2 Infrared calibration 74
3.2.3 Experimental uncertainty 75
3.3 Experimental plan 77
3.3.1 Engine range of momentum flux ratio 78
3.4 Numerical methods 79
3.4.1 Calculation of momentum flux ratio 82
3.5 Results and discussion 83
3.5.1 Overall film effectiveness distributions: upstream endwall . . . 83
3.5.2 Overall film effectiveness: downstream endwall 87
3.5.3 Film effectiveness distributions at lines 1 to 4 89
3.5.4 Comparison of CFD and experimental results at two conditions 95
3.5.5 Laterally averaged film effectiveness at lines 1 to 4 98
3.5.6 Total pressure profile in the near-wall region: comparison of CFD and experiment 101
3.6 Conclusions 105

4 Development of a Rapid Optimization Routine Based on the Scalar Tracking Method 107
4.1 Introduction 108
4.2 The scalar tracking method 109
4.3 Optimization methodology 112
4.3.1 Life objective function 115
4.3.2 Film cooling loss function 117
4.3.3 Optimization algorithm 119
4.3.4 Dakota setup 121
4.4 Discussion on the limitations of the method 122
4.5 Test case design 123
4.6 CFD methods 127
4.6.1 Solver settings 127
4.6.2 Computational mesh 128

4.6.3 CFD set up for scalar tracking calculations 128
4.7 Results and discussion 128
4.8 Conclusions 137

5 Design and Manufacture of Reverse-Pass High-Pressure Vane Platforms 139
5.1 Introduction 140
5.2 Computational domain 141
5.3 Aerodynamic modelling 142
5.3.1 Baseline platform cooling design 143
5.3.2 Pedestal total pressure loss correlation 144
5.3.3 Impingement total pressure loss estimation 145
5.3.4 Updated holes diameter estimation 146
5.4 Thermal modelling 146
5.4.1 Thermal boundary conditions 147
5.4.2 Pedestal bank internal HTC correlation 149
5.4.3 Smooth wall internal HTC correlation 150
5.4.4 Prediction of wall and coolant temperatures 150
5.5 Aerothermal design results 152
5.6 CFD assessment of aero-thermal field 160
5.7 Corrected design coolant mass flow rate 162
5.8 Manufacture 165
5.8.1 Plastic models for visualization purposes 165
5.8.2 Material selection 166
5.8.3 Laser-sintered vanes 166
5.9 Conclusions 170

6 Experimental Investigation of High-Pressure Reverse-Pass Vane Platforms 172
6.1 Introduction 172
6.2 The Oxford ECAT facility 173
6.2.1 Operation of the Oxford ECAT facility 174
6.2.2 Facility layout and principles of operation 174
6.3 Facility commissioning for platform tests 177
6.3.1 Front and rear platform view design 177
6.4 Infra-Red thermography 179
6.4.1 Infra-Red thermography theory 180

6.4.2 Grey-body calibration theory 182
6.4.3 Surrounding radiance correction 185
6.4.4 Infra-Red hardware 192
6.5 Experimental uncertainty 193
6.6 Experimental test matrix 195
6.7 Coolant capacity test results 196
6.8 Test conditions 199
6.9 Description of the field-of-view 199
6.10 Overall cooling effectiveness results 201
6.10.1 Effect of coolant-to-mainstream pressure ratio 202
6.10.1.1 Baseline design 203
6.10.1.2 Reverse-passed ARP1-1 design 209
6.10.1.3 Reverse-passed ARP1-2 design 215
6.10.2 Impact of cooling arrangement 221
6.11 Conclusions 224

7 Conclusions 226
7.1 Non-dimensional groups in film cooling studies 226
7.2 Effect of momentum flux ratio on HP-NGV endwall cooling systems . 229
7.3 Film cooling optimization based on the scalar tracking method 229
7.4 Design and assessment of HP-NGV reverse-pass platforms 231
7.5 Application of the research and future work 232

A Demonstration that VR and VFRR are Inversely Proportional to BR when Varying BR Alone 234

B Demonstration that for TR Either Side of Unity there is a Reduction in Density in the Mixing Layer 236

List of Figures

1.1 Example of total temperature radial profiles downstream of conventional rich-burn and modern lean-burn combustors. 5

2.1 Physical situation and parameters of interest for a film-cooled adiabatic wall. 16
2.2 CFD domain showing the binary, intermediate and mixed-out post-processing lines. 22
2.3 Computational domain (a) and detail of the cooling hole mesh (b) used for RANS simulations. 24
2.4 Film effectiveness distribution in the binary, intermediate and mixed-out regions obtained during the grid sensitivity study. The test conditions were: $E = I =$ BR $= 1.000$ and TR $= 0.800$. 26
2.5 Computational mesh employed for LES simulations. (a) slice of volume mesh and (b) detail of the cooling hole grid. 28
2.6 (a) Fast Fourier Transform; (b) Power Density Spectrum of the transient velocity signal downstream the central cooling hole. 29
2.7 Lateral distribution of η in the binary region ($x = 0d$) as a function of I. Test conditions were: $E = 1.000$, BR $= 1.000$ and TR $= 0.800$. . . 31
2.8 Lateral distribution of η on intermediate region ($x = 24d$) as a function of the I Test conditions were: $E = 1.000$, BR $= 1.000$ and TR $= 0.800$. 31
2.9 Lateral distribution of film effectiveness on mixed-out region ($x = 48$d) as a function of the momentum flux ratio Test conditions were: $E = 1.000$, BR $= 1.000$ and TR $= 0.800$. 32
2.10 Lateral average of film effectiveness as function of I. Test conditions were: $E = 1.000$, BR $= 1.000$ and TR $= 0.800$. 33
2.11 Effect of specific heat capacity flux ratio on film effectiveness on the binary region ($x = 0d$). Test conditions were $I = 1.000$, BR $= 1.000$ and TR $= 0.800$. 34

2.12 Effect of specific heat capacity flux ratio on film effectiveness on the intermediate region ($x = 24d$). Test conditions were $I = 1.000$, BR = 1.000 and TR = 0.800. 35
2.13 Effect of specific heat capacity flux ratio on film effectiveness on the mixed-out region ($x = 48d$). Test conditions were $I = 1.000$, BR = 1.000 and TR = 0.800. 36
2.14 Lateral average of film effectiveness as function of E. Test conditions were: $I = 1.000$, BR = 1.000 and TR = 0.800. 37
2.15 Normalized volume flow rate ratio (normalized by the value at BR = 1) and absolute velocity ratio u_2/u_1 as a function of blowing ratio. Test conditions were $I = 1.000$, $E = 1.000$, and TR = 0.800. 38
2.16 Effect of blowing ratio on film effectiveness in the binary region ($x = 0d$). Test conditions were $I = 1.000$, $E = 1.000$ and TR = 0.800. . . 40
2.17 Effect of blowing ratio on film effectiveness in the intermediate region ($x = 24d$). Test conditions were $I = 1.000$, $E = 1.000$ and TR = 0.800. 41
2.18 Effect of blowing ratio on film effectiveness in the mixed-out region ($x = 48d$). Test conditions were $I = 1.000$, $E = 1.000$ and TR = 0.800. 41
2.19 Lateral average of film effectiveness as function of blowing ratio. Test conditions were $I = 1.000$, $E = 1.000$ and TR = 0.800. 43
2.20 Iso-surfaces at $\eta = 0.3$ for BR = 0.500 (red surface), BR = 1.000 (green surface), and BR = 2.000 (blue surface). 44
2.21 Iso-lines at $\eta = 0.3$ at several axial planes for the cases with BR = 0.500, 1.000 and 2.000. 46
2.22 Iso-lines at $\eta = 0.4$ at several axial planes for the cases with BR = 0.500, 1.000 and 2.000. 46
2.23 RANS results of non-dimensional temperature ($\phi = \frac{T_{01}-T_0}{T_{01}-T_{02}}$) distribution at $x = 24d$ for BR = 0.500, 1.000, and 2.000. Iso-lines at $\eta = 0.3$ are marked with a black line. 48
2.24 Iso-levels of Lambda-2 criterion for the case with BR = 0.500, 1.000 and 2.000. Iso-lines at $\eta = 0.4$ are also marked in the figures at planes $x = 0d$ and $x = 12d$, respectively. 49
2.25 RANS results of laterally mass-averaged shear strain rate profiles for various BR at plane $x = 0d$. 50
2.26 LES instantaneous vortex structures (Lambda-2 criterion) coloured by the normalized distance from the wall (z^*). (a) TR = 0.350, (b) TR = 0.950, (c) TR = 1.520, and (d) TR = 1.995. 54

2.27 Laterally averaged axial distributions of time averaged film effectiveness for LES simulations TR = 0.350, 0.950, 1.520, and 1.995. 55
2.28 LES results of mass-averaged time-averaged density ratio distribution at plane $x = 0$, 24, and $48d$. 56
2.29 LES predictions of the mass-averaged $\overline{uu'}$ component of Reynolds stresses, along the normalized wall distance at planes $x = 0$, 24, and $48d$. . . . 58
2.30 Lateral average of film effectiveness as function of temperature ratio Test conditions were $I = 1.000$, $E = 1.000$ and BR = 1.000. 59

3.1 CAD model and components of the Super-Scale Platform Cooling Facility; (a) front view and (b) rear view. A—vane and platforms; B—rear cameras; C—front cameras; D—combustor simulator; E—tailboards; F—hub cassette; G—casing cassette. 71
3.2 NGV cascade viewed from upstream; (b) detail of the casing endwall; (c) casing film cooling pattern; (d) vane hub and casing cooling hole inclinations angles. 72
3.3 CFD-predicted single vane capacity at six pressure ratios fitted with isentropic trend. 73
3.4 Fields of view: (a) upstream endwall; (b) downstream endwall. 74
3.5 Typical calibration curve of detector signal as a function of the surface temperature (thermocouple). 75
3.6 Contours of the absolute uncertainty (to 95% confidence) in η as a function of T_∞/T_c and η. 77
3.7 Range of momentum flux ratio for endwall cooling systems at typical engine conditions. 79
3.8 (a) Surface mesh detail; (b) film cooling hole mesh detail; (c) computational domain. 80
3.9 Measured normalized radial total pressure profile at the combustor-NGV interface. 82
3.10 Film effectiveness distribution along the vane exit line obtained during the grid independency study. The flow conditions were: MFR = 3.3% and $I = 3.89$. 83
3.11 Endwall adiabatic film effectiveness contours (upstream view) for $0.40 < I < 6.40$. 85
3.12 Endwall adiabatic film effectiveness contours (upstream view) for $11.65 < I < 26.99$. 86

3.13 Endwall adiabatic film effectiveness contours (downstream view) for $0.40 < I < 26.99$. 88
3.14 Measured tangential distribution of adiabatic film effectiveness downstream the first cooling row (line 1). 91
3.15 Measured tangential distribution of adiabatic film effectiveness downstream the second cooling row (line 2). 92
3.16 Measured tangential distribution of adiabatic film effectiveness on vane mid-passage (line 3). 93
3.17 Measured tangential distribution of adiabatic film effectiveness on vane outlet line (line 4). 95
3.18 Comparison of adiabatic film effectiveness between CFD and experiment for $I = 6.40$ (MFR = 4.3%). (a) experimental results; (b) CFD prediction; (c) comparison at vane inlet and outlet lines with indication of experimental uncertainty, u_η. 96
3.19 Comparison of adiabatic film effectiveness between CFD and experiment for $I = 11.65$ (MFR = 6.3%). (a) experimental results; (b) CFD prediction; (c) comparison at vane inlet and outlet lines with indication of experimental uncertainty, u_η. 97
3.20 Laterally averaged adiabatic film effectiveness on lines 1 to 4 as a function of the momentum flux ratio: experiment (solid markers) and CFD (open markers). 100
3.21 (a) Normalized total pressure radial profile, $(p_0 - p_0^*)/(p_{0,in} - p_2^{ave})$, for different momentum flux ratios; (b) axial and pitchwise location of the radial traverse. 102
3.22 Normalized total pressure contours at vane inlet and coolant streamline traces; case with low I (a) and high I (b). 103
3.23 PS view of Lambda 2-criterion for: (a) $I = 0.40$; (b) $I = 11.65$. . . . 104
3.24 SS view of Lambda2-criterion and total pressure loss coefficient, c_p0, for: (a) $I = 0.40$; (b) $I = 11.65$ 105

4.1 Film cooling control volume. 111
4.2 Scalar tracking-MOGA method flow chart. 114
4.3 Life objective (Obj_1) as a function of the temperature difference. . . . 117
4.4 Block diagram of the MOGA algorithm. 120
4.5 Prediction of streamwise film effectiveness distribution for two holes spaced by $x/d = 25$ using Sellers model. 124

4.6 Prediction of lateral film effectiveness distribution for two holes spaced by $y/d = 3$ using Sellers model. 125
4.7 Computational domain and initial film effectiveness distribution for the optimization test case. 126
4.8 (a) axial distribution of flow variables and (b) momentum flux ratio for the optimization test case. 127
4.9 Detail of the computational mesh used for the scalar-tracking study. . 128
4.10 Example of convergence of Pareto front during a MOGA run. 130
4.11 Comparison of hole mass flow rates between method involving Equation 4.12 and CFD prediction. 132
4.12 Optimization results of film effectiveness distribution at domain exit (line 1). 134
4.13 Change in hole diameters at the end of optimization process (after 5 global runs). 135
4.14 Optimized film effectiveness distribution predicted with CFD. 136
4.15 Overall optimization results for each global run. 136

5.1 Computational domain of the reverse-pass platform. 142
5.2 (a) CAD view and (b) pressure margin distribution of the baseline cooling design (predicted with CFD). 143
5.3 Contours of external heat transfer coefficient on hub platform (a), and distribution along the normalized axial location (b). Data were obtained from conjugate simulations at engine conditions. 148
5.4 Contours of adiabatic film effectiveness on hub platform (a), and laterally averaged distribution along the normalized axial location (b). Data were obtained from conjugate simulations at engine conditions. 149
5.5 Spanwise-averaged heat transfer coefficient enhancement (with respect to smooth wall) for a pedestal bank with $Re = 30000$ and $S/d = 4$. . 150
5.6 Sketch of the coolant mass flow balance with the reverse-pass system. 153
5.7 Section sketch of design ARP1-1 (a), design ARP1-2 (b), and top view of vane platform (c). 154
5.8 External wall temperature (a) and pressure margin distribution (b) of design ARP1-1. External wall temperature (c) and pressure margin distribution (d) of design ARP1-2. 159
5.9 Laterally-averaged axial external wall temperature distribution (a), and laterally-averaged internal HTC distribution (b). 160

5.10 CFD comparison of adiabatic film effectiveness between baseline (a) and ARP1-1 (b) design. 161
5.11 CFD comparison of hub platform (RIDN) coolant mass flow rate distribution between baseline and ARP1-1 design. 162
5.12 Updated external wall temperature (a) and pressure margin distribution (b) of design ARP1-1. External wall temperature (c) and pressure margin distribution (d) of design ARP1-2. 164
5.13 Updated laterally averaged axial external wall temperature distribution and (a) laterally averaged internal HTC distribution (b). 165
5.14 Full-scale visualization of a 3D-printed plastic model: (a) front view and (b) top view 166
5.15 ARP1-1 and ARP1-2 as laser sintered. ARP1-1:(a) leading edge view, (b) hub platform view, and (c) trailing edge view. ARP1-2: (d) leading edge view, (e) hub platform view, and (f) trailing edge view. 168
5.16 Laser-sintered vane: detail of the hub platform holes (RIDN). 169
5.17 3D scan of Ti6Al4V ARP1-1 vane. (a) Pressure side view and(b) suction side view. Values represent the deviation in mm. 170

6.1 Flow-path schematic of the Oxford ECAT Facility. 175
6.2 The main components of the Oxford ECAT Facility. 175
6.3 The working section of the Oxford Capacity Facility. 176
6.4 Camera view obtained from the CAD model (a), and view from the IR camera acquired during a test (b). 178
6.5 Photo of upstream cassette with IR mirror. Top cassette body (a), bottom cassette body (b), angled support bracket (c), and gold-coated IR mirror (d). 178
6.6 Photo of the vane test section (viewed from downstream); (a) IR mirror, (b) angled support bracket, (c) vane casing ring, and (d) vane hub ring. 179
6.7 Sketch of ray traces for (a) rear view and (b) front view during nominal operation. 185
6.8 Picture of *in-situ* downstream endwall calibration system. (1) Rohacell layer, (2) surface thermocouple, and (3) thin copper disk. 187
6.9 Equivalent black-body temperature field on downstream calibration region after heater mesh cut-off (a), and during heater on (b). 188

6.10 Picture of *in-situ* front platform calibration system. (1) instrumentation cassette, (2) gold-coated mirror, (3) Rohacell layer, and (4) surface thermocouple. 189
6.11 Surrounding radiance for a high-powered run (80% heater power settings). (1) camera refocus. 190
6.12 Surrounding radiance as a function of mainstream temperature measured on rear endwall, for 70% and 80% heater power runs. Cyan and magenta points are due to camera refocus and therefore excluded from the fitting. 191
6.13 Surrounding radiance as a function of mainstream temperature measured on front endwall, for 70% and 80% heater power runs. 191
6.14 Photo of metal box containing the IR camera (a) for vane SS view. . 192
6.15 Uncertainty in overall cooling effectiveness u_θ as a function of temperature ratio and θ, for a recovery ratio $c = 0.995$. 195
6.16 Dynamic leak test results for previous build (red and black lines) and new build (blue line). 198
6.17 Comparison of hub and casing plena pressure difference between the previous build (red and black lines) and the new build (blue line). . . 198
6.18 Example of ECAT test conditions for a typical run. 199
6.19 Front platform field-of-view (upstream IR camera). 200
6.20 Rear platform field-of-view (downstream IR camera). 201
6.21 Overall cooling effectiveness distribution on upstream endwall (a–c), and downstream endwall (d–f) at various pressure ratios for the baseline design. 204
6.22 Overall cooling effectiveness distribution on upstream endwall (a–c), and downstream endwall (d–f) at various pressure ratios for the baseline design. 207
6.23 Overall effectiveness distribution (baseline design) on lines 1, 2, and 3 for PR = 1.01, 1.02, and 1.03. 208
6.24 Overall cooling effectiveness distribution on upstream endwall (a–c), and downstream endwall (d–f) at various pressure ratios for the ARP1-1 design. 211
6.25 Overall cooling effectiveness distribution on upstream endwall (a–c), and downstream endwall (d–f) at various pressure ratios for ARP1-1 design. 213

6.26 Overall effectiveness distribution (ARP1-1 design) on lines 1, 2, and 3 for PR = 1.01, 1.02, and 1.03. 214
6.27 Overall cooling effectiveness distribution on upstream endwall (a–c), and downstream endwall (d–f) at various pressure ratios for ARP1-2 design. 216
6.28 Overall cooling effectiveness distribution on upstream endwall (a–c), and downstream endwall (d–f) at various pressure ratios for the ARP1-1 design. 219
6.29 Overall effectiveness distribution (ARP1-2 design) on lines 1, 2, and 3 for PR = 1.01, 1.02, and 1.03. 220
6.30 Overall cooling effectiveness distribution on line 1 for PR = 1.02 for all designs tested. 222
6.31 Overall cooling effectiveness distribution on line 2 for PR = 1.02 for all designs tested. 222
6.32 Overall cooling effectiveness distribution on line 3 for PR = 1.02 for all designs tested. 223

B.1 Variation of coolant gas constant R_2 (normalized by R_1, which is constant with TR), and coolant gas density ρ_2 (normalized by ρ_1, which is constant with TR) as a function of temperature ratio. 237
B.2 Control volume for a partially mixed coolant film. 238
B.3 Variation of R_3 (normalized by R_1, which is constant with TR) and T_{03} (normalized by T_{01}, which is constant with TR) as a function of TR. 239
B.4 Variation with TR of: density ratio of the partially mixed layer ρ_3/ρ_1; volume flow rate ratio of the partially mixed layer $\dot{V}_3/(\dot{V}_1 + \dot{V}_2)$; kinematic viscosity ratio of the partially mixed layer ν_3/ν_2. 240

List of Tables

3.1 Indication of operating parameters for the data presented in Figure 3.14, 3.15 , 3.16, and 3.17. 90

5.1 Boundary conditions for the thermal model. 147
5.2 Change in hole diameter for holes included in the revese-pass channel with respect to the baseline case. 160

6.1 Experimental test matrix. 196

Nomenclature

Acronyms

DR	Density ratio, ρ_c/ρ_∞
HTC	Heat transfer coefficient
LE	Leading edge
MFR	Mass flow ratio, $\dot{m}_c/\dot{m}_\infty$
PS	Pressure side
RP	Reverse pass
SS	Suction side
TE	Trailing edge
TET	Turbine entry temperature
VFRR	Volume flow rate ratio
VR	Velocity ratio, u_2/u_1

Greek symbols

α	Flow angle, deg
η	Adiabatic film effectiveness
Γ	Flow capacity, kg s^{-1} $K^{0.5}$ Pa^{-1}
Γ	Scalar diffusivity, m^2 s^{-1}
γ	Isentropic specific heats ratio
κ	Kolmogorov length scale, m

μ Viscosity, Pa s

ϕ Non-dimensional temperature, $\frac{T_{01}-T_0}{T_{01}-T_{02}}$

ϕ Non-dimensional temperature, $\frac{T_{0\infty}-T_w}{T_{0\infty}-T_{0c}}$

ϕ Scalar quantity

π_i Non-dimensional group

ρ Density, kg m^{-3}

ρ Reflectivity

τ Transmittance

θ Overall cooling effectiveness

θ Viewing angle, deg

ε Surface emissivity

ε Turbulent dissipation rate, m^2 s^{-3}

Roman symbols

$\dot{m}$ Mass flow rate, kg s^{-1}

$\dot{V}$ Volume flow rate, m^3 s^{-1}

Bi Biot number

c Recovery factor

C_d Discharge coefficient

c_{p0} Total pressure loss coefficient

c_p Specific heat capacity, J kg^{-1} K^{-1}

D Pedestal (or pin fin) diameter, m

d Film cooling hole diameter, m

E Power density, dB Hz^{-1}

f Frequency, Hz

f	Friction factor
f	Objective function
H	Pedestal (or pin fin) height, m
h	Convective heat transfer coefficient, W m^{-2} K^{-1}
k_{eff}	Effective turbulent thermal diffusivity, m^2 s^{-1}
L	Characteristic length, m
L_f	Life coefficient
N	Number of pedestal rows
Nu	Nusselt number
$p_{0,in}$	Mass-averaged total pressure at vane inlet, Pa
p_0^*	Reference total pressure at 50% vane span, Pa
Pr	Prandt number
q^*	Surrounding radiance, W m^{-2} sr^{-1}
R	Specific gas constant, J kg^{-1} K^{-1}
Re	Reynolds number
S	Entropy, J kg^{-1} K^{-1}
S	Pedestal (or pin fin) spacing, m
s	Streamwise coordinate, m
t	Time, s
t_w	Wall thickness, m
Tu	Turbulent intensity
U	Overall heat transfer coefficient, W m^{-2} K^{-1}
U	Velocity, m s^{-1}
u	Velocity component along x, m s^{-1}

u_η Absolute uncertainty in film effectiveness

v Velocity component along y, m s^{-1}

W Mass fraction

w Channel width, m

w Velocity component along z, m s^{-1}

x^* Nondimensional axial location, $x^* = x/d$

y^* Nondimensional tangential location, $y^* = (y - y_{min})/(y_{max} - y_{min})$

y^+ Nondimensional wall distance (based on Reynolds number)

z^* Nondimensional wall distance, $z^* = z/d$

z^+ Nondimensional wall distance (based on Reynolds number)

I Momentum flux ratio, $\rho_c u_c^2/\rho_\infty u_\infty^2$

k Thermal conductivity, W m^{-1} K^{-1}

M Mach number

P Vane pitch, m

p Static pressure, Pa

s Nondimensional spanwise coordinate

V Velocity, m s^{-1}

v Velocity, m s^{-1}

Subscripts

∞ Mainstream conditions

ave Averaged value

aw Adiabatic wall

c Coolant conditions

e Exit location

in	Inlet conditions
KE	Kinetic energy
max	Maximum value
Q	Thermal mixing
T	Turbulent
$targ$	Target
TC	Thermocouple location
w	Wall
0	Total conditions
1	Internal wall
1	Mainstream gas conditions
2	Coolant conditions
2	External wall
2	Vane exit conditions

Chapter 1

Introduction

This thesis aims to develop improved designs of high-pressure nozzle guide vanes (HP-NGV) platform cooling systems. The first objective of this thesis is to give insight into the understanding of the physics and scaling of film cooling. It also contributes to the development of rapid optimization strategies for film cooling systems, and to the design and testing of novel integrated endwall cooling architectures based on the *reverse-pass* concept.

In this chapter, a literature review is presented on HP-NGV heat transfer, secondary flows, turbine cooling requirements and film cooling. Further reference to the relevant literature is given in the specific chapters.

To date, the work in this thesis has been the subject of one paper presented at an international conference (Ornano and Povey 2017*a*), and two journal articles (Ornano and Povey 2017*b*), and (Ornano and Povey 2018).

1.1 Flow in turbine passages

The classical picture of secondary flows in gas turbines was originally proposed by Langston et al. (1977). Models for the development of secondary flows in turbine cascades have been proposed by Sieverding (1985), Sharma and Butler (1987), and Wang et al. (1997). Secondary flow structures are generated by the interaction be-

tween the incoming boundary layer and the vane pressure gradients. Considering two streamlines (A and B) along the boundary layer, the radial equilibrium within the passage can be written in the following form:

$$\frac{\partial p}{\partial n} = \varrho_A \frac{V_A^2}{R_A} = \varrho_B \frac{V_B^2}{R_B} \tag{1.1}$$

where V is the velocity of a particle following the streamline, ϱ its density, and R the streamline radius of curvature. Assuming that the streamline A lies outside the boundary layer and B inside, then $V_A > V_B$. According to Eq. 1.1, this will result in the streamline B having a smaller radius of curvature than A ($R_A < R_B$). This will cause the generation of secondary flow vorticity and the development of the so-called *passage* vortex. The vane potential field is also responsible for the generation of secondary vorticity upstream of the turbine passage. In fact, the incoming boundary layer interacts with the vane radial static pressure gradients in the proximity of the leading edge region. A separation bubble is generated in the junction between the vane leading edge and the endwall, leading to the formation of the so-called *horseshoe* vortex. The horseshoe vortex is then divided into two legs which develop further deep into the passage and eventually merge with the passage vortex.

A conspicuous number of studies has been presented on the strategies to reduce secondary flows in turbine passages. These studies involve the effect of blade lean and sweep, such as in the study by Han and Golstein (2005) and Pullan and Harvey (2008), and fillet/endwall contouring, as investigated by Ingram (2003), Bagshaw (2009), and Zess and Thole (2005). A completely novel design approach of nozzle guide vanes has been proposed by Wang et al. (2017). It is based on the inherent 3D design of the vane flow path. Despite the conventional design methods, this design (called FLOvane) starts from a fully three-dimensional approach. The vane flow path is designed as an oval, trumpet-shape passage which turns into a squared duct to deliver the design

inflow to the downstream rotor (i.e. velocity flow angle, Mach number distribution, etc.). With this approach, they obtained the complete suppression of secondary flow structures, with the elimination of high heat transfer regions on vanes and platforms.

1.2 Cooling requirements

Horlock et al. (2001) reviewed established methods for determining the amount of coolant required and the semi-empirical relations for film cooled blading and total pressure loss. They used these correlations on a simple open gas turbine cycle with cooling. The results of calculations suggested that, for a maximum plant efficiency, there may be a limiting temperature *below* the stoichiometric combustion value. It was also found that, for a given combustion temperature, the optimum pressure ratio is reduced by the effect of cooling air. It was shown that gains in thermal efficiency with increasing the turbine entry temperature (TET) can become marginal when large coolant flows are considered. In fact, a maximum thermal efficiency is reached at values below the stoichiometric conditions. The conclusions drawn by Horlock et al. (2001) highlighted the doubt on whether considerable efforts should be made in increasing the TET much further, except for the case in which a further development in the materials and improved heat transfer mechanisms can reduce the amount of cooling air required. This conclusion has motivated substantial efforts made by designers and researchers in the past decades in developing improved turbine cooling systems and understanding complex heat transfer mechanisms.

Turbine entry temperatures of around 2100 K are common in modern gas turbines. This is possible thanks to enhanced cooling systems, single crystal casting and thermal barrier coatings. A substantial body of research has been performed on the development of film cooling. Film cooling is employed to protect the high-pressure turbine components from the hot gas coming from the combustor. Relatively cold air

is ejected from an internal cavity through cooling holes to form a protective film over the metal surfaces and therefore to reduce the heat load.

One of the most critical components in the HP section of a gas turbine is the vane endwall. As described in the next section, this region is exposed to the hot gas coming from the upstream combustor section and it is characterized by three-dimensional flows and high heat transfer.

1.3 Endwall cooling

Turbine endwalls are large surfaces exposed to the hot combustion gases. The flow field across these surfaces is highly three-dimensional. The near wall flow structures (mainly represented by the horseshoe vortex) affect the local state of the boundary layer (separation and subsequent reattachment), leading to the generation high heat transfer regions. In a film cooling system, the vane mid-passage pressure gradients are also responsible for the migration of the low-momentum coolant flow from the pressure side (PS) to the suction side (SS) of the passage, causing degradation of the film cooling performance. Giel et al. (1998) presented a detailed picture of the heat transfer on a transonic turbine endwall. The Stanton number (proportional to the heat transfer coefficient) was highly influenced by the complex three-dimensional flowfield within the vane passage. Substantially high Stanton numbers were observed near the endwall LE stagnation region (LE corner vortex). As the flow accelerated along the SS region, high heat transfer values were also measured due to the thinning of the boundary layer, with resulting increased heat transfer to the wall.

The importance of developing effective and efficient endwall cooling systems is also crucial in light of the recent developments in combustor architectures. In fact, the modern lean-burn combustor architectures will potentially deliver flatter temperature profiles when compared to their rich-burn counterparts. In this case, endwalls will

experience higher temperature, which will lead to increased cooling requirements to prevent early failure of the component (Thomas 2014). Figure 1.1 shows an example of temperature profiles downstream of rich-burn and lean-burn combustors.

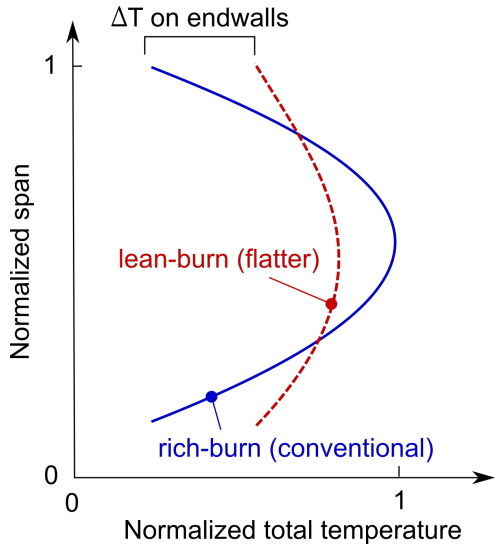


Figure 1.1: Example of total temperature radial profiles downstream of conventional rich-burn and modern lean-burn combustors.

Modern lean-burn combustors involve the use of flow swirlers in order to create optimal combustion conditions. The impact of flow swirl on HP-NGV aerodynamics and heat transfer has been intensively studied, as reported in Qureshi et al. (2011), Qureshi et al. (2012), and Salvadori et al. (2011). Although endwalls have received little attention on this aspect, the impact of flow swirl is tremendous. In this regard, a recent paper by Zhang et al. (2017) investigated the effect of inlet swirl on endwall vane film cooling in neighbouring vane passages.

Film cooling is widely employed in gas turbines as a primary method to reduce the heat load experienced by the endwalls. Friedrichs et al. (1999) and Barigozzi et al. (2010) have investigated the development of the endwall aero-thermal field and the interaction between mainstream and coolant flows. The classical picture of endwall flows often implies that the coolant flow is generally driven by the mainstream flow, resulting in local migration of coolant from PS to SS (subject to vane pressure gra-

dients), and therefore causing the deterioration of the film performance. At nominal operating conditions, however, the coolant momentum may become sufficiently high to actively control the local development of the endwall flow structures. This thesis aims to show that the classical picture of secondary flows may be altered depending on the injected coolant momentum. It is shown that, at engine values of momentum flux ratios (I), the secondary flows are dramatically reduced and—for sufficient high values of I—completely suppressed by the highly energized coolant injected.

1.4 Film cooling

A review of past literature has shown increased efforts in the investigation of endwall cooling with discrete holes. Many authors have studied the dependence of film effectiveness on hole orientation, geometry and arrangement. Harasgama and Burton (1992) investigated the Nusselt number distribution on a NGV endwall with discrete holes upstream the vane and inside the passage, where holes were distributed along iso-Mach lines. Friedrichs et al. (1999) investigated the effect of secondary flow on endwall film cooling. Gao et al. (2009) experimentally studied the effect of different hole configurations on endwall film cooling. Thole and Knost (2005) performed measurements of adiabatic film effectiveness combining both cooling from a slot and discrete film cooling holes on the vane endwall.

The importance of the radial total pressure distribution at the vane inlet, including the influence of cooling flow, was investigated by Thomas and Povey (2016). They investigated the effect of coolant-to-mainstream pressure ratio, hole inclination angle, hole diameter, vane potential field, and overall mass flux ratio using validated CFD. The role of blowing ratio and density ratio on film cooling was investigated by Sinha et al. (1992). Thole et al. (1990) highlighted the importance of selecting the appropriate non-dimensional parameter to scale the film cooling data.

This thesis focuses on the importance of scaling film cooling parameters from experiments to engine conditions. Due to physical limitations, laboratory experiments are performed at conditions which might not be fully representative of the engine environment in terms of temperature and pressure. The selection of these non-dimensional groups is rather important to reach complete similarity of the film performance. Film cooling performance (typically film effectiveness, under either adiabatic or diabatic conditions) is almost universally presented as a function of one or more of three commonly used non-dimensional groups: blowing—or local mass flux—ratio; density ratio; and momentum flux ratio. Despite the abundance of studies in this field, there is some confusion in the literature about the best way of presenting such data. In fact, the three non-dimensional groups in common use are not independent of each other. The aim of this thesis is to bring clarity to the correct scaling of film cooling data, and show the region-dependence of film effectiveness on each—independently varied—scaling parameter.

1.5 Research contribution

The research contribution of this thesis is divided into four main areas of interest and can be summarized as reported in the next paragraphs.

Theory of Non-dimensional Groups in Film Effectiveness Studies This section aims to bring clarity to the best way of presenting data to scale film effectiveness. Indeed, the very existence of a discussion on this topic points to lack of clarity. The work includes a detailed dimensional analysis to define the set of non-dimensional groups which influence the film effectiveness. Based on a physical interpretation of the problem, four groups are defined and their influence is *independently* investigated in a parametric study with the aid of extensive RANS and LES simulations.

Development of a scalar tracking method for rapid optimization of film cooling systems This section presents a method to accelerate CFD optimization of film cooling systems. Despite the progress on the development of design and optimization strategies (e.g. adjoint formulation, improved surrogate modelling, etc.), there is still a considerable benefit that can be gained from the use of reduced-order models for specific film cooling applications. This is mainly due to the considerably large number of CFD simulations necessary to obtain an optimized design. In the case of film cooling of HP-NGVs, this number can be of the order of hundred or even thousand runs (Johnson et al. 2014), depending on the size of the design space. In this regard, the recent development on superposition models to predict film cooling (Thomas 2014) can be combined with standard optimization strategies to perform rapid optimizations of film cooling systems. This thesis exploits the use of scalar tracking models combined to Multi-Objective Genetic Algorithms (MOGA) to optimize film cooling systems. It is shown that the number of CFD simulations can be reduced by at least two orders of magnitude when compared to standard optimization strategies. Limitations of the combined scalar tracking-MOGA approach are also discussed and an optimization test case presented.

Effect of momentum-flux ratio on endwall cooling systems This section describes the experimental and computational study on the effect of momentum flux ratio on NGV endwall cooling systems. Experiments are carried out on a linear, low-speed cascade with engine-realistic combustor simulator from a modern engine geometry. The range of momentum flux ratio tested is designed to span the typical engine range for HP-NGV endwall cooling systems.

Design and development of reverse-pass HP-NGV platforms This section includes the development of a HP-NGV endwall cooling system based on the reverse-pass scheme. The HP-NGV platforms are developed using a bespoke conjugate heat

transfer model. The model includes the prediction of internal and external metal and coolant temperatures as well as an estimation of the aerodynamic loss introduced by the internal cooling system. The work also includes the design and manufacture of the reverse-pass platforms for testing at high speed conditions at the Engine Aero-Thermal (ECAT) facility.

Experimental investigation of reverse-pass HP-NGV platforms This section includes the aero-thermal characterization of novel platform designs based on the reverse-pass cooling scheme. Tests of engine components are performed at engine-matched Reynolds number, Mach number, Biot number, and coolant-to-mainstream pressure ratio, on a full-annulus test section. Detailed overall cooling effectiveness distributions on vane platforms are measured by means of infrared thermography. The novel designs are then compared to the baseline engine platform cooling system.

Chapter 2

Theory of Non-dimensional Groups in Film Effectiveness Studies

The desire to improve gas turbines has led to a significant body of research concerning film cooling optimization. The open literature contains many studies considering the impact on film cooling performance of both geometrical factors (hole shape, hole separation, hole inclination, row separation, etc.) and physical influences (effect of density ratio, momentum flux ratio etc.). Film cooling performance (typically film effectiveness, under either adiabatic or diabatic conditions) is almost universally presented as a function of one or more of three commonly used non-dimensional groups: blowing—or local mass flux—ratio; density ratio; and momentum flux ratio. Despite the abundance of papers in this field, there is some confusion in the literature about the best way of presenting such data. Indeed, the very existence of a discussion on this topic points to lack of clarity. In fact, the three non-dimensional groups in common use are not independent of each other making aspects of this discussion rather meaningless, and there is at least one further independent group of significance that we can find no mention of in the literature. The purpose of this chapter is to bring clarity to this issue of correct scaling of film cooling data. It is shown that the film effectiveness is a function of eleven (additional) non-dimensional groups. Of these, seven can be regarded as boundary conditions for the main flow path, and should be matched where complete similarity is required. The remaining four non-dimensional

groups relate specifically to the introduction of film cooling. These can be cast in numerous ways, but we show that the following forms allow clear physical interpretation: the momentum flux ratio, the blowing ratio; the temperature ratio; and the heat capacity flux ratio. Two of these parameters are in common use, a third is rarely discussed, and the fourth is not discussed in literature. To understand the physical mechanisms that lead to each of these groups being independently important for scaling, we isolate the contribution of each to the overall thermal field with a parametric numerical study using 3D RANS and LES. The results and physical interpretation are discussed.

The work in this chapter is object of a journal article (Ornano and Povey 2018).

2.1 Introduction

In a simple analysis of the gas turbine—in which the impact of cooling flows is neglected—for a given compression ratio and compressor outlet temperature, overall thermal efficiency increases with increasing turbine entry temperature (TET). Using more sophisticated analyses, which count the impact of cooling flows, is possible to show that the efficiency gain associated with higher TET is quite modest for a given material temperature capability. This is because of the thermal and aerodynamic cycle penalties associated with internal and film cooling. Thus, despite improvements in material technology, much of the effort in HP turbine optimization surrounds aerothermal optimization of the cooling system. The vast majority of experimental work, and indeed a considerable proportion of computational work, is conducted at physical conditions that are different from the engine (typically lower temperature and pressure). It is rare in these studies for all relevant non-dimensional groups to be simultaneously matched to engine conditions. Compromises therefore have to be made in the scaling of experiments. Despite the significant body of work on this topic,

there is still discussion in the literature about the best way of scaling film effectiveness experiments and data. In some cases the non-independence of certain redundant non-dimensional groups is neglected, making the discussion of the relative importance of these groups somewhat meaningless. Other independent groups are often ignored, leading to scaling differences that mean the simulated system is only a partial representation of the engine situation. The purpose of this chapter is to bring clarity to the full set of non-dimensional groups required for engine similarity in experiments or numerical simulations of film cooling, explain the physical significance of each group, and quantify the error introduced when only partial scaling is achieved.

2.1.1 Dimensional analysis of film cooling: literature review

2.1.2 Practice in experiments

Non-dimensional parameters in common use in the literature to represent film performance characteristics are: blowing (or mass flux) ratio, BR; momentum flux ratio, I; and density ratio, DR. The impact of blowing ratio and density ratio on film cooling was investigated by Sinha et al. (1992). They showed that at low blowing ratios (i.e. low local mass flux ratios), the jet was attached to the surface and the centreline film effectiveness was primarily a function of the blowing ratio; for higher blowing ratios, the jet detached (and potentially reattached) and the film effectiveness was also strongly dependent on the density ratio (because of its effect on momentum flux ratio). Thole et al. (1990) describe the momentum flux ratio as the appropriate parameter to characterize the flow structure (attached, separated, etc.) of the cooling jet close to the hole. Haas et al. (1991) agree that penetration of a jet is mainly a function of the momentum flux ratio and injection angle (their study included different geometries).

Thole et al. (1990) defined the range of momentum flux ratio for which a row of cylindrical jets (with 35 degrees inclination angle) was separated or attached. They found that a complete jet detachment occurred for $I > 0.8$, whereas a fully attached jet was found for $I < 0.4$. In the range $0.4 < I < 0.8$, cooling jets were found to separate and subsequently reattach. In their review paper, Bogard and Thole (2006) observed similar effects.

Pedersen et al. (1977) measured the film effectiveness downstream of a row of cylindrical jets for different density ratios. At low blowing ratio (BR = 0.2), they found that the film effectiveness was approximately constant for density ratios in the range DR = 0.8 to 4. The conclusion was that at this BR, the jets were well attached to the wall and the film effectiveness was primarily function of BR. At higher BR, they showed that better film effectiveness was reached for higher DR, at fixed BR. This was attributed to the reduced tendency of the jets to separate, due to lower momentum flux associated with higher density ratio.

Shiau et al. (2016) carried out an experimental work to study endwall film effectiveness distributions on an annular NGV sector with laidback fan-shaped and cylindrical holes using the pressure sensitive paint (PSP) technique. The test matrix included experiments at three values of the mass flow ratio, each of them at two different density ratios. They concluded that the lateral coverage was improved by increasing the density ratio, for a given mass flow ratio. This was attributed to the reduced momentum flux ratio. Prost and Acharya (1991) performed temperature and heat flux measurements in a film-cooled, heated cascade of nozzle guide vanes. Tests were conducted for three values of blowing ratio, each of them at three values of the density ratio. They found that jets spreading was improved for higher DR. This was attributed to reduced momentum flux ratio.

Some studies, such as by Vinton et al. (2017), report results from a single cylindrical and fan-shaped hole, as a function of three parameters: blowing ratio, density

ratio, and momentum flux ratio. They compared two tests at the same momentum flux ratio and different density ratios (DR = 1 and DR = 4). Differences in the lateral spreading of the jet were observed: the higher density (DR = 4) jet had improved lateral spreading in the near-hole region and reduced film effectiveness on the downstream region compared to the lower density ratio case (DR = 1). This may be attributed to greater mass flux. A recent work on scaling parameters has been presented by Rutledge and Polanka (2014). They performed a computational study to evaluate the effect of a number of scaling parameters on adiabatic film effectiveness and heat transfer coefficient for a single hole located on a turbine blade leading edge. Results indicated that thermal properties such as heat capacity and thermal viscosity are important when scaling experimental work to engine-representative conditions. They described the importance momentum flux ratio for predicting the trajectory of the film and of heat capacity ratio for the level of film effectiveness. Greiner et al. (2014) computationally investigated the non-dimensional parameters important when scaling from ambient to engine temperatures. They found that, in addition to blowing ratio, momentum flux ratio and density ratio, the mainstream and coolant Reynolds numbers should be matched for accurate scaling of film performance. When matching BR, I, DR, and Pr, between ambient experimental conditions and engine temperatures, the simultaneous matching of both mainstream and coolant Reynolds numbers was, however, not possible. The authors found that matching the coolant Reynolds number led to an improved scaling between the two situations.

In summary, we find the following from reviewing the literature in this area:

(i) there is good agreement about the importance and physical significance of momentum flux ratio as the dominant parameter for aerodynamics, or jet trajectory, in the near hole region;

(ii) there is confusion in a considerable number of papers of the interrelationship of blowing ratio, density ratio, and momentum flux ratio. These parameters are

not—from the point of view of similarity—truly independent, and discussion should not imply they are;

(iii) there is very limited awareness—and then only in very recent papers—of the importance of specific heat capacity ratios on film effectiveness;

(iv) most discussions of scaling are somewhat partial, in that a complete set of independent non-dimensional groups—and a discussion of their relative importance in experiments with incomplete scaling—appears not to have been presented;

(v) the physical significance/interpretation of scaling parameters is rarely discussed;

(vi) there is some confusion over the complete independent set of scaling parameters, how they arise, and how best to choose a set which allows clear physical interpretation of film cooling data.

The purpose of this chapter is to bring additional clarity to the problem of defining the correct scaling parameters for film cooling data, understand sensitivities in a properly controlled (orthogonally separated) numerical study, and add physical interpretation of each parameter so its individual effect may be better understood.

2.2 Dimensional Analysis

For the situation of a film-cooled adiabatic wall there are 16 physical quantities that define the problem:

$$p_{01}, T_{01}, c_{p1}, \gamma_1, \mu_1, k_1, p_{02}, T_{02}, c_{p2}, \gamma_2, \mu_2, k_2, p, T_w, s, L, \tag{2.1}$$

where $p_0, T_0, \gamma, k, p, T_w$, and L are the total pressure, total temperature, heat capacity, isentropic exponent, thermal conductivity, static pressure, wall temperature, surface streamwise coordinate, and the characteristic length downstream the cooling holes,

respectively. The subscripts 1 and 2 refer to mainstream and coolant conditions, respectively. Figure 2.1 shows the physical situation and parameters of influence.

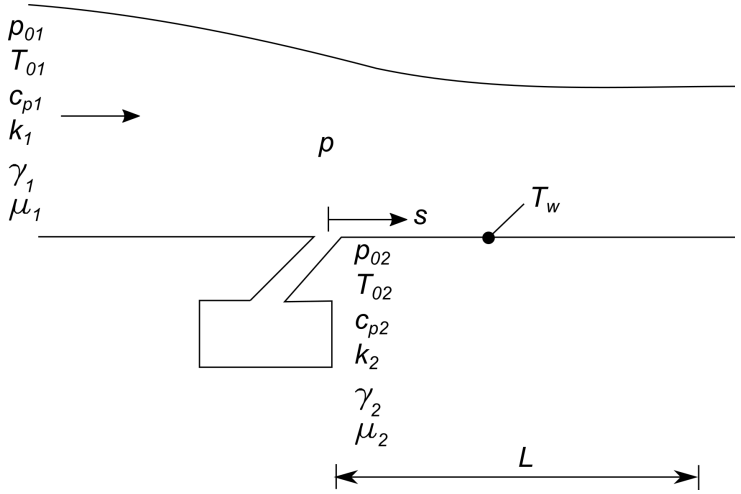


Figure 2.1: Physical situation and parameters of interest for a film-cooled adiabatic wall.

The problem contains four dimensions (mass, length, temperature and time) and we therefore expect—by the Buckingham Pi theorem—that not less than 12 non-dimensional groups will be required to fully describe the system. That is:

$$\pi_{12} = f\left(\pi_1, \pi_2, ..., \pi_{11}\right). \tag{2.2}$$

Making film effectiveness the subject, a dimensional analysis confirms the possibility of the following form:

$$\frac{T_{01} - T_w}{T_{01} - T_{02}} = f\left(\frac{p_{02} - p}{p_{01} - p}, \frac{\gamma_2\left(\gamma_1 - 1\right)}{\gamma_1\left(\gamma_2 - 1\right)}, \frac{c_{p2}}{c_{p1}}, \frac{T_{02}}{T_{01}}, \frac{\mu_2}{\mu_1}, \frac{k_2}{k_1}, \frac{s}{L}, Re_1, Pr_1, M_1, \gamma_1\right), \tag{2.3}$$

where the subject is $\pi_{12} = \eta$. The remaining terms will be discussed in the following sections. Here we have taken as direct a route as possible from the underlying variables, and cast the non-dimensional groups in the simplest possible form. We now seek to manipulate certain groups into forms which are recognizable (e.g. blowing ratio, momentum flux ratio, etc.) or into forms which we believe have clear physical

interpretation (e.g. temperature ratio, specific heat capacity flux ratio, etc.) For incompressible flow, the momentum flux ratio can be expressed as follows:

$$I \equiv \frac{\rho_2 u_2^2}{\rho_1 u_1^2} = \frac{p_{02} - p}{p_{01} - p} = \pi_1. \tag{2.4}$$

That is, momentum flux ratio is interchangeable with the first group in Equation 2.3.

Noting that for incompressible flow ($\rho \sim \rho_0$ and $T \sim T_0$):

$$\frac{\rho_2}{\rho_1} = \frac{p_{02}}{p_{01}} \frac{T_{01}}{T_{02}} \frac{cp_1}{cp_2} \frac{\gamma_2}{\gamma_1} \frac{\gamma_1 - 1}{\gamma_2 - 1}, \tag{2.5}$$

we can write the blowing ratio (BR) in terms of the momentum flux ratio (I) and the density ratio as follows:

$$BR \equiv \frac{\rho_2 u_2}{\rho_1 u_1} = \left(I \frac{\rho_2}{\rho_1} \right)^{\frac{1}{2}} = \left(\frac{p_{02}}{p_{01}} \frac{T_{01}}{T_{02}} \frac{cp_1}{cp_2} \frac{\gamma_2}{\gamma_1} \frac{\gamma_1 - 1}{\gamma_2 - 1} \frac{p_{02} - p}{p_{01} - p} \right)^{\frac{1}{2}} = \pi_2. \tag{2.6}$$

We replace $\frac{\gamma_2}{\gamma_1} \frac{\gamma_1 - 1}{\gamma_2 - 1}$ in Equation 2.3 with the blowing ratio. The influence on the film performance of different heat capacities for mainstream gas and coolant gas is accounted for by the *specific heat capacity flux ratio*, E, which we defined by:

$$E \equiv \frac{\rho_2 u_2 c_{p2}}{\rho_1 u_1 c_{p1}} = BR \frac{c_{p2}}{c_{p1}} = \pi_3. \tag{2.7}$$

We replace $\frac{c_{p2}}{c_{p1}}$ in Equation 2.3 with the specific heat capacity flux ratio.

The last parameter of interest is the temperature ratio, defined by :

$$TR \equiv \frac{T_{02}}{T_{01}} = \pi_4, \tag{2.8}$$

which arises naturally in the dimensional analysis leading to Equation 2.3.

The relationship implied by Equation 2.3 is recast in the following 12 dimensionless

groups:

$$\frac{T_{01}-T_w}{T_{01}-T_{02}} = f\left(I, BR, E, TR, \frac{\mu_2}{\mu_1}, \frac{k_2}{k_1}, \frac{s}{L}, Re_1, Pr_1, M_1, \gamma_1\right). \tag{2.9}$$

The first four groups on the right hand side have been discussed:

$$\pi_1 = I = \frac{p_{02}-p}{p_{01}-p},$$

$$\pi_2 = BR = \left(I\frac{\rho_2}{\rho_1}\right)^{\frac{1}{2}} = \left(\frac{p_{02}}{p_{01}}\frac{T_{01}}{T_{02}}\frac{cp_1}{cp_2}\frac{\gamma_2}{\gamma_1}\frac{\gamma_1-1}{\gamma_2-1}\frac{p_{02}-p}{p_{01}-p}\right)^{\frac{1}{2}}, \tag{2.10}$$

$$\pi_3 = E = BR\frac{c_{p2}}{c_{p1}},$$

$$\pi_4 = TR = \frac{T_{02}}{T_{01}}.$$

Groups π_5 and π_6 relate to fluid property ratios between the mainstream and coolant gas:

$$\pi_5 = \frac{\mu_2}{\mu_1}, \pi_6 = \frac{k_2}{k_1}. \tag{2.11}$$

Group π_7 is the non-dimensional surface length:

$$\pi_7 = \frac{s}{L}. \tag{2.12}$$

Groups π_8, π_9, and π_{10} are the Reynolds number, Prandtl number, and Mach number for the mainstream flow.

$$\pi_8 = Re_1 = \sqrt{\frac{2R_1T_1\left(p_{01}-p\right)}{p}}\frac{L}{\mu_1},$$

$$\pi_9 = Pr_1 = \frac{\mu_1 c_{p1}}{k_1}, \tag{2.13}$$

$$\pi_{10} = M_1 = \frac{\sqrt{2\left(p_{01}-p\right)}}{\sqrt{\gamma_1}}.$$

The mainstream Reynolds number (π_8) and mainstream Mach number (π_{10}) are

based on incompressible relations. This is justified by the fact that both were held constant in this study, and that the Mach number was in the incompressible regime.

Group π_{12} is the subject, the adiabatic film effectiveness.

$$\pi_{12} = \frac{T_{01} - T_w}{T_{01} - T_{02}}, \tag{2.14}$$

The independent dimensionless groups are by definition orthogonal and can be varied independently to study the effect of each of them on film effectiveness. In particular we are interested in groups π_1 to π_4. We believe these to be the dominant groups in relationship 2.9 (recast from relationship 2.3), and also to be amenable to physical interpretation.

To isolate the sensitivity of $\pi_{12} = \eta$ to groups π_1 to π_4, we construct a numerical experiment in which we individually vary one of the groups π_1 to π_4, whilst keeping all the remaining groups (π_1 to π_{11}) constant. Thus, four studies are set-up in which we study the impact of groups π_1 to π_4 in isolation. The 11 independent groups in Equation 2.9 have a non-linear relationship with the 15 independent variables of Equation 2.2.

$$p_{01}, T_{01}, c_{p1}, \gamma_1, \mu_1, k_1, p_{02}, T_{02}, c_{p2}, \gamma_2, \mu_2, k_2, p, T_w, s, L.$$

Our object in each of the four studies is to maintain ten of the groups (π_1 to π_{11}) constant whilst varying one of π_1 to π_4. Examining the equations, we determine that this is possible for fixed values of the following input variables

$$p_{01}, T_{01}, c_{p1}, \gamma_1, p, s, L. \tag{2.15}$$

These *fixed independent variables* were not changed during our study. The re-

maining independent variables

$$p_{02}, T_{02}, c_{p2}, \gamma_2, \mu_1, \mu_2, k_1, k_2 \tag{2.16}$$

were regarded as *free independent variables* in this study and were adjusted to achieve the required test matrix of π_1 to π_{11}.

The free independent variables in Equation 2.16 were solved iteratively in MATLAB by using the function *lsqnonlin*. The combined variable sets (7 fixed, 8 free) were used as boundary conditions for CFD simulations. The outputs from the CFD simulations were the adiabatic wall temperature distributions T_w, representing the dependent group in the study ($\pi_{12} = \eta$).

2.3 Region-specific scaling parameters

In this section, we introduce the concept that the relative importance of scaling parameters is region-specific (with respect to the cooling hole). That is, the dominant independent groups depend on the location with respect to the cooling hole. We introduce the definitions of the *binary region* (near hole), *intermediate region*, and *mixed-out region*. These regions are used in the analysis section later in this chapter.

Binary region

The binary region, or near-hole region, is the part of the flow in which the films are *substantially unmixed*. This is identified by a locally binary distribution of the film effectiveness (values close to 0, 1). In this region, the circumferential (line) average can take any value, and depends on the local aerodynamics, film cooling hole spacing etc. For a given geometry, the flow structure (jet trajectory, and to a lesser extent the jet mixing rate) is primarily controlled by the momentum flux ratio. The most

obvious structural difference is between an attached and a separated jet, but more generally, the momentum flux ratio determines the jet trajectory.

It is argued that in the binary region the dominant scaling parameter local for film effectiveness is the momentum flux ratio, because it is the most important parameter for aerodynamic similarity between scaled physical situations.

Mixed-out region

We define the mixed-out region to be the region far downstream of the hole where the circumferential variation of film effectiveness is small in comparison to the circumferential average value of film effectiveness. We arbitrarily take a value for the ratio of variation to average value of 0.2.

In this region, we argue that the mixed-out film effectiveness depends primarily on the balance of heat storage capacity of the coolant and mainstream. We believe that similar mixing can be assumed in many real situations (in which other independent groups are changed), because far downstream of the hole the mixing is dominated by the mainstream turbulence and not by, for example, near hole flow-structure differences or turbulence differences caused by changes in coolant momentum flux ratio.

In the mixed-out region the dominant scaling parameter for film effectiveness is the specific heat capacity flux ratio, E, because this represents the relative heat storage capacity of the coolant and mainstream flows.

Intermediate region

We define the intermediate region more loosely to be the region between the binary region (approximately binary values of film effectiveness) and the mixed-out region (low circumferential variation in film effectiveness). In the intermediate region, films are partially mixed and the film effectiveness is neither entirely dependent on momentum flux ratio (due to the primary dependence on flow structure) nor specific heat

capacity flux ratio (due to the primary dependence on heat storage capacity). In this transition region, the behavior is complex and significantly dependent on more than one of the key scaling groups.

Figure 2.2 shows the CFD domain used in this study, with the locations of the binary, intermediate and mixed-out post-processing lines, at 0, 24 and 48 diameters downstream of the holes respectively. The domain includes 15 cooling holes with a spacing-to-diameter ratio of 2 and fixed hole inclination of 30 degrees.

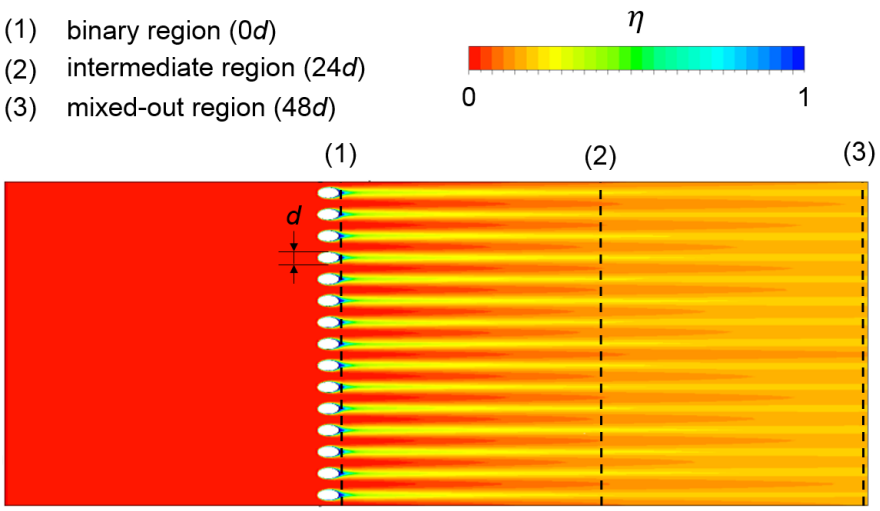


Figure 2.2: CFD domain showing the binary, intermediate and mixed-out post-processing lines.

2.4 Test matrix

The CFD experiments were designed to investigate the independent effect of changing π_1, π_2, π_3 and π_4 (I, BR, E and TR). For each group π_1 to π_4, ten values around a nominal design point were investigated whilst maintaining the remaining ten of the independent groups (of π_1 to π_{11}) constant.

2.5 Numerical methods for RANS simulations

2.5.1 Solver settings

The numerical analysis was performed using ANSYS-CFX, with Reynolds Averaged Navier-Stokes (RANS) settings and *high resolution* discretization (second order accurate) for both advection and turbulence terms. The k-ω SST turbulence model with automatic wall functions and reattachment prediction model was used. The flow conditions were incompressible.

2.5.2 Mesh and boundary conditions

The computational domain is shown in Figure 2.3a. Meshing was performed using BOXERMesh. The domain included a single row of 15 cylindrical cooling holes fed by a single coolant plenum. The cooling holes had an inclination of 30 degrees with respect to the horizontal plane and a diameter of 2 mm. The hole spacing was $2d$ (where d is the hole diameter). Mesh interfaces at the cooling hole inlets were managed using the GGI option to allow individual cooling holes mass flow rates to be determined during post-processing. The mesh had approximately 5.2 million hybrid cells (hexahedral and tetrahedral). In the near wall region, the grid was refined with 10 prism layers with an expansion ratio of 1.2. The value of the non-dimensional wall distance—based on the Reynolds number, z^+—was approximately 1 on most of the wetted surfaces, with only some localized areas having a maximum value below 5. Figure 2.3b shows the detail of the cooling hole mesh.

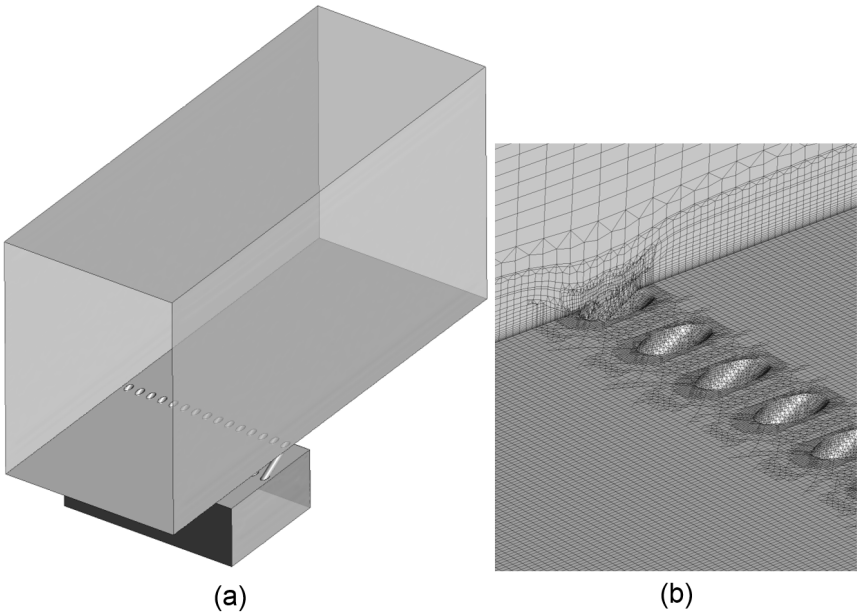


Figure 2.3: Computational domain (a) and detail of the cooling hole mesh (b) used for RANS simulations.

The inflow boundary condition was imposed at the domain inlet, with specified total pressure, total temperature, flow direction (normal to the inlet boundary), and turbulence intensity ($Tu = 10\%$). A value of static pressure was imposed at the domain outlet. The coolant was fed from the plenum, with fully-meshed cooling holes (Figure 2.3b). Total pressure and total temperature were specified at the plenum inlet. The sides of both the main passage and plenum domain were set to be periodic. For the 40 computational experiments that comprise this study, the mainstream and coolant gas properties were varied to set relevant values of non-dimensional groups. This was done using the pre-processing routine CFX-Pre. The coolant flow was simulated as a foreign gas, with a molar fraction of 1.0 at the coolant plenum inlet and 0.0 at the mainstream domain inlet. Thus, coolant properties could be varied independently of the mainstream gas. The CFD solution was performed by considering an additional transport equation for the coolant fluid.

2.5.3 Grid independency study

A grid independency study was performed in order to select the minimum adequate mesh resolution to capture all significant flow features. The domain was solved with four levels of grid refinement on the cooled wall: M1, M2, M3, and M4, with total element counts 4.3×10^6, 4.7×10^6, 5.2×10^6 and 7.2×10^6, respectively. The grid refinement was performed by halving the edge of the squared cells close to the cooled wall for each refinement level. The test conditions were: $E = I = \mathrm{BR} = 1.000$ and $\mathrm{TR} = 0.800$. The results were compared in terms of lateral distribution of film effectiveness in the binary ($x = 0d$), intermediate ($x = 24d$) and mixed-out ($x = 48d$) regions. Figure 4 shows the results of the grid independency study. Approximate grid independency was achieved for 5.2×10^6 elements (mesh M3 in Figure 4) for all the three regions. This mesh resolution was chosen for the RANS calculations in the current study.

2.6 Numerical methods for LES

Due to the large design space of the parametric study presented in this chapter, RANS simulations were used for the majority of the study, and capture many of the important aspects of the flow mixing despite being based on turbulence models rather than direct simulation. To explain more complex local mixing phenomena, higher-fidelity LES simulations are used to complement the RANS simulations where necessary.

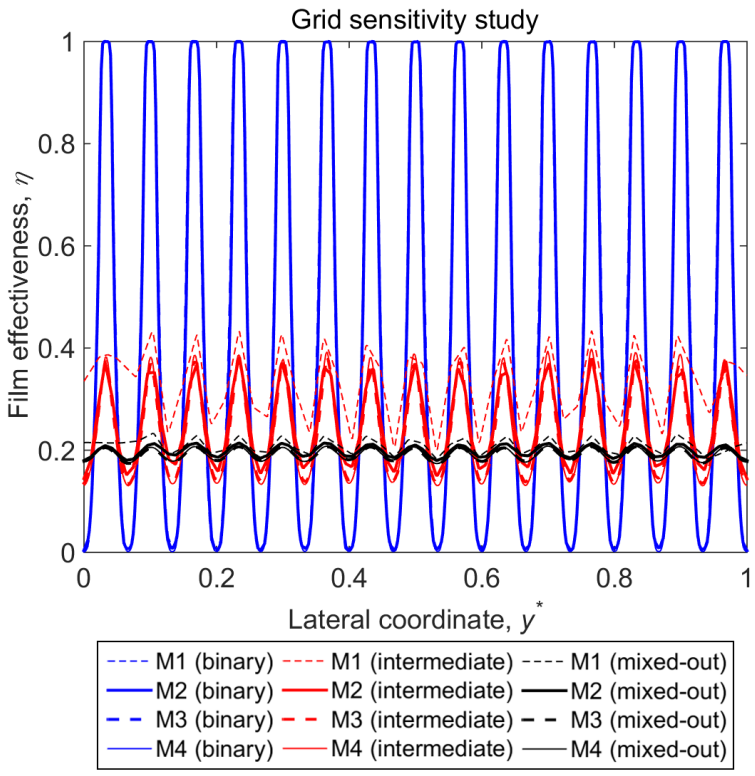


Figure 2.4: Film effectiveness distribution in the binary, intermediate and mixed-out regions obtained during the grid sensitivity study. The test conditions were: $E = I =$ BR $= 1.000$ and TR $= 0.800$.

2.6.1 Solver settings

The LES sub-grid WALE model (Nicoud and Ducros 2014) was selected for the present work, with second order discretization in space and time. As for the RANS setup, the fluid domain was simulated by using two gas species: mainstream gas and coolant. An additional transport equation for the mainstream gas was solved each iteration and the coolant mass fraction was directly computed from its solution. The mainstream mass fraction was set to 1.0 at the domain inlet and to 0.0 at the plenum inlet. The ideal gas law was selected for the equation of state. The flow conditions were incompressible.

2.6.2 Mesh resolution for LES study

An additional computational domain was meshed for the LES including only three cooling holes. The entire volume mesh was highly refined, with enhanced resolution from the wall up to $5d$ in the direction perpendicular to the wall, and spanning the entire axial length of the domain. The global mesh had 17 million hybrid (tetrahedral/hexahedral) cells, as shown in Figure 2.5. Particular attention was paid on the near-wall region, which had 15 prism layers in the boundary layer region with an expansion ratio of 1.2. The value of the non-dimensional distance from the wall based on the Reynolds number (Δz^+) was kept less than 1 over the entire cooled wall and cooling hole surfaces. The grid spacing on the x (streamwise) and y (lateral) directions were set to be Δx^+, $\Delta y^+ < 10$, as recommended by Tyacke and Tucker (2015) on LES best practice.

The level of refinement of the mesh close to the wall was set to the order of the Kolmogorov microscale for length, $\eta = (\nu^3/\varepsilon)^{1/4}$, the scale below which energy is dissipated primarily by viscous forces. Parallel steady simulations were used to estimate the value of turbulent eddy dissipation rate, ε. The Kolmogorov microscale was found to be approximately $\eta = 2.35 \times 10^{-5}$ m. The mesh size for the layer closest to the cooled wall was set smaller than the Kolmogorov microscale for length, with the first cell height being $\Delta z_1 = 1.5 \times 10^{-5}$ m . The resolved energy spectrum is given in the next section.

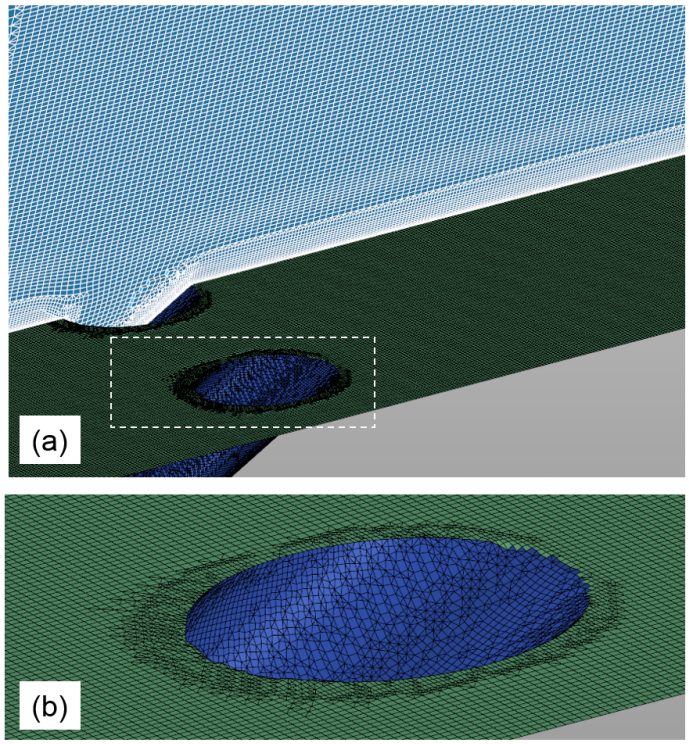


Figure 2.5: Computational mesh employed for LES simulations. (a) slice of volume mesh and (b) detail of the cooling hole grid.

2.6.3 Choice of time step

In cross-flows, the Strouhal number typically takes a value of approximately 0.2 (Lin et al. 2015). The corresponding vortex shedding frequency is calculated as follows:

$$f = \frac{St\,U}{D} \sim \frac{0.2\,U}{D}, \tag{2.17}$$

where D is the hole diameter and U is the freestream velocity magnitude. Considering the current geometry and flow conditions, a shedding frequency of approximately 3.4 kHz is estimated. In order to obtain enough resolution to resolve the unsteady flow features, a time step of 10^{-5} s was selected for the present study.

2.6.4 Frequency analysis

Figure 2.6a shows the amplitude spectrum obtained by performing a Fast Fourier Transform (FFT) of the velocity signal acquired with a monitor point located approximately $1.0d$ downstream the centerline of the central cooling hole. The velocity frequency spectrum is dominated by a peak at 3.5 kHz, very close to the vortex shedding frequency predicted based on the typical Strouhal number for jets in cross-flow.

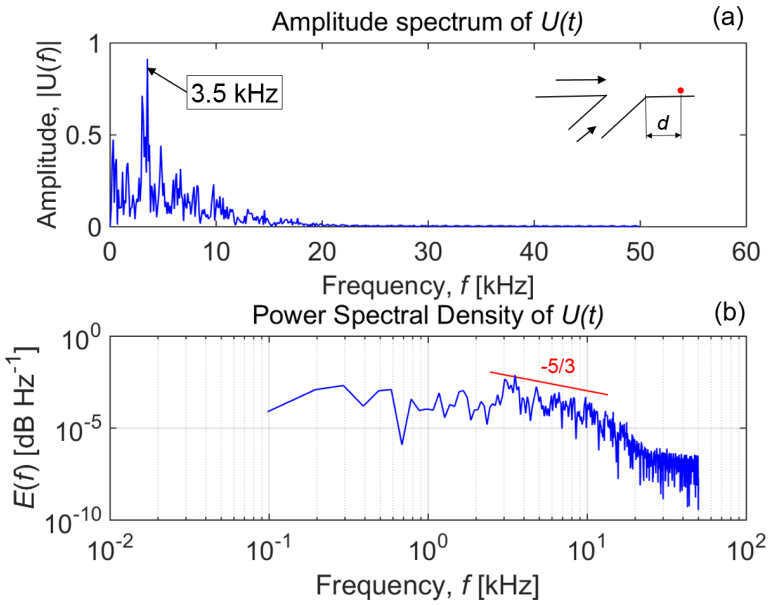


Figure 2.6: (a) Fast Fourier Transform; (b) Power Density Spectrum of the transient velocity signal downstream the central cooling hole.

The power density spectrum (PSD) of the velocity time-signal is depicted in Figure 2.6b as function of the frequency, f. At low frequencies ($f < 1$ kHz), the energy is associated with the largest eddies which typically are dependent on the geometry of the domain. At higher frequencies ($1 < f < 10$ kHz), the spectrum is defined by the inertial subrange, identified by the relationship $E(f) \propto f^{-5/3}$. The eddies in this region have the highest energy content. The smallest eddies, which are responsible for the viscous dissipation, occur at the highest frequencies ($f > 10$ kHz). Figure 2.6b shows that the LES results were able to predict the inertial subrange (by direct comparison with the slope equal to -5/3 in this region), and the most relevant flow

features were therefore fully resolved.

2.7 Results and discussion

In this section we discuss the significance of the key non-dimensional groups in turn, and in particular consider how the relative importance of these groups differs in the binary, intermediate, and mixed out regions of flow. First we consider the momentum flux ratio, I.

2.7.1 Momentum flux ratio

In the region close to the cooling holes (the binary region), the coolant jets are substantially unmixed and the film effectiveness has a binary-like distribution assuming values close to either 0 or 1. In this region the film effectiveness distribution has a strong dependence on the momentum flux ratio, because this controls the aerodynamic state of the jets i.e. the coolant trajectory and shape of the jet.

Figure 2.7 shows RANS results for the lateral distribution of film effectiveness on the binary region as a function of the momentum flux ratio (in the range $0.500 < I < 2.000$). The normalized lateral coordinate y^* is defined as $y^* = (y - y_{min})/(y_{max} - y_{min})$. The film effectiveness decreases with increasing momentum flux ratios as the region in which jets are detached increases as a proportion of the surface area.

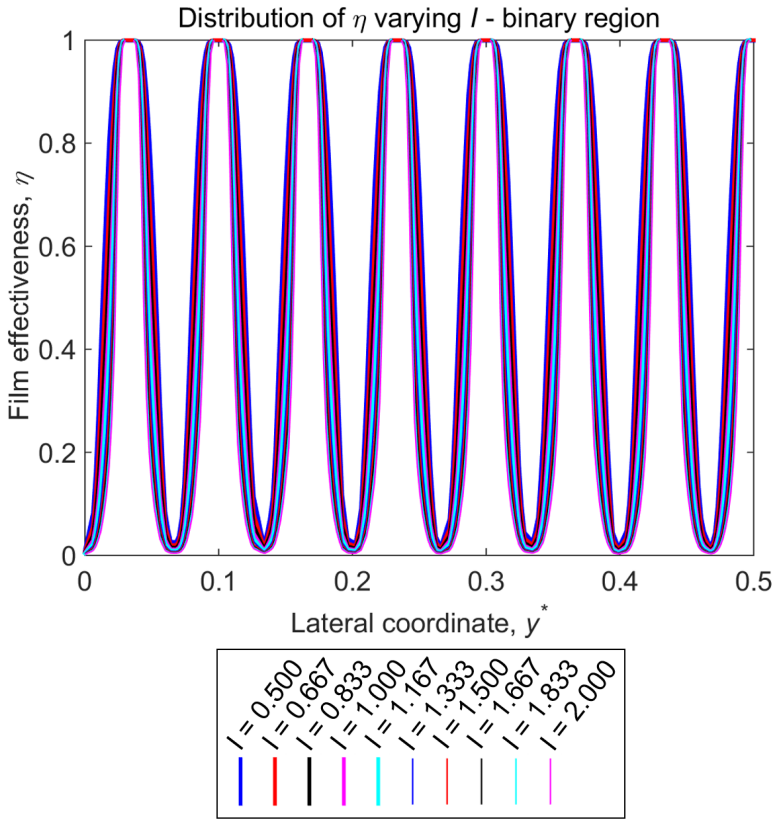


Figure 2.7: Lateral distribution of η in the binary region ($x = 0d$) as a function of I. Test conditions were: $E = 1.000$, BR $= 1.000$ and TR $= 0.800$.

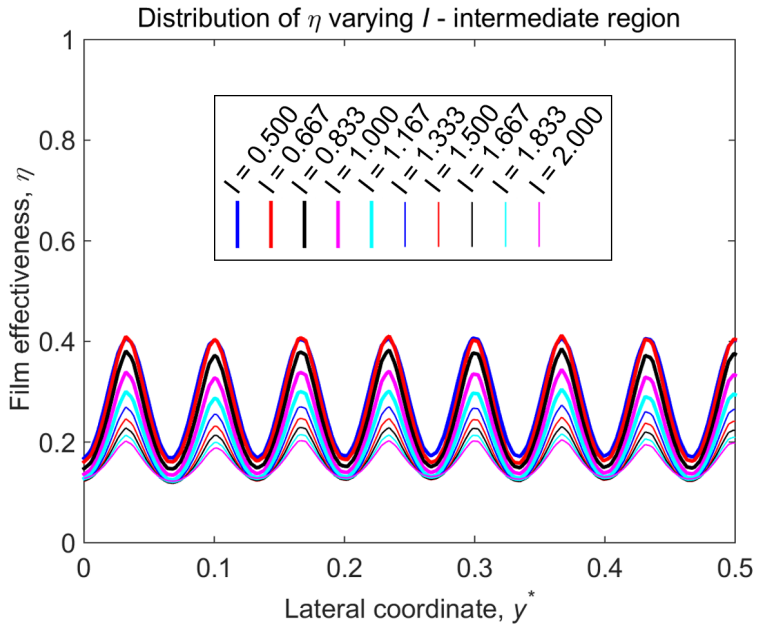


Figure 2.8: Lateral distribution of η on intermediate region ($x = 24d$) as a function of the I Test conditions were: $E = 1.000$, BR $= 1.000$ and TR $= 0.800$.

Results for the intermediate region (at an axial location of $x = 24d$) are shown in Figure 2.8. In this region, there is still significant dependence of the film effectiveness distribution on I. For increasing I, the peaks in film effectiveness are reduced from a value of approximately 0.4 to a value of approximately 0.2. This region is beyond the reattachment point, so the effect is likely associated with changes in mixing caused by different initial coolant trajectories.

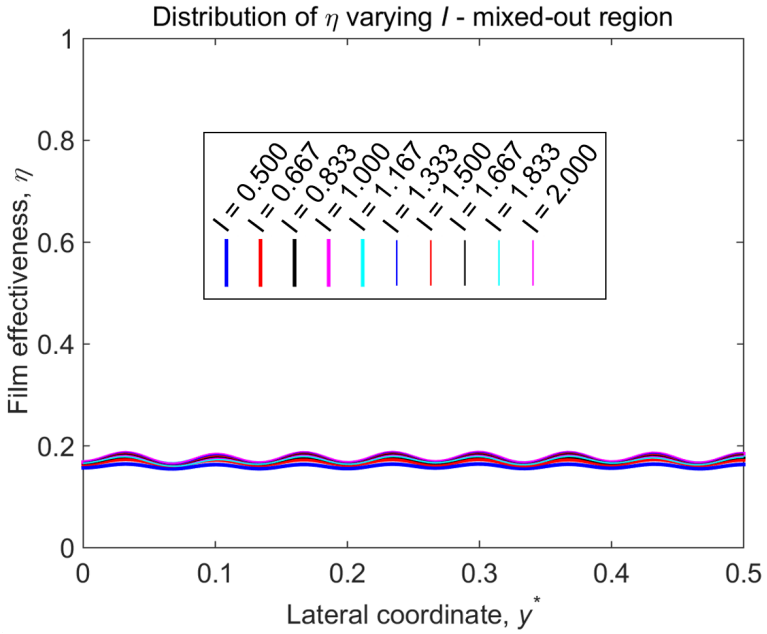


Figure 2.9: Lateral distribution of film effectiveness on mixed-out region ($x = 48$d) as a function of the momentum flux ratio Test conditions were: $E = 1.000$, BR $=$ 1.000 and TR $= 0.800$.

Results for the mixed-out region ($x = 48d$) are shown in Figure 2.9. In this region the lateral film effectiveness distribution is essentially independent of I. The curves have a similar average value (approximately 0.18), and relatively similar variation from the mean. For constant specific heat capacity flux ratio, blowing ratio and temperature ratio, the film effectiveness is insensitive of the momentum flux ratio in the mixed-out region.

Laterally averaged film effectiveness values for the three regions are shown Figure 2.10, normalized with respect to the case with the nominal momentum flux ratio $I =$

1.000. As discussed, the laterally averaged film effectiveness has a strong trend with I in both binary and intermediate regions (normalized variation from the baseline value of 0.25 to -0.25), indicating a large sensitivity to I in these regions. The sensitivity of the laterally averaged film effectiveness to I in the mixed-out region is considerably lower (-0.09 to $+0.005$).

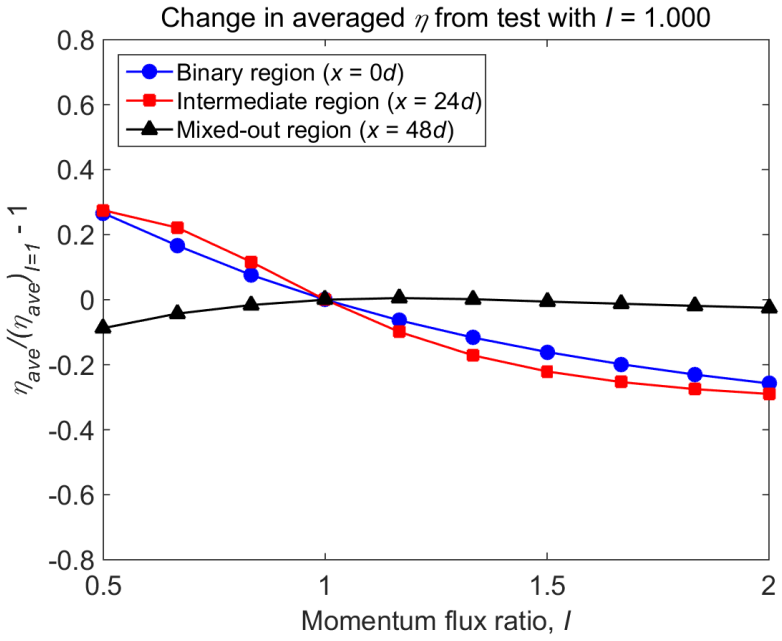


Figure 2.10: Lateral average of film effectiveness as function of I. Test conditions were: $E = 1.000$, BR $= 1.000$ and TR $= 0.800$.

In summary, the binary and intermediate regions show strong sensitivity of the laterally averaged film effectiveness to I, but in the mixed out region there is little sensitivity. This is the first evidence of region-dependence of the relative importance of different scaling parameters.

2.7.2 Specific heat capacity flux ratio

In this section we consider the significance of the specific heat flux capacity ratio, E.

Results of RANS simulations for the binary region ($x = 0d$) are shown in Figure 2.11 for test conditions $I = 1.000$, BR $= 1.000$ and TR $= 0.800$, and for values of

E in the range $0.500 < E < 2.000$. In the binary region, the film effectiveness is essentially unaffected by the value of E. Here the coolant flow is relatively unmixed, and changes in heat capacity flux have a small effect on the essentially binary value the film effectiveness takes.

Results for the intermediate region ($x = 24d$) are shown in Figure 2.12. The peak in film effectiveness is enhanced from a value of approximately 0.25 to a value of approximately 0.55 as E is increased from 0.500 to 2.000. The average value of film effectiveness also increases in the same direction. As E increases (independent of the momentum flux ratio, blowing ratio, and temperature ratio), the relative (with respect to the mainstream) potential of the coolant to store heat is enhanced. Thus, for the same amount of heat transferred into the lower—cooler—layers of flow, the proportional temperature change is reduced.

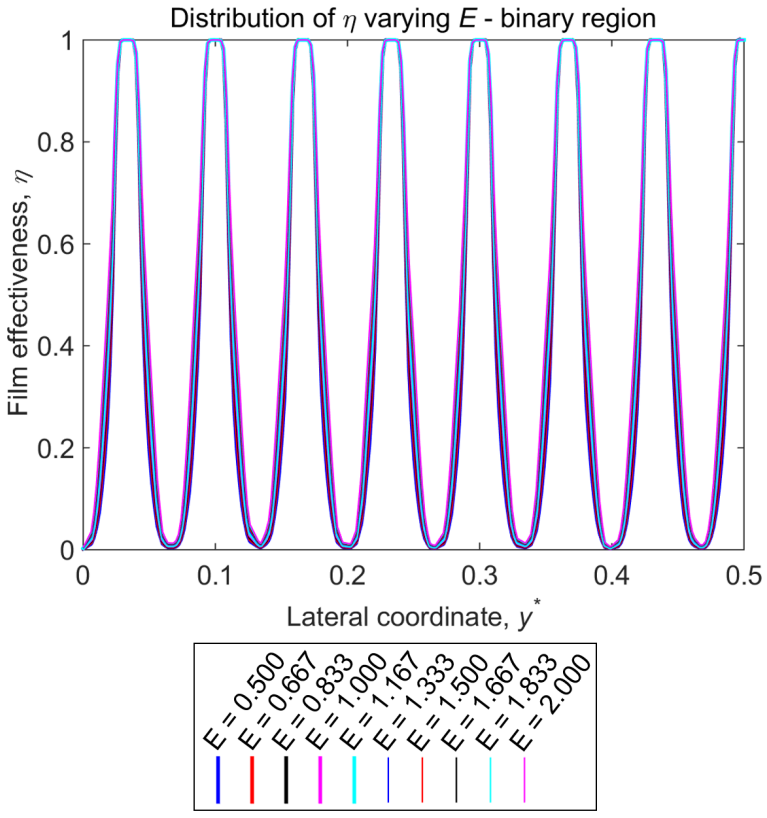


Figure 2.11: Effect of specific heat capacity flux ratio on film effectiveness on the binary region ($x = 0d$). Test conditions were $I = 1.000$, BR $= 1.000$ and TR $= 0.800$.

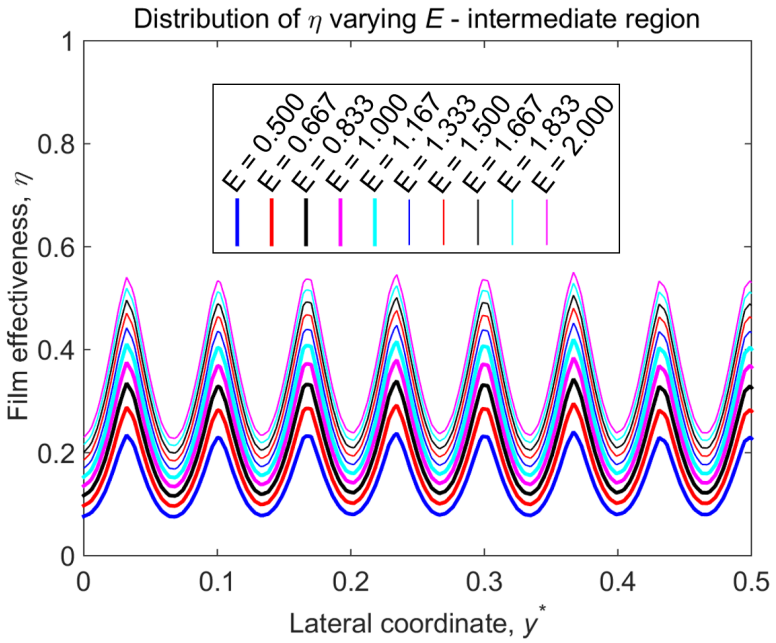


Figure 2.12: Effect of specific heat capacity flux ratio on film effectiveness on the intermediate region ($x = 24d$). Test conditions were $I = 1.000$, BR = 1.000 and TR = 0.800.

The same effect is even more pronounced in the mixed-out region, where the balance of specific heat capacity fluxes (between coolant and mainstream) are the primary controlling parameter for the mixed-out temperature. This is shown in Figure 2.13 ($x = 48d$). In this region, there is a relatively weak lateral variation in the film effectiveness, but a strong and approximately proportional relationship between the lateral mean value of the film effectiveness and E. The mean value increases from approximately 0.10 to approximately 0.30 as E increases from 0.500 to 2.000.

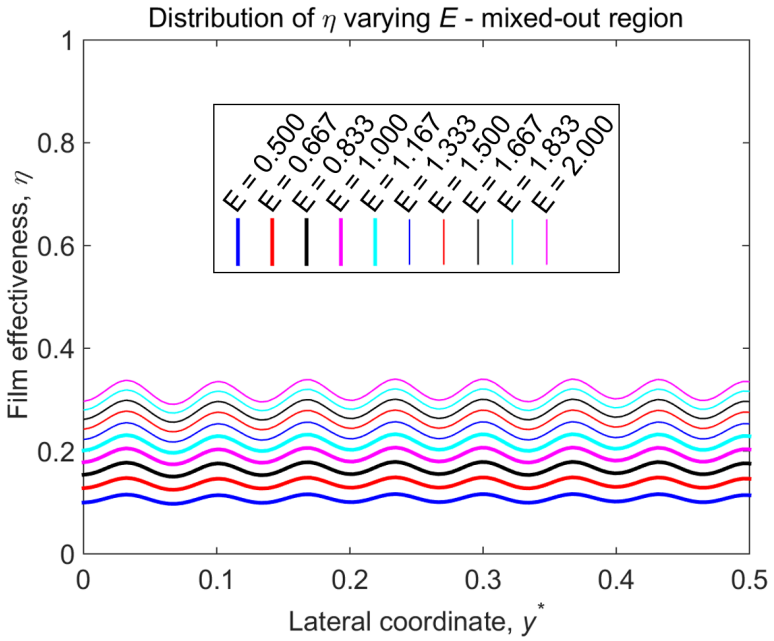


Figure 2.13: Effect of specific heat capacity flux ratio on film effectiveness on the mixed-out region ($x = 48d$). Test conditions were $I = 1.000$, BR $= 1.000$ and TR $=$ 0.800.

Figure 2.14 shows the laterally averaged film effectiveness as a function of the specific heat capacity flux ratio for the three regions (binary, intermediate and mixed-out), normalized with respect to the case of $E = 1.000$. The dependence of film effectiveness on E is very weak in the binary region (variation less than 0.1 over the wide range of E). In the intermediate and mixed-out regions, a strong and approximately proportional dependence of the laterally averaged film effectiveness on E is observed: -0.4 to 0.55 in the intermediate region and -0.4 to 0.6 in the mixed out region.

In summary, in un-mixed regions of flow, the balance of specific heat capacity flux is unimportant, because it has little effect on the approximately binary values the film effectiveness takes (here it is the structure of the flow that is important, as has been described). In contrast, where the flow is relatively mixed (in both the intermediate and mixed out regions) the relative heat storage capacity of the coolant and mainstream flows is important, and there is an approximately linear relationship

between the laterally averaged film effectiveness and the heat capacity flux ratio.

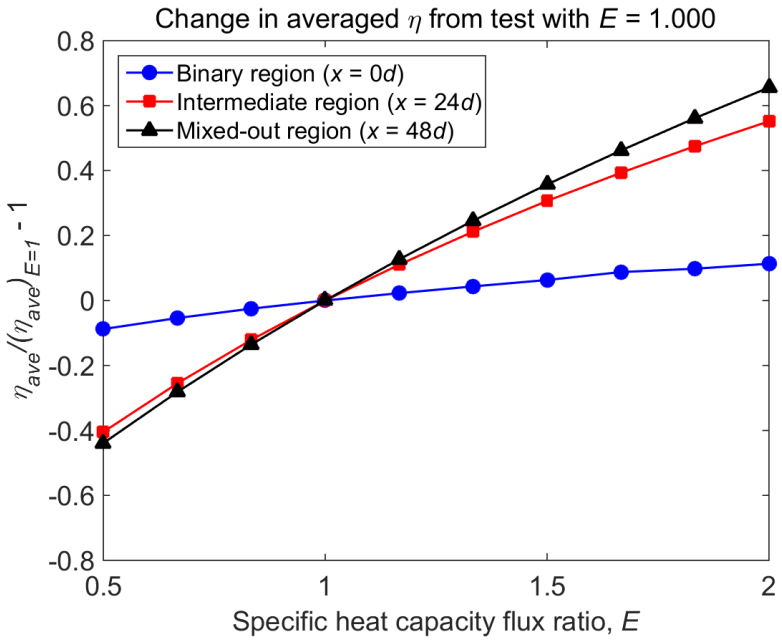


Figure 2.14: Lateral average of film effectiveness as function of E. Test conditions were: $I = 1.000$, BR $= 1.000$ and TR $= 0.800$.

2.7.3 Blowing ratio – main physical processes

The blowing ratio describes the coolant-to-mainstream mass flux ratio for a given geometry. This is a commonly-used parameter in turbomachinery literature primarily because it relates to the input controls in an experiment (generally the mass flow is measured) or the cycle cost (aerodynamic and thermodynamic) in engine applications (generally directly proportional to the coolant mass flow), rather than because it has particularly useful physical significance in controlling the flow field. Indeed, it is relatively hard to understand what physical role this parameter plays when other non-dimensional parameters are held strictly constant, and, likewise, the sensitivity of the flow field to blowing ratio (when all other non-dimensional groups are held constant) is much lower than to other groups.

An important way in which blowing ratio *does* differ from other non-dimensional parameters, is in the way it describes the initial *volume flow rate ratio* or *velocity ratio*

of the cooling jet with respect to the mainstream flow (when coolant is expanded to the local static pressure at the hole exit). The physical significance of the velocity ratio, in particular, is that it is directly related to the rate of shear at the interface between the emerging film cooling jet, and the mainstream flow. The shear at this interface causes the jet to destabilize, which affects the rate of mixing with the mainstream flow.

These ratios describe aspects of the film that are distinct from those described by the specific heat capacity flux ratio (a measure of the degree to which the film resists temperature change on mixing or heat exchange) or the momentum flux ratio (which determines trajectory). We therefore describe blowing ratio in terms of the corresponding *volume flow rate ratio* or *velocity ratio*.

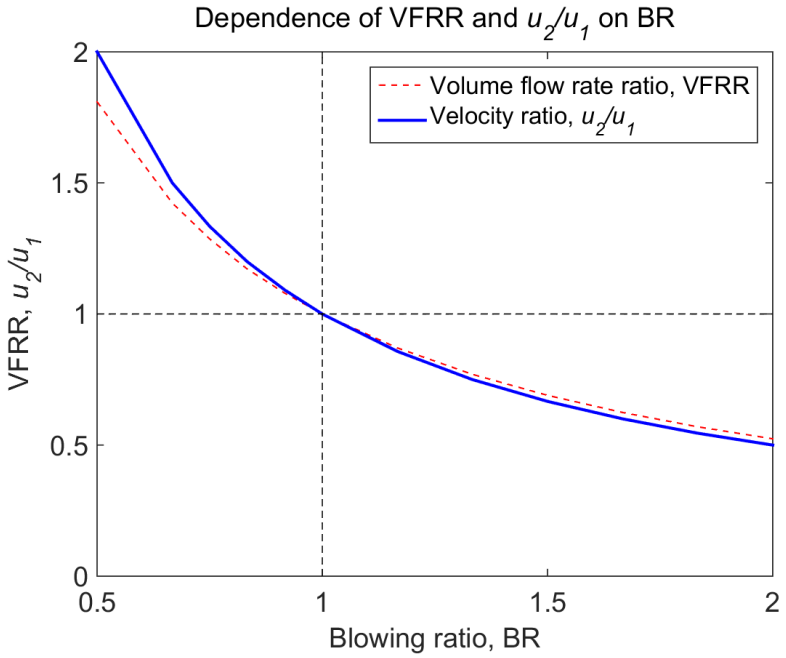


Figure 2.15: Normalized volume flow rate ratio (normalized by the value at BR = 1) and absolute velocity ratio u_2/u_1 as a function of blowing ratio. Test conditions were $I = 1.000$, $E = 1.000$, and TR = 0.800.

For fixed momentum flux ratio, specific heat capacity flux ratio, and temperature ratio, the blowing ratio and volume flow rate ratio at the hole exit are inversely proportional. It follows that the velocity ratio is also inversely proportional to blowing

ratio. These slightly counter-intuitive results are derived in Appendix A. These relationships are shown in Figure 2.15.

Figure 2.16 shows the tangential distribution of η as a function of the blowing ratio in the binary region ($x = 0d$). Across the blowing ratio range $0.500 < BR < 2.00$ the data collapse onto a single trend, indicating that there is essentially no sensitivity of film effectiveness to blowing ratio in the binary region. Recalling that shear-induced destabilization of the jet tube is the main mechanism for mixing, this result is perhaps unsurprising for real flows or fully resolved simulated flows: in the vicinity of the hole exit the flow for all velocity ratios (or blowing ratios) the jet is not sufficiently destabilized for there to be a measurable difference between the cases. This will be discussed more in the context of LES simulations presented later in this section. So far as the RANS simulations are concerned, despite the lower fidelity of the modelling, a similar argument can be applied with respect to the shear-induced mixing of the flow (in this case introduce in the time averaged flow via a turbulence model).

Figure 2.17 shows the tangential distribution of η as a function of the blowing ratio in the intermediate region. In this region, the film effectiveness is found to have a fairly significant dependence on the blowing ratio. The laterally averaged film effectiveness decreases for values between BR = 0.500 and BR = 0.833. For values above BR = 0.833 (BR = 1.000 upwards), the film effectiveness increases monotonically. Although the complex trend is hard to explain, the fact that in there is significant dependence of η on BR in the intermediate region alone (and not in the binary region, or—as we will see—the mixed-out region) is consistent with the argument that shear-induced destabilization of the jet tube is the main mechanism for mixing. It is in the intermediate region that there is onset of destabilization, and where there is most rapid mixing of the coolant jet with the mainstream flow. The extent and nature of the shear-induced destabilization leads to complex flow

effects which change the structure of the counter-rotating vortex pair, and lead to differences in the separation-reattachment behavior *for the same momentum flux ratio and same value of other non-dimensional parameters.* These complex phenomena are incompletely described with RANS modelling, but some of the driving mechanism (for example, shear leading to a counter-rotating vortex pair structure) are qualitatively captured. The mechanisms are discussed in more detail in the later section on LES results.

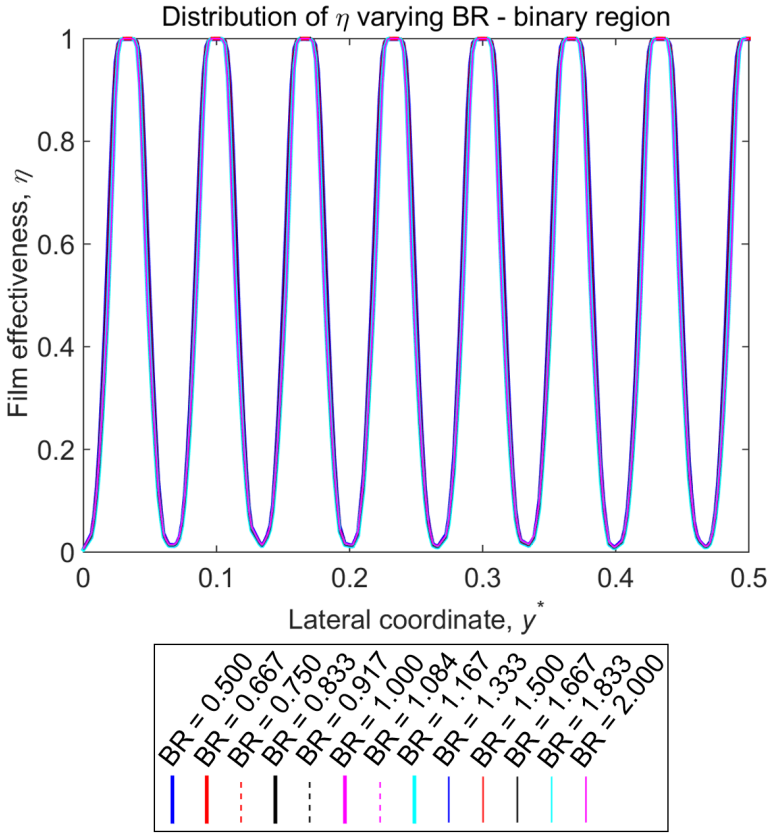


Figure 2.16: Effect of blowing ratio on film effectiveness in the binary region ($x = 0d$). Test conditions were $I = 1.000$, $E = 1.000$ and TR = 0.800.

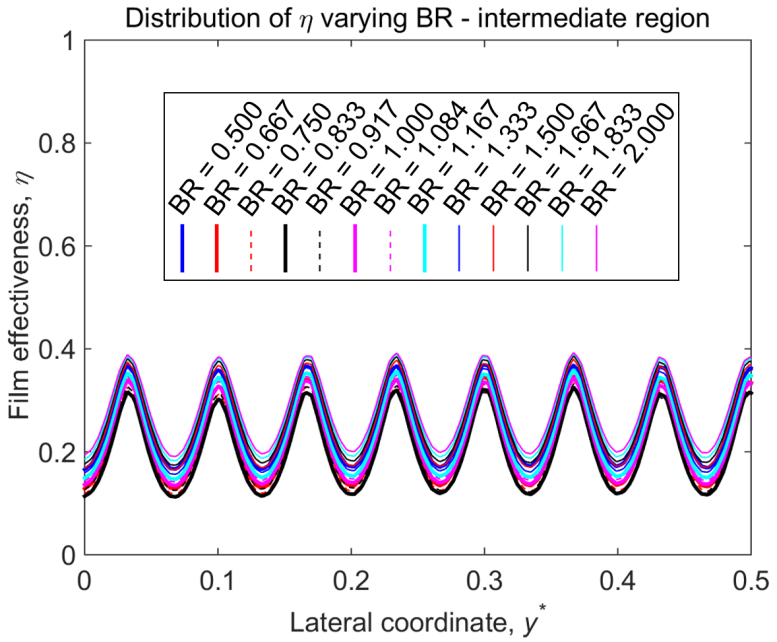


Figure 2.17: Effect of blowing ratio on film effectiveness in the intermediate region ($x = 24d$). Test conditions were $I = 1.000$, $E = 1.000$ and TR = 0.800.

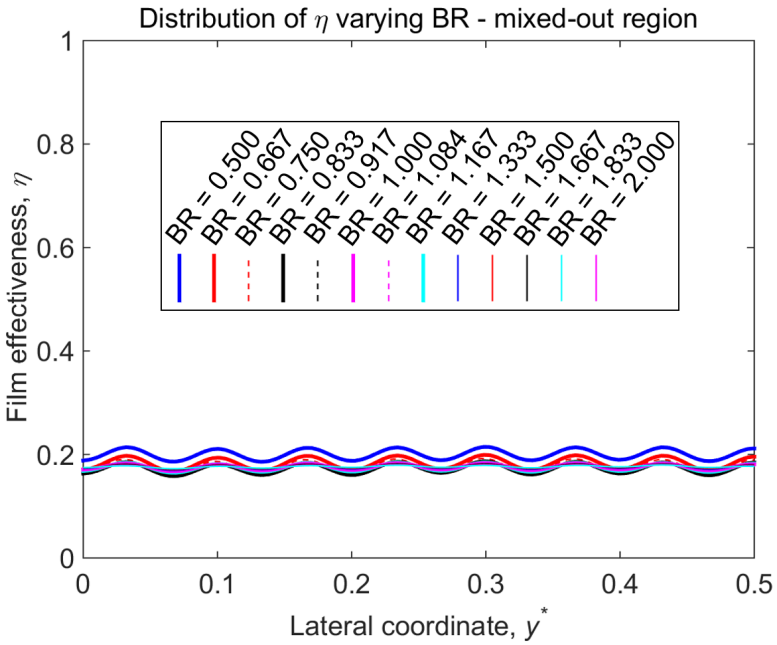


Figure 2.18: Effect of blowing ratio on film effectiveness in the mixed-out region ($x = 48d$). Test conditions were $I = 1.000$, $E = 1.000$ and TR = 0.800.

Figure 2.18 shows the effect of BR on the lateral film effectiveness distribution in the mixed-out out region ($x = 48d$). There is little sensitivity of film effectiveness

to BR in this region. This is expected—the rate of shear in the mixed-out region is low, and structures generated by velocity differences in the upstream flow (in the intermediate region) have largely dissipated. Structurally speaking, the flow in the mixed out region is very insensitive to the blowing ratio.

Figure 2.19 shows laterally averaged film effectiveness as a function of blowing ratio, normalized with respect to a nominal condition at BR = 1.000. In the binary region, velocity difference driven shear forces have not yet taken hold, and there is little shear-induced structural difference between the flow fields. There is essentially no sensitivity of the laterally averaged film effectiveness to the blowing ratio across a wide range of conditions. In the mixed out region we have the same result (almost no sensitivity of laterally averaged η to BR). Here shear induced destabilization has occurred some way upstream, and both the initial velocity discrepancy between coolant and mainstream and the structural differences generated by shear-initiated flow phenomena are largely mixed out. It is only in the intermediate region that there is significant sensitivity of laterally averaged η to BR. In the intermediate region, the laterally averaged η varies between a minimum value of approximately -0.1 (BR = 0.833) and a maximum value of approximately 0.27 (BR = 2.000). In this region, shear-induced destabilization of the jet leads to complex flow structures that affect the rate of coolant jet and mainstream flow mixing, and influence the way in which the mixing region interacts with the wall (extent and shape of bulk flow features like the counter-rotating vortex pair).

It is tempting to hypothesize that the reason the film effectiveness in the intermediate region rises either side of a minimum at approximate BR = 0.8 (see trend in Figure 2.19) is because this is a *minimum shear point*. Either side of this point, there is greater velocity discrepancy between the two flows, more rapid destabilization of the flow, greater mixing, and therefore the possibility of enhanced near wall coolant flow in the partially mixed intermediate region. Indeed, with reference to Figure 2.15,

and noting that the lay angle of the holes with respect to the surface is 30 degrees, the minimum velocity discrepancy point taking account of the hole angle is probably close to BR = 0.8. Although there is some reasonableness in this physical argument, it is not fully supported by all of the evidence. We believe the effect warrants further investigation, however.

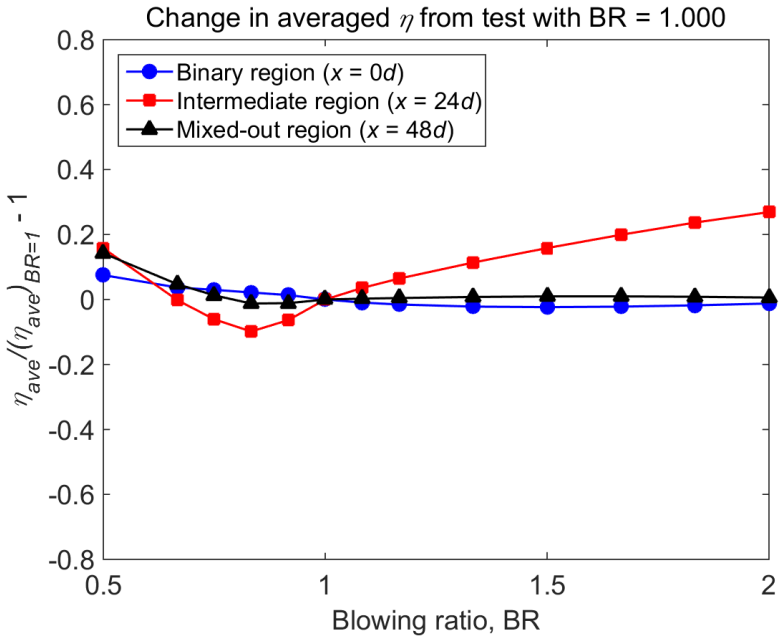


Figure 2.19: Lateral average of film effectiveness as function of blowing ratio. Test conditions were $I = 1.000$, $E = 1.000$ and TR = 0.800.

Figure 2.20 shows visualizations (obtained with RANS simulations) of iso-surfaces at $\eta = 0.3$ for BR = 0.500, BR = 1.000, and BR = 2.000. The trajectory of the coolant "tubes" is similar for the three cases—a result that is expected because the momentum flux ratio is the same in these simulations. The "volume" (what is visualized is the combined effect of the ejected volume flow rate ratio—see Figure 2.15—and the mixing rate) of the tubes are different however, with the volume of the BR = 0.500 case being substantially greater than for the BR = 1.000, consistent with the result of Figure 2.15. The reduction in "volume" for the BR = 2.000 case (as compared to the BR = 1.000 case) is less evident, most likely because of shear-induced structural changes in the flow field, which affect the mixing.

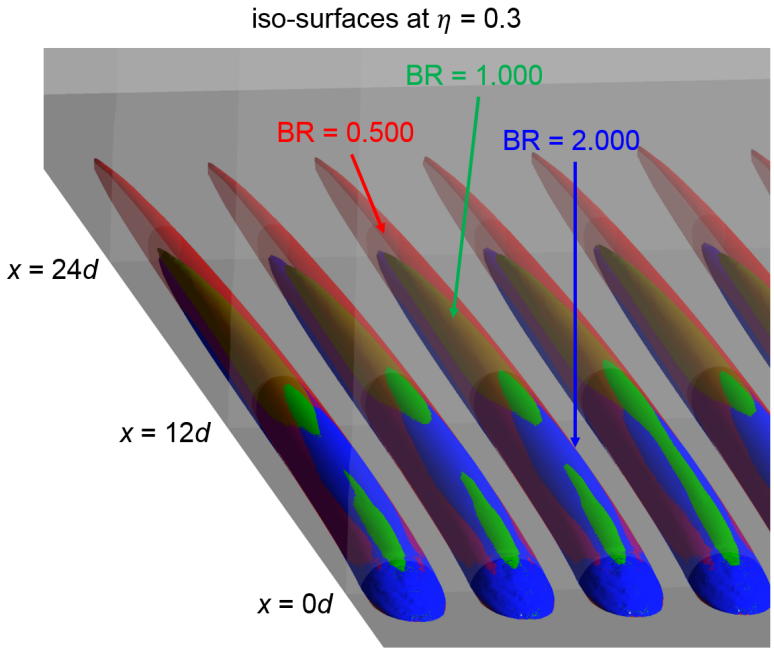


Figure 2.20: Iso-surfaces at $\eta = 0.3$ for BR = 0.500 (red surface), BR = 1.000 (green surface), and BR = 2.000 (blue surface).

As a thought experiment, we now consider the impact of volume flow rate changes on the "tube" containing the coolant.

At the hole exit, the jet cross section is determined by the hole area, angle, and momentum flux ratio—increased volume flow rate is carried by velocity excess within the tube (compared to the mainstream) rather than by an increased cross-sectional area of the tube. The effect of *friction* without mixing would be to gradually slow the tube to the velocity of the mainstream. As the velocity excess is reduced (eventually to zero), the tube cross sectional area would increase. In the *fully accommodated state* (no velocity discrepancy with respect to the mainstream flow—i.e. a hypothetical case of the velocity accommodation through shear, without turbulent mixing) the cross-sectional area of the tube would take a ratio with respect to the nominal cross-sectional area equal to the normalized volume flow rate ratio presented in Figure 2.15. That is for BR = 0.500, the cross-sectional area would be twice that of the baseline case (BR = 1.000), and for BR = 2.000, the cross-sectional area would be half that

of the baseline case.

This argument is important for understanding the driving influence of the volume flow rate ratio, but in practice, this effect is conflated with two additional competing drivers. Firstly, *even in the absence of turbulent mixing* (recall the thought experiment above), when higher-than-nominal (for example) volume flow rate ratio is achieved by decreasing the blowing ratio independent of other parameters, *the energy flux ratio within the tube remains the same as for the nominal case* (by definition). For a hypothetical tube for which velocities are fully accommodated and where the tube cross sectional area has increased on account of the increased volume flow rate, but in which there is no turbulent mixing, the resistance of the tube contents to changes in temperature due to heat transfer are reduced (over given linear penetration distance) because the specific heat capacity flux per unit area in the tube is lower than the nominal case (by definition the specific heat capacity flux *within the tube* is the same as the nominal case). This effect tends to mitigate the impact of changes in volume flow rate (at both ends of the scale). The second effect is that higher-than-nominal (and, by the same token, lower-than-nominal) volume flow rate ratios have associated higher velocity differences (between coolant "tube" and mainstream flow) at the point of ejection into the mainstream flow. These velocity differences cause shear, which leads both to destabilization of the jet and associated turbulent mixing, but also structural differences in the way the jet develops (extent of counter-rotating vortex pair etc.). Naturally, these effects are extremely complex in nature.

Further visualizations of the flow are presented in Figure 2.21 and Figure 2.22 which show iso-lines of $\eta = 0.3$ and $\eta = 0.4$, respectively, at planes $x = 0d$, $12d$, $24d$, for cases of BR = 0.500, BR = 1.000, and BR = 2.000.

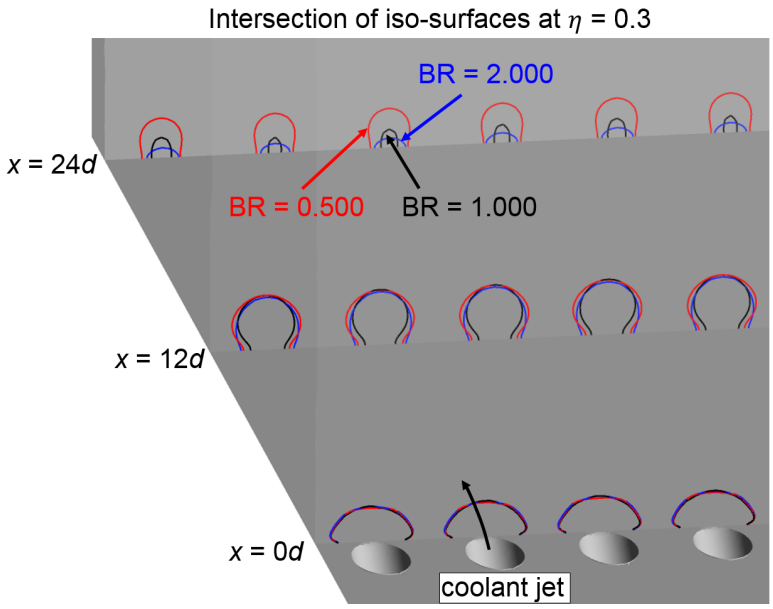


Figure 2.21: Iso-lines at $\eta = 0.3$ at several axial planes for the cases with BR = 0.500, 1.000 and 2.000.

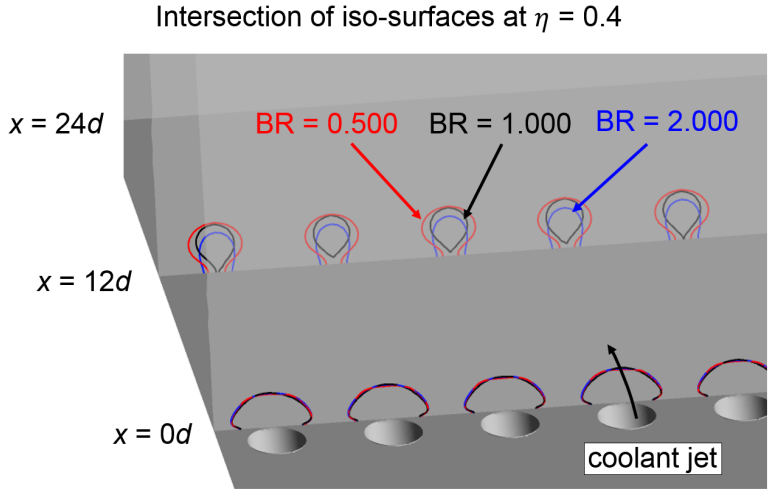


Figure 2.22: Iso-lines at $\eta = 0.4$ at several axial planes for the cases with BR = 0.500, 1.000 and 2.000.

At the coolant hole exit (binary region), the iso-lines of effectiveness for the three blowing ratios collapse to the same trend, indicating that the volume flow has essentially no effect in this region. This is consistent with the argument that at the hole exit, the jet cross section is determined by the hole area, angle, and momentum

flux ratio, with increased volume flow rate being carried by velocity excess within the tube.

In the intermediate region ($x = 12d$ and $x = 24d$) there is a significant change in the both the tube size and shape with BR. Iso-lines for both $\eta = 0.3$ and $\eta = 0.4$ show substantially larger tube volume for BR = 0.500 compared to the case with BR = 2.000. The tube volumes for the BR = 1.000 and BR = 2.000 cases are more similar (in line with Figure 2.15), and the trend is hard to distinguish when conflated with shear-driven structural changes in the flow. Despite caveats associated with structural changes in the flow field due to shear-stress differences, which are discussed in detail below, this is consistent with the general argument regarding the effect of *friction* without mixing. That is, as the tube is gradually slowed (in the case of velocity excess in the coolant, which occurs at lower BR), the tube cross sectional area increases, and in the intermediate region (and also the mixed-out region, but in general other effects are overriding here) the tube cross sectional areas are larger for lower BR due to the associated excess volume flow rate.

Figure 2.23 depicts the adiabatic film effectiveness distribution at $x = 24d$ (intermediate region) for BR = 0.500, 1.000, and 2.000. Iso-lines at $\eta = 0.3$ are marked in the figure. The distribution of η across the flow-normal plane is a strong function of BR, and this affects the lateral distribution at the wall. Although the trends agree with the results presented in Figure 2.19, and demonstrate the effects of increased (at low BR) and decreased (at high BR) volume flow rate, the particular structures are not easy to explain, being the combined result of both volume changes in the mixing jet and shear-induced effects at the jet boundary, the latter leading to three dimensional flow structures.

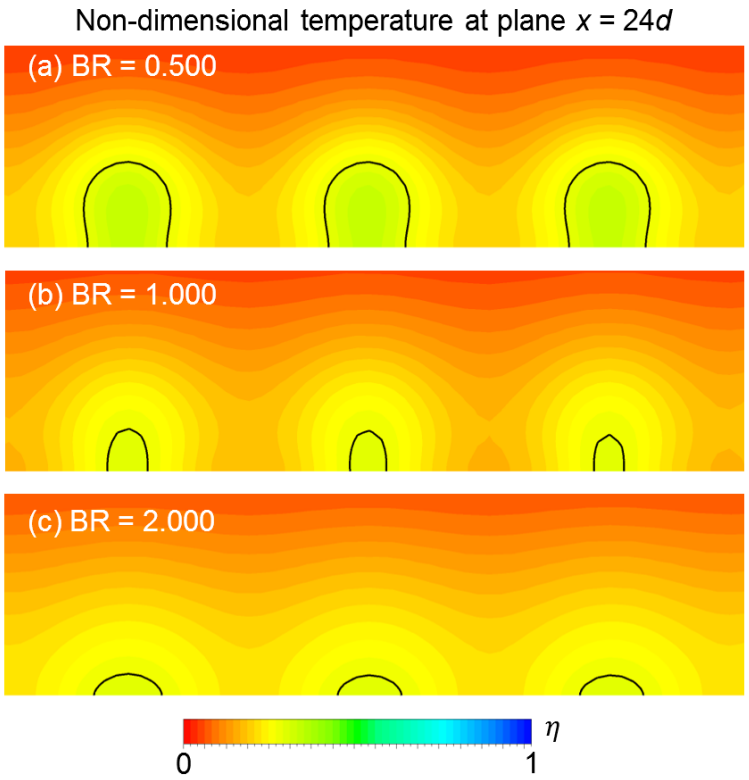


Figure 2.23: RANS results of non-dimensional temperature ($\phi = \frac{T_{01}-T_0}{T_{01}-T_{02}}$) distribution at $x = 24d$ for BR = 0.500, 1.000, and 2.000. Iso-lines at $\eta = 0.3$ are marked with a black line.

2.7.4 Blowing ratio – structural changes caused by shear

Let us now consider how velocity differences caused by changes in blowing ratio introduce different shear profiles, which lead to structural differences in the flow field (changes in jet-destabilization, extent of counter-rotating vortex pair etc.).

Figure 2.24 shows results from RANS simulations visualized by iso-level of Lambda-2 criterion for BR = 0.500, BR = 1.000, and BR = 2.000. Iso-lines with $\eta = 0.4$ (visible only up to $x = 12d$, before the jet mixes with the mainstream and η decays rapidly below 0.4) are also marked in the figure at the plane $x = 0d$ and $x = 12d$, for reference with Figure 2.22. The RANS-predicted secondary flow structures are different for the different BR cases. The axial extent of the counter-rotating vortex decreases for increasing BR (from BR = 0.500 to BR = 2.000). It is clear that the shape of

these, whilst difficult to explain from the contour pattern alone (e.g. Figure 2.23, becomes clearer with reference to the full secondary flow field). When the full flow field is visualized, the complex behaviour of the laterally averaged film effectiveness in the intermediate region (see Figure 2.19) is not unexpected: it is here that there is most shear-induced secondary flow and associated mixing.

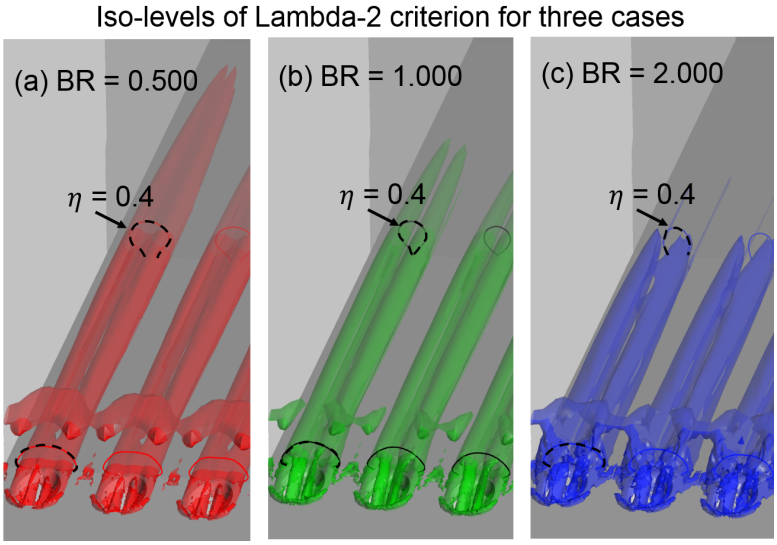


Figure 2.24: Iso-levels of Lambda-2 criterion for the case with BR = 0.500, 1.000 and 2.000. Iso-lines at $\eta = 0.4$ are also marked in the figures at planes $x = 0d$ and $x = 12d$, respectively.

Figure 2.25 shows the laterally mass-averaged distribution of the shear strain rate as a function of normalized wall distance ($z^* = z/d$), for a number of blowing ratios, in the region where the jet first encounters the mainstream: $x = 0d$. It is clear from the figure that the BR has a significant impact on the development of the shear strain rate profile. As we hypothesized in relation to Figure 2.15, maximum shear strain rate at the outer edge of the mixing layer (for a given BR) is a strong function of the velocity discrepancy between the coolant and mainstream flows (for a given BR). This velocity-discrepancy-induced shear is responsible for secondary flows, jet-destabilization and associated mixing effects. We now examine these effects.

We start by considering the case of BR = 1.000, for which the velocity ratio is u_2/u_1

= 1.000, and for which—by definition—the velocity discrepancy is zero (ignoring compound angle effects, which are relatively small). For this case the shear strain rate profile decrease monotonically away from the wall (increasing z^*). The profile is typical of that for a boundary layer, and is well-behaved with no peaks in the region of the coolant jet core (roughly between $0 < z^* < 0.6$). Excluding the high gradient region near the wall (laminar sublayer), the case of BR = 1.000 has the minimum shear strain of all the BR cases tested ($0.500 < BR < 2.000$). This is expected because the initial velocity discrepancy is zero (here we ignore relatively small effects due to angle variation).

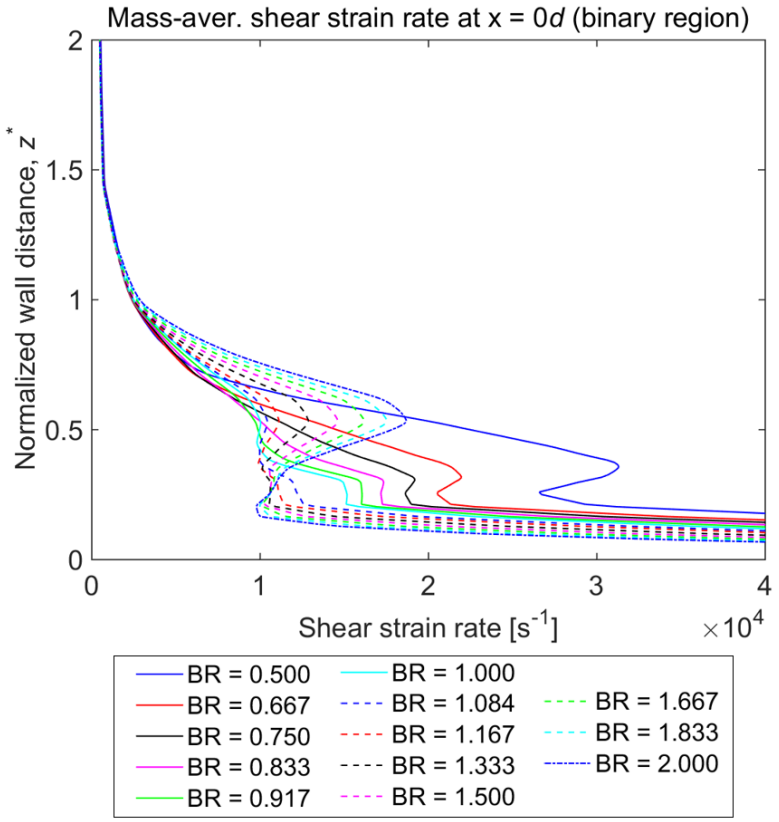


Figure 2.25: RANS results of laterally mass-averaged shear strain rate profiles for various BR at plane $x = 0d$.

For cases with BR > 1.000 there is an increasing velocity discrepancy (see Figure 2.15) caused by relatively slow coolant flow. For the highest case tested—BR = 2.000—the velocity discrepancy is equal to half the mainstream flow velocity. For all

these cases, as BR increases, and as the corresponding velocity discrepancy increases, there is an increasing peak in shear strain rate in the region $0.25 < z^* < 1.0$. This is caused by shear on the outer surface of the jet tube. The approximate location of the peak in shear strain rate is $z^* \approx 0.6$. The baseline value of shear strain rate (BR = 1.000) is approximately 1×10^4 s^{-1}. For the highest case tested—BR = 2.000—the impact of velocity discrepancy is to increase the shear strain rate by 1×10^4 s^{-1} to approximately 2×10^4 s^{-1}.

For cases with BR < 1.000 there is an increasing velocity discrepancy (see Figure 2.15) caused by relatively fast coolant flow. For the lowest case tested—BR = 0.500—the velocity discrepancy is equal to the mainstream flow velocity (i.e. twice the velocity discrepancy for the BR = 2.000 case). In like manner to the previous cases, as BR decreases, and as the corresponding velocity discrepancy increases, there is an increasing peak in shear strain rate in the region $0.25 < z^* < 0.8$. For the lowest case tested—BR = 0.500—the impact of velocity discrepancy is to increase the shear strain rate by 2×10^4 s^{-1} to approximately 3×10^4 s^{-1}.

The increase in shear strain rate is almost exactly twice that for the BR = 2.000 case. This is quantitatively as expected because the velocity discrepancy is twice the magnitude of the BR = 2.000 case.

2.7.5 Temperature ratio

In this section, we consider the effect of changing temperature ratio (TR), T_{02}/T_{01}, when all other groups (10, of 11 in total) are held constant, including the blowing ratio, momentum flux ratio and specific heat capacity flux ratio. To achieve variation in TR whilst maintaining the other groups constant, it is necessary to vary both T_{02} and R_2. The constraints on the system lead to the following interesting results, which are proven, and discussed in some detail, in Appendix B.

(i) The density of the coolant film at the point of issuing from the hole is *not* a

function of TR.

(ii) The density of a *partially mixed* layer of coolant decreases (from a maximum at TR = 1) for temperature ratios *either side of unity.*

(iii) A consequence of (ii) is that the kinematic viscosity increases from a minimum at TR = 1, *either side of a TR of unity* leading to higher momentum diffusivity for both TR > 1 and TR < 1 than for TR = 1. It is worth noting that the constraints on the system mean that dynamic viscosity, which is a fluid property, remains constant with TR.

(iv) A second consequence of (ii) is that the exit-to-inlet volume flow rate ratio across a mixing domain containing the film and a fraction of entrained mainstream gas increases from a minimum at TR = 1, *either side of a TR of unity.* This is equivalent to volume dilation during the mixing process. For TR > 1 and TR < 1 this effect acts to push flow structures—including turbulent structures—further into the main-flow than would be the case for TR = 1.

Results (ii), (iii) and (iv) are particularly interesting and have significant consequences for the behaviour of the mixing film. The results are not intuitive, and the reader is referred to Appendix B for derivations of the results and discussion. The results are developed by way of a control-volume approach, and whilst they are initially counter-intuitive, they are in extremely good agreement (both qualitatively and quantitatively) with the LES results that follow.

We now examine LES results for the following temperature ratios: 0.350, 0.950, 1.520 and 1.995. In these studies blowing ratio, momentum flux ratio and specific heat capacity flux ratio were kept constant, as were the remaining 10 of 11 (in total) non-dimensional groups for this problem. As we will see, the results for mixing layer (as opposed to boundary layer) density ratio, volume flow rate ratio, and kinematic viscosity ratio are in good agreement with the results from the control volume method.

Figure 2.26 shows instantaneous (t = 2 ms) vortex structures (Lambda-2 criterion) for LES for cases with TR = 0.350, 0.950, 1.520, and 1.995. The structures are coloured by the normalized distance from the wall (z^*). The size of turbulent structures (and the intensity, measured by Reynolds stress) increases either side of a TR of unity. This is the result of two effects, volume dilation of the mixing layer either side of TR = 1, and an increase in kinematic viscosity either side of TR = 1, driven by a reduction in density either side of TR = 1. The size and intensity of turbulent structures by visually ranking the images is, in descending order of intensity, TR = 0.350, TR = 1.995, TR = 1.520 and TR = 0.950. This ranking is precisely consistent with the kinematic viscosity ratio (increase in momentum diffusivity in the flow) and volumetric flow rate ratio (dilation effect) ranking in Figure B.4 (Appendix B). This is a satisfying qualitative (the visualizations of Figure 2.26) and semi-quantitative result.

The laterally averaged axial distributions of film effectiveness corresponding to the LES plot of Figure 2.26 are shown in Figure 2.27. As expected, solutions for both TR > 1 and TR < 1 have effectiveness distributions lower than for the case with TR = 0.950 (i.e. TR $\approx$ 1), on account of the enhanced kinematic viscosity ratio *both sides* of TR = 1. Indeed, the ranking of results is pleasingly consistent with the ranking of the kinematic viscosity ratios in Figure B.4 that is, the magnitude of the deficit in film effectiveness in Figure 2.27 (greatest for TR = 0.350, followed by 1.995 followed by 1.520) is ordered according to the surplus in kinematic viscosity (Figure B.4). It is worth noting that there is some sensitivity of the kinematic viscosity ratio in the mixing layer to mixing ratio, $\dot{m}_1/\dot{m}_2$, which *decreases* with axial distance (see Figure B.4) as the film effectiveness reduces. This kinematic viscosity ratio is a function both of the density variation with mixing ratio and temperature ratio (see Figure B.4) and a direct function of the mass balance of input dynamic viscosities (noting that μ_1 and μ_2 are different).

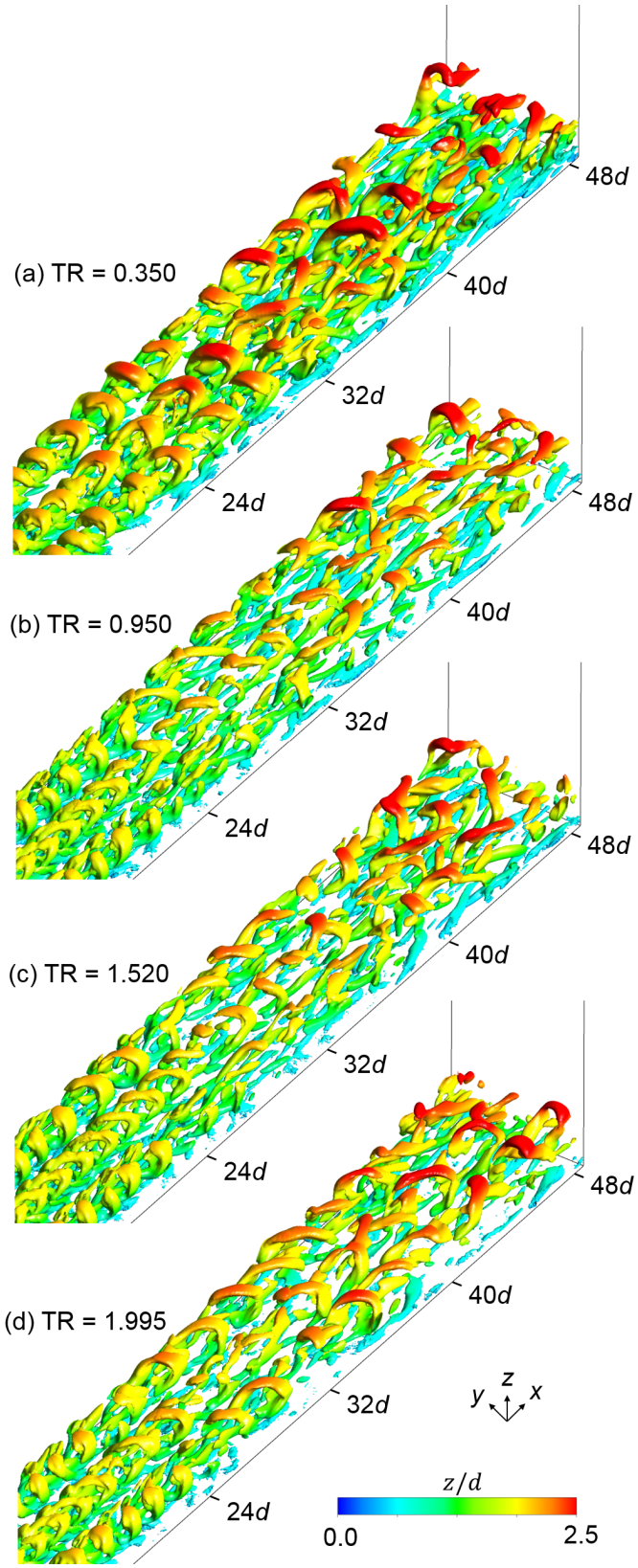


Figure 2.26: LES instantaneous vortex structures (Lambda-2 criterion) coloured by the normalized distance from the wall (z^*). (a) TR = 0.350, (b) TR = 0.950, (c) TR = 1.520, and (d) TR = 1.995.

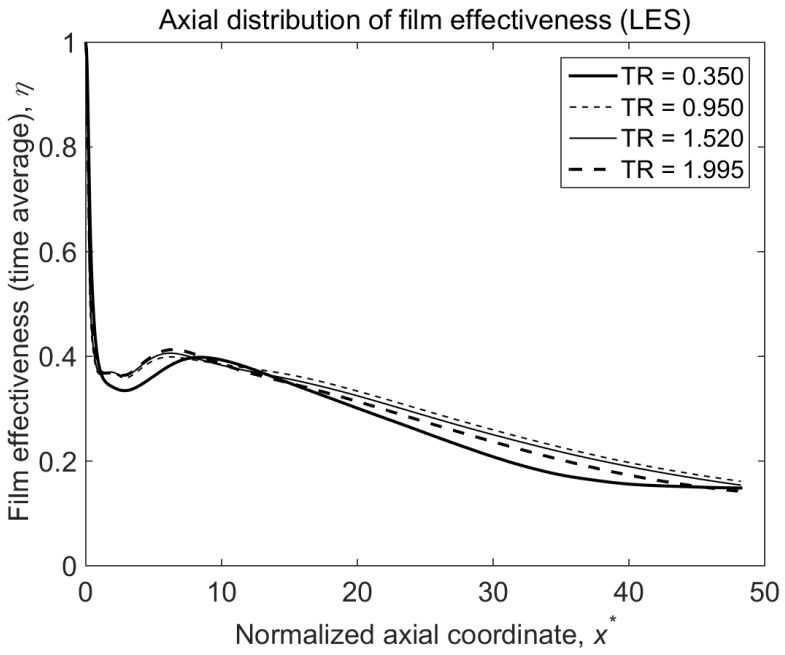


Figure 2.27: Laterally averaged axial distributions of time averaged film effectiveness for LES simulations TR = 0.350, 0.950, 1.520, and 1.995.

We now consider changes in the flow with respect to wall normal distributions of density and Reynolds stress

Figure 2.28 shows LES-predicted mass-averaged distributions of time-averaged density ratio in the partially mixed cooling layer (ρ_3/ρ_1) as a function of normalized wall distance at planes $x = 0d$, $24d$, and $48d$, for TR = 0.350, 0.950, 1.520, and 1.995. Here the temperature ratio is defined at the hole exit ($x = 0d$).

In accordance with our result (ii)—full argument in Appendix B—for a temperature ratio close to unity (TR = 0.950), the density ratio at all axial planes is approximately unity. For temperature ratios *either side of unity*, however, the density of the partially mixed layer decreases from a maximum for TR = 1. The reduction in density in the partially mixed layer depends on both the TR, and also the degree of mixing (ratio of entrained mainstream gas to coolant gas in partially mixed layer). It is worth recalling that the density ratio *at the hole exit* is unity for all values of TR.

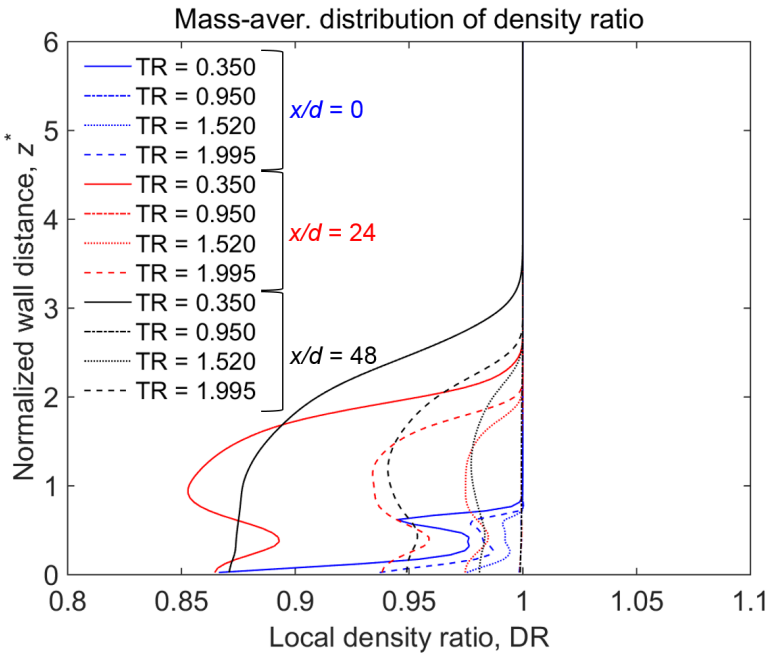


Figure 2.28: LES results of mass-averaged time-averaged density ratio distribution at plane $x = 0$, 24, and $48d$.

Looking at the trends in Figure 2.28, we see that for all stations ($x = 0d$, $24d$, or $48d$) the maximum reduction in density is achieved for TR = 0.350. This is consistent with the result of Appendix B, Figure B.4. For $x = 0d$, the degree of entrainment of mainstream flow is small, with a correspondingly small reduction in density ratio. For $x = 24d$ and $x = 48d$, the entrainment of mainstream flow is greater, and a more significant reduction in density ratio is seen. For $x = 24d$ the reduction is from $\rho_3/\rho_1 = 1.00$ to $\rho_3/\rho_1 = 0.85$ in the region $0 < z^* < 2$. For $x = 48d$, the results are very similar, with a maximum density reduction to $\rho_3/\rho_1 = 0.87$, with most of the effect localized in the region $0 < z^* < 3$. Similar trends, but with decreasing magnitude, are observed for TR = 1.995 and TR = 1.520 respectively. This ranking is in accordance with the results of Appendix B, Figure B.4.

In interpreting these results, it is worth noting that the density ratio in the mixing layer (ρ_3/ρ_1) is a weak function of the mixing ratio which decreases with axial distance (see Figure B.4) as the film effectiveness reduces. The general effect is that for greater

x/d, the film effectiveness is lower due to a lower mixing ratio, $\dot{m}_1/\dot{m}_2$, due to more entrained mainstream gas. At x/d equal to 24 and 48 (intermediate and mixed-out regions) the mixing ratios are approximately $\dot{m}_1/\dot{m}_2 = 0.3$ and $\dot{m}_1/\dot{m}_2$, $= 0.2$, respectively. The inference from the data of Figure B.4 (trend line shown for $\dot{m}_1/\dot{m}_2 = 0.5$, but not directly for 0.3 or 0.2) is that the low mixing ratios ameliorate the temperature ratio dependent density reduction effect by about of order 0.01 (from the maximum at a mixing ratio of $\dot{m}_1/\dot{m}_2 = 1$).

Temperature ratio induced reductions in density in the mixing layer (Figure B.4) cause a corresponding increase in the kinematic viscosity. This increase is observed *either side of a TR of unity* leading to higher momentum diffusivity for both TR > 1 and TR < 1 than for TR $= 1$. This is for a system in which both the dynamic viscosity and density ratio at hole exit are constant for all temperature ratios. Figure 2.29 shows LES-predicted mass-averaged distributions of the $\overline{uu'}$ component of Reynolds stress as a function of normalized wall distance for $x = 0d$, $24d$ and $48d$.

For $x = 0d$ where there has been relatively little mixing between the coolant and mainstream, and relatively little shear-induced destabilisation of the flow, the $\overline{uu'}$ component of Reynolds stress is similar for all temperature ratios and takes a low value. Further downstream, where the flow has been destabilized and there has been substantial mixing between coolant and mainstream, the Reynolds stress increases, and is significantly affected by temperature ratio induced density changes. At $x = 24d$ there is a peak in Reynolds stress within the mixing layer (between $0 < z^* < 2$), with peak magnitude ranked according to the temperature ratio induced change in density within the mixing layer. That is, the greatest enhancement in Reynolds stress due to temperature ratio effects is observed for TR = 0.350, followed by TR = 1.995. The Reynolds stress profiles for TR = 1.520 and TR = 0.950 are essentially indistinguishable. It is interesting to note that the Reynolds stress enhancement for the TR = 0.350 case extends further from the wall then for the other cases, consistent

with a volume dilation effect within the mixing layer.

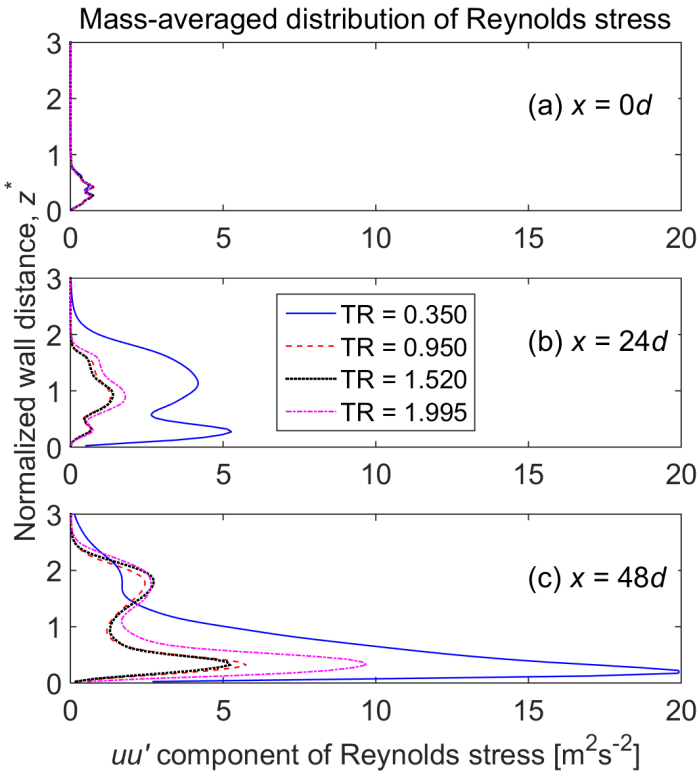


Figure 2.29: LES predictions of the mass-averaged $\overline{uu'}$ component of Reynolds stresses, along the normalized wall distance at planes $x = 0$, 24, and $48d$.

Similar trends are observed at $x = 48d$. Here the peak stresses are higher than at $x = 24d$ (perhaps consistent with continuing growth in turbulent structures downstream of the cooling holes), and the ranking of enhancement in Reynolds stress over the baseline case (TR = 0.950) due to temperature ratio effects is consistent with the results at $x = 24d$, and in line with the density variation discussed in relation to Figure B.4.

Figure 2.30 shows laterally averaged film effectiveness as a function of temperature ratio, normalized with respect to a nominal condition at TR = 0.950.

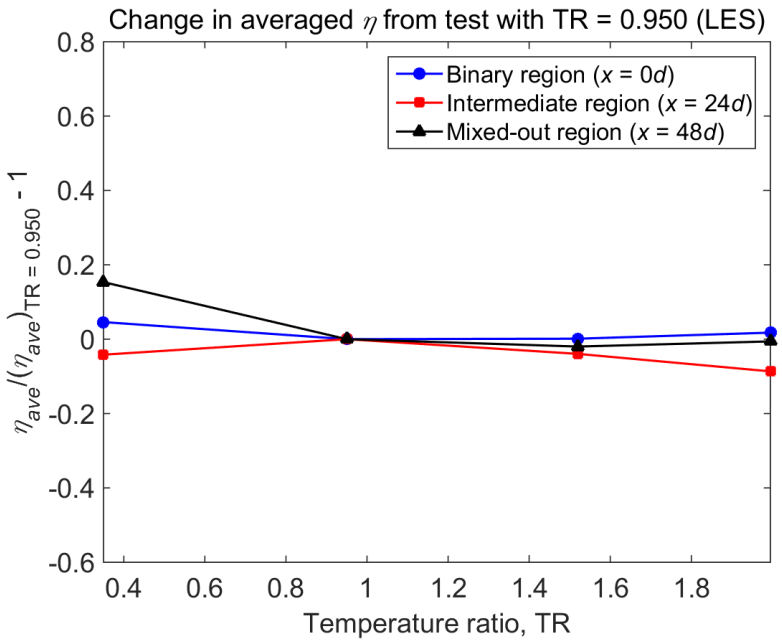


Figure 2.30: Lateral average of film effectiveness as function of temperature ratio Test conditions were $I = 1.000$, $E = 1.000$ and BR = 1.000.

In the binary region, the impact of temperature ratio is extremely small, and there is very little difference between cases for TR = 0.350, 0.950, 1.520 and 1.995. This is perhaps to be expected, because the three physical effects discussed (see start of this section) develop as the coolant entrains mainstream gas (leading to density variations, and subsequent volume dilation effects and changes in kinematic viscosity). At $x = 0d$, although both coolant and mainstream gas are present on the surface (discreet cooling jets with gaps between), effects due to mixing (see control volume argument in Appendix B) have not yet been initiated. In the intermediate region ($x = 24d$) there is a very small reduction in film effectiveness either side of TR = 1. The general shape of this relationship (a maximum at TR = 1) is consistent with the general principle that the key physical processes have the same sign either side of TR = 1. The small reduction in effectiveness is most likely due to enhanced kinematic viscosity (either side of TR = 1) leading to faster (momentum based) diffusion between the coolant and entrained mainstream layers. This can be seen in Figure 2.29, which shows larger and more intense turbulent structures for TR < 1 and TR > 1 than for TR = 1.

In the mixed-out region ($x = 48d$) there is a very small increase in film effectiveness for TR = 0.350 (note that these data are presented as proportional changes, and the underlying value is small). The data at TR = 0.950, 1.520 and 1.995 are extremely similar to each other. There is a suggestion of a minimum in the data that simulations at more extreme conditions could explore. If such a minimum exists, it would be consistent with the argument that the physical processes take the same sign either side of TR = 1. Noting that the underlying value of film effectiveness is small, it is speculated that the increase in film effectiveness may be due to volume dilation effects (maximum for the TR = 0.350 condition) in an already fully turbulent and well-mixed coolant region. This effect reduces the penetration of freestream turbulent structures into the mixed layer (due to the mixed layer assuming greater thickness on account of volume dilation, in relation to the length scale of turbulent structures in the mainstream flow). This hypothesized mechanism is not believed to be robust and would benefit from further investigation at more extreme temperature ratios, in which the rate of entrainment into various segmented near wall regions could be analyzed.

2.8 Conclusions

By conducting a dimensional analysis of a flow field with a mixing coolant film, we have shown that the situation is governed by twelve non-dimensional groups. Making film effectiveness the subject, we can show that seven of the remaining eleven groups can be regarded as boundary conditions for the main flow path—and must be matched for complete similarity—and the remaining four relate specifically to the introduction of film cooling. We believe there is lack of clarity in the literature both about the best form for these groups (they can be cast in numerous ways), and about the *independent* role they play in determining the film effectiveness distribution in a given situation.

We argue that the most natural (that is, the forms that allows the clearest physical interpretation of *independent* effects; or, mathematically speaking, make the axes as orthogonal as possible) forms for groups on which the film effectiveness has a strong functional dependence are:

(i) the momentum flux ratio, $I \equiv \rho_2 u_2^2/\rho_1 u_1^2$;

(ii) the blowing ratio, BR$\equiv \rho_2 u_2/\rho_1 u_1$;

(iii) the heat capacity flux ratio, $E \equiv \rho_2 u_2 c_{p2}/\rho_1 u_1 c_{p1}$;

(iv) the temperature ratio, TR$\equiv T_{02}/T_{01}$.

With the aid of extensive RANS and LES predictions, we independently vary each of these four groups whilst keeping the remaining three groups—and an additional seven group associated with the bulk flow field—constant. This enabled the independent effect of each group to be studied.

An important observation that departs from previous literature is that we see strong *region dependence* of the sensitivity of the film effectiveness to each of these four parameters. We define three regions for analysis: a *binary region* in which the films are essentially unmixed; an *intermediate region* in which the films are partially mixed; and a *mixed-out region* in which the films are well mixed. The key results of these four studies (one per controlling non-dimensional group) are now summarized in turn.

Momentum flux ratio. In the binary region we find the film effectiveness distribution has a strong dependence on the momentum flux ratio, because this controls the aerodynamic state of the jets i.e. the coolant trajectory and shape of the jet. This result is consistent with a large body of literature. In the intermediate region there is still significant dependence of the film effectiveness distribution on momentum flux ratio. This is beyond the reattachment point of the jets, so the sensitivity is likely

associated with changes in mixing caused by different initial coolant trajectories. We find that in the mixed out region, the film effectiveness is insensitive of the momentum flux ratio. This shows the importance of region-dependent analysis, which departs from most literature in this area which generally only extends to discussing the relative dominance of particular groups in holistic terms. In addition, there are many examples in the literature of studies of this type in which groups are not properly separated from each other.

Blowing ratio. This a commonly-used parameter in turbomachinery literature primarily because it relates to the input controls in many experiments, or the cycle cost (aerodynamic and thermodynamic) in engine applications. In this work, it is found, however, that the relatively subtle physical processes this parameter controls are not those discussed in existing literature, and further observe that the sensitivity of film cooling to blowing ratio (when varied on its own) is much lower than to other non-dimensional parameters. Indeed, in much of the literature, changes in film effectiveness which should correctly be attributed to energy flux ratios changes are incorrectly attributed to blowing ratio changes. Although there is less sensitivity of film cooling to blowing ratio than to other parameters, it has been shown that the blowing ratio is responsible for describing the initial *volume flow rate ratio* or *velocity ratio* of the cooling jet with respect to the mainstream flow (when coolant is expanded to the local static pressure at the hole exit). The velocity ratio governs the rate of shear at the interface between the emerging film cooling jets and the mainstream flow, which in turn dictates the rate of jet destabilization, which affects the rate of mixing of coolant with the mainstream flow. We therefore believe that thinking of the blowing ratio as controlling initial (near hole exit) velocity ratio (or velocity difference) provides the most intuitive explanation of the resulting physical effects. For fixed momentum flux ratio, specific heat capacity flux ratio, and temperature ratio, the velocity ratio and corresponding volume flow rate ratio are inversely proportional

to blowing ratio, a counter-intuitive result that is proved in this chapter. Changes in blowing ratio cause three complex, competing effects: velocity excess/deficit in the coolant tube is accommodated by friction leading to increased/decreased tube cross sectional area in the fully-accommodated state; tube area expansion/reduction due to volume flow rate changes is offset by a reduced/increased resistance to temperature change (over a given linear distance) because the tube specific heat capacity flux remains unchanged; both velocity excess and deficit cause shear, which leads to jet destabilization, turbulent mixing, and structural differences in the way the jet develops. By examining shear strain rate profiles along the wall-normal direction in RANS simulations, we see that the last effect is extremely complex in nature. Although the effects are competing, and complex, the sensitivity of laterally averaged effectiveness to blowing ratio is relatively low. In the binary region, velocity difference driven shear forces have not yet taken hold, and there is little shear-induced difference in the flow. Here sensitivity of η to BR is negligible. In the mixed-out region we have the same result (almost no sensitivity of laterally averaged η to BR). Here shear-induced destabilization has occurred some way upstream, and both the initial velocity discrepancy between coolant and mainstream and the structural differences generated by shear-initiated flow phenomena are largely mixed out. It is only in the intermediate region that there is some sensitivity of laterally averaged η to BR. This is attributed to complex flow structures (resulting from shear induced destabilization) affecting the rate of coolant jet and mainstream flow mixing.

Heat capacity flux ratio. The heat capacity flux ratio is a measure of the relative (with respect to the mainstream) potential of the coolant stream to store heat. In the binary region, where the flow is essentially unmixed, the balance of specific heat capacity flux is unimportant, because it has little effect on the approximately binary values the film effectiveness takes (here it is only the structure of the flow that is important). In the intermediate and mixed-out regions where the flow is relatively

well mixed, the relative heat storage capacity of the coolant and mainstream flows is extremely important, and there is an approximately linear relationship between the laterally averaged film effectiveness and the heat capacity flux ratio. In these regions, the film effectiveness is more sensitive to this parameter than any other. It is worth noting that in the literature there are many examples of sensitivity to specific heat capacity flux ratio being incorrectly attributed to changes in blowing ratio. To conflate these two sensitivities is entirely wrong, and should be avoided.

Temperature ratio. A change in temperature ratio alone does not cause a change in density (or density ratio) of the coolant film at the point of issuing from the hole, but, interestingly, does cause a change in the density of a *partially mixed* layer of coolant. A key result is the density of such a layer decreases (from a maximum at TR = 1) for temperature ratios *either side of unity.* There are two consequences of this effect: firstly, the kinematic viscosity increases *either side of a TR of unity* leading to higher momentum diffusivity and greater mixing within the near wall region; secondly, there is a volume dilation effect during the mixing process (of coolant gas with entrained mainstream). These effects appear to be opposed in terms of their impact on the film effectiveness: the kinematic viscosity increase appears to enhance early mixing of the film, leading to slightly lower film effectiveness in the intermediate region either side of a temperature ratio of unity; the volume dilation may be responsible for slowing the entrainment of mainstream gas in the mixed out region (length scale ratio of turbulent structure to mixed layer), but further study is required to validate this hypothesis. There is no impact on the binary region, consistent with the argument that the effects are driven by density variation in a *partially*-mixed layer.

The purpose of this chapter was to bring clarification to the following topics: the full set of non-dimensional groups that control film cooling problems; the way in which the groups independently control features of the flow, and the form of groups that allows clearest physical interpretation; the strong region-dependence of the sensitivity

of film effectiveness to certain groups; and the physical mechanisms that lead to changes in film effectiveness when blowing ratio, momentum flux ratio, specific heat capacity flux ratio, and temperature ratio are independently varied. A number of fundamentally new mechanisms and concepts have been discussed that we hope will be referenced by future studies, either by way of further validating or challenging the theses.

Chapter 3

Effect of Momentum-Flux Ratio on HP-NGV Platform Cooling

High pressure nozzle guide vane endwalls are often characterized by three-dimensional flows. The flow structure depends on the incoming boundary layer state (inlet total pressure profile) and the (static) pressure gradients within the vane passage. In many engine applications this can lead to strong secondary flows. The prediction and design of optimized endwall film cooling systems is therefore challenging, and a topic of current research interest.

A detailed experimental investigation of the film effectiveness distribution on an engine-realistic endwall geometry is presented in this chapter. The film cooling system was a fairly conventional axisymmetric double row configuration. The study was performed on a large-scale, low-speed wind tunnel using infrared thermography. Adiabatic film effectiveness distributions were measured using IR cameras and tests were performed across a wide range of coolant-to-mainstream momentum-flux and mass flow ratios. Complex interactions between coolant film and vane secondary flows are presented and discussed. A particular feature of interest is the suppression of secondary flows (and associated improved adiabatic film effectiveness) beyond a critical momentum flux ratio. Jet lift-off effects are also observed, and discussed in the context of sensitivity to local momentum flux ratio. Full coverage experimental results are also compared to three-dimensional, steady-state CFD simulations.

This chapter provides insights into the effects of momentum flux ratio in establishing similarity between cascade conditions and engine conditions, and gives design guidelines for engine designers in relation to minimum endwall cooling momentum flux requirements to suppress endwall secondary flows.

The aim of this chapter is to investigate the endwall flows behaviour and their dependence on the interaction between mainstream and coolant flows. As concluded in the previous chapter, the main parameter to control the aerodynamic behaviour of the cooling jets and therefore their interaction with the mainstream flow is the momentum flux ratio. In this regard, the momentum flux ratio is the controlling parameter varied in this study.

The work in this chapter has been published in Ornano and Povey (2017*b*).

3.1 Introduction

In Joule-Brayton cycles, the thermal efficiency is maximized at the highest possible ratio between the turbine entry temperature (TET), and the compressor exit temperature. TET is limited by oxidation life and creep of component materials. The use of super-alloys, single crystal casting and thermal barriers have allowed considerable increases in TET. Nevertheless, high pressure turbine components operate at higher temperature than the melting point of their materials. This is possible by cooling these components using relatively cold air from the last stage of the compressor. External cooling is realized via machining discrete holes on turbine components (e.g. vane, blade, endwall) exposed to the high temperature gas. The coolant is fed from an internal cavity and ejected from cooling holes to create a protective film and reduce the heat load.

The high pressure (HP) nozzle guide vane (NGV) endwall (or platform) is a relatively large exposed surface directly downstream of the combustor exhaust. Uniform

cooling film distribution is normally challenging to achieve due to complex secondary flow structures on the endwall surfaces. These are generated by the interaction between the incoming boundary layer, which is generally a low momentum region, and the cross-passage pressure gradient (Langston et al. (1977), Sieverding (1985), Sharma and Butler (1987), and Thomas et al. (2013)). Particularly high heat load is registered on the horseshoe vortex reattachment regions, where hot flow impinges the endwall with high heat transfer coefficient. High heat transfer is also observed downstream the horseshoe vortex separation lines, where a fresh thin boundary layer is generated. These aspects motivate the current research in studying and developing improved endwall film cooling systems.

Many authors have studied the dependence of film effectiveness on hole orientation, geometry and arrangement. A review of past literature has shown increased efforts in the investigation of endwall cooling with discrete holes. Harasgama and Burton (1992) investigated the Nusselt number distribution on a NGV endwall with discrete holes upstream the vane and inside the passage, where holes were distributed along iso-Mach lines. Friedrichs et al. (1999) investigated the effect of secondary flow on endwall film cooling. They developed an improved configuration with cooling holes downstream of separation lines where a fresh boundary layer was observed to develop. Gao et al. (2009) experimentally studied the effect of different hole configurations on endwall film cooling. The endwall was cooled by a purge flow from a gap between stator and rotor rows in addition to discrete film cooling on the rotor hub endwall. Film holes within the passage were arranged with two configurations and film effectiveness distributions were investigated by means of the pressure sensitive paint technique (PSP).

Thole and Knost (2005) performed measurements of adiabatic film effectiveness combining both cooling from a slot and discrete film cooling holes on the endwall of a turbine vane. They concluded that upstream conditions play a crucial role on

the development of secondary flows within the turbine passage and therefore affect cooling performance. The role of blowing ratio and density ratio on film cooling was investigated by Sinha et al. (1992). They found that for low blowing ratios (i.e. low mass flux ratios), the film was attached to the wall and that the centerline film effectiveness was primarily a function of the mass flux ratio. At higher blowing rates, detachment (and possible reattachment) of the cooling jets became more important and the film effectiveness was strongly dependent on the momentum flux ratio. Thole et al. (1990) noted that selection of the appropriate scaling parameter is important to characterize the film cooling performance. Common parameters (not all entirely independent) include coolant-to-mainstream mass flow ratio (MFR), blowing or (mass flux) ratio (BR), momentum flux ratio (I) and density ratio (DR).

The use of the momentum flux ratio as scaling parameter allows to define the state of the cooling jet (separated/attached) in the near hole region, as suggested by Thole et al. (1990) and Ekkad et al. (1998). In their work, Thole et al. (1990) defined ranges of momentum flux ratio in which the jet was attached or separated. They found that for $I < 0.4$ coolant jets were fully attached to the surface, and were completely detached for $I > 0.8$. Coolant jets were found to separate and subsequently reattach for $0.4 < I < 0.8$. Similar general conclusions are observed by Bogard and Thole (2006).

Pedersen et al. (1977) investigated the sensitivity of the jet behaviour to the density ratio. They found that for low momentum flux ratio ($I < 0.4$) film effectiveness performance for low density coolant was essentially the same as high density coolant when compared at the same mass flux ratio. This because jets were fully attached and the film effectiveness was primarily a function of the mass flux ratio. This is consistent with Thole et al. (1990). Shiau et al. (2016) investigated endwall film effectiveness distributions on an annular NGV sector with laidback fan-shaped and cylindrical holes using the pressure sensitive paint technique. Tests were carried out

for three values of mass flow ratio, each with two different density ratios. Increasing the density ratio for a given mass flow ratio improved lateral coverage. This was attributed to reduced momentum flux ratio with increasing density for a given mass flow ratio. This is in accord with the conclusion that it is important to match momentum flux ratio to achieve aerodynamic mixing similarity of cooling jets. The importance of the radial total pressure distribution at the vane inlet, including the influence of cooling flow, was investigated by Thomas and Povey (2016). They investigated the effect of coolant-to-mainstream pressure ratio, hole inclination angle, hole diameter, vane potential field, and overall mass flux ratio using validated CFD. They concluded that the endwall flow is substantially influenced by the inlet radial total pressure profile, and that the impact of cooling on modifying this profile can be significant even at low cooling mass flow rates. The present study is a combined experimental and numerical investigation of the behavior of the film effectiveness field on a HP NGV endwall. The momentum flux ratio is varied over a wide range for an engine-realistic geometry, and full-surface film effectiveness measurements conducted using IR thermography. The data offer insights into the effect of inlet radial total pressure profile on the behavior of endwall secondary flows. Design guidelines are offered for minimum endwall cooling momentum injection to suppress endwall secondary flows.

3.2 Experimental methods

Tests were performed at the Super-Scale Platform Cooling Facility (SSPCF) at the University of Oxford (Thomas 2014). The facility is a large-scale, low-speed linear cascade with seven vanes. The aerodynamic profile is based on modern engine geometry. The vane and endwall geometries include engine realistic features such as the combustor-turbine gap, hub and casing annulus line profiles, and vane fillets. The endwall film cooling scheme is typical of a modern engine. A drawing of the test

facility is shown in Figure 3.1.

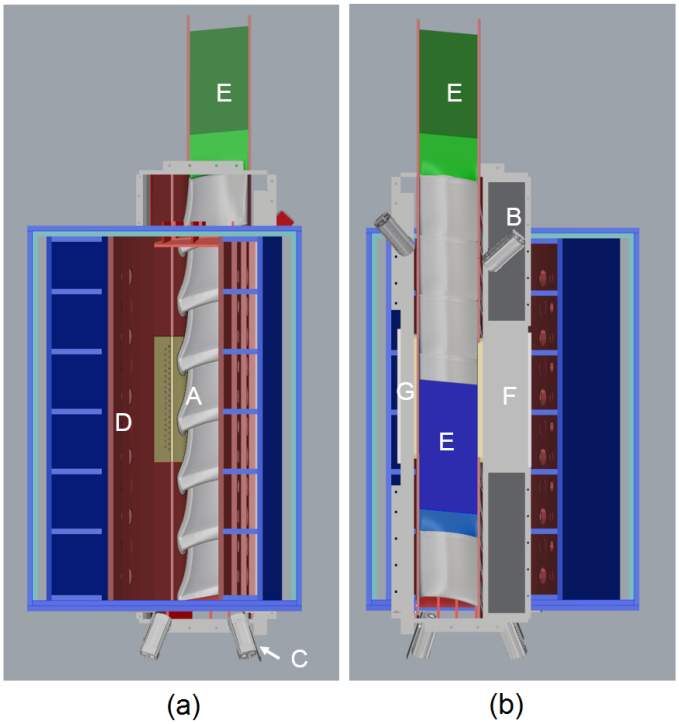


Figure 3.1: CAD model and components of the Super-Scale Platform Cooling Facility; (a) front view and (b) rear view. A—vane and platforms; B—rear cameras; C—front cameras; D—combustor simulator; E—tailboards; F—hub cassette; G—casing cassette.

The facility includes a rich-burn combustor simulator with scaled dilution holes to set high turbulence intensity with representative length scales upstream of the NGV cascade. A turbulence plate upstream the NGV section was designed using the correlation suggested by Roach (2016). A turbulence intensity of approximately 16% was estimated at the vane inlet at nominal conditions. Removable cassettes at the hub and case allow back-to-back tests of different endwall cooling designs. The removable cassettes, NGV endwalls and combustor simulator were manufactured from Rohacell, a structural material with very low thermal conductivity ($k = 0.03$ W m^{-1} K^{-1}), to allow film effectiveness measurements to be performed using infrared thermography with minimal conduction error. After an experimental periodicity study, the central passage was used to perform these measurements. The mainstream inlet flow was

heated by typically 30 K with a 100 kW heater mesh. Hub and casing endwall coolant mass flow rates were measured using critical-flow Venturi nozzles.

The NGV chord was 290 mm and inlet blade angle was 74 degrees. The pitch-to-chord ratio was 0.76 and the inlet and outlet span-to-chord ratios were 0.9 and 0.75, respectively. This paper considers the behavior of the casing endwall in detail (similar experiments were performed on the hub endwall). The general arrangement is shown in Figure 3.2a.

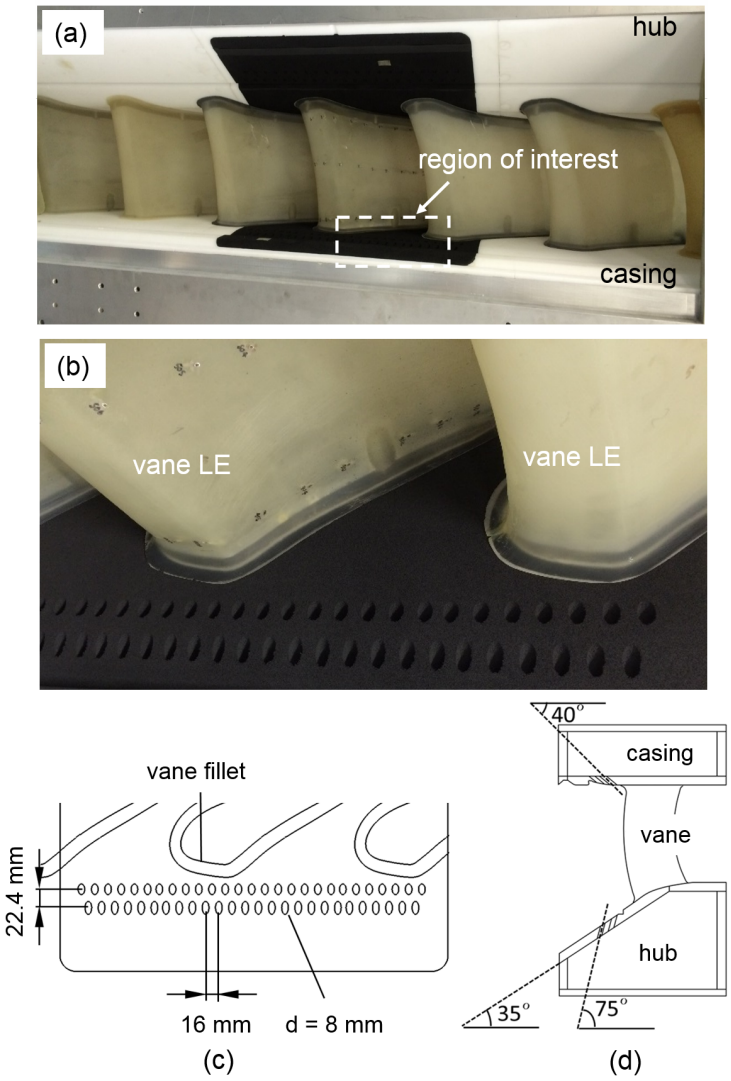


Figure 3.2: NGV cascade viewed from upstream; (b) detail of the casing endwall; (c) casing film cooling pattern; (d) vane hub and casing cooling hole inclinations angles.

The cooling hole geometry included 2 rows of 53 cylindrical holes in total, with a diameter of 8 mm and an inclination angle of 40 deg (see Figure 3.2c and d). The pitch-to-diameter ratio of the cooling holes was 2.The mainstream mass flow rate for the central passage was evaluated using experimental measurements of pressure, and a CFD-predicted vane capacity curve for a periodic passage with the same boundary conditions as measured for the central passage in the experiment. CFD predictions for a single vane passage at six pressure ratios are shown in Figure 3. The data are fitted with a 1D isentropic capacity trend which shows a very good match in form. Nominal test conditions are marked by the dashed line (pressure ratio of p_2/p_{01} = 0.993). The single-passage mass flow rate at this condition is approximately 0.45 kg s^{-1}. The Reynolds number was 6.6×10^5 (based on exit average velocity and vane chord length) and was kept constant for all the experiments. The mainstream and coolant flow temperatures were measured with thermocouples. Surface temperature measurements were obtained with foil thermocouples on the endwall surfaces.

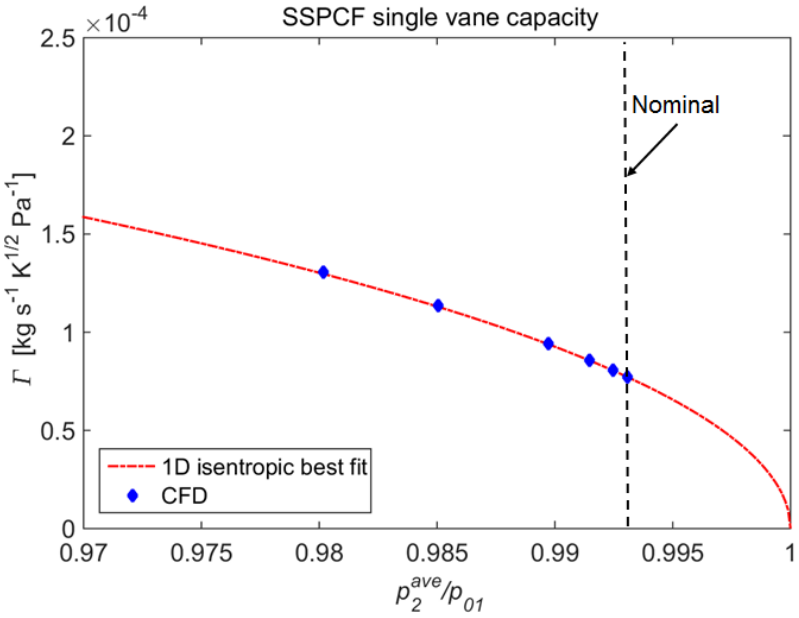


Figure 3.3: CFD-predicted single vane capacity at six pressure ratios fitted with isentropic trend.

3.2.1 Infrared thermography

Infrared data were simultaneously acquired from two FLIR (A655sc) infrared cameras. The camera software software was used to set focus position, ambient drift compensation, trigger settings and sample rate. The upstream and downstream cameras were equipped with 24.6 mm and 13.1 mm lenses respectively. Labview was used to simultaneously acquire signals from the pressure and temperature sensors and cameras. Measurements were averaged over six video frames. Endwalls were coated with high emissivity Autotek black paint. The emissivity of the paint was measured in the laboratory to be $\epsilon = 0.97$. The field of view of the front and rear sections of the endwall is shown in Figure 3.3a and Figure 3.4b. Four post-processing lines were chosen to analyze the data: downstream of the first row of cooling holes (line 1), downstream of the second cooling row (line 2), at vane mid-chord line (line 3) and vane exit line (line 4). These lines are marked in Figure 3.4. To aid the interpretation of the experimental results showed in Figure 3.13, the vane boundaries are also marked.

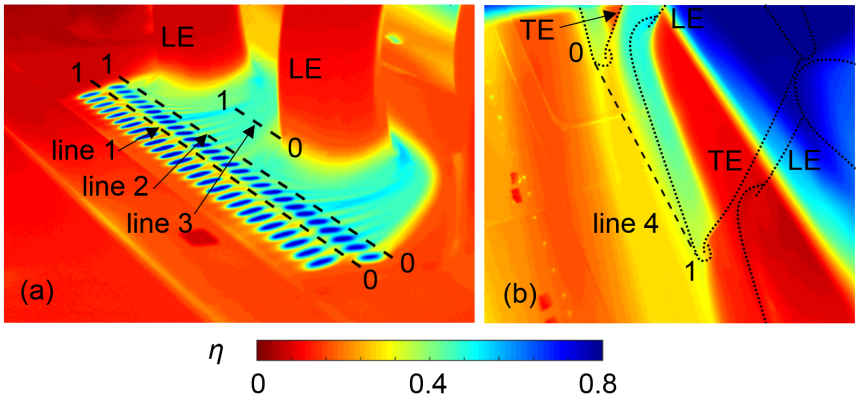


Figure 3.4: Fields of view: (a) upstream endwall; (b) downstream endwall.

3.2.2 Infrared calibration

The IR cameras were calibrated in-situ, during a test in which both warm mainstream and cool coolant flow were turned on. Thus the calibration environment was highly

representative of all test data (similar small reflection terms etc.). Detector signal evaluated for four surface patches was plotted against temperature measured using four thermocouples at the same locations. A wide range of viewing angles was covered by the four thermocouples. Separate calibrations were performed for upstream and downstream endwalls. The IR raw signal was found to be highly linear with thermocouple-measured temperature within the calibration range. The regions with surface thermocouples were checked to give very similar calibrations and the averaged linear calibration function was applied to the entire surface. A typical calibration curve for the front camera is shown in Figure 3.5.

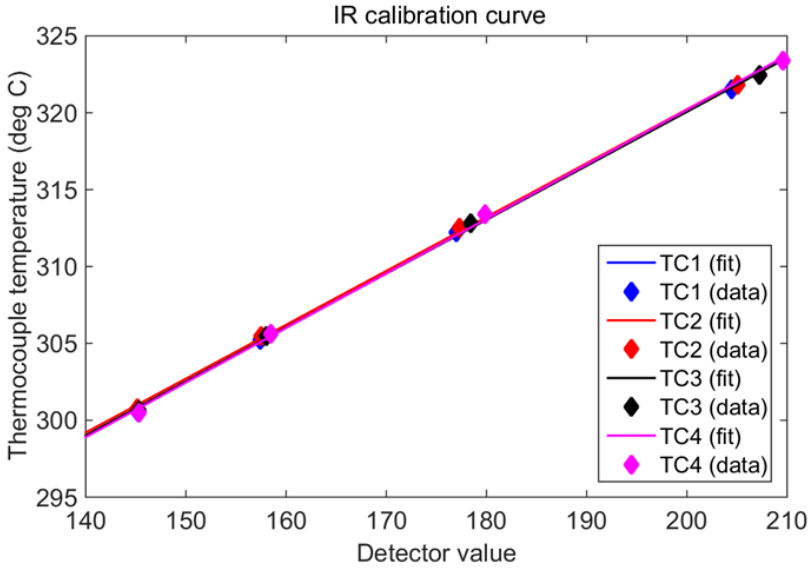


Figure 3.5: Typical calibration curve of detector signal as a function of the surface temperature (thermocouple).

3.2.3 Experimental uncertainty

An uncertainty analysis was performed for the measurements of adiabatic film effectiveness using the method described by Moffat (1988). The film effectiveness was defined as follows:

$$\eta = \frac{T_\infty - T_w}{T_\infty - T_c} = \frac{A}{B} \tag{3.1}$$

where T_w is the local wall temperature measured with the IR cameras and T_∞ and T_c are the mainstream and coolant temperatures measured with thermocouples. Measurements are taken at steady state conditions. The absolute uncertainty of the film effectiveness was calculated using:

$$u_\eta = \sqrt{\left(\frac{\partial \eta}{\partial A}\right)^2 u_A^2 + \left(\frac{\partial \eta}{\partial B}\right)^2 u_B^2} = \sqrt{\left(\frac{1}{B}\right)^2 u_A^2 + \left(-\frac{1}{B^2}\right)^2 u_B^2} \tag{3.2}$$

The error in B, the temperature difference $T_\infty - T_c$, is dominated by bias errors caused by the actual thermocouple constants not being equal to the nominal calibration. This error was estimated to be 1 K in 100 K and proportional to the temperature difference from the isothermal state. The precision error due to noise was assumed to be small compared to the bias error when a large number of samples are averaged. The error in A has two principle sources: firstly, a bias error in T_∞ caused by the actual thermocouple constants not being equal to the nominal calibration—this was taken to be 1 K in 100 K and proportional to the temperature difference from the isothermal state; secondly, a bias error in T_w of 0.35 K due to calibration fit of the IR camera (this error was assumed constant). It is worth noting that we do not account for an additional bias error in T_w due to the linearity of the calibration, because this is correlated to the bias in T_∞ (the IR cameras were calibrated against the thermocouples that measure T_∞).

Figure 3.6 depicts the contours of the absolute uncertainty of film effectiveness measurements, calculated using Equation 6.19, as a function of mainstream-to-coolant temperature ratio (T_∞/T_c) and film effectiveness. At the nominal test conditions of $T_\infty/T_c = 1.1$ (blue dashed line), the absolute uncertainty was approximately 0.02 for the entire range of η.

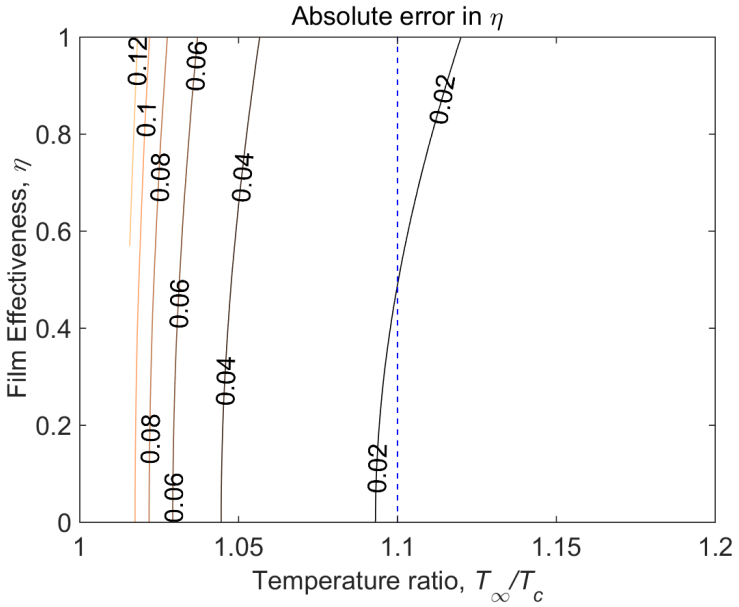


Figure 3.6: Contours of the absolute uncertainty (to 95% confidence) in η as a function of T_∞/T_c and η.

3.3 Experimental plan

In this chapter we examine the influence of bulk momentum flux ratio on the adiabatic effectiveness of the endwall. We define the bulk momentum flux ratio by

$$I = \frac{\sum_i^n I_i}{n} \quad \text{where} \quad I_i = \left(\frac{\rho_c u_c^2}{\rho_\infty u_\infty^2} \right) \tag{3.3}$$

where ρ_c and ρ_∞ are the density of the coolant and mainstream gas, respectively, and u_c and u_∞ are the velocity magnitudes of the coolant and mainstream gas respectively. All of these variables were computed local to each cooling hole (extracted by using the methodology described in the section 3.4). The bulk momentum flux ratio was computed as the average of local values over the number of holes, n. This methodology was justified by the fact that all holes had the same area.

Experiments were performed for a density ratio of DR = 1.1, with air as coolant, in the mass flow ratio range 1.1% < MFR < 13.4%. This corresponds to bulk momentum

flux ratios in the range $0.40 < I < 26.99$. The engine condition for large engines are given in the section 3.3.1. The adiabatic film effectiveness is defined by

$$\eta = \frac{T_\infty - T_w}{T_\infty - T_c} \tag{3.4}$$

where T_w is the local wall temperature measured with the IR cameras and T_∞ and T_c are the mainstream and coolant temperatures measured with thermocouples, at steady state conditions.

3.3.1 Engine range of momentum flux ratio

The results of this work can be analyzed in the context of comparison with engine conditions by defining the typical engine range of momentum flux ratio for endwall cooling. The coolant-to-mainstream total pressure ratio ($p_{0c}/p_{0\infty}$) is the parameter which defines the momentum flux ratio and the typical design value is 1.02 (Day et al. 2000). Parallel CFD investigations at engine conditions were performed to evaluate the mainstream inlet Mach number in proximity of the endwall. The range obtained was $0.05 < M < 0.15$. This is consistent with Shiau et al. (2016). Using the isentropic flow relations, the momentum flux ratio is calculated for the conditions reported above.

Figure 3.7 shows the contour lines of momentum flux ratio as a function of Mach number and coolant-to-mainstream pressure ratio.The momentum flux ratio at typical engine conditions for endwall cooling ($0.05 < M < 0.15$ and $1.02 < p_{0c}/p_{0\infty} < 1.03$) is in the range $2 < I < 18$. Thus experiments span the engine range of momentum flux ratios.

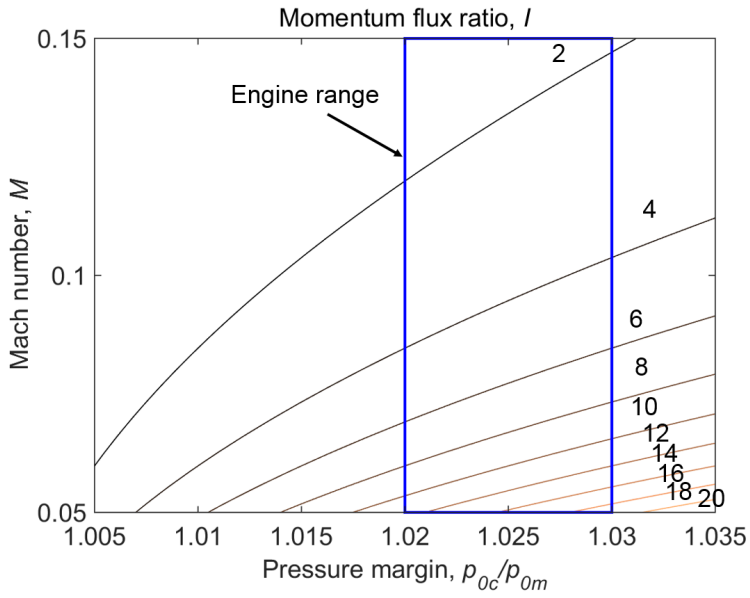


Figure 3.7: Range of momentum flux ratio for endwall cooling systems at typical engine conditions.

3.4 Numerical methods

A numerical analysis was performed using ANSYS-CFX, with RANS settings and *high resolution* discretization (second order accurate) for both advection and turbulence terms. The $k-\omega$ SST turbulence model with automatic wall functions and reattachment prediction model was used. The flow conditions were incompressible. The geometry (Figure 3.8) was modelled with Rhinoceros 3D (CAD) and meshed using BoxerMesh. The numerical domain included two passages and a common coolant plenum, with fully meshed holes. Mesh interfaces at the cooling hole inlets were managed using the GGI option to allow individual cooling holes mass flow rates to be determined during post-processing. The domain had approximately 17 million hybrid cells (hexahedral and tetrahedral). In the near-wall region, the mesh was refined with 10 prism layers with an expansion ratio of 1.2. The value of y^+ was within the operating range of ANSYS-CFX enhanced wall functions. A review of the past literature has shown that wall functions have been widely used in case of adiabatic

walls for film cooling investigations (Nemdili et al. (2008), Shalash et al. (2013), and Cresci et al. (2015)). In particular, Mazzoni et al. (2015) showed the capability of wall functions to predict the flowfield for adiabatic simulations. Figure 3.8 depicts the numerical domain and the detail of the cooling hole mesh.

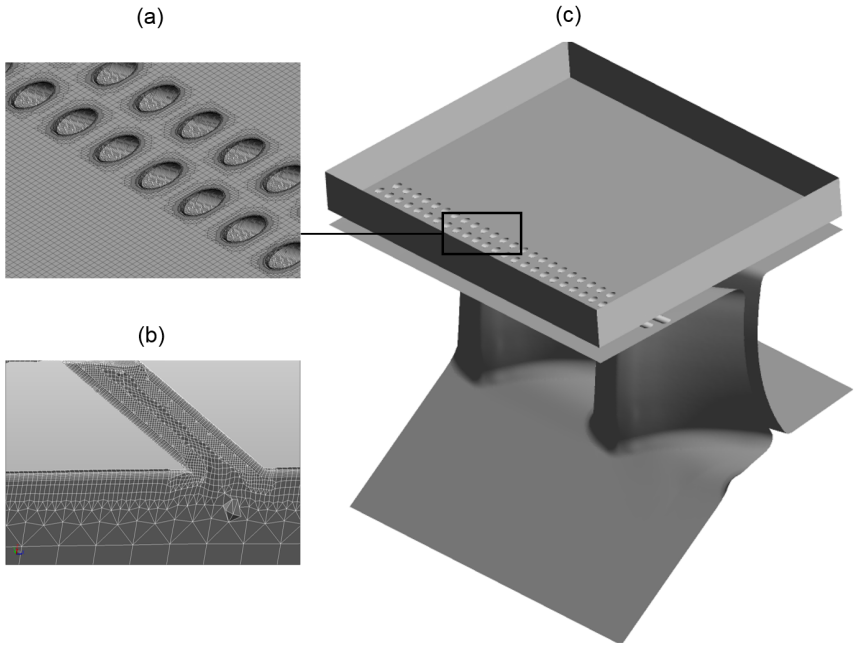


Figure 3.8: (a) Surface mesh detail; (b) film cooling hole mesh detail; (c) computational domain.

The CFD inlet total pressure field was representative of experimental measurements. Measurements were conducted at 0.42 vane axial chord upstream of the vane leading edge at five pitch locations ($0.0P$, $0.25P$, $0.5P$, $0.75P$, $1.0P$). Total pressure data are presented in Figure 3.9 as a difference from the value at the vane inlet ($p_{0,in}$) and normalized with respect to the measured exit dynamic head ($p_{0,in} - p_2^{ave}$). On the hub and casing regions, the pressure profiles collapse on a single curve indicating that the combustor dilution holes have a small effect on the endwall total pressure profile at the vane inlet. A variation in the total pressure profile is observed between $0.3 < s < 0.65$ due to the turbulence plate geometry upstream from the combustor simulator. This effect, however, is limited to the mid-span region and the maximum

deviation between profiles is only 2% of the exit dynamic head. Because this location is upstream of the two cooling rows, it is not expected to be influenced by the particular coolant to mainstream momentum flux ratio (which depends on the test condition).

An uniform value of the exit static pressure (corresponding to the ambient pressure) was imposed at the CFD domain outlet. The passage sides were periodic with translational periodicity and all wetted surfaces had realistic value of roughness. The coolant flow was simulated by imposing a mass flow rate boundary condition at the plenum inlet. Values were set to experimental conditions on a run by run basis. The temperature was set to be the same as the experimental values measured in the plenum. The turbulence intensity at the plenum inlet was set to 5%.

A grid independency study was performed in order to select the minimum adequate mesh resolution to capture the expected film effectiveness at the vane exit. The solution of the whole domain was run with four levels of grid refinement (11×10^6, 15×10^6, 17×10^6 and 27×10^6 elements). The flow conditions were MFR = 3.3% and $I = 3.89$. The results were analyzed in terms of film effectiveness distribution at the vane exit line (marked in Figure 3.18 and 3.19). Figure 3.10 shows the results of the grid independency study. Approximate grid independency was achieved for 17×10^6 elements (mesh M3 in Figure 3.10). This resolution was chosen for the current study.

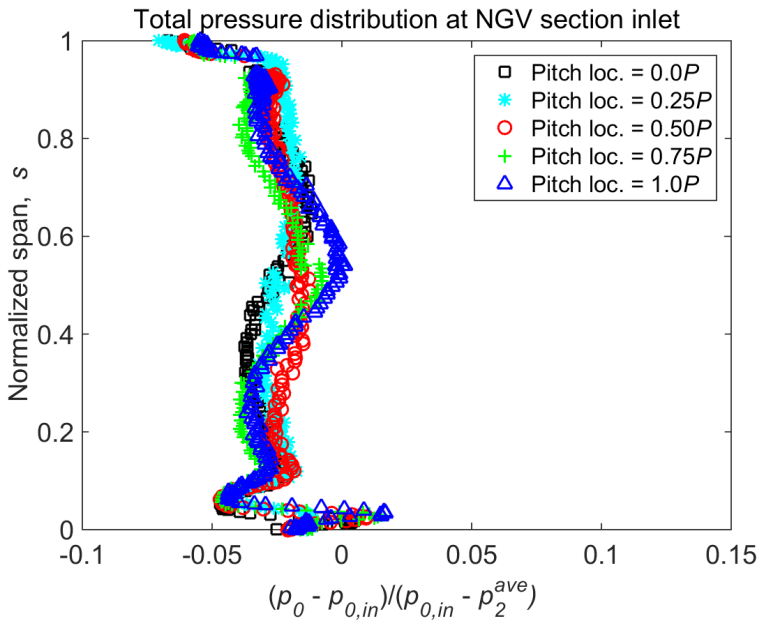


Figure 3.9: Measured normalized radial total pressure profile at the combustor-NGV interface.

3.4.1 Calculation of momentum flux ratio

To calculate momentum flux ratio, an automated post-processing routine was written using CEL expressions in CFX. Values of coolant and mainstream velocity as well as values of density were extracted from CFD using *probe locators* in CFD-Post. The coolant velocity was extracted at the cooling hole inlet, and the mainstream velocity was taken at a point lying just outside the boundary layer just upstream of the hole of interest. This allowed the local value of the momentum flux ratio (relative to each cooling hole) to be calculated, and thus the global value which was taken to be the average over n cooling holes. This methodology was justified by the fact that the weight function (i.e. the sectional hole area) was constant for all holes.

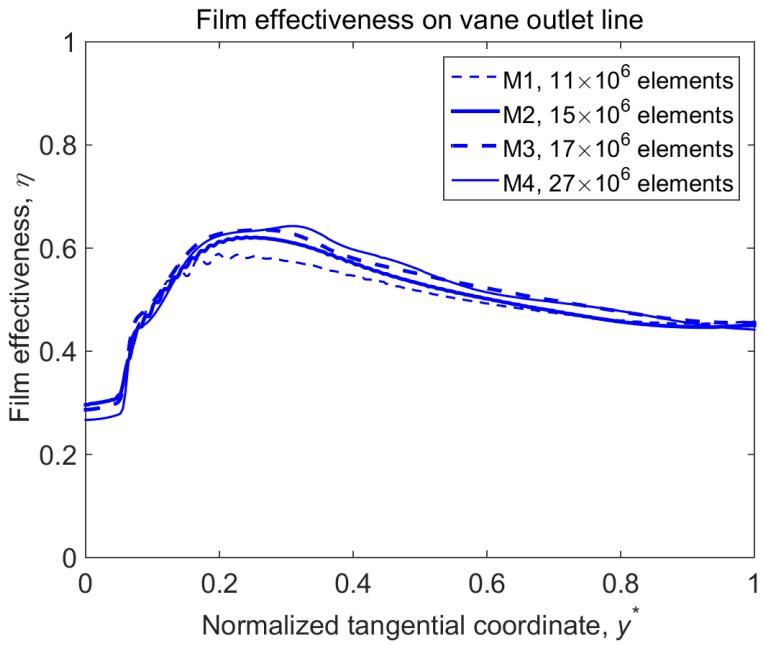


Figure 3.10: Film effectiveness distribution along the vane exit line obtained during the grid independency study. The flow conditions were: MFR = 3.3% and $I = 3.89$.

3.5 Results and discussion

3.5.1 Overall film effectiveness distributions: upstream endwall

The coolant-to-mainstream momentum flux ratio defines both the initial state of the cooling jet (attached or separated) and the near-wall total pressure profile, which—in turn—affects the secondary flows and the overall film effectiveness distribution. Figure 11 shows adiabatic film effectiveness contours on the upstream endwall in the mass flow ratio range 1.1% <MFR< 4.3%. Constant density ratio (DR = 1.1) was used giving a bulk momentum flux ratios range $0.40 < I < 26.99$.

In Figure 3.11a, for MFR = 1.1% and $I = 0.40$, we see strong secondary flows marked by coolant flow, forming a classical horseshoe vortex. Both the first (upstream) and second (downstream) rows of film cooling are attached. There is evi-

dence of flow starvation for holes near the leading edge pressure side of the vane. Strong migration of coolant towards the vane SS (secondary flow) is caused by low momentum endwall fluid being overturned by the vane potential field (cross passage pressure gradient).

In Figure 3.11b, for MFR = 2.1% and $I = 1.71$, we observe a more uniform distribution of the film effectiveness. Although the horseshoe vortex is still present, the strength of this secondary flow is significantly reduced due to increased near-wall momentum. Coolant jets downstream of both the leading and trailing rows are still attached (although the leading row appears to begin to detach), however, leading to good film cooling coverage. There is some evidence of reduced flow for holes near the pressure side leading edge. The radial migration of endwall cooling is restricted to the height of the vane fillet (approximately 5% span). It is interesting to note that secondary flows are suppressed with a relatively low momentum flux ratio, suggesting that low-pressure-margin endwall cooling systems (perhaps with internal loss elements to drop pressure) may perform well at whatever range of mass flow ratio is required in the application (by varying exit hole areas).

Figure 3.11c shows results of measurements for MFR = 4.3% and $I = 6.40$. Although film effectiveness is enhanced by increased mass flow rate, leading to full coverage with no secondary flow, the cooling is used less effectively than for lower momentum flux ratios. The leading films are completely detached (low effectiveness region between leading and trailing films), and appear to be riding above the trailing films and impinging on the vane surface in the 0-15% span region. The trailing films appear to have light lift-off followed by early reattachment, leading to good surface coverage. The suggestion is that this momentum flux ratio may be above the optimum for endwall cooling systems, and that a means of total pressure reduction may be beneficial in many engine applications.

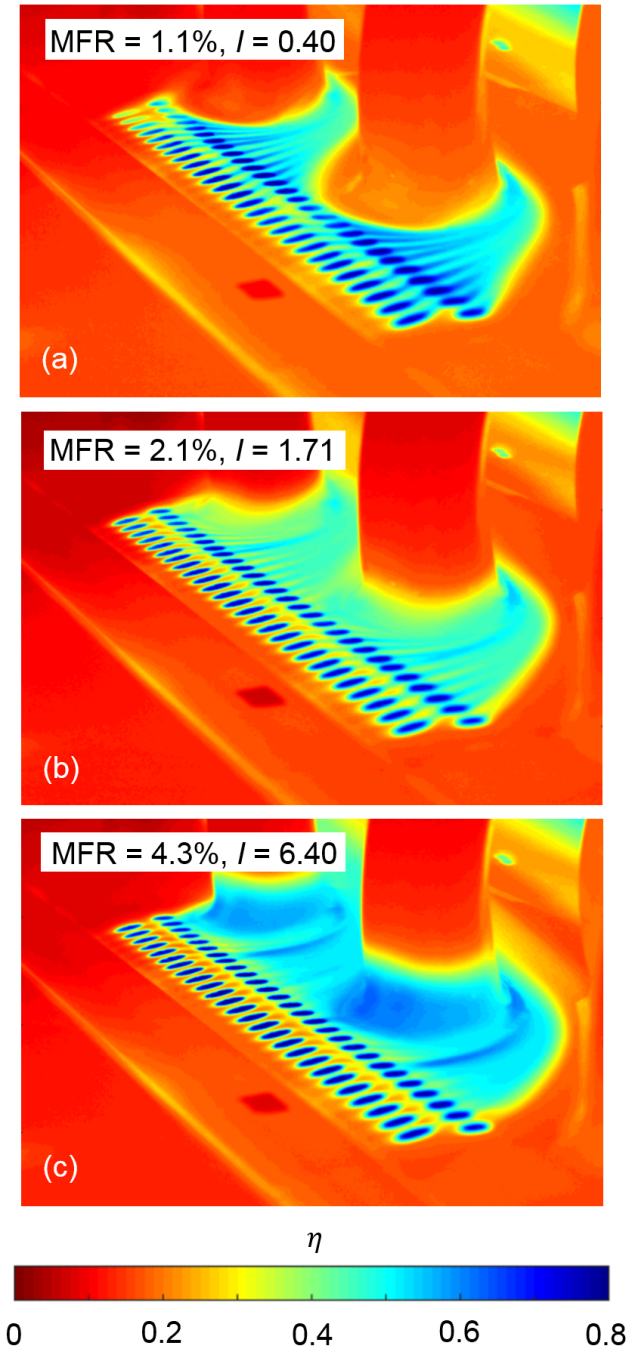


Figure 3.11: Endwall adiabatic film effectiveness contours (upstream view) for $0.40 < I < 6.40$.

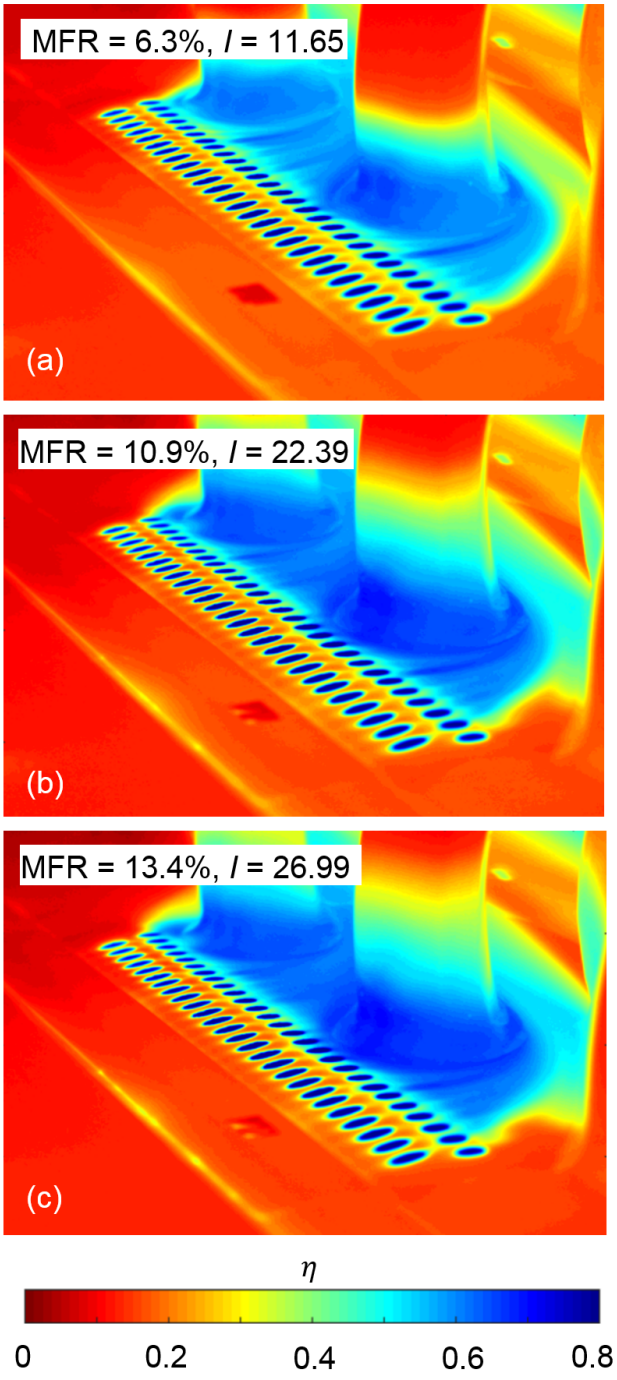


Figure 3.12: Endwall adiabatic film effectiveness contours (upstream view) for $11.65 < I < 26.99$.

Figure 3.12a shows measured film effectiveness for MFR = 6.3% and $I = 11.65$ (middle of engine range). Although well within typical engine operating ranges, the films of the first cooling row are entirely separated (very low film effectiveness between

leading and trailing rows), and there is very significant upwash on the vane surface (coolant extending to 20% span). The second row of films are also lifted off, with slightly increased surface distance to the reattachment point than the previous case. The platform is now well cooled on account of high mass flow ratios, but coolant is being inefficiently targeted at the endwall.

In Figure 3.12b, for MFR = 10.9% and $I = 22.39$ (upper limit of engine range), the first row of jets remains lifted-off and the substantial vane upwash is further increased. Coolant extends to 25% span. This cooling system is clearly very inefficient. Similar effects are observed in Figure 3.12c, for MFR = 13.4% and $I = 26.99$ (above typical upper limit on engine range), with upwash of coolant to almost 40% span.

In summary, strong secondary flows (horseshoe vortex system) begin to be suppressed for $I > 1.71$, being almost entirely eliminated by $I = 6.40$. This is below the typical engine range, suggesting that many engine systems may be operating at higher momentum flux ratio than required for secondary flow suppression. For $I = 6.40$ and higher, the leading cooling row in a double row system begins to separate, with the trailing row separating for $I \geqslant 11.65$. In this range ($6.40 < I < 11.65$) the cooling starts to penetrate significantly into the mainstream flow, leading to upwash on the vane surface and inefficient use of cooling. The suggestion is that systems which require high mass flow rates should be operated with lower momentum flux ratio by means of systems which manage the internal pressure drop.

3.5.2 Overall film effectiveness: downstream endwall

Figure 3.13 shows measured adiabatic film effectiveness distribution on the downstream endwall in the mass flow ratio range 1.1% < MFR < 13.4%, and constant density ratio of DR = 1.1 (c.f. typical engine DR = 2.0, Bogard and Thole (2006)) and therefore bulk momentum flux ratios in the range $0.40 < I < 26.69$. (c.f. typical engine range $2 < I < 18$).

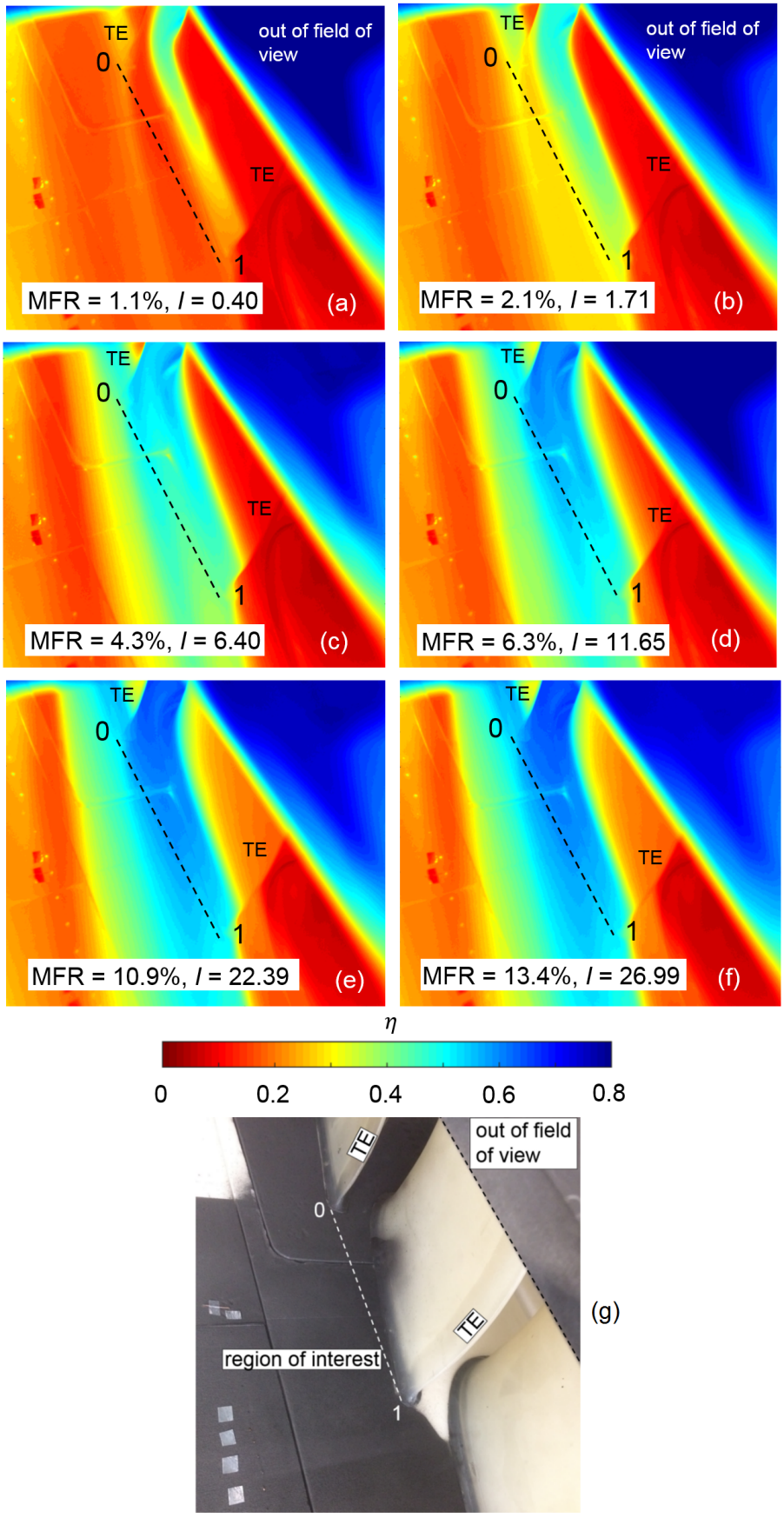


Figure 3.13: Endwall adiabatic film effectiveness contours (downstream view) for 0.40 $< I <$ 26.99.

In Figure 3.13a, for MFR = 1.1% and $I = 0.40$, we see an effectiveness distribution dominated by strong secondary flows. The coolant film is swept into the horseshoe vortex and migrates from PS to SS, collecting as a streak on the vane surface in the SS corner. In Figure 3.13b, for MFR = 2.1%, and $I = 1.71$, we see improved film effectiveness, but evidence of endwall secondary flows collecting coolant towards the SS corner. In Figure 3.13c, for MFR = 4.3%, and $I = 6.40$, in agreement with the leading endwall results of Figure 11c, we see that secondary flows are almost entirely eliminated and there is good film coverage of the entire endwall surface. We see some evidence of coolant upwash in the 0-10% span region. In Figure 3.13d, for MFR = 6.3%, and $I = 11.65$ the film effectiveness is further enhanced due to increased mass flow, secondary flows are entirely eliminated, but there is evidence of significant penetration of coolant into the mainstream (upwash to 20% span). In Figure 3.13e (MFR = 10.9%, and $I = 22.39$) and Figure 3.13f (MFR = 13.4%, and $I = 26.99$), the film effectiveness is further increased due to large increases in the mass flow rate, but upwash and mixing with mainstream flow are significant (ineffective use of cooling flow). Figure 3.13g depicts a photograph of the test section to aid interpretation of the IR images.

3.5.3 Film effectiveness distributions at lines 1 to 4

Quantitative comparisons of the overall film effectiveness distributions (Figure 3.11, 3.12, and 3.13) are now presented at four evaluation lines. The lines are marked in Figure 3.4. At each evaluation line, 13 experimental conditions are reported covering the range $1.1\% < \text{MFR} < 13.4\%$ and $0.40 < I < 26.99$. A summary of the conditions is given in Table 3.1. Experimental film effectiveness distributions evaluated at line 1 (between first and second film cooling rows) are shown in Figure 3.14. The processing lines are normalized as: $y^* = (y - y_{min})/(y_{max} - y_{min})$. The normalized tangential coordinate of lines 1 and 2 are defined to increase from right (value of 0) to left (value

of 1), as shown in Figure 3.4a. The normalized tangential coordinate of lines 3 and 4 are defined to increase in the direction of flow turning: from PS (value of 0) to SS (value of 1), as depicted in Figure 3.4a and 3.4b.

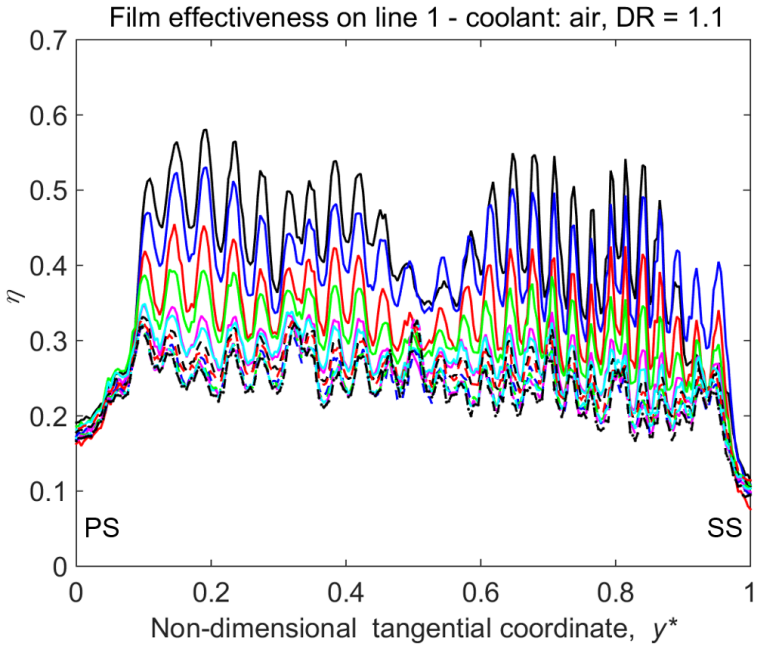
In Figure 3.14, for the lowest momentum flux ratio case ($I = 0.40$; solid black line) we see a strong signature from individual cooling rows, with well-defined peaks ($\eta = 0.5$) consistent with attached discrete film cooling traces.

Line style	Exp. number	I	MFR (%)
———	1	0.40	1.1
———	2	0.94	1.6
———	3	1.71	2.1
———	4	3.89	3.3
———	5	6.40	4.3
———	6	9.37	5.5
- - -	7	11.65	6.3
- - -	8	14.77	7.5
- - -	9	17.56	8.7
- - -	10	20.77	10.0
- - -	11	22.39	10.9
- - -	12	24.18	11.7
- - -	13	26.99	13.4

Table 3.1: Indication of operating parameters for the data presented in Figure 3.14, 3.15 , 3.16, and 3.17.

Flow starvation near the PS leading edge is evident between $0.40 < y^* < 0.55$. Interestingly, even for small increases in momentum flux ratio, in a range much lower than the typical engine condition, both the peak and mean effectiveness are reduced. This is caused by jet-lift off, which occurs for momentum flux ratios as low as $I = 0.94$, well below typical engine ranges. As the momentum flux ratio is increased in the range $I = 1.71$ to $I = 26.99$ (11 further experimental test cases) there is a monotonic

decrease in peak film effectiveness and a monotonic decrease in pitchwise average effectiveness. Both of these effects are driven by increasing jet lift-off. The result is significant enough to offset the significantly increasing coolant to mainstream mass flow ratios in this range. Two other effects are noted with increasing momentum flux ratio, firstly the monotonic decrease in the peak to trough height in the effectiveness distributions, and also the decrease in the local minimum in effectiveness around the PS leading edge. This latter effect is due to lower pitchwise variations in local mass flow ratio for higher momentum flux ratios.

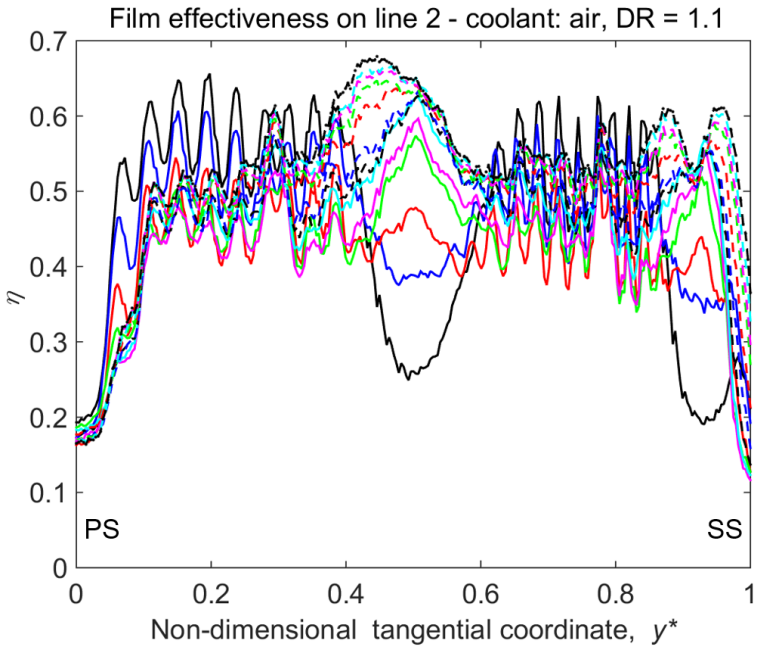


Line style	I	MFR (%)
———	0.40	1.1
———	0.94	1.6
———	1.71	2.1
———	3.89	3.3
———	6.40	4.3
———	9.37	5.5
- - -	11.65	6.3
- - -	14.77	7.5
- - -	17.56	8.7
- - -	20.77	10.0
- - -	22.39	10.9
- - -	24.18	11.7
- - -	26.99	13.4

Figure 3.14: Measured tangential distribution of adiabatic film effectiveness downstream the first cooling row (line 1).

In Figure 3.15, pitchwise cooling effectiveness data are presented for line 2, an evaluation line downstream of the second row of cooling holes and upstream of the vane leading edge. Interestingly, even at an axial station close to the vane leading edge (downstream of both cooling rows), the highest effectiveness over most of the passage is observed for the lowest momentum flux ratio (and therefore mass flow ratio), $I = 0.40$. In the range $0.40 < y^* < 0.60$, however, there is a very significant

film cooling deficit (decrease from average value of 0.55 to approximately 0.3). This deficit is caused by a combination of two effects; flow starvation due to the potential field of the vane acting preferentially to suppress flow near the PS leading edge; and boundary layer separation and roll-up into a classical horseshoe vortex system. At this low momentum flux ratio both effects are significant.



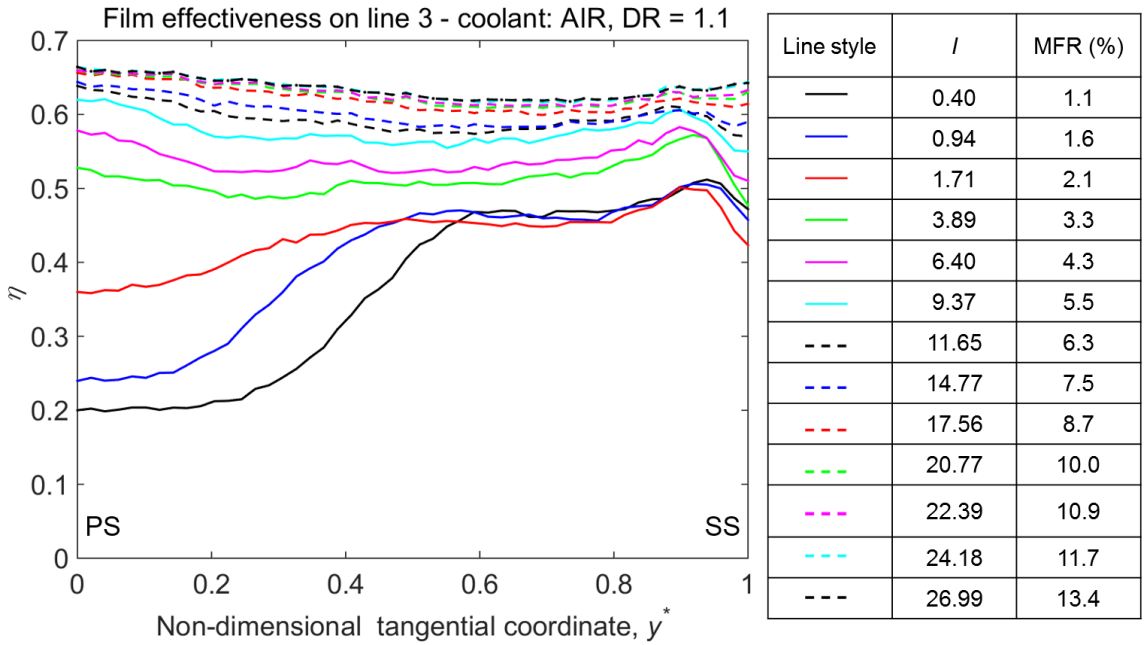
Line style	I	MFR (%)
———	0.40	1.1
———	0.94	1.6
———	1.71	2.1
———	3.89	3.3
———	6.40	4.3
———	9.37	5.5
- - -	11.65	6.3
- - -	14.77	7.5
- - -	17.56	8.7
- - -	20.77	10.0
- - -	22.39	10.9
- - -	24.18	11.7
- - -	26.99	13.4

Figure 3.15: Measured tangential distribution of adiabatic film effectiveness downstream the second cooling row (line 2).

Between $I = 0.94$ (solid blue line) and $I = 1.71$ (solid red line), the effect of near wall momentum injection is sufficient to entirely eliminate secondary flow upstream of the vane leading edge. This is shown clearly in Figure 3.11b. It is interesting that even at this very low momentum flux ratio, well below the typical engine operating range, even strong secondary flows are entirely eliminated. The effect of flow starvation persists however, accounting for the significant trough in effectiveness in the range $0.40 < y^* < 0.60$. For $I = 3.89$ (solid green line) and above the effect of flow starvation is reduced (trough eliminated) because the proportional impact of the vane potential field on near-PS holes is reduced. It is perhaps interesting to note that, other than

the sudden changes in flow structure near the PS leading edge in the range $0.40 < I < 1.71$ (well below the engine range), over a very wide range of momentum flux ratio (and corresponding mass flow ratio) there is only a relatively small increase in the endwall effectiveness.

In Figure 3.16, the film effectiveness at line 3 is presented: an evaluation line at roughly mid-passage. Here the non-dimensional tangential co-ordinate runs from 0 (PS) to 1 (SS), within the vane passage. For $I = 0.40$ (solid black line) there is a significant cooling deficit in the range $0.0 < y^* < 0.5$: that is, the endwall near the PS of the vane. This is caused by the combined effects of flow starvation and strong passage migration, as discussed above. For $I = 0.94$ (solid blue line), and $I = 1.71$ (solid red line) these effects are suddenly weakened, and effectiveness distribution becomes approximately uniform.



Line style	I	MFR (%)
———	0.40	1.1
———	0.94	1.6
———	1.71	2.1
———	3.89	3.3
———	6.40	4.3
———	9.37	5.5
- - -	11.65	6.3
- - -	14.77	7.5
- - -	17.56	8.7
- - -	20.77	10.0
- - -	22.39	10.9
- - -	24.18	11.7
- - -	26.99	13.4

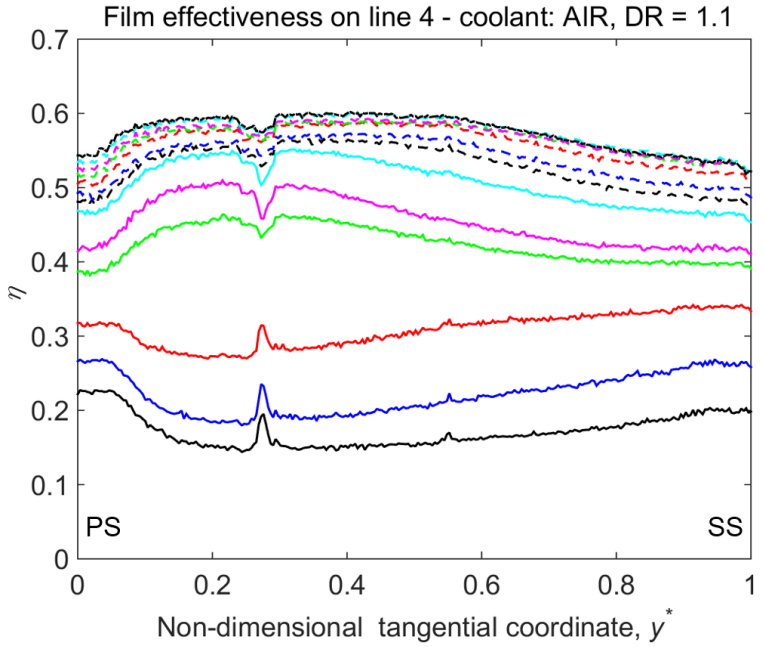
Figure 3.16: Measured tangential distribution of adiabatic film effectiveness on vane mid-passage (line 3).

For $I = 3.89$ (solid green line) and above, secondary flow is essentially eliminated and flow starvation becomes proportionally less significant. In this range the effec-

tiveness distribution is essentially uniform. A monotonic increase in the pitchwise mean value of effectiveness is observed across the entire range of momentum flux ratio ($0.40 < I < 26.99$), but interestingly the increase becomes negligible above I = 9.37. The mechanisms for this have been discussed (significant lift-off and mixing with freestream flow), and send a clear message about the useful design range of such systems. In many engine applications, introducing internal pressure drop mechanisms may be beneficial.

In Figure 3.17, the film effectiveness at line 4 is presented: an evaluation line at the vane exit plane running across a single passage from PS (0) to SS (1). Line 4 is shown in Figure 3.4b. In this heavily mixed flow, we see a monotonic increase in the pitchwise mean value of effectiveness across the entire range of momentum flux ratio. In particular we see: a very significant improvement in effectiveness in the range $0.40 < I < 1.71$, as secondary flow is reduced, and more uniform discharge is established due to the weakening proportional influence of the vane potential field; a sudden jump in effectiveness between $I = 1.71$ (solid red line) and $I = 3.89$ (solid green line) when the secondary flow is essentially eliminated throughout the passage (enhanced near wall momentum flux); and a very weak influence on effectiveness of increasing momentum flux ratio (and associated increase in mass flow ratio) over the wide range $9.37 < I < 26.99$, due to substantially enhanced mixing (deep penetration of the cooling flow into the mainflow) substantially offsetting large increases in mass flow ratio.

The clear conclusion is that beyond momentum flux ratios of $I = 3.89$, in the lower limit of engine ranges, the cooling performance (for unit mass flow) deteriorates rapidly due to enhanced mixing of the cooling with the mainstream flow. For engine systems requiring high mass flow ratios, designs with internal pressure drop systems would be advantageous.



Line style	I	MFR (%)
———	0.40	1.1
———	0.94	1.6
———	1.71	2.1
———	3.89	3.3
———	6.40	4.3
———	9.37	5.5
- - -	11.65	6.3
- - -	14.77	7.5
- - -	17.56	8.7
- - -	20.77	10.0
- - -	22.39	10.9
- - -	24.18	11.7
- - -	26.99	13.4

Figure 3.17: Measured tangential distribution of adiabatic film effectiveness on vane outlet line (line 4).

3.5.4 Comparison of CFD and experimental results at two conditions

We now compare CFD and experimental results at two conditions: $I = 6.40$ (MFR = 4.3%) and I = 11.65 (MFR = 6.3%). The purpose of the CFD comparison is to assess the degree to which common tools (RANS solver, with well resolved explicitly meshed cooling holes) can be used for preliminary design and optimization of endwall cooling systems. The flow is sufficiently complex that good agreement cannot reasonably be assumed without validation of the method.

Figure 3.18a (experiment) and Figure 3.18b (CFD) show effectiveness distributions for $I = 6.40$. Quantitative comparisons at the outline evaluation line (Line 4) are shown in Figure 3.18c. Qualitative agreement between CFD and experiment was good, with very similar predictions of the degree of upwash of coolant onto the vane surface (to approximately 15% span in both experiment and CFD), and a high degree

of similarity between the effectiveness distributions across the endwall surface. Jet lift-off of the leading row was well predicted, as was light lift-off and subsequent reattachment of flow from the second cooling row.

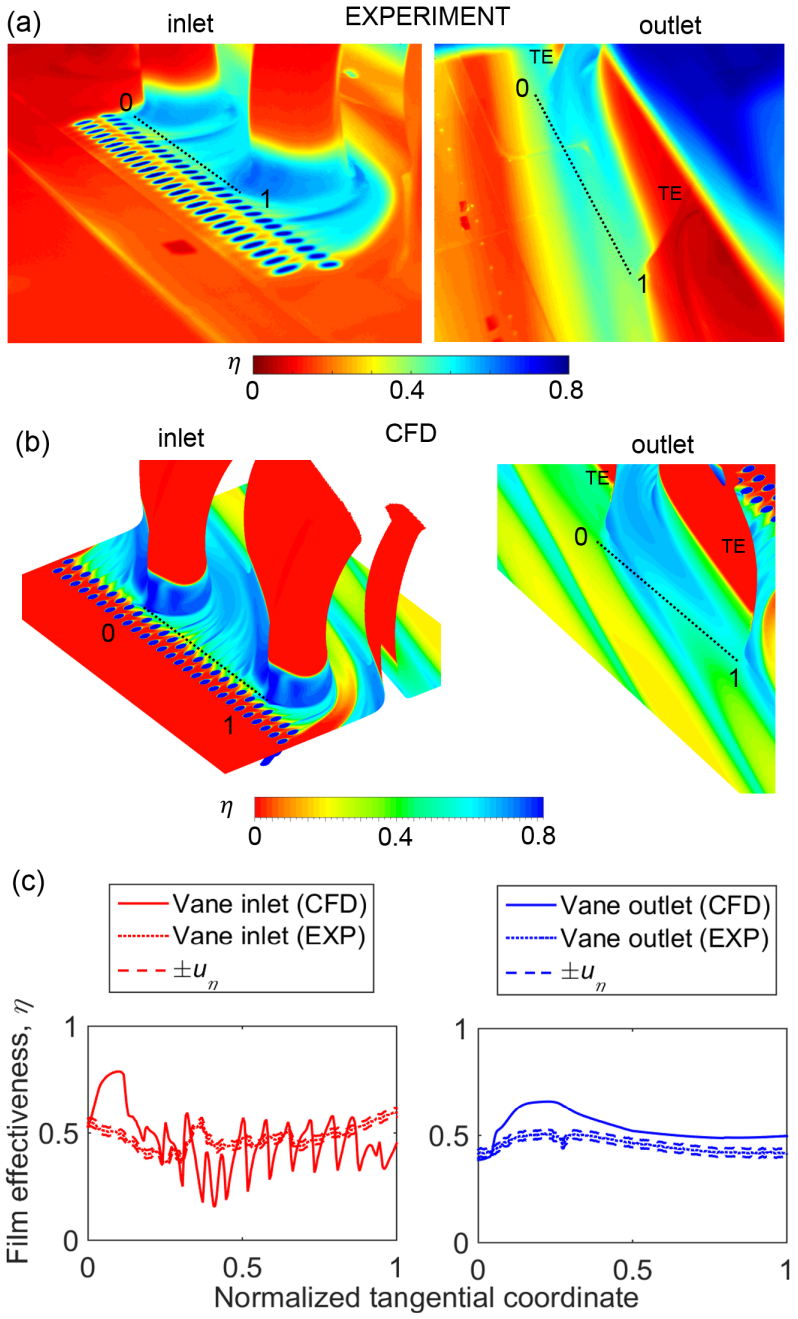


Figure 3.18: Comparison of adiabatic film effectiveness between CFD and experiment for $I = 6.40$ (MFR = 4.3%). (a) experimental results; (b) CFD prediction; (c) comparison at vane inlet and outlet lines with indication of experimental uncertainty, u_η.

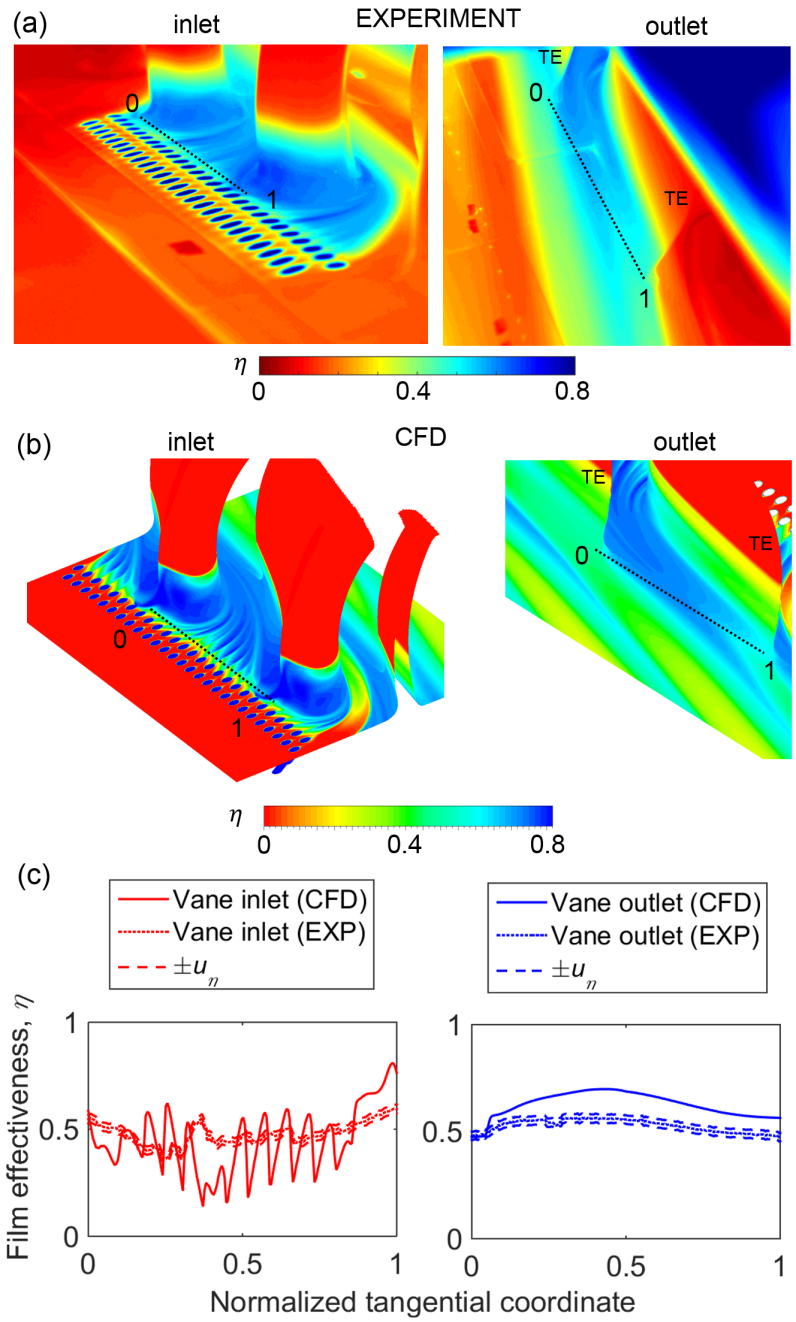


Figure 3.19: Comparison of adiabatic film effectiveness between CFD and experiment for $I = 11.65$ (MFR = 6.3%). (a) experimental results; (b) CFD prediction; (c) comparison at vane inlet and outlet lines with indication of experimental uncertainty, u_η.

In Figure 3.18c we compare quantitative film effectiveness distributions on vane inlet and exit lines for the case with $I = 6.40$ and MFR = 4.3%. Both inlet and

exit lines are normalized with respect to their minimum and maximum values and are oriented as follows: the normalized vane inlet line runs from L ($y^* = 0$) to R ($y^* = 1$); the normalized outlet line runs from PS ($y^* = 0$) to SS ($y^* = 1$). Both lines are marked in Figure 3.18a and Figure 3.18b with dashed lines. In Figure 3.18c, we see that the film effectiveness distribution at vane inlet predicted by the CFD has a spiky behaviour. This is found to not agree well with experimental results, which show a smoother distribution along the entire inlet line. This suggests that the CFD is underpredicting the lateral mixing of the cooling jets with the mainstream flow. Comparison between CFD and experiments at the vane outlet line is also shown in Figure 3.18c. The CFD well predicts the shape of the distribution (i.e. the peak on $y^* = 0.3$). Film effectiveness levels are overpredicted by the CFD, with maximum offset of 0.15. In Figure 3.19c we show the quantitative distributions of film effectiveness on vane inlet and exit lines for the case with $I = 11.65$ and MFR = 6.3%. The definition of both inlet and outlet normalized coordinates is kept the same as in Figure 3.18c. CFD results show a spiky distribution of film effectiveness on vane inlet line, whereas experimental data show a more uniform and smooth behavior. The same conclusions are drawn by looking at the comparison on the vane outlet line, where the CFD is found to overpredict the levels of film effectiveness by approximately 0.15. This is likely due to CFD underprediction of both lateral and streamwise mixing of coolant jets with main flow.

3.5.5 Laterally averaged film effectiveness at lines 1 to 4

We now consider laterally averaged values of the film effectiveness at the four evaluation lines, and compare experimental results to CFD.

Figure 3.20 shows the laterally averaged values of film effectiveness at evaluation lines 1 to 4 (see Figure 3.4). Experimental results are presented for 13 experimental conditions in the range $0.40 < I < 26.99$. The corresponding mass flow ratio range

was 1.1% < MFR < 13.4% (DR = 1.1). At line 1, between the leading and trailing film cooling rows, the average film effectiveness decreases with increasing momentum flux ratio due to jet lift-off. This effect is significant enough that average effectiveness reduces even with increasing mass flow rate. Between $I = 0.40$ and $I = 3.98$, the laterally averaged effectiveness drops from 0.41 to 0.29. A monotonic decrease in laterally averaged effectiveness continues in the range $6.40 < I < 26.99$, reaching a value of 0.23 for $I = 26.99$. For line 2, downstream of the second row of cooling holes and upstream of the vane leading edge, a more complex trend with I is observed. An initial decrease in laterally averaged effectiveness (from 0.46 to 0.42) in the range $0.40 < I < 3.89$ is dominated by lift-off of the first row of cooling holes. In the range $6.40 < I < 26.99$, there is a monotonically increasing trend in effectiveness. For low I the trend is steep, and caused by the suppression of secondary flows in the leading edge region of the vane. For higher I, the trend is less steep, and caused by the increased mass flow rate more than compensating for the worsening jet-lift off effect. In this region the overall effectiveness improves from 0.42 to 0.52, but the cooling flow is used increasingly ineffectively. For line 3, which is approximately mid passage, the laterally average effectiveness monotonically increases with I. For very low I, in the range $0.40 < I < 11.65$ there is a steep increase in effectiveness (from an average value of approximately 0.36 to 0.59), caused by the combined effect of increased mass flow rate and secondary flow suppression. In the range $11.65 < I < 26.99$, the increase in effectiveness plateaus, reaching a value of approximately 0.64. In this region cooling is inefficiently used due to jet lift off.

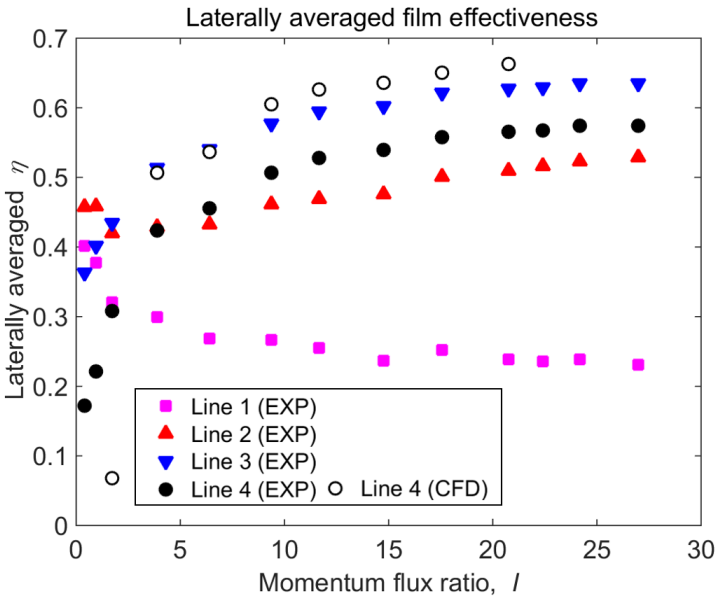


Figure 3.20: Laterally averaged adiabatic film effectiveness on lines 1 to 4 as a function of the momentum flux ratio: experiment (solid markers) and CFD (open markers).

The laterally averaged effectiveness trend at line 4 is similar to that at line 3, but with a steeper initial trend in the range $0.40 < I < 11.65$ (effectiveness increasing from 0.17 to 0.50) and a plateau at a lower value (approximately 0.58). The steeper initial trend is due to the more significant effect of secondary flows on the trailing endwall (more path length for flow to collect on the passage SS): in this region increased momentum flux ratio significantly improves the rear endwall effectiveness. The lower plateau is due to further entrainment of freestream flow into the cool near wall region as the flow migrates from mid passage to the rear endwall.

Experimental results at line 4 are also compared with CFD predictions. For the lowest momentum flux ratio simulated ($I = 1.71$) there is significant under-prediction of the laterally averaged effectiveness. This is due to slightly more dominant secondary flows in the CFD than the experimental case. For higher I, in the range $3.89 < I < 20.77$ the general trend of effectiveness with I is well matched to the experiment, but there is significant over-prediction of the endwall effectiveness (by approximately 0.1 due to under-prediction of mixing between coolant and mainstream flow using the

RANS method. This is a well-known problem which must be accounted for in CFD based design.

3.5.6 Total pressure profile in the near-wall region: comparison of CFD and experiment

Experimental measurements were performed of the inlet radial total pressure profile, to understand its role in secondary flow suppression. In this section we compare measurement to CFD simulations.

The radial distribution of total pressure was measured using a pitot probe mounted to a traverse system with LVDT sensors. Results are presented for the location indicated in Figure 21b. Data are presented as: $(p_0 - p_0^*)/(p_{0,in} - p_2^{ave}))$, where p_0^* is the total pressure value at 50% span and $(p_{0,in} - p_2^{ave})$ is the dynamic head at the vane exit, measured for each run. The y-axis in Figure 3.21a is the normalized span, s. Figure 3.21a presents experimental results for three momentum flux ratios, $I =$ 0.40, 6.40 and 11.65. These are chosen to be nominal low value of I (0.40), a value typical of that at which the leading secondary flow are suppressed (6.40) and a value at which secondary flows are eliminated even towards the rear of the passage (11.65). Examining the normalized near-wall radial total pressure field at the case, we see that for $I = 0.40$, we have a mild deficit in total pressure in the region between $0.95 < s <$ 1.00. For $I = 6.40$ there is surplus total pressure in the near wall region, peaking at 8% of the exit dynamic head, at $s = 0.95$. For $I = 11.65$ there surplus total pressure in the near wall region is further increased, peaking at 22% of the exit dynamic head at $s = 0.95$. Similar trends are observed in the CFD predictions at the same location, but slightly lower peak values of total pressure and a more well defined peak.

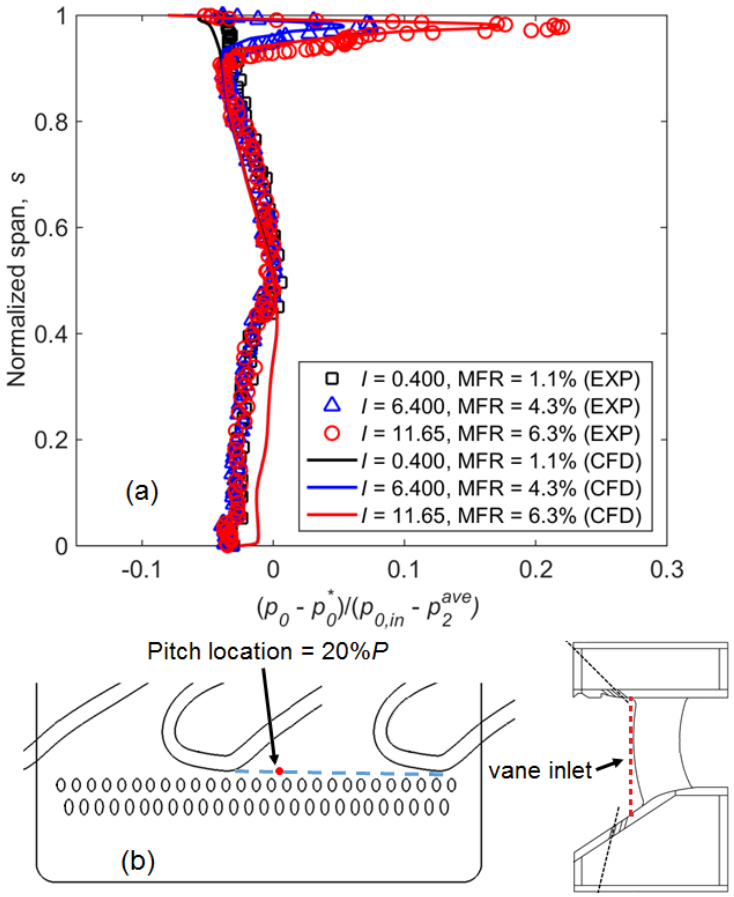


Figure 3.21: (a) Normalized total pressure radial profile, $(p_0 - p_0^*)/(p_{0,in} - p_2^{ave})$, for different momentum flux ratios; (b) axial and pitchwise location of the radial traverse.

The experimental and CFD measured radial total pressure trends are consistent with the full surface effectiveness tests (Figure 3.12), in that the near wall total pressure profile dictates the severity of the endwall secondary flow. A deficit in near wall total pressure (with respect to the rest of the passage) can result in secondary flow formation (low values of I), whereas a surplus in near wall total pressure first (for moderate values of I) reduces the secondary flow strength, then (for higher values of I, and therefore near wall total pressure) leads to lift-off of cooling jets, and in extreme cases (high values of I) reversal of secondary flow and upwash onto the NGV surface.

Figure 3.22 shows CFD-predicted non-dimensional total pressure contours at the

same plane as the experimental traverse (just downstream of the second row of cooling holes) for $I = 0.40$ and $I = 11.65$. In the low momentum flux ratio case ($I = 0.40$) both film rows are well attached to the surface, and there is a deficit in near wall total pressure (with respect to the mid-span). For the higher momentum flux ratio case ($I = 11.65$) the total pressure contours show both that the first row is lifted-off, and that there is a significant surplus in near wall total pressure. This is consistent with the experimental results of Figure 3.21, which show an increase in the near wall total pressure peak, and a shift away from the endwall (lower s) for higher values of I.

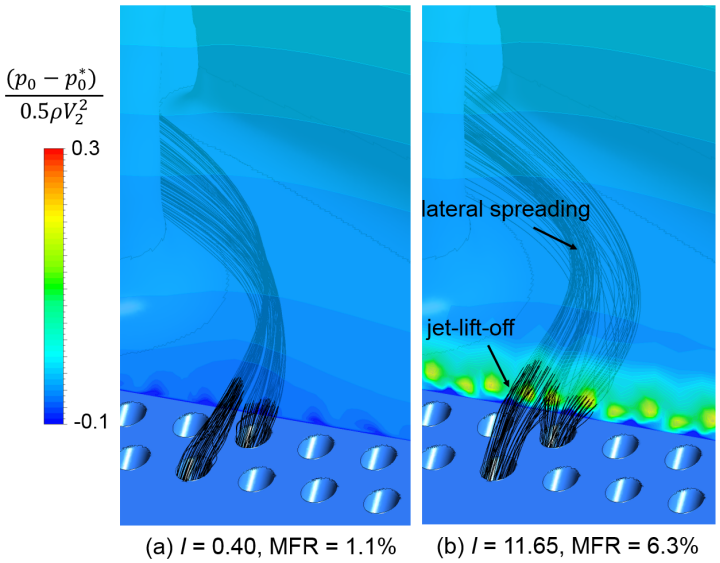


Figure 3.22: Normalized total pressure contours at vane inlet and coolant streamline traces; case with low I (a) and high I (b).

Figure 3.23 shows the Lambda-2 vortex detection criterion for $I = 0.40$ and $I = 11.65$ (PS view). For low I ($I = 0.40$), the horseshoe vortex detaches the films and transports low momentum coolant towards the SS of the vane, resulting in a well-defined passage vortex at 80% span. For higher momentum flux ratios ($I = 11.65$), the horseshoe vortex is weakened and is pushed away from the endwall surface.

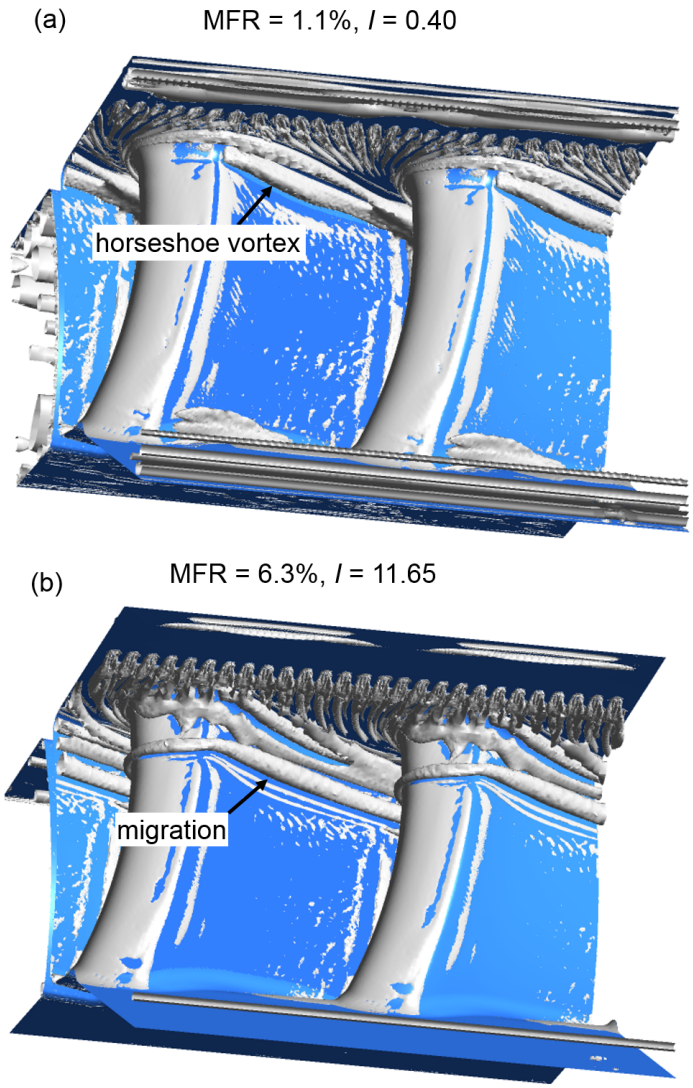


Figure 3.23: PS view of Lambda 2-criterion for: (a) $I = 0.40$; (b) $I = 11.65$.

Figure 3.24 shows the Lambda-2 vortex detection criterion and the CFD-predicted total pressure loss coefficient contours at the vane exit (at the TE plane) for $I = 0.40$ and $I = 11.65$. The total pressure loss coefficient is defined as: $c_{p0} = (p_{0,in} - p_0)/0.5\rho V_2^2$, where $p_{0,in}$ is the mass-averaged total pressure at the vane inlet and $0.5\rho V_2^2$ is the dynamic head at the vane exit plane. Increasing the coolant flow injection (moving from $I = 0.40$ and $I = 11.65$) weakens the passage vortex, and displaces it from approximately 80% span to 65% span. There is an additional low total pressure region at 75% span associated with coolant which has lifted off and

washed up the vane leading edge (Figure 3.12a).

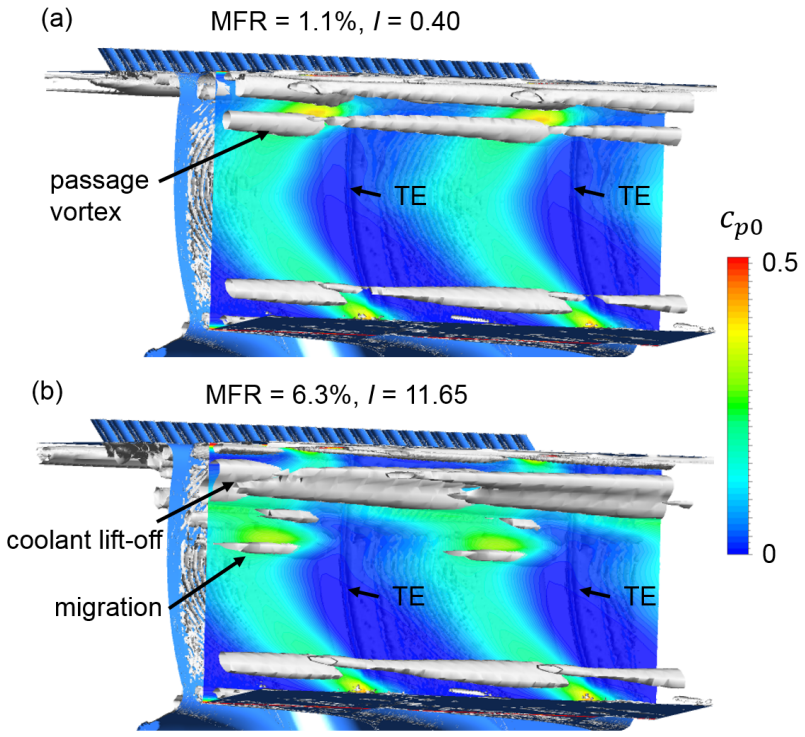


Figure 3.24: SS view of Lambda2-criterion and total pressure loss coefficient, c_p0, for: (a) $I = 0.40$; (b) $I = 11.65$

3.6 Conclusions

In this chapter we have investigated the effect of momentum flux ratio on the development of the effectiveness distribution for an engine-realistic turbine endwall geometry. By using high resolution IR thermography, we present a detailed evolution of the effectiveness profile across a wide range of conditions spanning the full engine range. We analyze the data quantitatively at a number of axial evaluation planes to understand the effect of mechanisms such as jet lift-off and secondary flow suppression. Extensive experimental results are complimented with CFD predictions to aid analysis and demonstrate the limitations of conventional CFD methods for design of these systems.

We show that the coolant flow plays an active role in the development of the aerodynamic field in the near-wall region, rather than being subject to an existing secondary flow field. We show that there are key transition points in the global flow field, at which secondary flows are suppressed, or even reversed in direction. For a given cooling system the transition points occur at particular values of coolant to mainstream momentum flux ratio, and have a significant effect on the overall effectiveness distribution of the endwall. A key result is that secondary flows are entirely suppressed at relatively low values of momentum flux ratio with respect to the typical engine range, and that beyond a critical value of momentum flux ratio the coolant flow is very ineffectively used (very weak improvement in overall effectiveness with increasing mass flow rate). The conclusion is that engine systems operating at relatively high mass flow ratios would benefit significantly from reduced momentum flux ratio by introducing internal loss: the total cooling hole area would need to be increased if the mass flow rate were to be maintained.

A number of other insights are given which it is hoped will be useful to turbine designers in developing improved turbine endwall cooling system.

Chapter 4

Development of a Rapid Optimization Routine Based on the Scalar Tracking Method

This chapter presents a method to accelerate CFD optimization of film cooling systems. The scalar tracking method is combined with linear superposition models which act as a supplementary proxy model for the CFD solver. The proxy model is both initialized with a CFD solution, and periodically recalibrated with further CFD solution, but replaces CFD for the main optimization loop. The number of CFD runs is substantially reduced when compared to standard optimization techniques. The scalar tracking method identifies the contributions of individual holes to an overall cooling effectiveness distribution by associating a unique passive scalar variable to the flow associated with each hole, and solving an additional advection-diffusion (scalar transport) equation. Individual contributions to overall effectiveness are dealt with by superposition techniques in the proxy model, achieving convergence of the proxy model using an automated optimization routine before recalibration with a further CFD run.

An optimization routine involving the film cooling of a flat plate with external flow acceleration is performed by minimizing the temperature difference from a target distribution whilst minimizing mixing loss. Physical limitations of the method are also discussed in detail.

4.1 Introduction

Automated optimization of film cooling systems was exploited by several authors. The open literature reports only a few studies on multi-hole configurations with full three-dimensional geometries. Ayoub (2014) developed a three-dimensional aero-thermal optimization of a two-hole configuration for a vane suction side geometry. This study employed a multi-objective optimization strategy combining Artificial Neural Networks (ANN) and genetic algorithms (GA). The ANN was trained with CFD simulations and the maximum error in ANN predictions was approximately 20%. External film effectiveness and aerodynamic loss introduced by the film cooling were selected as objective functions. Weight functions were used to generate a set of optimal designs based on two concurrent objectives. The optimization involved 60 generations, each of them including 80 individuals. Jiang et al. (2017) performed an aero-thermal optimization on multi-row film cooling of a high pressure turbine vane. They considered aerodynamic efficiency and adiabatic film cooling effectiveness to evaluate the overall performance. They employed response surface approximation with the Non-dominated Sorting Genetic Algorithm (NSGA-II). Their optimization converged after 30 generations, each of them including a population of 20 individuals. Johnson et al. (2014) investigated the heat transfer characteristics of a full scale cooled HPT vane as result of genetic algorithm optimization. Cooling configurations were simulated with full 3D RANS, by modeling the coolant injection with a transpiration boundary condition (i.e. the coolant injection was simulated as a mass flux source). They considered a discrete design space for the film cooling process variables (hole location, jet inclination angle, etc.). The optimization process involved 1800 CFD simulations.

From the literature survey, we can conclude that advanced optimization strategies based on surrogate and non-surrogate models still require a consistent number of CFD runs to train these models and—more broadly—to reach an optimal design. In the case of film cooling, some physical assumptions and model simplifications (e.g. the use

of a mass flux boundary condition in place of fully resolving the hole geometry) can be applied to reduce the complexity of the problem. However, the need for expensive simulations still depends on the accuracy of the surrogate models or interpolation functions. One way to dramatically reduce the impact of computational cost can be achieved through the use of reduced order models and linear superposition techniques. As described in the next paragraphs, for certain classes of film cooling problems, linear superposition models can be used to quickly predict the film effectiveness distribution as a function of the coolant mass flow rate. Inexpensive models can be therefore developed and combined with standard optimization techniques, such as GAs. The next sections describe the optimization methodology developed in the present work, which combines the scalar tracking model and multi-objective genetic algorithms to optimize film cooling systems.

4.2 The scalar tracking method

An optimization methodology based on the scalar tracking method was developed for the present work. The scalar tracking method for film cooling systems was originally developed by Thomas (2014) and Thomas and Povey (2016). The scalar tracking method is based on the solution of a passive scalar concentration (associated with each hole), which is used to estimate the individual contribution of a single hole to the overall film effectiveness.

The adiabatic film effectiveness can be defined as:

$$\eta = \frac{T_{0,\infty} - T_{aw}}{T_{0,\infty} - T_{0,c}}, \tag{4.1}$$

where $T_{0,c}$ and $T_{0,\infty}$ are the total temperature of coolant and mainstream gas and T_{aw} is the adiabatic wall temperature. For compressible flows, the driving temperature is the recovery temperature, T_r, which takes into account compressibility effects. For

the present work, we consider fairly low Mach number and the difference between the recovery temperature and mainstream total temperature is assumed to be small. The scalar tracking method evaluates the coolant concentration by solving a passive scalar transport equation. The scalar concentration is modelled by means of the steady-state advection equation and solved subsequently the momentum and continuity equations. The concentration of the scalar i (ϕ_i) is defined as:

$$\frac{\partial \left(\rho u_j \phi_i\right)}{\partial x_j} = \Gamma \frac{\partial^2 \phi_i}{\partial x_j \partial x_j}, \tag{4.2}$$

where Γ is the scalar diffusivity and u_j is the velocity vector. The energy equation for a steady-state flow is:

$$\frac{\partial \left(\rho u_j c_p T\right)}{\partial x_j} = k_{eff} \frac{\partial^2 c_p T}{\partial x_j \partial x_j}, \tag{4.3}$$

where k_{eff} is the effective turbulent thermal diffusivity, defined as:

$$k_{eff} = k + \left(\frac{c_p \mu_T}{Pr_T}\right), \tag{4.4}$$

where k is the thermal conductivity, μ_T is the turbulent viscosity and Pr_T is the turbulent Prandtl number. The thermal field can be reproduced via a passive scalar if the scalar diffusivity is set equal to the effective turbulent thermal diffusivity ($\Gamma = k_{eff}$).

The flow issued from each cooling hole is associated to a unique passive scalar. The boundary condition for each hole inlet is defined as follows:

$$\begin{cases} \phi_j = 1 \quad \text{for} \quad j = i \\ \phi_j = 0 \quad \text{for} \quad j \neq i. \end{cases} \tag{4.5}$$

The condition $\phi_j = 0$ is set at the freestream domain inlet.

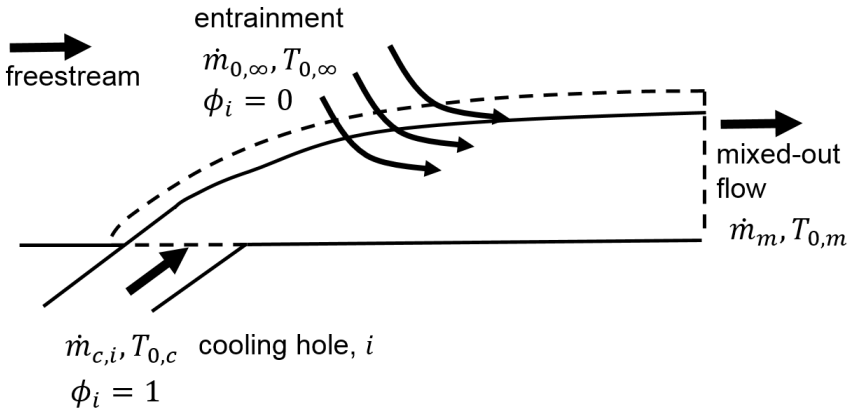


Figure 4.1: Film cooling control volume.

With reference to Figure 4.1, the mixed-out conditions for the scalar concentration are given by the following equation:

$$\phi_i = \frac{\dot{m}_{c,i}\phi_i\rfloor_{c,i} + \dot{m}_\infty\phi_i\rfloor_\infty}{\Sigma_i\dot{m}_{c,i} + \dot{m}_\infty} = \frac{\dot{m}_{c,i}}{\dot{m}_m}, \tag{4.6}$$

where the concentration of the scalar i is $\phi_i\rfloor_{c,i}$ at the cooling hole i inlet, and $\phi_i\rfloor_\infty$ at the freestream conditions. In Equation 4.6, the term ϕ_i is therefore equal to the local coolant mass fraction due to hole i. The overall coolant mass fraction can be obtained by the sum of all scalar concentrations:

$$\Sigma_i\phi_i = \frac{\dot{m}_c}{\dot{m}_m}. \tag{4.7}$$

The continuity and energy equation can be written respectively as:

$$\dot{m}_m = \dot{m}_c + \dot{m}_\infty \tag{4.8}$$

$$\dot{m}_m c_{pm} T_{0,m} = \dot{m}_\infty c_{p\infty} T_{0,\infty} + \dot{m}_c c_{pc} T_{0,c}. \tag{4.9}$$

Assuming that $c_{pm} = c_{p\infty} = c_{pc}$, dividing Equation 4.9 by $\dot{m}_m$ and rearranging using

Equation 4.6, the following expression can be obtained:

$$T_{0,m} = T_{0,\infty} - (\Sigma_i \phi_i) \left(T_{0,\infty} - T_{0,c}\right). \tag{4.10}$$

Assuming that the difference between the recovery temperature, T_r, and $T_{0,m}$ is small, and substituting η (Equation 4.1) into Equation 4.10, the following expression can be derived:

$$\eta = \Sigma_i \phi_i = \frac{T_{0,\infty} - T_{aw}}{T_{0,\infty} - T_{0,c}}. \tag{4.11}$$

Equation 4.11 allows the use of the overall scalar concentration as a proxy for the overall cooling effectiveness. In this way, the contribution of each individual hole i to the overall effectiveness can be assumed to be equal to the local concentration of the passive scalar ϕ_i. The model is simple to implement and inexpensive to run. It can be used as a proxy of the CFD in standard optimization techniques.

4.3 Optimization methodology

A rapid optimization routine for film cooling systems based on the scalar tracking method was developed for the present work. The scalar tracking method identifies the contribution of each hole to the overall film effectiveness distribution. Based on the knowledge of the local scalar concentration, a rapid optimization can be performed by using a linear superposition model as a proxy for the CFD.

The optimization process begins with an initial design (with given film effectiveness distribution, hole diameter and initial mass flow rate). A rapid Multi-Objective Genetic Algorithm (MOGA) optimization is performed using Equation 4.6 as proxy for the CFD, and the mass flow rate of each hole is varied during the optimization. Two objective functions are chosen: the difference from an adiabatic film effectiveness target distribution (later defined as *life objective*) and the mixing losses introduced

by the films. These two objectives define the fitness of each design generated by the MOGA algorithm. After the MOGA process is converged, a *Pareto* front is generated with the set of non-dominated designs included in the last population. One design is arbitrarily chosen from the Pareto front—this selection process is discussed later in the text. CFD solution is performed and values of the objective functions are compared to the optimizer prediction. The loop is repeated until the objectives cannot be further improved.

The whole process depicted in Figure 4.2 and described in detail below:

1. A CFD simulation of the initial geometry is performed to obtain an initial solution. In particular, the CFD is set to solve n passive scalar transport equations (where n is the number of cooling holes involved in the optimization) and is run until the solution of each passive scalar transport equation is converged. This step is represented in Figure 4.2 by the block *CFD*.

2. Results of mass flow rates, external static pressure field, and passive scalar concentrations from CFD are passed onto the proxy model. The latter uses linear superposition techniques to estimate the adiabatic film effectiveness.

3. Knowledge of film effectiveness as well as mass flow rates, external pressure field, and passive scalar concentration are used to calculate the objective functions.

4. Information of life objective and mixing loss are then sent to the MOGA routine for the GA optimization phase. The MOGA routine iterates the process including step 2-4 until the convergence criteria of the optimization method are met. This process is computationally inexpensive, and it is referred to here as the *inner loop*.

5. When the inner loop is converged, the values of mass flow rate for each cooling hole are used to calculate the updated hole diameters.

6. A new CFD solution is run and the process repeated from step 1 until the entire process is converged. Each phase involving CFD is computationally expensive, and it is referred to here as the *outer loop* or *global run*.

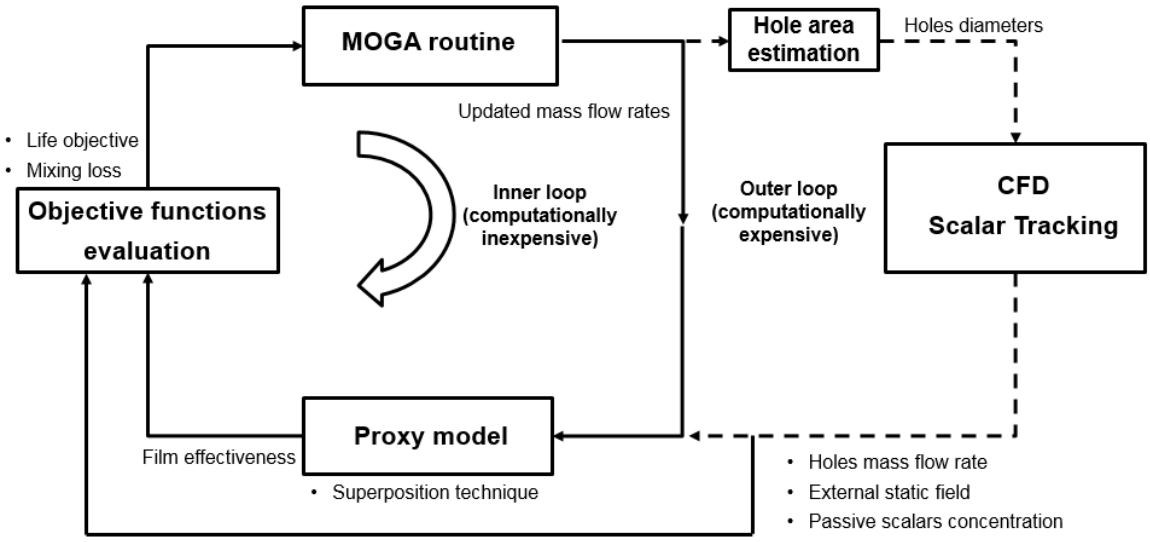


Figure 4.2: Scalar tracking-MOGA method flow chart.

The MOGA settings (step 4) are chosen in such a way that, for each MOGA cycle, the variation of mass flow rate for each hole remains within ±20% of its initial value. As will be discussed in the following sections, this limitation is imposed to reduce the impact of nonlinear effects due to changes in the flowfield (e.g. flow structures) generated by variations in hole mass flow rate within each *global run*.

In step 4, the diameter of each hole is calculated by means of the following relation:

$$\dot{m}_i = C_d \frac{\pi d_i^2 p_0}{4\sqrt{T_0}} \sqrt{\frac{\gamma}{R}} M \left(1 + \frac{\gamma+1}{2} M^2\right)^{-\frac{\gamma+1}{2(\gamma-1)}} \tag{4.12}$$

where p_0 is the stagnation pressure, T_0 is the stagnation temperature, M is the Mach number, γ is the isentropic exponent, R is the specific gas constant and C_d is the discharge coefficient. The discharge coefficient is calculated by using the previous CFD solution at each global run *or outer loop* and it is assumed to be constant

within each MOGA run (or *inner loop*). This assumption is assumed to be valid due to the small variation of the hole mass flow rate allowed for a MOGA run.

4.3.1 Life objective function

A multi-objective strategy is developed for the present study, in which two concurrent objective functions—one that relates to the life of the component, and another one that accounts for losses introduced by the film cooling—are optimized. The first function is related to the temperature of the component and it is therefore used to characterize its life. This function is based on the temperature difference between the component temperature and a target—arbitrarily chosen—distribution. The temperature difference is calculated as follows:

$$T(y) - T_{targ}(y) = (\eta_{targ}(y) - \eta(y))\,(T_{0,c} - T_{0,\infty})\,, \tag{4.13}$$

where $T(y)$ is a function of the lateral coordinate y and it is calculated by using Equation 4.11. $T_{targ}(y)$ is the target temperature, also function of the lateral coordinate y. The target temperature is based on the distribution of a target film effectiveness. The latter is chosen as an arbitrary complex distribution to demonstrate the capability of the method. The target film effectiveness distribution is a function of the normalized lateral coordinate y^* and it is described by the following function:

$$\begin{cases} \eta = 0.4 \quad \text{for} \quad 0.0 \leq y^* < 0.5 \\ \eta = 0.2 \quad \text{for} \quad 0.5 \leq y^* \leq 1.0. \end{cases} \tag{4.14}$$

The above distribution can be thought as a test exercise for the optimization process to improve the design from an initial configuration in which some regions are *over-cooled* ($\eta > \eta_{target}$) and others are *under-cooled* ($\eta < \eta_{target}$).

A life coefficient, L_f, is defined to relate the temperature difference to the *oxida-*

tion life of the component. L_f is defined as the ratio between the oxidation life (in arbitrary units) associated with the temperature T and its value associated to the target temperature T_{targ}. The equation for calculating the life coefficient is given as follows:

$$L_f = \frac{L}{L_{targ}} = \frac{a}{(T - T_{targ})\, b}, \tag{4.15}$$

where a and b are arbitrary constants. The life coefficient decreases for increasing temperature difference from the target distribution. The model constants a and b are chosen in such a way that the life coefficient is halved for every 20 K of increase temperature difference. In order to limit the generation of overcooled designs (which would result for negative values of the life coefficient, i.e. for $T - T_{targ} < 0$), the *life objective* function, Obj_1, is therefore defined as follows:

$$\begin{cases} Obj_1 = 1 - \dfrac{1}{L_f} & \text{for} \quad T - T_{targ} > 0 \\ Obj_1 = 1 & \text{for} \quad T - T_{targ} < 0. \end{cases} \tag{4.16}$$

The objective function Obj_1 is depicted in Figure 4.15 as a function of the temperature difference $(T - T_{targ})$. The definition of Obj_1 in Equation 4.16 is chosen to optimize for temperatures below life limits, though avoiding overcooled designs. In fact, no benefit is gained for designs with $T - T_{targ} < 0$ as—for any value in this range—the life objective is equal to 1.

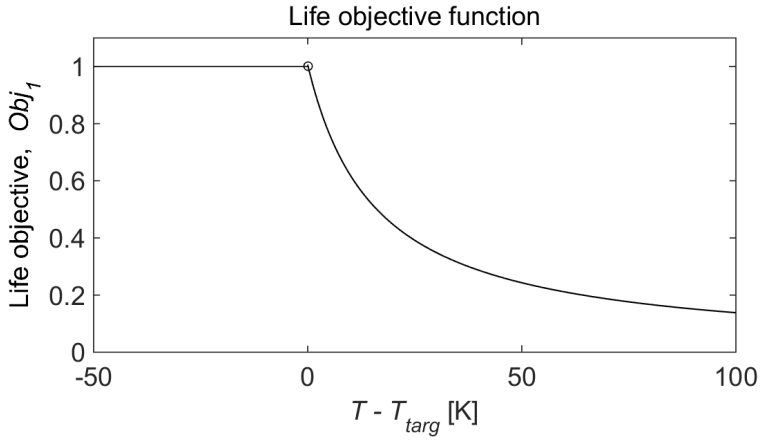


Figure 4.3: Life objective (Obj_1) as a function of the temperature difference.

Finally, the *global life objective* function, f_1, is defined as the minimum value of Obj_1 calculated at the specified post-processing line.

4.3.2 Film cooling loss function

Losses due to film cooling injection were calculated as the sum of two contributions: the kinetic energy loss due to aerodynamic mixing and the loss due to thermal mixing between coolant and mainstream gas. The kinetic energy loss was estimated by means of the model developed by Kollen and Koschel (1985). The method was introduced to calculate the loss due to the mixing process between the coolant injected into the mainstream gas at various locations on a blade profile. The method is based on the following assumptions:

1. friction is neglected;

2. coolant and mainstream fluid are perfect gases;

3. coolant and mainstream fluid have same specific heats, independent of temperature;

4. the freestream total temperature, total and static pressures at the exit of the cascade are not influenced by the coolant injection;

5. the mainstream velocity at the location of injection (before mixing takes places) is not influenced by coolant injection.

After deriving the equation of mass, momentum and energy conservation for the control volume including coolant injection into a freestream, we can write the expression for the mixed-state Mach number, M_m:

$$M_m^2 = \left(\frac{(1+Y_c)\left(T_{0,\infty} + Y_c T_{0,\infty}\right)\left(1+\frac{\gamma-1}{2}M_\infty^2\right)}{\left(Y_c \frac{u_c}{u_\infty} cos(\alpha)+1\right) M_\infty^2 T_{0,\infty}} - \frac{\gamma-1}{2} \right)^{-1}, \tag{4.17}$$

where u_c and u_∞ are the coolant and freestream velocity and $Y_c = (\rho_c u_c A_c)/(\rho_\infty u_\infty A_\infty)$. α is the hole inclination angle with respect to the horizontal direction. Assuming that $p_m = p_\infty$, the total pressure loss can be computed by using the following equation:

$$\frac{p_{0,m}}{p_{0,\infty}} = \frac{\left(1+\frac{\gamma-1}{2}M_m^2\right)^{\frac{\gamma-1}{\gamma}}}{\left(1+\frac{\gamma-1}{2}M_\infty^2\right)^{\frac{\gamma-1}{\gamma}}}. \tag{4.18}$$

Thermal mixing losses were also included in the overall loss estimation during the optimization. The entropy generation due to the temperature difference between coolant and mainstream is given by the following equation:

$$\Delta S_Q = \frac{\dot{m}_c}{\dot{m}_c} \int_{T_c}^{T_\infty} c_p \left(\frac{1}{T} - \frac{1}{T_\infty} \right) dT. \tag{4.19}$$

The loss—or cost—function thus included both kinetic energy and thermal mixing losses and was expressed in terms of entropy generation, as reported below:

$$f_2 = \Delta S_{KE} + \Delta S_Q. \tag{4.20}$$

The optimization algorithm was therefore set to maximize the life function f_1 and minimize the cost function f_2.

4.3.3 Optimization algorithm

The JEGA genetic algorithm library, developed within the DAKOTA software, was selected as the central core of the optimization process. DAKOTA is a C++ based, open source platform developed by the Sandia National Laboratories (Adams et al. 2015). Genetic Algorithms (GAs) are widely exploited for function optimization. GAs mimic the evolution process of the biological systems in nature and are based on genetic reproduction of individuals (genomes). During the optimization, populations of genomes are generated and individuals with the highest fitness are selected for the next population. In GAs, each individual is a binary string which represents a design. Natural processes such as crossover and mutation are simulated in GAs via recombination of bits within binary strings. In particular, crossover is performed through the construction of a new genome (child) using portions of 2—or more—designs (parents). The mutation process is used in GAs to preserve or introduce diversity by altering one or more bits in a binary string. Without mutation, genomes may become too similar and the process may be slowed or even trapped in local minima.

For the present work, the MOGA algorithm, developed by Eddy and Lewis (2001), was employed for the optimization. MOGA is a rank-based fitness assignment algorithm for multi-objective optimization problems (Fonseca and Fleming 1993). Unlike single objective strategies, the solution of the multi-objective optimization is a set of non-dominated values of the objective functions. All the non-dominated designs populate the so-called *Pareto front*. The Pareto front is formed by all designs for which none of the objective functions can be improved without degrading one of the other objectives. Designs belonging to the Pareto set are called *non-dominated* or *Pareto optimal*.

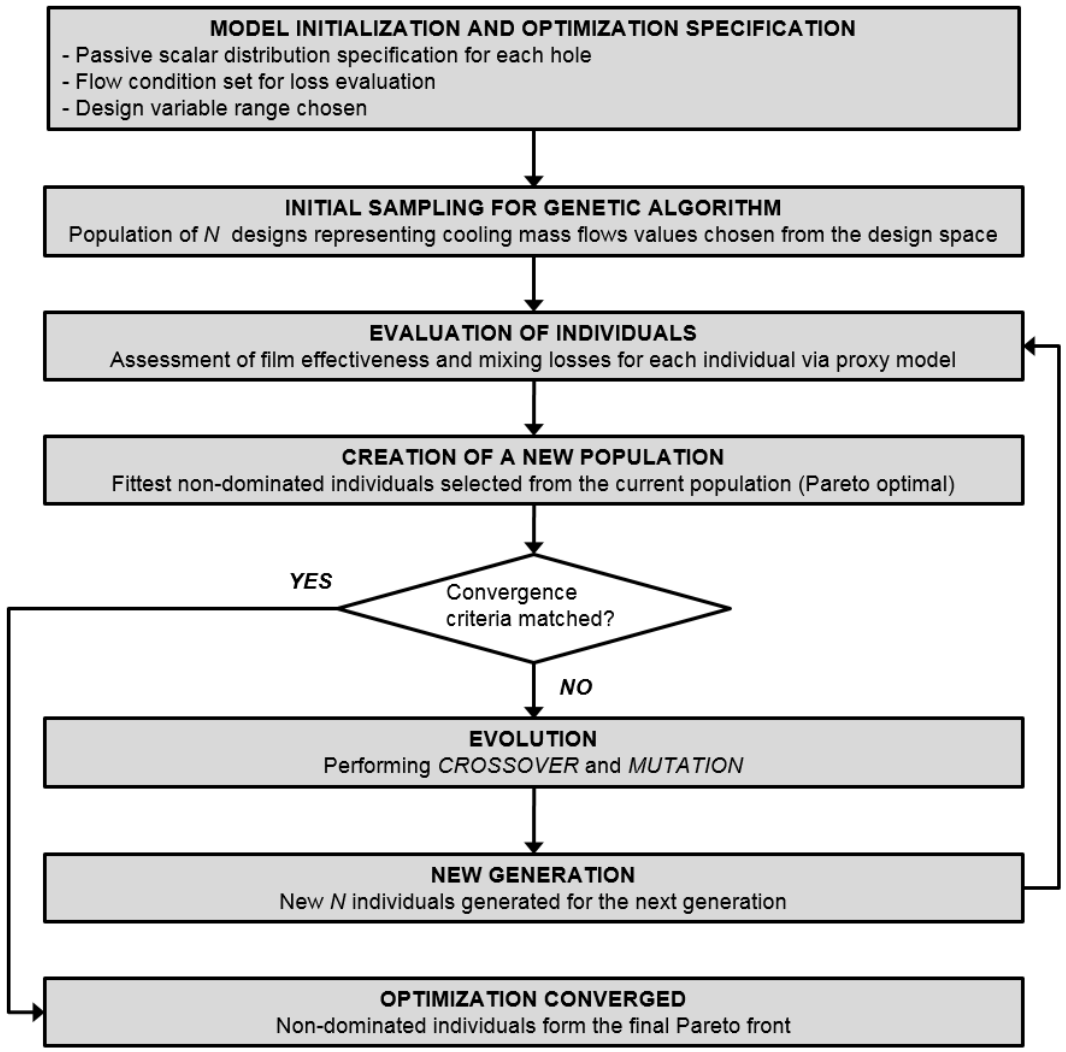


Figure 4.4: Block diagram of the MOGA algorithm.

Figure 4.4 shows the flow chart for the automated routine based on the MOGA algorithm. The proxy model is initialized with the values of the passive scalar relative to each cooling hole, at the selected post-processing line. The main flow conditions (e.g. external Mach number, coolant supply total pressure and temperature, mainstream total pressure and temperature, etc.) are also specified in the model for loss calculation. The optimizer starts by performing a random sampling to obtain the initial set of designs (i.e. the first population). Subsequently, the life objective (f_1) and loss function (f_2) are computed using a Matlab script. This process is repeated until

the maximum population size is reached. The selection process (including crossover and mutation) is performed and the population is updated to include only the fittest designs. The process is repeated until the convergence criteria of the MOGA are met. The decision-making optimization core is linked to Matlab for the evaluation of the objective functions via Unix shell scripting. The next section describes the DAKOTA optimization setup.

4.3.4 Dakota setup

The parameters for the MOGA optimization are specified via the Dakota input file (*dakota.in*). The input file contains the parameters concerning *environment*, *method*, *model*, *variables*, *interface*, and *responses*, needed to run the Dakota software. The main sections of the file are: method, variables, interface, and responses. In the first one, the parameters concerning the genetic algorithm setup are specified. These include: population size, crossover, mutation rate, convergence criteria, etc. For the specific optimization case, a number of 25000 function evaluations was set for the MOGA solver. The convergence of the algorithm was reached within 3 hours (with 10 simultaneous evaluations) for each MOGA run. The maximum population size was set to 500 designs. Crossover was performed with *shuffle random* technique with 2 parents and crossover rate of 0.8. Mutation occurred by means of the *replace uniform* technique with a mutation rate of 0.1. The second section, *variables*, included the necessary parameters concerning the design variables. The design variables were *continuous* and represented by the values of the mass flow rate of each cooling hole. In particular, they were specified as the ratio between the value at the current evaluation and its initial value. Lower and upper bounds of design variables were set to 0.8 and 1.2 respectively, allowing a change in coolant mass flow rate of only 20% for each MOGA run. The third section, *interface*, defined the files to be compiled and run during the MOGA process. The fourth section, *responses*, defined the number of ob-

jective functions and the direction of the optimization (minimization or maximization problem).

4.4 Discussion on the limitations of the method

Limitations of the method arise from the fundamental assumption of the superposition model. That is, the relationship between coolant mass flow rate and adiabatic film effectiveness is linear. In fact, the main error contribution comes from the inaccuracy of the linear entrainment model in predicting the scalar concentration (and therefore the film effectiveness distribution) when compared with CFD. This error is related to the inability of the model to account for *global* and *local* changes in the flow field due to the change in hole mass flow rate. In particular, the following sources of error are identified:

1. *Global* flow regime shifts. These are related to the effect of the bulk momentum flux ratio on the vane secondary flows. In a turbine endwall with active film cooling, the amount of bulk momentum introduced with the coolant flow can dramatically change the development of the secondary flows within the passage (flow regime shift). This regime shift occurs at specific values of the momentum flux ratio, for which the secondary flows are switched-off. Simple entrainment models do not account for this complex flow behaviour;

2. *Local* flow regime shifts. The jet momentum flux ratio affects the local state of the cooling jets (attached or separated) and therefore the local three-dimensional flow structures. This effect is not predicted by the simple entrainment model;

3. Hole-to-hole interaction. There is a local change in the flowfield due to the interaction between film jets. The change in hole diameter—and mass flow rate—affects the local development of the three-dimensional flow structures (i.e.

extent of the horseshoe vortex, counter-rotating vortex pair, separation and reattachment, etc.) and therefore the coolant trajectory;

4. Stratification problem. The mass flow rate entrained from the upper gas layer into the mixing layer is assumed to be constant along the lateral direction. In reality, the local entrained mass flow rate will be a result of the contributions of both mainstream gas and neighbouring holes.

The potential sources of error listed above are inherent to the complex three-dimensional nature of the flowfield. The main objective of the present strategy is, however, to develop simple tools for rapid design optimizations, permitting a considerable reduction in the number CFD simulations needed. The model can be used if the present strategy is applied to cases in which errors due to global and local regime shift effects, hole-to-hole interaction and lateral stratification are small. These cases are represented by cooling applications where both streamwise and lateral hole spacing is large (such as combustor liners and afterburners), with small variation of momentum flux ratio.

The next section describes the results obtained for a test case, representative of a potential application of the proposed optimization method.

4.5 Test case design

The Sellers model (Sellers 1963) was employed to predict the adiabatic film effectiveness resulting from a multi-row film cooling configuration. The objective was to assess the minimum distance between two rows of holes that would allow for substantial mixing of the films (i.e. $\eta < 0.3$) and therefore reduce hole-to-hole interaction effects. Firstly, a CFD simulation was run for a single hole with a value of the momentum flux ratio representative of the optimization case. The maximum domain length was equal to $50d$ to allow for complete mixing of the films. Secondly, the Sell-

ers model was used to predict the film effectiveness distribution whilst varying the hole spacing along the streamwise direction. The Sellers model was selected for this preliminary study because of its simplicity and good accuracy in case of small number of film cooling rows (Kirollos and Povey 2015). More accurate models based on the conservation of energy, such as the model developed by Kirollos and Povey (2015), are recommended for a more accurate prediction of the resulting film effectiveness due to multi-row superposition.

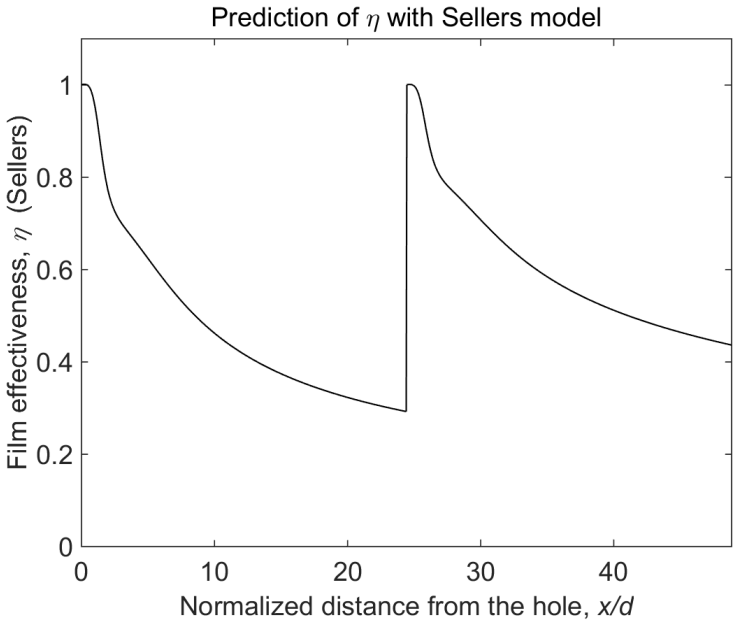


Figure 4.5: Prediction of streamwise film effectiveness distribution for two holes spaced by $x/d = 25$ using Sellers model.

Figure 4.5 shows the film effectiveness distribution obtained with the Sellers model for two holes spaced by $x/d = 25$ along the streamline direction. This distance is sufficient to allow for complete mixing of the film ($\eta < 0.3$) between two rows of holes. To this end, the fully-mixed jet will be insensitive to changes in mass flow rate taking place $25d$ upstream and therefore hole-to-hole interaction effects to be reduced.

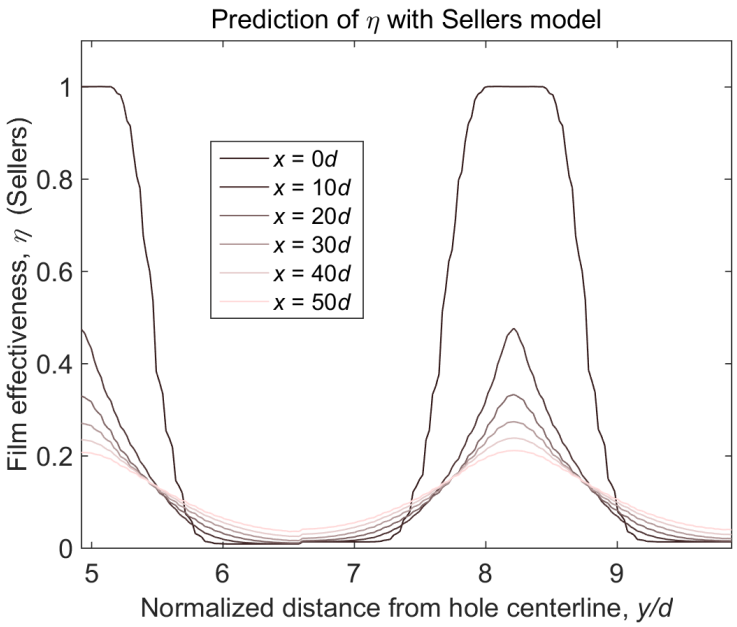


Figure 4.6: Prediction of lateral film effectiveness distribution for two holes spaced by $y/d = 3$ using Sellers model.

The minimum distance along the lateral direction was obtained by using the Sellers model to predict the lateral film effectiveness distribution of multi-hole configurations. Figure 4.6 shows the lateral film effectiveness distribution for two holes spaced by $y/d = 3$ for several axial locations ($x/d = 0$, 10, 20, 30, 40, and 50). A hole spacing of $y/d = 3$ allows for substantial mixing of the films over the entire domain length (the value of the adiabatic film effectiveness is $\eta < 0.1$).

The final setup was therefore chosen to have 6 rows of 10 cooling holes per row, with streamwise and lateral hole spacing of $25d$ and $5d$, respectively. Figure 4.7 depicts the computational domain and initial adiabatic film effectiveness distribution for the optimization test case.

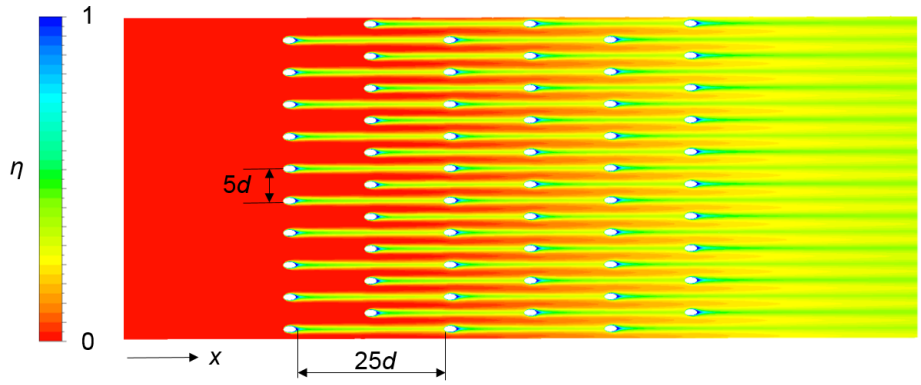


Figure 4.7: Computational domain and initial film effectiveness distribution for the optimization test case.

An aerodynamic routine based on isentropic relations was written in MATLAB to perform a preliminary assessment of the flow variables. A gradual flow acceleration was imposed by an area reduction along the axial length of the domain. Mixing losses were therefore dependent on local external Mach number. The exit Mach number was set to be approximately 0.5. Figure 4.8a shows the streamwise distributions pressure ratio ($p/p_{0\infty}$), Mach number (M), temperature ratio ($T/T_{0\infty}$), and flow area-to-inlet area ratio (A/A_{max}).

Figure 4.8b depicts the momentum flux ratio distribution along the axial direction. Results of the isentropic calculations show that the momentum flux ratio varies within the range $1.05 < I < 1.30$. As described in the later section, the momentum flux ratio of each cooling hole was kept constant throughout the optimization study. In fact, the mass flow rate of each cooling hole was varied by changing the hole diameter and keeping the total pressure the hole inlet constant.

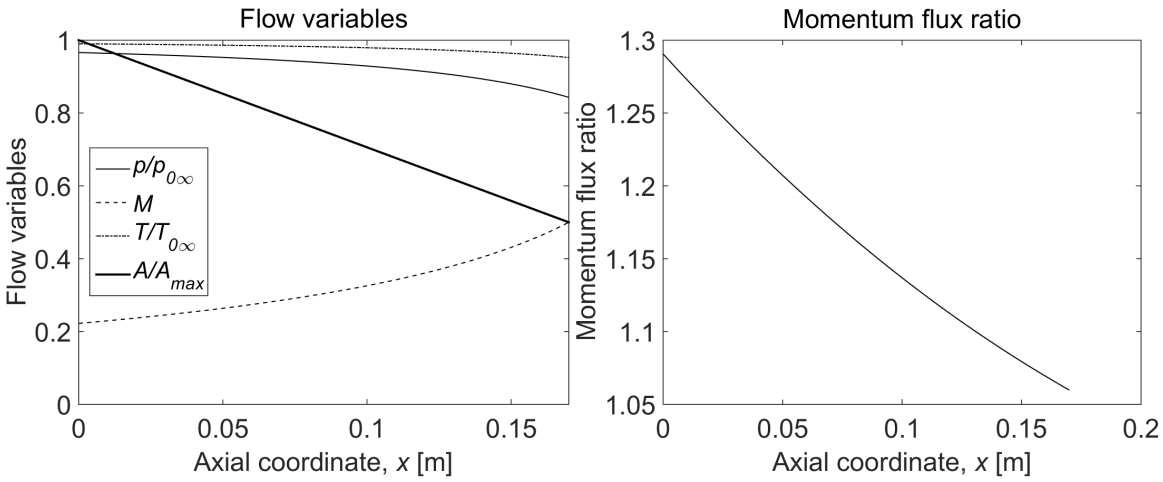


Figure 4.8: (a) axial distribution of flow variables and (b) momentum flux ratio for the optimization test case.

4.6 CFD methods

4.6.1 Solver settings

CFD simulations were performed with a steady-state solver using ANSYS-CFX. Mainstream gas and coolant were simulated as ideal gases with gas properties dependent on temperature. The $k-\omega$ SST turbulence model was selected for the turbulence closure with second order space discretization. The coolant concentration of each cooling hole was tracked by solving an additional passive-scalar transport equation. A total number of scalar transport equations equal to the number of holes was defined by using the pre-processing software CFX-Pre. The value of each passive scalar (ϕ_i) was set equal to 1.0 at the inlet of the corresponding cooling hole i, and to 0.0 at all other cooling hole inlets, as reported in Equation 4.5. The value of each passive scalar was set equal to 0.0 at the domain inlet and outlet. At the domain inlet, total pressure and temperature conditions were specified, as well as the value of the turbulent intensity. Static pressure value was imposed at the domain outlet, and symmetry boundary conditions were set on both sides of the computational domain.

4.6.2 Computational mesh

The computational grid was generated by using BOXERMesh and had 16.9×10^6 tetrahedral and hexahedral elements. A detailed view of the cooling hole and surface mesh is reported in Figure 4.9. The grid resolution on the cooled wall and the film holes was increased to capture high temperature gradients. The near-wall region was refined with 12 prism layers with an expansion ratio of 1.2. The value of the normalized wall distance was within the range $0 < z^+ < 5$ over all wetted surfaces.

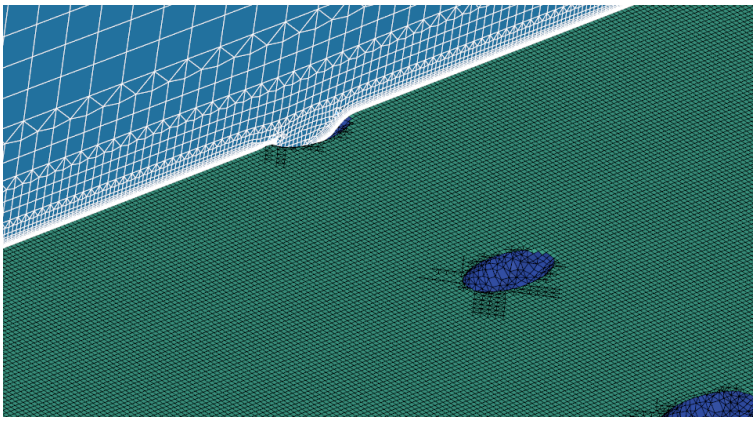


Figure 4.9: Detail of the computational mesh used for the scalar-tracking study.

4.6.3 CFD set up for scalar tracking calculations

In the CFX solver, the kinematic diffusivity is used to solve the additional transport equations for each passive scalar. The kinematic diffusivity is defined as the ratio between the turbulent thermal diffusivity (Γ) and the density-heat capacity product ρC_p. The additional scalar transport equations are defined by using a script written in CEL—a Perl-based CFX programming language.

4.7 Results and discussion

This section presents the results of the optimization of the cooling system depicted in Figure 4.7 and using the methodology described above. The system includes six

rows of film cooling holes, each including ten holes. An external pressure gradient is imposed along the axial domain length. Inlet/outlet boundary conditions as well as hole feed total pressure are kept constant throughout the optimization. The location of the cooling holes is also kept the same during the optimization.

The objective of the optimization is to minimize the difference in film effectiveness from a target distribution at the domain exit line *whilst* minimizing film cooling mixing loss. The target distribution at the domain exit (Figure 4.7) is depicted in Figure 4.12. In particular, the target η is arbitrarily chosen to take a value $\eta = 0.4$ for $y^* \leq 0.5$, and $\eta = 0.2$ for $y^* > 0.5$, where y^* is the non-dimensional lateral coordinate. The optimization is initiated with a uniform hole diameter distribution in which $d =$ 2 mm.

Figure 4.10 shows an example of the convergence of the Pareto front for a MOGA run. It is worth recalling that both objective functions in the figure—i.e. life objective, f_1, and mixing loss, f_2—are evaluated by using a Matlab script and passed onto the Dakota optimization core for the selection process of the genetic algorithm. Only at the end of this process—and therefore only after the convergence of the Pareto front—the geometry is re-evaluated in CFD and the results from the optimizer compared against CFD predictions.

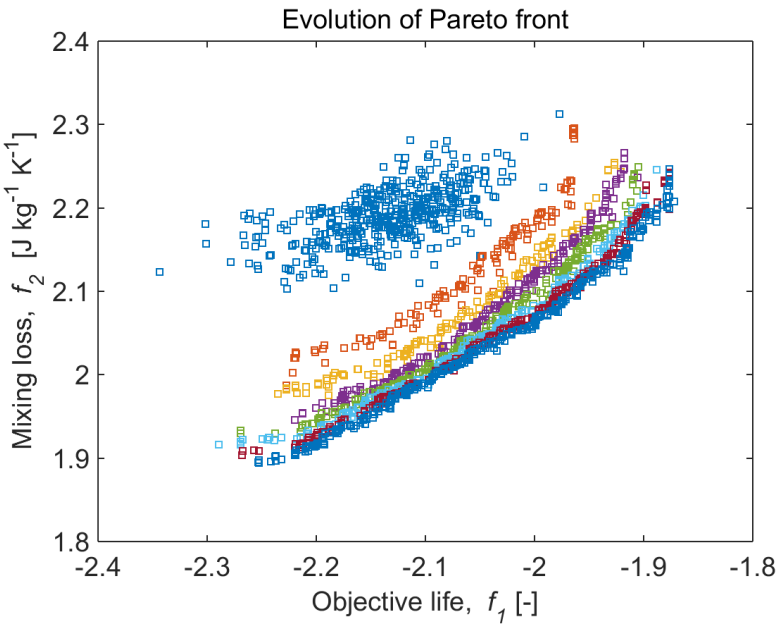


Figure 4.10: Example of convergence of Pareto front during a MOGA run.

A Pareto front is generated at the end of each global run, and contains the set of all non-dominated designs. Figure 4.10 depicts an example of the Pareto front evolution during a MOGA run within a global iteration. During the MOGA run, objective functions—i.e. component life (f_1) and loss (f_2)—are continuously improved until the MOGA process is converged and a new set of non-dominated designs is generated. In Figure 4.10, a population every 20 is plotted with a different color. For the particular case plotted, convergence of the Pareto set is reached after 120 populations. Each design on the Pareto front is different and characterized by an optimal combination of the objective functions f_1 and f_2. Depending on the location of each individual solution on the Pareto set, the design will perform with improved objective life or mixing loss with respect to other designs of the front.

The choice of the design from a converged Pareto front is arbitrary and affects the following global iterations. This aspect is inherent in the fact that there is no unique optimal solution for each global run—instead there is a *set* of optimal solutions. There is therefore a certain degree of arbitrariness in the selection of the optimal

design which can have an influence the following global iterations. This aspect could be improved by consistently selecting the design for the next global iteration from approximately the centre of the Pareto front. In this way, designs with similar weights for f_1 and f_2 were selected for all global runs, reducing the variability in the final optimized solution. The sensitivity of the optimization results to the design selection process is, however, unknown.

To predict the coolant mass flow rate of each hole, the present method employs the compressible relation of Equation 4.12. In this equation, the discharge coefficient (C_d) is estimated based on the CFD solution from the previous global iteration and kept constant within the MOGA run. At the end of the MOGA run, the optimized mass flow rate of each cooling hole is compared to a new CFD run with updated hole diameters. Figure 4.11 shows an example of the comparison of mass flow rate prediction (all film holes) between the method employing the model of Equation 4.12 and CFD. Hole mass flow rate values obtained from optimizer estimation and CFD prediction are very similar for each cooling hole, indicating that the method involving Equation 4.12 is accurate.

Figure 4.12 depicts the film effectiveness profile at the exit of the domain (line 1) for (i) target function, (ii) initial cooling configuration, (iii) optimizer output (after 5 global runs), and (iv) CFD prediction of optimized configuration. It is worth recalling that the target function was chosen as an arbitrary complex distribution to demonstrate the capability of the method. The target distribution is described by the following function:

$$\begin{cases} \eta = 0.4 \quad \text{for} \quad 0.0 \leq y^* < 0.5 \\ \eta = 0.2 \quad \text{for} \quad 0.5 \leq y^* \leq 1.0. \end{cases} \tag{4.21}$$

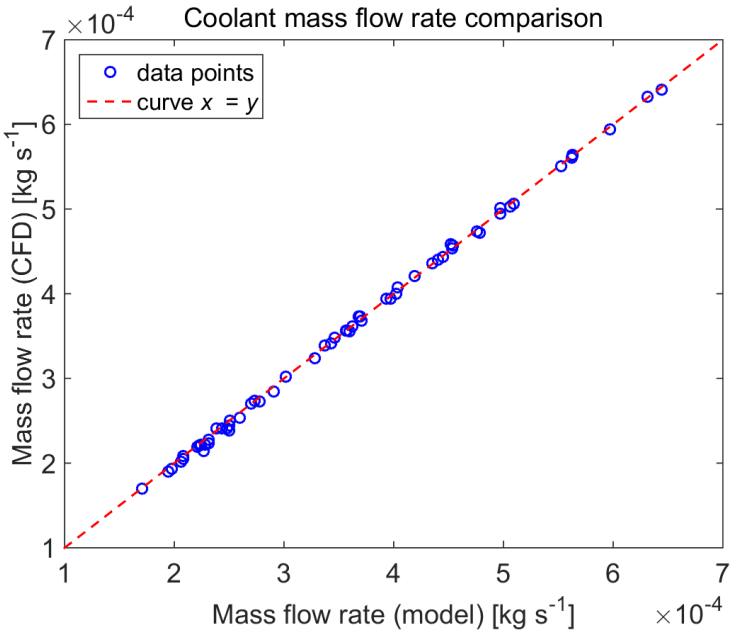


Figure 4.11: Comparison of hole mass flow rates between method involving Equation 4.12 and CFD prediction.

The above function can be thought as a test exercise for the optimization process to optimize from an initial configuration in which some regions are *over-cooled* ($\eta > \eta_{target}$) and others are *under-cooled* ($\eta < \eta_{target}$).

The initial configuration operates with values of film effectiveness in the range $0.25 < \eta < 0.50$. Film effectiveness is higher than the target distribution in the region $y^* < 0.5$ and lower in the region $y^* \geq 0.5$. In addition, the highest value of film effectiveness ($\eta = 0.5$) is reached at $y^* = 1.0$ and lowest value ($\eta = 0.25$) is attained at $y^* = 0.0$. After 5 global runs, the difference from the target distribution was reduced. Figure 4.12 shows the comparison of optimizer estimation and CFD prediction of film effectiveness for the last global run. In the figure, the film effectiveness is defined using Equation 4.11. Results of film effectiveness trends obtained from the optimizer (which employs the proxy model of Equation 4.6) are in very good agreement with the CFD prediction.

In the region $y^* \geq 0.5$, we observe three main improvements: firstly, the difference in film effectiveness from the target distribution is substantially reduced, which leads

to the elimination of—as defined in this particular case—the over-cooled region. Secondly, the maximum peak in film effectiveness is dramatically reduced from $\eta = 0.5$ to $\eta = 0.25$. Thirdly, the difference between high peaks and low peaks is reduced, yielding a slightly more uniform distribution along the region $y^* \geq 0.5$.

In the region $y^* < 0.5$, there is still a very good agreement between optimizer (proxy model) output and CFD predictions. Further insights can be gained by comparing the results of the initial configuration to the final optimized distribution. Firstly, the minimum film effectiveness attained for the initial distribution ($y^* = 0.0$) is increased from $\eta = 0.24$ to $\eta = 0.30$, therefore leading to improved component life—see Equation 4.16). Secondly, it may be observed that the film effectiveness distribution could not be improved from the initial distribution in this region (i.e. the difference from the target function could not be reduced). This is mainly due to the fact that, at the domain exit line (i.e. line 1—$25d$ downstream of the last row of holes) the films are fully mixed and a further increase in mass flow rate has a very small effect in improving the film effectiveness on the wall. This can be attributed to increased turbulence within the mixing layer and therefore increased entrained mainstream mass flow rate.

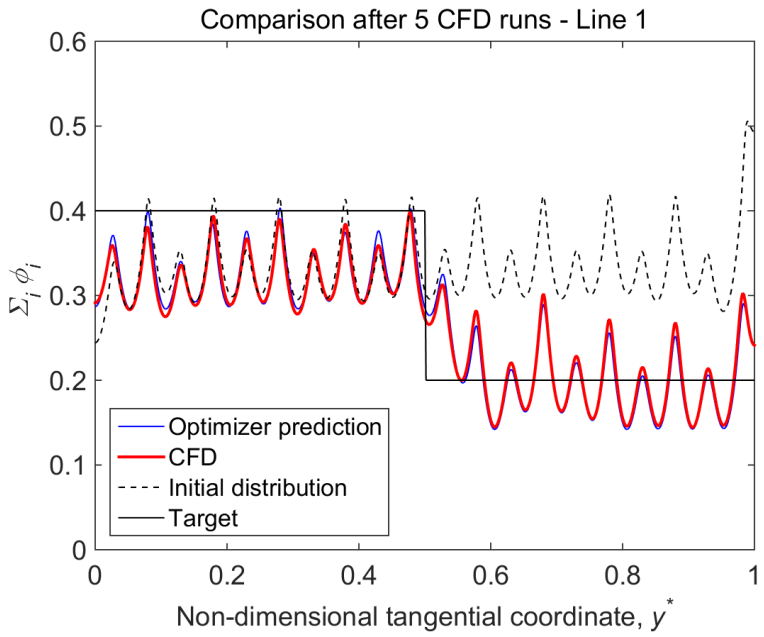


Figure 4.12: Optimization results of film effectiveness distribution at domain exit (line 1).

Despite the final film effectiveness distribution was not improved in terms of the difference from the target in the region $y^* < 0.5$, the redistribution of hole diameters for the optimized configuration was modified by the optimizer in such a way that mixing loss was minimized and coolant coming from rows 1 to 4 was prioritized. In fact, the impact on film mixing loss due to the first rows is minimal compared to last rows—as a result of lower external Mach number. This is an interesting result which can be observed in Figure 4.13 and indicates the complexity of an optimization scenario in which film effectiveness and loss are strongly coupled. In Figure 4.13, we observe that—from the initial uniform distribution with $d = 2$ mm—the optimized configuration is characterized by larger diameters for the first five holes from the bottom edge of the domain (for each row), and by smaller diameters for the top five holes along the lateral direction y (for each row). This configuration is similar for all rows as expected in order to minimize the difference from the target distribution. Figure 4.13 also shows (in black dashes) a central moving average of hole diameter, with a window size of ten holes. The latter indicates that the averaged hole diameter

is decreased towards the domain exit, suggesting that higher weight was given by the optimizer to the mass flow rate issued from rows 1 to 4.

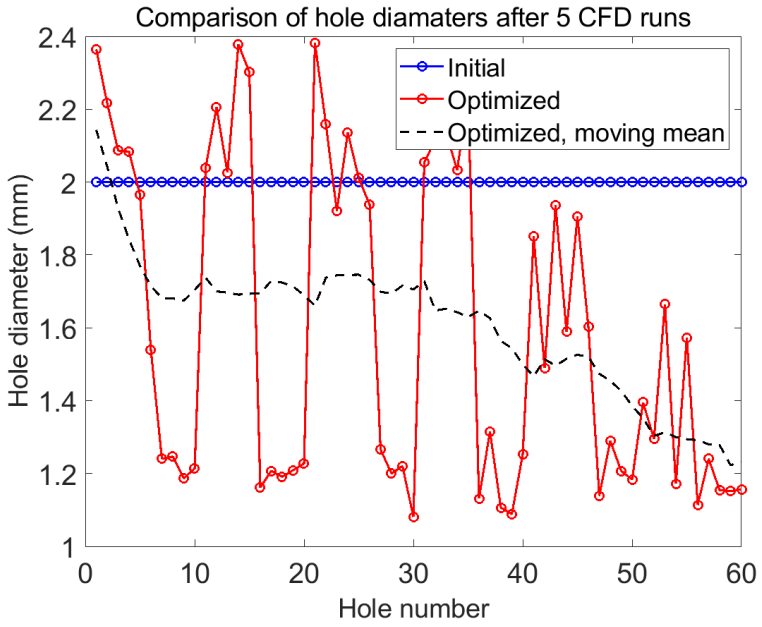


Figure 4.13: Change in hole diameters at the end of optimization process (after 5 global runs).

The film effectiveness distribution on the cooled wall is showed in Figure 4.14. The final distribution is represented by high film effectiveness (average value $\eta = 0.35$) in the region $0.0 < y^* \geq 0.5$ and low film effectiveness (average value $\eta = 0.20$) in the region $0.5 < y^* < 1.0$. In both diameter distribution (Figure 4.13) and film effectiveness contours (Figure 4.14) it may be observed that the optimization algorithm improved the final design by increasing the mass flow rate of the first four row of holes. In fact, minimal mixing loss are introduced by the first rows, whereas a large impact is due to the last rows—for which the coolant is issued at higher external Mach number.

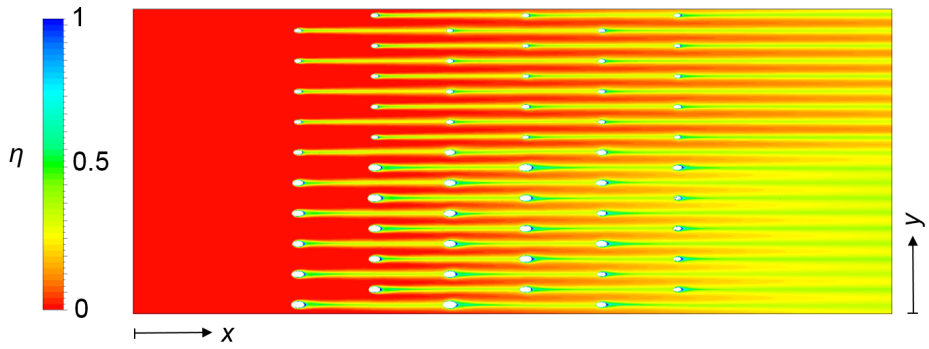


Figure 4.14: Optimized film effectiveness distribution predicted with CFD.

Overall optimization results for each global iteration are depicted in Figure 4.15. The figure shows the overall results for the optimization methodology applied to the system of 4.7. The entire optimization process was stopped after five global iterations because the improvement in both objective functions between two subsequent global runs was less than 3%. Results in Figure 4.15 are obtained from the CFD solution after each global run. At the end of the optimization, the component life objective function (f_1) was improved by 10% and mixing loss objective function (f_2) reduced by 23%.

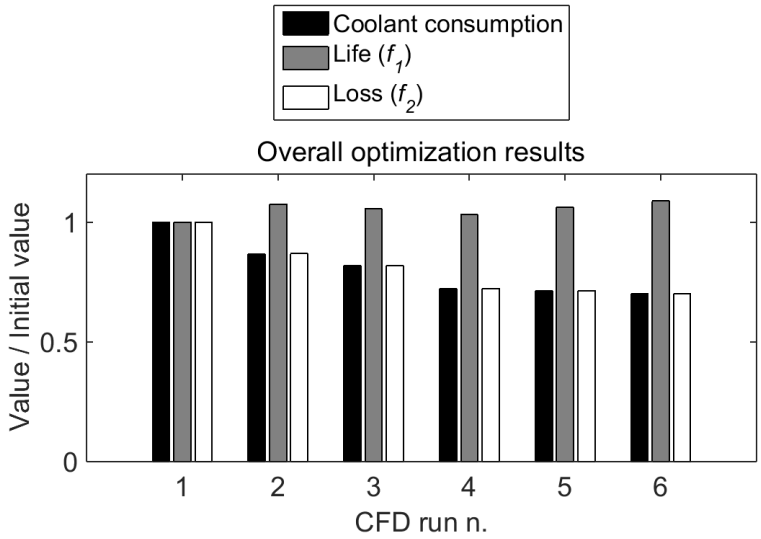


Figure 4.15: Overall optimization results for each global run.

4.8 Conclusions

In this chapter, an optimization methodology based on the scalar tracking method and multi-objective genetic algorithm has been presented and discussed. The method aims to substantially reduce the number of CFD runs when optimizing film cooling systems. CFD simulations are replaced by a proxy model based on superposition technique and used only for recalibration of the proxy model. The latter requires the knowledge of coolant concentration for each film cooling hole. To this end, a passive scalar is attributed to each cooling hole and its concentration predicted by solving an additional scalar transport equation. Standard optimization techniques—such as GAs—can be therefore employed to optimize the system by using the proxy—and computationally inexpensive—model. A CFD solution is then run to recalibrate the model.

A detailed discussion on the main limitations of the models is also presented in this chapter. In particular, it is argued that the model is suitable for certain classes of film cooling problems, in which the interaction between holes and flow regime shifts are relatively small. That is, the local change in flowfield—e.g. flow structures, film stratification, etc.—due to the change in hole mass flow rate is small. The assumptions of the linear model do not hold for cases in which flow regime shifts take place—e.g. a drastic change in jet secondary flow structures—which the simple linear superposition model cannot account for. The method is unsuitable for cases in which stratification of the films is important. In fact, the model is based on the assumption that the mainstream mass flow rate which enters the mixing layer is constant along the lateral direction and is insensitive to the effect of neighbouring holes. In reality, for low hole spacing, the entrained mass flow rate *does* change due to interaction of neighbouring holes. This phenomenon is well captured by CFD but is neglected by the linear model.

In order to determine the applicability of the model, a test case has been designed

and an optimization performed for a flat plate with external pressure gradient and multiple rows of holes. The optimization was defined in order to minimize the difference in film effectiveness from a target distribution at a specific processing line *whilst* minimizing mixing losses introduced by film cooling. The first objective is representative of the life of the component, whereas the second objective is function of cooling mass flow rate and external static field. The main optimization loop converged after five global iterations and involved five CFD runs. Results on the processing line show reduced difference from target film effectiveness profile and more uniform distribution for lateral normalized coordinate $y^* > 0.50$. For the region $y^* \leq 0.50$, very little improvement is gained due to the local flowfield being highly mixed. However, overall results show a reduction in mixing loss objective function (f_2) of 23% and an increase in objective life (f_1) of 10%. Results of optimized diameters distribution show that leading rows (1-4) have larger diameters and trailing rows (5-6) reduced diameter. This result is in line with the argument that trailing rows have higher impact on film mixing loss.

The optimization method presented in this chapter has been critically analyzed and its validity discussed in relation to its potential applicability to film cooling systems. The aim of the present work has been mainly to understand the major limitations of the use of linear superposition for film cooling systems and represents an assessment of the main sources of error rising from their use. In summary, some concerns exist on the applicability of the method in case of complex flowfields and in cases where holes are clustered (e.g. NGV platforms). However, it is believed that the method could be taken into consideration for simpler cases, such as combustor liners or afterburners.

Chapter 5

Design and Manufacture of Reverse-Pass High-Pressure Vane Platforms

The need for effective cooling systems in response to more aggressive temperature traverses (characteristic of modern lean combustors) and complex three-dimensional endwall flows, has motivated the work on design (and testing) of advanced endwall cooling arrangements developed in this chapter. In NGVs, often the endwall cooling systems are characterized by simple arrangements in which both casing and hub vane platforms are mainly cooled by film holes fed from a common plenum. This chapter describes the design and manufacture of high-pressure vane platforms based on the the reverse-pass arrangement. The design strategy implies that the coolant flows in the opposite direction to the mainstream gas before being discharged through a number of film cooling holes in the platform. This approach is applied to an existing high-pressure nozzle guide vane hub endwall cooling system from a modern jet engine.

A bespoke conjugate thermal network is implemented to predict both aerodynamic loss and the temperature distribution of the cooling system. The design is performed with the aim of flattening the temperature distribution and reducing maximum metal temperature of the platform when compared to the engine configuration. Results of external wall temperature and aerodynamic loss are reported and discussed in details. The design is shown to reduce the external endwall temperature by approximately

100 K in the front portion and 200 K in the trailing region, when compared to the baseline case. The components are manufactured by metal laser-sintering using a titanium alloy. Details of the manufacturing process are also described in this chapter.

5.1 Introduction

The reverse-pass design approach was originally presented and developed by Kirollos and Povey (2014) and Kirollos (2016). The *reverse-pass* design is based on a counter-current arrangement between mainstream gas and internal coolant, i.e. the internal coolant flows in the opposite direction to the mainstream flow. A reverse-pass system differs from a counter-current system in that the cold fluid is also used for film cooling. In this chapter, a reverse-pass design is integrated into an existing engine platform cooling system of a modern jet-engine. A bespoke aero-thermal network is implemented for the prediction of pressure loss and temperature distributions for various designs. The aim of the design is to improve the baseline system by both reducing and flattening the external metal temperature of the endwall. The aim is therefore to improve the life of the component—usually limited by the effects of creep and oxidation at high temperatures—and to reduce thermal stresses induced by temperature gradients. The design also aims to limit the total pressure loss introduced by the reverse-pass system and hence ensure a minimum pressure margin. The latter is vital for avoiding hot gas ingestion by the film cooling system.

The design involves two main steps: a first estimation of the aerodynamic losses and a subsequent thermal assessment. In the first step, the total pressure losses are estimated using correlations found in the literature. The integration of a reverse-pass system into the engine platform determines an increase of total pressure loss due to the presence of internal heat transfer enhancement devices (e.g. ribs, pedestals, etc.) and changes in the coolant flow area. A minimum pressure margin must be

therefore ensured to allow for a robust operation of the cooling system, even in case of pressure fluctuations in the mainstream field. A minimum pressure margin of 2% was considered during the design.

Once the aerodynamic design has been performed, the system is thermally assessed. This phase is performed by means of a conjugate routine in which a system of differential equations with engine-realistic boundary conditions is solved. Results of the wall temperature distribution are used to assess the thermal performance of each design in terms of the maximum incurred metal temperature and temperature uniformity.

The following paragraphs describe the design strategy and tools developed to predict the aero-thermal performance of the reverse-pass cooling system. Manufacturing strategies for high-speed tests are also presented and discussed.

5.2 Computational domain

The design is applied to an existing HP-NGV platform from a modern engine. The geometry is approximated by projecting the boundary points of a single-passage platform from a solid CAD model onto a two-dimensional plane. During the modelling, the domain is divided into a number of artificial channels (i.e. no physical boundaries are considered in between channels) to allow for circumferential resolution. Each individual channel is solved as a one-dimensional problem, as described in the next sections. The results of each section are subsequently interpolated by using *Lowess* surface fitting to partially compensate for lateral conduction and circumferential coarseness.

Figure 5.1 depicts the computational domain. The latter is divided into six one-dimensional artificial sub-domains to improve the circumferential resolution (the boundaries of the sub-domains are marked with a black line). Each domain is dis-

cretized with 100 points along the axial coordinate, and is treated independently during both aerodynamic and thermal evaluations. The discretization points are used to calculate the local width of the channel, always perpendicular to the local flow direction.

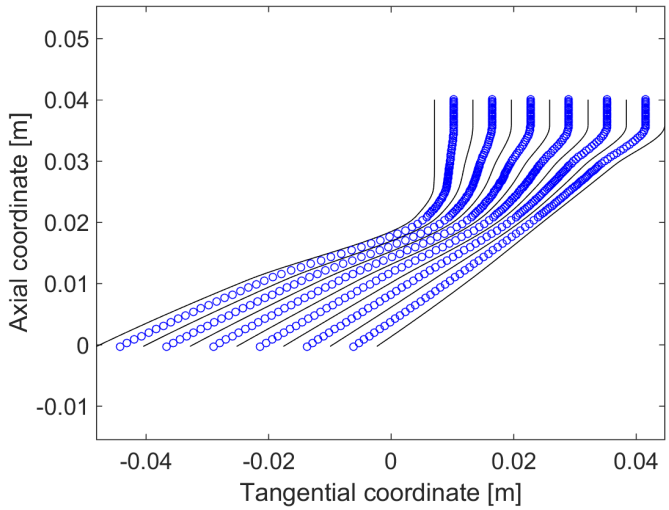


Figure 5.1: Computational domain of the reverse-pass platform.

5.3 Aerodynamic modelling

The internal pressure loss estimation for the reverse-pass system is predicted by means of zero-dimensional correlations for incompressible flows. The total pressure loss is estimated based on the internal flow parameters and geometry of the coolant channels. Values of coolant feed total pressure as well as total temperature are set to engine conditions. The mass flow rate through each channel is known since it is a design objective. Pressure loss within each section is estimated by using the local dynamic head and the characteristic loss of the element. The feed pressure of the cooling holes is therefore estimated by subtracting the pressure loss through the channel from the total pressure at the coolant plenum inlet.

5.3.1 Baseline platform cooling design

The baseline platform cooling configuration consists of two rows of ballistic film cooling holes located upstream of the vane leading edges (Figure 5.2a). The two rows of film cooling holes have uniform hole diameter. A numerical simulation was performed at engine conditions to obtain the external static pressure field. This allowed to quantify the pressure margin across the cooling holes and select the holes to be included in the reverse-pass channel.

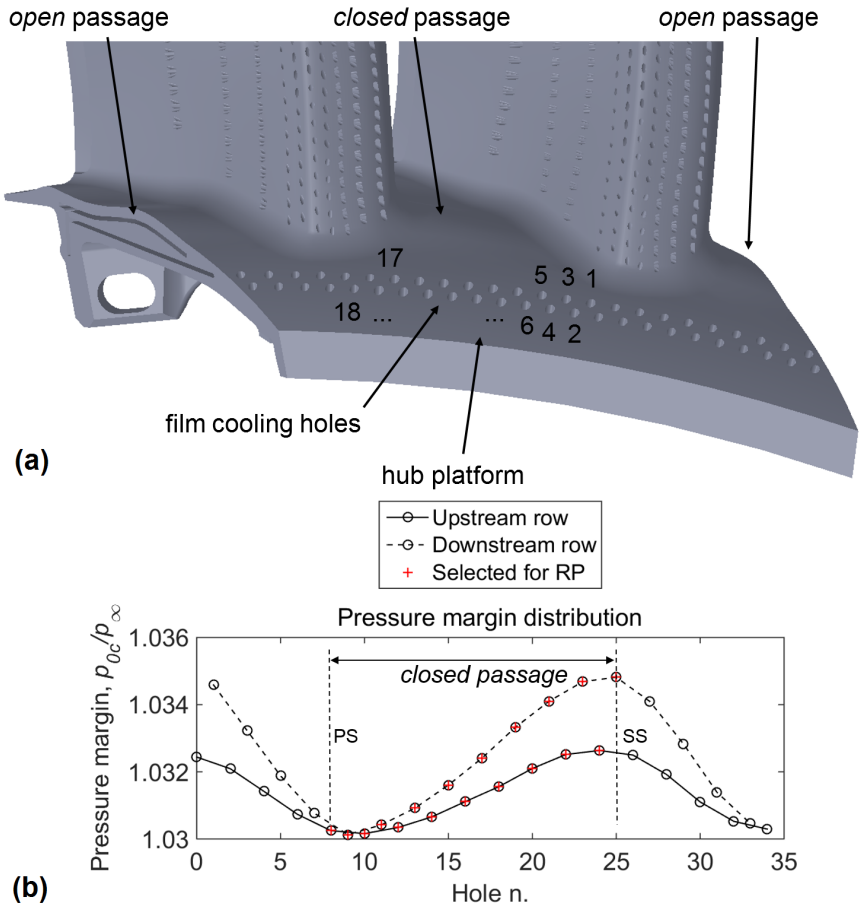


Figure 5.2: (a) CAD view and (b) pressure margin distribution of the baseline cooling design (predicted with CFD).

Figure 5.2b depicts the pressure margin distribution across the two rows of film cooling of the hub platform for the baseline design. The minimum local pressure margin without reverse-pass was 1.03. This value was sufficiently large to accept the

losses introduced by the reverse-pass design. Only the holes belonging to the mid-portion of the platform (called *closed passage*) were selected for reverse-pass (for a total number of 18 holes). This choice was made due to the complex geometry of the *open passages*—especially due to the complex arrangement with which the vane pairs are joined together and the presence of sealing strips. The holes included in the reverse-pass are marked in Figure 5.2a with numbers increasing from PS to SS and in Figure 5.2b with red markers.

In the baseline design, the coolant is fed from the hub plenum and primarily flows into the vane internal coolant system and through the hub platforms holes. The coolant flow is not guided within the platform and the system is not optimized for any purpose. The designs proposed in this chapter aim to enhance the internal coolant heat pick-up by guiding the coolant flow underneath the hub platform, and by performing this with a *reverse-pass* arrangement. In the latter, the internal convective cooling is maximized at the minimum film effectiveness—i.e. the hottest external film exchanges heat with the coolant at its minimum temperature. This system—characteristic of counter-current heat exchangers—maximizes the temperature difference between hot and cold streams, with relative improved overall perfromance. In order to maximize the internal HTC, and reduce local temperature peaks, heat transfer enhancement devices (e.g. pedestals) are also introduced within the passage.

5.3.2 Pedestal total pressure loss correlation

The total pressure loss introduced by the pedestal banks is calculated by using the correlations of Metzger et al. (1982) and Armstrong and Winstanley (1988) for the friction factor:

$$f = 1.76 Re_D^{-0.318}. \tag{5.1}$$

Equation 5.1 is valid for a Reynolds number in the range $10^4 < Re_D < 10^5$, pedestal height to diameter ratio in the range $0.5 < H/D < 6.0$, pedestal spacing (perpendicular to the flow direction) to diameter ratio $2.0 < S/D < 4.0$, and pedestal streamwise spacing to diameter ratio $1.5 < x/D < 5.0$. The total pressure loss (Δp_0) is calculated as follows:

$$\Delta p_0 = 2f\rho v_{max}^2 N, \tag{5.2}$$

where ρ is the density of the coolant, v_{max} is the maximum velocity within the pedestal bank, and N is the number of pedestal rows along the streamwise direction. As suggested by Kirollos (2016), the maximum velocity is calculated by considering the local mass flow rate through half of the channel area, in order to approximate the flow area reduction due to the pedestal bank:

$$v_{max} = \frac{2\dot{m}}{\rho A}. \tag{5.3}$$

The Reynolds number is calculated based on the maximum flow velocity and the diameter of the pedestals:

$$Re_D = \frac{\rho v_{max} D}{\mu}, \tag{5.4}$$

where μ is the dynamic viscosity of air at the coolant conditions.

5.3.3 Impingement total pressure loss estimation

According to Hippensteele (1974), the total pressure drop introduced by an impingement system can be approximately considered equal to the local dynamic head:

$$\Delta p_0 = 0.5\rho v^2, \tag{5.5}$$

where v is calculated by knowing the local mass flow rate and flow area.

5.3.4 Updated holes diameter estimation

An initial CFD simulation at engine conditions was run to predict the mass flow rate flowing through the film cooling holes included in the reverse-pass section. The mass flow rate through each channel was set as a design objective. The total pressure at the cooling hole inlet was estimated by subtracting the pressure loss through the channel from the total pressure at the coolant plenum inlet. The hole diameters were therefore increased in order to compensate for pressure losses introduced by the reverse-pass system. The discharge coefficient (C_d) of each reverse-pass section was calculated using the external static pressure distribution obtained with previous CFD simulations. The value of the discharge coefficient for each channel was assumed to be the same between the cases with and without reverse-pass. Finally, the updated hole areas were estimated using the hole total-to-static pressure ratio *with* reverse-pass, as reported below:

$$A_{new} = \frac{\dot{m}}{C_d \frac{p_{0,loc}}{\sqrt{T_0}} \left(\frac{p_{0,loc}}{p_d}\right)^{\frac{1-\gamma}{2\gamma}} \sqrt{\frac{2\gamma}{R(\gamma-1)} \left[\left(\frac{p_{0,loc}}{p_d}\right)^{\frac{\gamma-1}{\gamma}} - 1\right]}}, \tag{5.6}$$

where A is the total geometric flow area of the film cooling holes, $\dot{m}$ is the local mass flow rate of each reverse-pass section, $p_{0,loc}$ is the total pressure at the cooling hole inlet, p_d is the local hole exit static pressure, and T_0 is the total temperature at the coolant conditions. These quantities were averaged over the number of cooling holes included in each reverse-pass section. R is the specific gas constant for air and γ is the ratio of specific heats.

5.4 Thermal modelling

Subsequent to the aerodynamic design, the thermal performance of the reverse-pass system were assessed. The thermal evaluation was carried out by means of a bespoke

Parameter	Symbol	Units	Value
Coolant inlet temperature	$T_{0,c}$	K	923.9
Specific heat capacity of air	c_p	J kg^{-1} K^{-1}	1130
Thermal conductivity of air	k	W m^{-1} K^{-1}	0.065
Dynamic viscosity of air	μ	N m^{-2} s	4.0×10^{-5}
Prandtl number of air	Pr	-	0.7
Wall thickness	t_w	mm	2.0
Wall thermal conductivity	k_w	W m^{-1} K^{-1}	28

Table 5.1: Boundary conditions for the thermal model.

conjugate thermal network implemented in MATLAB.

The external boundary conditions included: local external Mach number (M), local external heat transfer coefficient (h_1), mainstream gas temperature ($T_{0,\infty}$), coolant total temperature ($T_{0,c}$), target coolant mass flow rate ($\dot{m}_c$), and local external adiabatic film effectiveness (η). These quantities were used to calculate the external wall temperature (T_{w1}), internal wall temperature (T_{w2}) and internal coolant temperature (T_c). Finally, the external wall temperature distribution was smoothed using *Lowess* interpolation in order to partially compensate for circumferential coarseness and lateral conduction.

5.4.1 Thermal boundary conditions

Overall boundary conditions were taken from engine data (Table 5.1). Local distributions of external heat transfer coefficient (h_1) and adiabatic film effectiveness (η) were extracted from numerical simulations at engine conditions. It was assumed that h_1 and η were not affected by the internal cooling geometry. In fact, h_1 depends on the mainstream conditions (e.g. external Mach number, Reynolds number, aerodynamic boundary layer), and the external film effectiveness is primarily a function of hole geometry, and coolant and mainstream flow conditions. Figure 5.3a shows the two-dimensional distribution of h_1. Data were extracted from conjugate simulations

at engine conditions. Figure 5.3b shows the h_1 axial distribution. The external heat transfer coefficient was found to be approximately independent of the circumferential location.

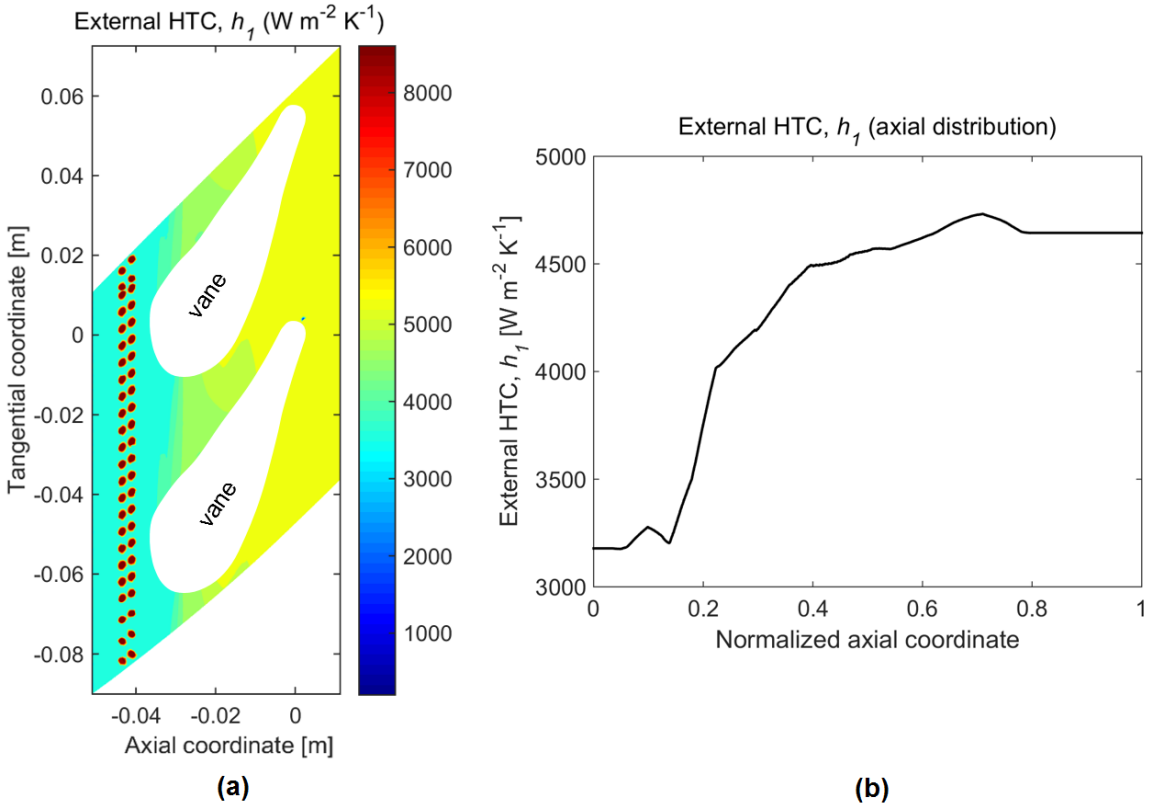


Figure 5.3: Contours of external heat transfer coefficient on hub platform (a), and distribution along the normalized axial location (b). Data were obtained from conjugate simulations at engine conditions.

The adiabatic film effectiveness is depicted in Figure 5.4. These results were obtained from conjugate simulations at engine conditions. Lateral distributions of η were averaged at six axial locations along the platform in order to obtain a one-dimensional profile as a function of the axial location (5.4b).

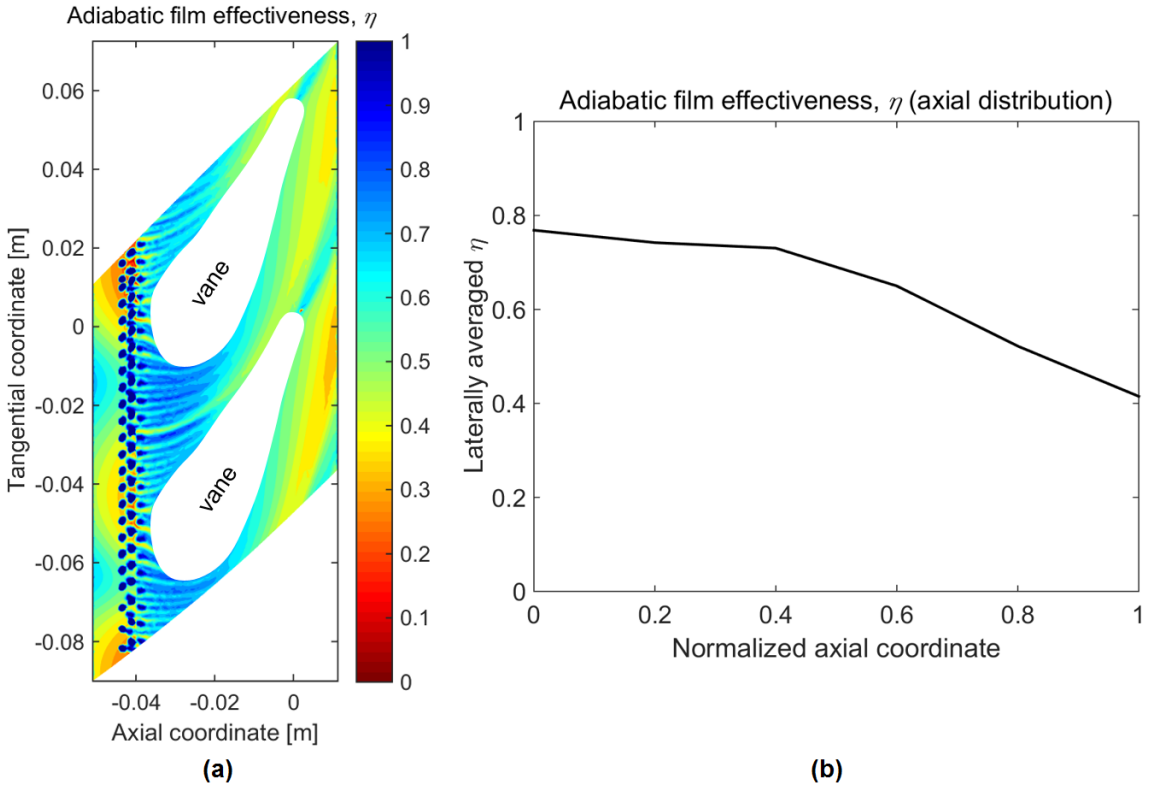


Figure 5.4: Contours of adiabatic film effectiveness on hub platform (a), and laterally averaged distribution along the normalized axial location (b). Data were obtained from conjugate simulations at engine conditions.

5.4.2 Pedestal bank internal HTC correlation

The internal heat transfer coefficient enhancement due to the pedestal bank was predicted using the results reported by Lyall (2006) for pin fins. In this work, values of Nusselt number enhancement with respect to the smooth wall were measured and presented for various Reynolds number and pin fin spacing (S/d). Correlations at flow conditions and geometry of the pin banks representative of the present design ($Re = 30000$ and $S/d = 4$) were adopted in this work and interpolated to obtain a realistic profile of the internal HTC. Figure 5.5 shows the spanwise-averaged Nusselt number enhancement of an array of pin fins with $S/d = 4$ and $Re = 30000$. These results were used in the present work to obtain a realistic profile of the internal HTC due to the pedestal row. Indication of the pedestal location and diameter is also given

in Figure 5.5.

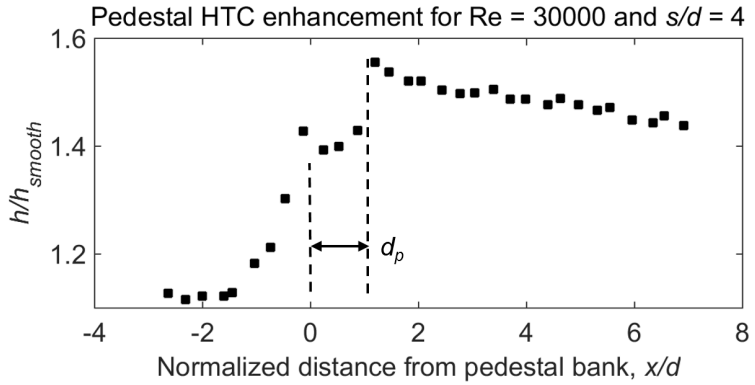


Figure 5.5: Spanwise-averaged heat transfer coefficient enhancement (with respect to smooth wall) for a pedestal bank with $Re = 30000$ and $S/d = 4$.

5.4.3 Smooth wall internal HTC correlation

The Nusselt number for channels without ribs is calculated by using the correlation suggested by Dittus and Boelter (1930) for turbulent, heated flow:

$$Nu_D = 0.023 Re_D^{0.8} Pr^{0.4}, \tag{5.7}$$

where Re_D and Pr are the Reynolds and the Prandtl numbers of the coolant. The Reynolds number is based on the hydraulic diameter of the channel (D). The area-averaged internal heat transfer coefficient is therefore calculated as follows:

$$\overline{h_2} = \frac{Nu_D k}{D}, \tag{5.8}$$

5.4.4 Prediction of wall and coolant temperatures

The 2D geometry of the platform was divided into a number of one-dimensional domains. Each domain was discretized with 100 points along the axial coordinate. The domain was also discretized along the circumferential direction to accept lateral circumferential variation of the mainstream inlet temperature (Figure 5.1). Each cooling

channel was resolved independently during the design and, within each channel, the coolant was assumed to be uniformly distributed along the circumferential direction. The streamwise distribution of the coolant temperature within each domain ($T_c(x)$) was calculated by solving the following ODE:

$$\frac{dT_c(x)}{dx} = \frac{w(x)U(x)}{\dot{m}_c c_p} \left(T_{aw}(x) - T_c(x)\right), \tag{5.9}$$

where x is the distance from the channel inlet and increases in the direction of the coolant flow (i.e. in the direction opposite to the mainstream flow), $\dot{m}_c$ is the coolant mass flow rate within each domain, c_p is the specific heat capacity of the coolant, $w(x)$ is the width of the channel, $U(x)$ is the overall heat transfer coefficient, and $T_{aw}(x)$ is the adiabatic wall temperature. The main assumption in Equation 5.9 is that the heat transfer is only transferred through one wall of the channel and all other walls are adiabatic.

The overall heat transfer coefficient is calculated as follows:

$$U(x) = \left(\frac{1}{h_1(x)} + \frac{1}{h_2(x)} + \frac{t_w}{k_w}\right)^{-1}, \tag{5.10}$$

where $h_1(x)$ is the external heat transfer coefficient (with axial distribution shown in Figure 5.3bc), $h_2(x)$ is the internal heat transfer coefficient calculated with correlations, t_w is the wall thickness, and k_w is the wall thermal conductivity.

The adiabatic wall temperature, $T_{aw}(x)$ in Equation 5.9, is computed as follows:

$$T_{aw}(x) = T_{0,\infty} - \eta(x)\left(T_{0,\infty} - T_{c,e}\right), \tag{5.11}$$

where $T_{0,\infty}$ is the total temperature of the mainstream, $\eta(x)$ is the local adiabatic film cooling effectiveness, and $T_{c,e}$ is the coolant temperature at the film ejection. $T_{c,e}$ also depends on $\eta(x)$ and hence Equations 5.9–5.11 are solved in MATLAB with

an iterative process. The solution of Equation 5.9 is initialized with a guess value of the coolant exit temperature $T_{c,e}$, and updated at each iteration. The process is run through a *while* loop which is stopped when $T_{c,e}$ converges inside 10^{-4}. Once the value of the coolant temperature is obtained, the external wall ($T_{w1}(x)$) and internal wall (T_{w2}) temperatures can be calculated with the following relations:

$$T_{w1}(x) = T_{aw}(x) - \frac{U(x)}{h_1(x)} \left(T_{aw}(x) - T_c(x)\right), \tag{5.12}$$

$$T_{w2}(x) = T_c(x) + \frac{U(x)}{h_2(x)} \left(T_{aw}(x) - T_c(x)\right). \tag{5.13}$$

Equation 5.12 and 5.13 are derived by considering the local conduction through the wall to the external convection. The one-dimensional distribution is assumed to be constant across the span of each domain. The overall temperature distribution is obtained by merging the temperature distributions of each domain and interpolating by using *Lowess* interpolation.

5.5 Aerothermal design results

The current design aims to reduce the endwall temperature peaks and flatten the temperature distribution with respect to the baseline case. These design objectives must be achieved with a system that ensures a minimum required pressure margin. For the present geometry, the geometrical constraints primarily comprised the vane internal cooling feed system, the vane platform rear mounting rail, and the hub platform film cooling holes location. These elements of the original geometry were not modified during the design to allow for a simple integration in to the existing engine hardware. The mounting components—such as the vane rear rail—were modelled in the thermal network, in order to take into account their effect on the metal temperature distribution.

A sketch of the coolant mass flow balance of the platform cooling system with reverse-pass is given in Figure 5.6. It is assumed that approximately 5.7% of the overall vane-passage mass flow rate is used for vane cooling (combined internal and film cooling), around 2.3% is used for the reverse-pass channel, and approximately 1.0% is fed into the the rotor slot for rotor platform cooling.

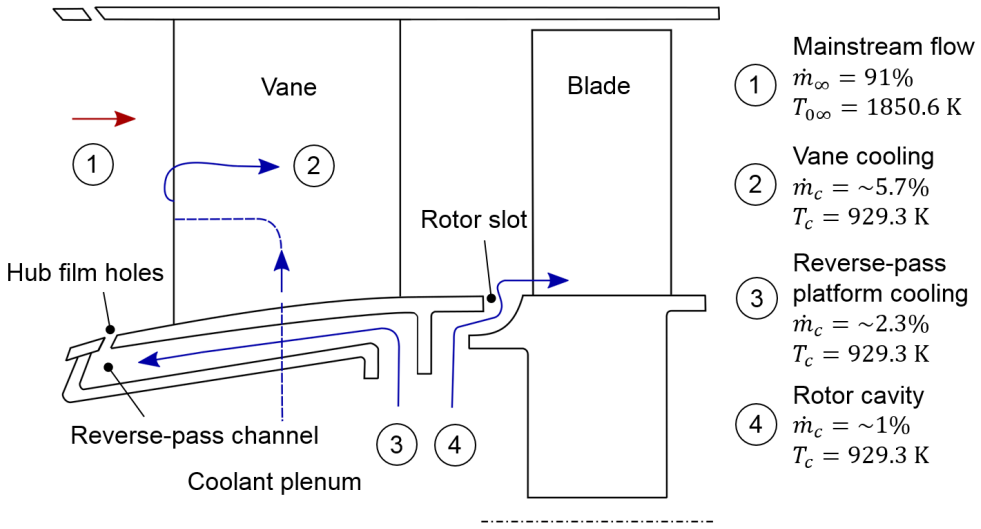


Figure 5.6: Sketch of the coolant mass flow balance with the reverse-pass system.

Figure 5.7 depicts the schematic of the selected designs, called ARP1-1 and ARP1-2. It also shows a sketch of the qualitative distributions of external heat transfer coefficient, adiabatic film effectiveness and internal heat transfer coefficient for the two designs. The design ARP1-1 (Figure 5.7a) includes a reverse-pass channel with height equal to 2.5 mm and inlet located close to the vane rear rail. A single row of pedestals (with spacing $S/D = 4$) is located downstream of the channel inlet. The coolant flows through the smooth internal channel and is ejected through the hub film holes (RIDN holes). The internal HTC is enhanced by the presence of the pedestals (peak in the black line). The local internal HTC enhancement results in a reduction in the temperature peak in the region of the vane rear rail. The flow within the rotor cavity is also modelled. The internal HTC in this region is lower due to small coolant mass flow rate flowing through the rotor slot (approximately 1%), and absence of

internal decorations. This region is also characterized by high external HTC and low adiabatic film effectiveness (red line in Figure 5.7).

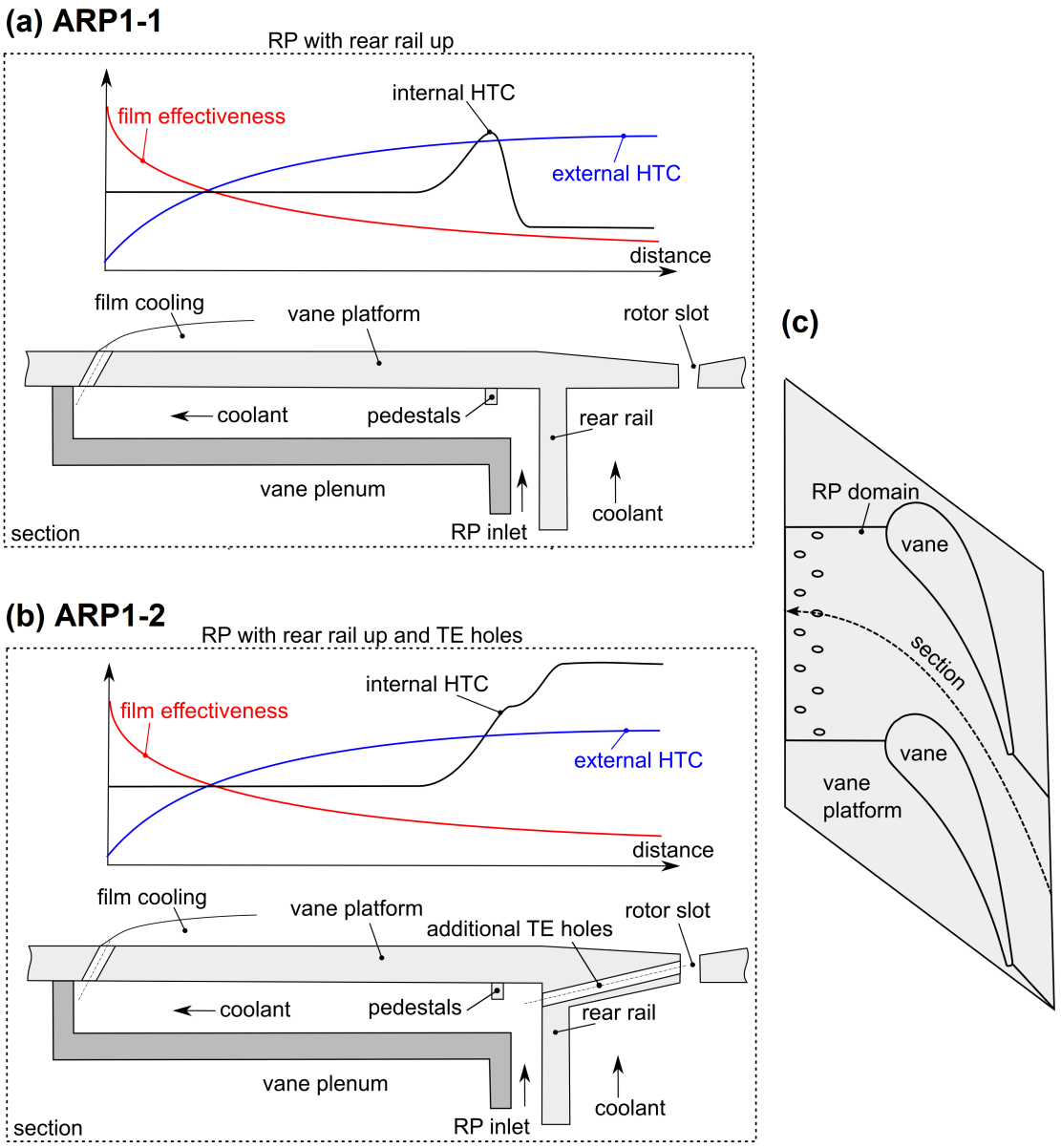


Figure 5.7: Section sketch of design ARP1-1 (a), design ARP1-2 (b), and top view of vane platform (c).

In order to improve the platform design and reduce the temperature peak in the trailing region of the platform, the design ARP1-1 is modified to include a number of internal holes (rim holes) located within the platform wall, downstream of the vane

rear rail (design ARP1-2, Figure 5.7b). These holes have the objective of enhancing the internal HTC (i.e. increasing the internal coolant heat pick-up) and therefore reducing the temperature peak in the trailing region. This effect is sketched in Figure 5.7b with an increase in internal HTC downstream of the rear rail. The coolant is then ejected directly through the rotor slot. The rim holes are oriented to approximately match the vane exit metal angle, in order to minimize mixing losses. This design includes approximately an additional 1% of the overall mass flow rate used to feed the rim holes.

The internal Nusselt number of the region due to the rim holes was predicted by using the correlation proposed by Dittus and Boelter (1930) for turbulent, heated flow:

$$Nu_D = 0.023 Re_D^{0.8} Pr^{0.4}, \tag{5.14}$$

where Pr is the Prandtl number of the coolant and Re_D the Reynolds number based on the diameter of the internal channel. The Reynolds number was calculated by estimating the local flow velocity based on the design Mach number at the rotor inlet.

Figure 5.8 shows the results of the conjugate thermal network, in terms of external wall temperature (T_{w1}) and pitchwise (from PS to SS) pressure margin ($p_{0,c}/p_\infty$) distribution for designs ARP1-1 and ARP1-2. Figure 5.8a depicts the external wall temperature distribution for the design ARP1-1. In the figure, the location of the rear rail is also indicated with a dashed black line. The coolant is fed from the internal reverse-pass inlet, located just upstream of the rear rail. The coolant impinges on the pedestal section, and flows in the opposite direction to the mainstream gas. The approximate axial location of the pedestal bank is marked in Figure 5.8 with black circles. Both rear rail and pedestal bank sketches in Figure 5.8a and c are reported for representation purposes only and are not scaled. The front part of the platform is at a relatively low temperature (approximately 1050 K). The aft portion of the

vane platform is characterized by high values of the external HTC and low values of adiabatic film effectiveness. The design coolant mass flow rate flowing through the rotor slot is approximately 1%. These combined effects result in a rapid increase in temperature across the platform trailing region (up to approximately $T_{w1} = 1300$ K).

Figure 5.8b shows the distribution of the pressure margin across the platform for each artificial reverse-pass channel. The pressure margin is reduced with reverse-pass due to increased loss across the system. However, the pressure margin is shown to be higher than 2% for all the artificial channels, as required by the design constraints.

5.8c depicts the external wall temperature distribution for the design ARP1-2. The front portion of the platform is at relatively low temperature (approximately 1050 K), similar to the results obtained for ARP1-1. For design ARP1-2, a number of internal holes is considered within the platform wall. These holes have the objective of enhancing the internal HTC in the region downstream of the rear vane mounting rail and maximizing the coolant heat pick-up. The approximate location of the rim holes is marked in Figure 5.8c. This design originates from the idea that the platform trailing region can be cooled in a similar way than the vane TE. In fact, both regions of the NGV are represented by thin geometrical features, for which cooling is rather challenging. The platform trailing section can be therefore equipped with a number of internal passages and the coolant discharged onto the downstream rotor slot. The mass flow rate through these holes is assumed to be approximately 1% of the overall passage mass flow rate. As shown in Figure 5.8c, the temperature levels are substantially reduced ($T_{w1} < 1150$ K) in this region.

The pressure margin of the reverse-pass system (5.8d) is reduced with respect to the baseline case and it is identical to the ARP1-1 design (indeed no modifications are introduced on the upstream reverse-pass channel).

The coolant mass flow rate through the film cooling holes included in the reverse-pass system was a design constraint. To this end, the diameter of these holes was

increased to match the design coolant mass flow rate. Table 5.2 reports the ratio between the updated diameters (with reverse-pass) and the baseline case.

The comparison of laterally-averaged external wall temperature among baseline design, ARP1-1, and ARP1-2, is reported in Figure 5.9a. Data from engine simulations were acquired to predict the value of the internal HTC for the baseline platform. This value was found to be approximately 840 W m^{-2} K. The surface distance is defined increasing in the direction of the mainstream gas (from left to right in Figure 5.9). The baseline case (black line) shows a rapid increase in temperature due to an increase in external HTC and decay in film effectiveness along the platform. Immediately upstream of the rear rail (-0.01 m), the predicted external wall temperature is 1270 K. Higher internal HTC in the region downstream of the rear rail determines a reduction in the external wall temperature. However, the temperature increases again due to high external HTC and low film effectiveness (see Figure 5.3 and 5.4). The thickness of the platform is also smaller in this portion (approximately 1.0 mm) compared to the region upstream of the rear rail (in which the wall thickness is 2.0 mm—see Table 5.1). Design ARP1-1 (blue line) shows a substantial temperature drop along the entire platform axial coordinate due to higher internal HTC, caused in turn by a better guided internal cooling flow. The reduction in temperature is approximately 70 K for most of the platform distance, and about 100 K in the region of the pedestal bank (-0.01 m). This corresponds to a decrease in non-dimensional temperature ϕ (where $\phi = (T_{0\infty} - T_w)/(T_{0\infty} - T_{0c})$) of 0.11. In this portion, a flatter temperature profile is observed (in particular for a surface distance from -0.02 to -0.01 m) thanks to the presence of the pedestal row. However, in the trailing region, the temperature increases again (up to values similar to the baseline case) due to lower internal HTC.

Design ARP1-2 (red line) shows similar behaviour than ARP1-1, with a wall temperature reduction up to 100 K just upstream of the rear rail. In the downstream

region, ARP1-2 performs with substantially lower external wall temperature than the baseline and ARP1-1 cases. In fact, the internal rim holes result in an enhancement of the coolant heat pick-up and in a substantial drop in the wall temperature.

Figure 5.9b depicts the axial distribution of the laterally-averaged internal HTC (h_2) for the three designs. The local area-averaged internal HTC is further laterally-averaged among all the reverse-pass artificial channels. Starting from the platform inlet (i.e. surface distance equal to -0.04 m) and proceeding in the direction of the mainstream gas (from left to right), the predicted HTC for the engine baseline case is 840 W m^{-2} K. Downstream of the rear rail, the internal HTC increases up to approximately 1800 W m^{-2} K. For the ARP1-1 case, the laterally averaged h_2 is approximately 4100 W m^{-2} K, as a result of the flow acceleration through the RP channel. The pedestal bank determines a further increase in h_2, following the profile estimated with the data reported by Lyall (2006). Downstream of the rear rail (values of surface distance smaller than -0.01 m), ARP1-1 has the same arrangement as the baseline case, and h_2 drops to around 1800 W m^{-2} K. On the other hand, the ARP1-2 design (red line) performs with a reduction in external wall temperature of approximately 200 K on the platform trailing region, due to a considerable increase in h_2 (up to 19300 W m^{-2} K). This corresponds to a decrease in non-dimensional temperature ϕ (where $\phi = (T_{0\infty} - T_w)/(T_{0\infty} - T_{0c})$) of 0.22.

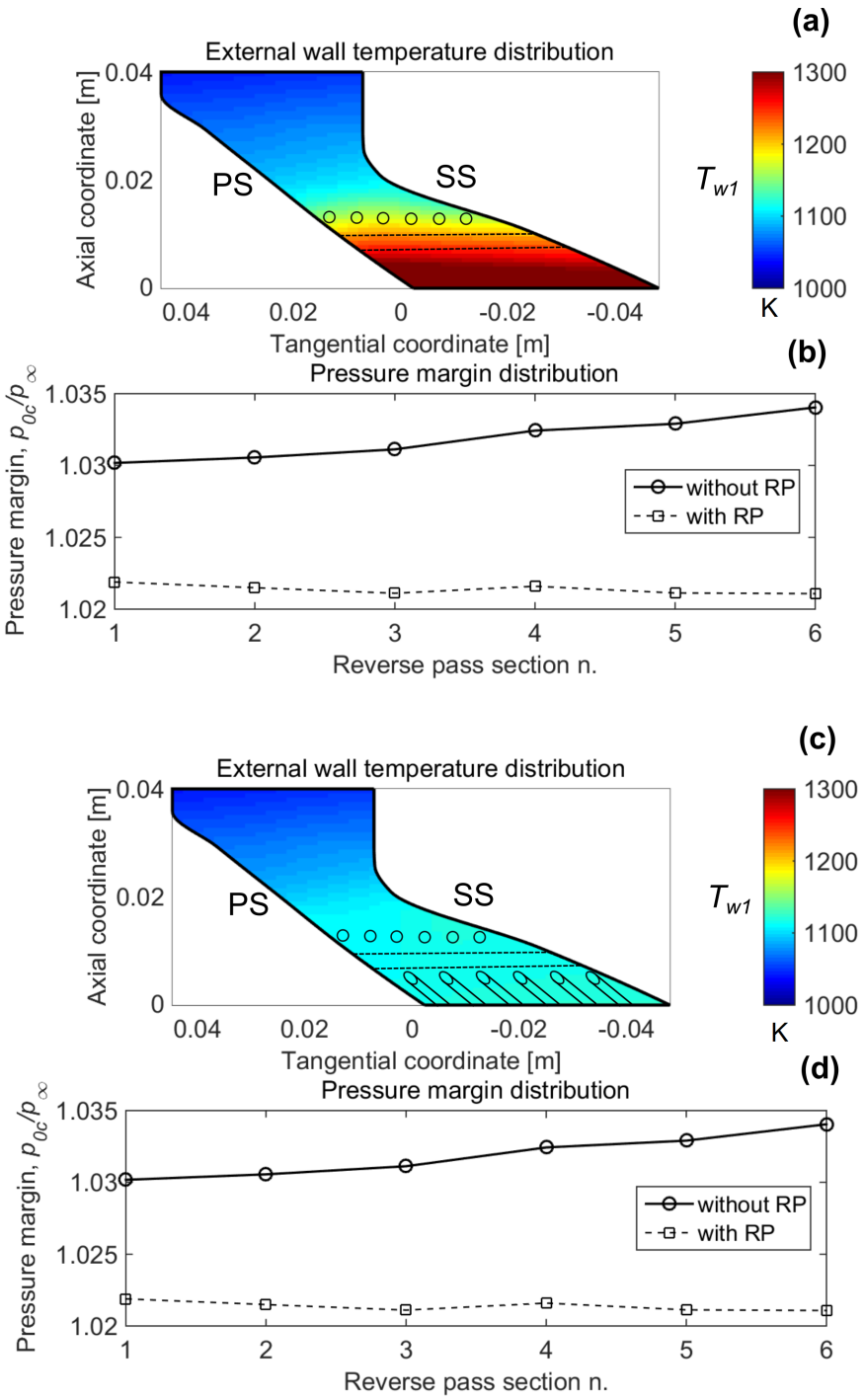


Figure 5.8: External wall temperature (a) and pressure margin distribution (b) of design ARP1-1. External wall temperature (c) and pressure margin distribution (d) of design ARP1-2.

Hole number	d_{RP}/d
1-3	1.127
4-6	1.117
7-9	1.107
10-12	1.102
13-15	1.092
16-18	1.083

Table 5.2: Change in hole diameter for holes included in the revese-pass channel with respect to the baseline case.

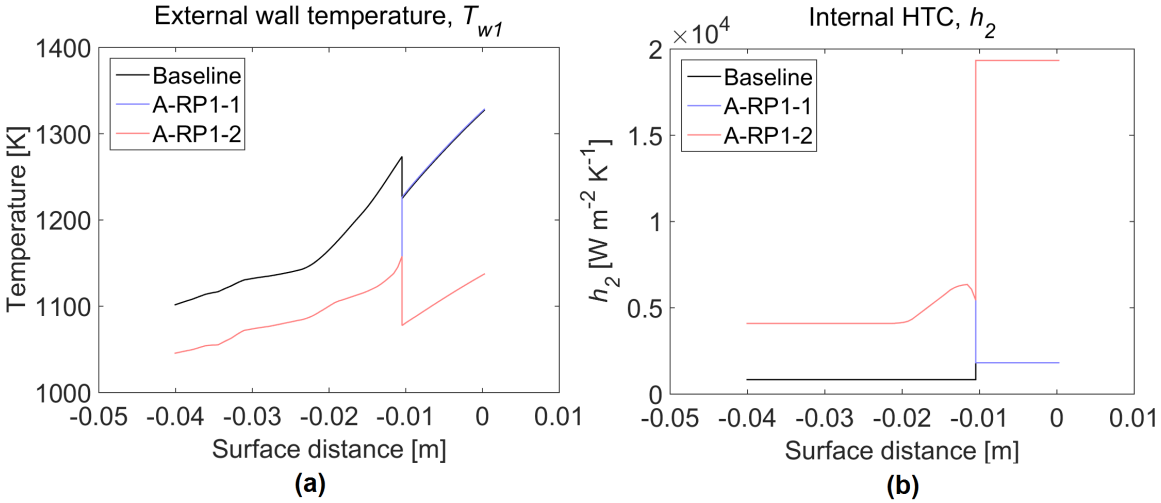


Figure 5.9: Laterally-averaged axial external wall temperature distribution (a), and laterally-averaged internal HTC distribution (b).

5.6 CFD assessment of aero-thermal field

CFD simulations with adiabatic walls were run with updated values of hole diameters and hole exit total pressure obtained with the aerothermal model to assess the influence of the reverse-pass arrangement on the external adiabatic film effectiveness. Numerical simulations were run with total pressure and temperature boundary conditions applied to each hole inlet, with no explicit modelling of coolant plenum and internal cooling system. This was assumed to be sufficiently accurate for the scope of the current analysis, as the the main objective was to estimate the effect of the change

in momentum flux ratio, introduced by the RP channel, on the external aero-thermal field.

For the reverse-pass case, the pressure margin across these holes is decreased and the momentum flux ratio is, in turn, reduced. Figure 5.10 depicts the film effectiveness distribution for the baseline design (5.10a) and ARP1-1 (5.10b). The reduced momentum flux ratio has a beneficial effect on the overall adiabatic film effectiveness field. In fact, higher effectiveness is observed across the platform, with substantial improvement registered in proximity of the SS-LE region. The film effectiveness is also observed to be generally more uniform over the entire endwall surface for ARP1-1 case.

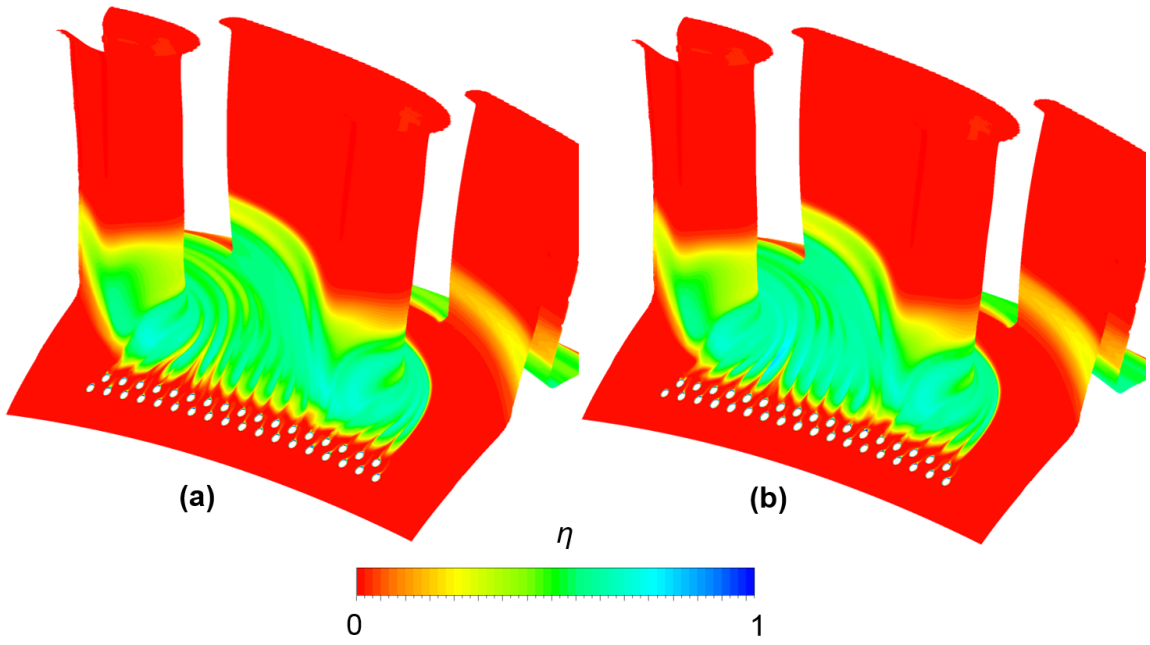


Figure 5.10: CFD comparison of adiabatic film effectiveness between baseline (a) and ARP1-1 (b) design.

Very good agreement of coolant mass flow rate distributions between the baseline and reverse-pass designs (ARP1-1 in this particular case) is observed for the RIDN system for both leading and trailing film cooling rows (depicted in Figure 5.11). Small differences are registered for the holes included in the reverse-pass section (holes n.

from 1 to 18), with a maximum local difference of 5%. The per-passage overall coolant consumption is found to be very similar between baseline case and ARP1-1, with a difference of only 0.8% between the two cases.

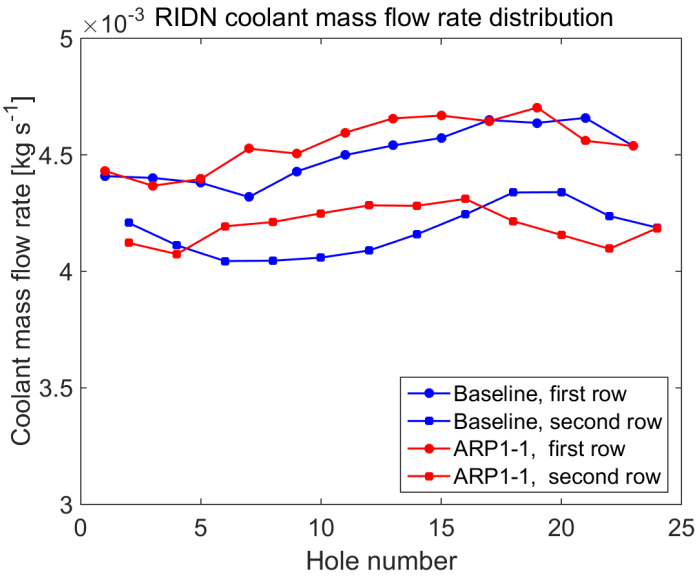


Figure 5.11: CFD comparison of hub platform (RIDN) coolant mass flow rate distribution between baseline and ARP1-1 design.

5.7 Corrected design coolant mass flow rate

Designs ARP1-1 and ARP1-2 were assessed and subsequently manufactured based on a design which included 18 holes feeding the RP channel. Results of a posteriori analysis revealed that the coolant mass flow rate of the RIDN holes included in the reverse-pass design was not periodic on a per-passage basis. That is, the design mass flow rate used to feed the RP channels was slightly smaller than per-passage mass flow rate value (flowing through the RIDN holes). The designs were corrected by accounting for the additional mass flow rate by increasing the number of holes included into the RP channel. However, the metal DMLS parts could not be modified. As reported in the next section, the channel height was increased in the corrected design to counter-balance the increased mass flow rate and therefore match the internal HTC

(h_2) values. As will be shown later, as a result of this correction, the external wall temperature distribution was found to be close to the initial design attempt. It was therefore believed that the mass flow correction had a limited impact on the overall thermal performance of the RP system and on the conclusions of the present study.

Figure 5.12 shows the external wall temperature (T_{w1}) across the platform (5.12a and c) and the pitchwise distribution (from PS to SS) of the pressure margin (5.12b and d) for the updated designs ARP1-1 and ARP1-2. Very similar external wall temperature is observed for both designs when compared to the results of Figure 5.8a and c. In order to counterbalance the increase in HTC due to higher coolant flow velocity through the system (i.e. higher mass flow rate for a given sectional area), the height of the RP channel was increased by 0.5 mm, leading to a total height of 3.0 mm. In particular, the increase in channel height served to reduce total pressure losses, and keep the pressure margin to around 2% (Figure 5.12b and d).

The laterally-averaged external wall temperature distribution with updated coolant mass flow rate for designs ARP1-1, ARP1-2 and the baseline case is depicted in Figure 5.13a. The temperature distribution is very similar to that of Figure 5.9a, as a result of similar distribution of the internal HTC (Figure 5.13b). In fact, the higher internal HTC due to higher mass flow rate for the corrected design is counterbalanced by an increase in channel height.

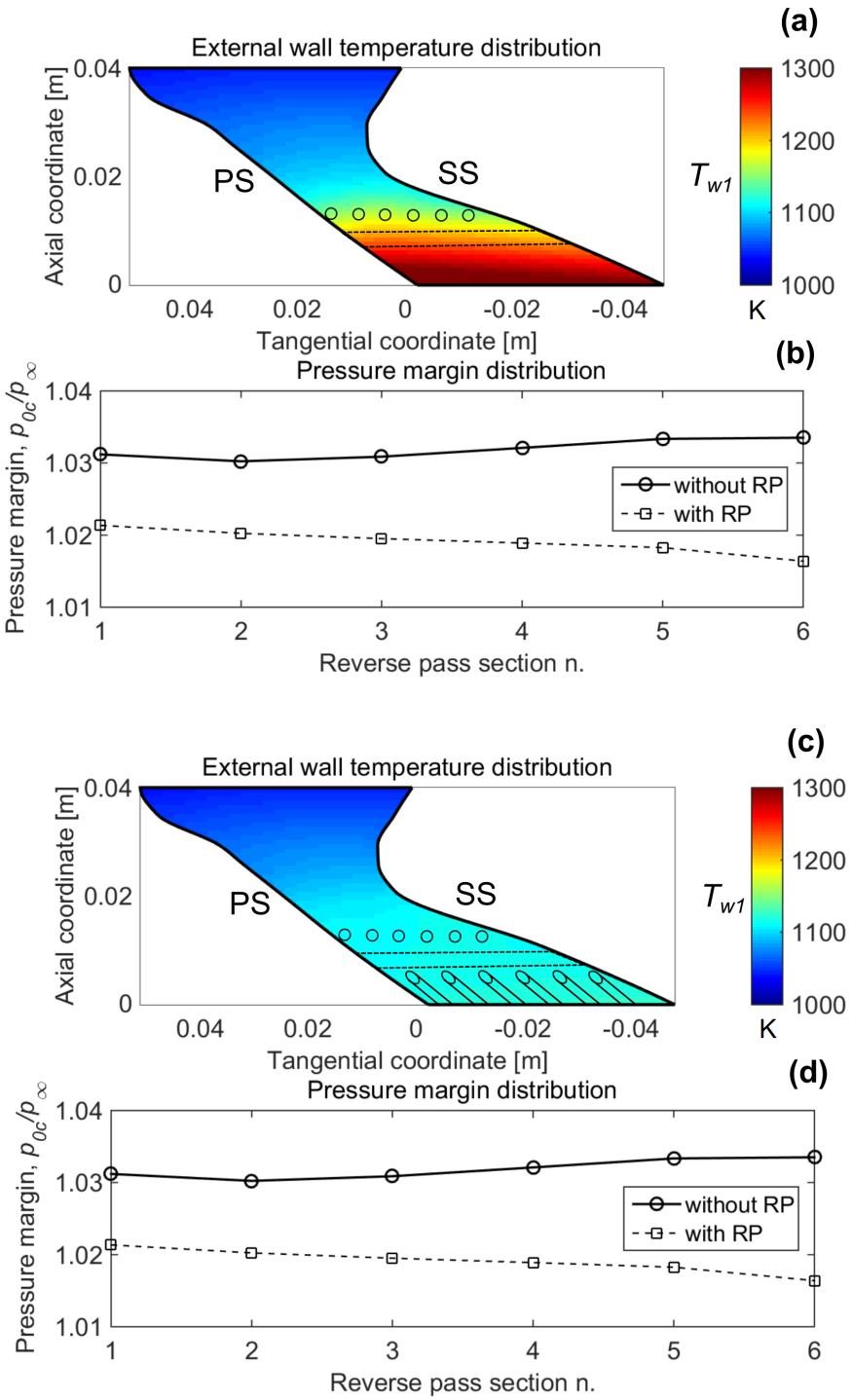


Figure 5.12: Updated external wall temperature (a) and pressure margin distribution (b) of design ARP1-1. External wall temperature (c) and pressure margin distribution (d) of design ARP1-2.

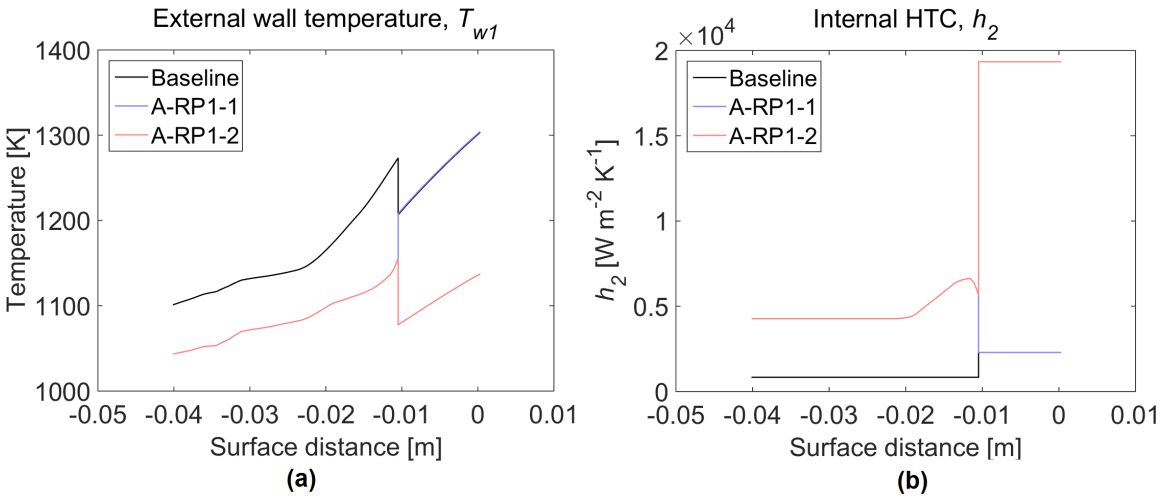


Figure 5.13: Updated laterally averaged axial external wall temperature distribution and (a) laterally averaged internal HTC distribution (b).

5.8 Manufacture

Two reverse-pass designs and the engine baseline vane were manufactured by laser-sintering for high speed testing. This section describes the 3D-printing of the parts by using plastic material for design visualization, material selection for the metal parts, and the metal printing process of the test components.

5.8.1 Plastic models for visualization purposes

In order to assess the manufacturability of the reverse-pass vanes, a rapid-prototyped model was built by using plastic material. The model (with vanes extruded only up to approximately 20% span) was created in the laboratory by using clear plastic to visualize the geometrical features. A view of the plastic model is shown in Figure 5.14. The reverse-pass channel located in between the two vanes (closed passage) is visible form the top view of Figure 5.14a. The pedestal bank is visible at approximately 70% of the vane axial chord (on the internal wall of the vane platform) in Figure 5.14b.

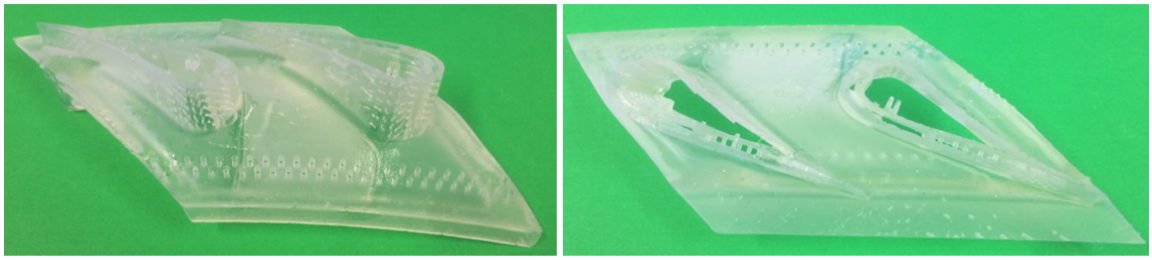


Figure 5.14: Full-scale visualization of a 3D-printed plastic model: (a) front view and (b) top view

5.8.2 Material selection

The laser-sintered platforms were manufactured from titanium alloy (Ti6Al4V) in order to match the ECAT facility metal Biot number to the engine value. In general, the Biot number is defined as follows:

$$Bi = \frac{h_1 t_w}{k_w}, \tag{5.15}$$

where h_1 is the external heat transfer coefficient, t_w is the thickness of the wall, and k_w is the wall conductivity. At engine conditions, the Biot number is approximately 0.8. At the nominal conditions encountered at the ECAT facility, the external HTC is approximately 25% of that at engine conditions. The thermal conductivity of the titanium alloy at ECAT conditions is around 25% of the thermal conductivity of the Nickel super-alloy at engine conditions. Overall, therefore, Biot number could be matched to the engine value.

5.8.3 Laser-sintered vanes

The vane pairs were manufactured by DMLS (Direct Metal Laser Sintering) by using Ti6Al4V titanium alloy by 3T RPD UK. Three builds were manufactured: ARP1-1, ARP1-2, and the engine baseline vane pair. Figure 5.15 shows pictures of the

laser-sintered vanes. Figures 5.15a–c depict: pressure side view, hub (coolant side) platform view, and suction side view of ARP1-1. Similar views are reported in 5.15d–f for the ARP1-2 design. The reverse-pass channel of both designs is visible in 5.15b and e (the coolant intake is located close to the vane overhang). The rim holes exits of design ARP1-2 are visible in 5.15f.

Figure 5.16 depicts the hub platform holes (RIDN) of the laser-sintered vane. As reported by Kirollos (2016) for a similar engine vane component, the DMLS process may perform with reduced accuracy in creating small geometrical features such as film cooling holes. In order to ameliorate this issue, the diameters of the RIDN endwall holes were increased in the CAD model by 0.15 mm for all three designs. This value was estimated based on previous experience on similar parts.

The external surfaces (vane, fillets and platforms) were not finished. Platform and vane film holes were inspected to check that no holes had been blocked during the extrusion. All three designs had same surface roughness, minimum manufacturing resolution, material, and emissivity (i.e. same paint), to allow for a fair back-to-back comparison.

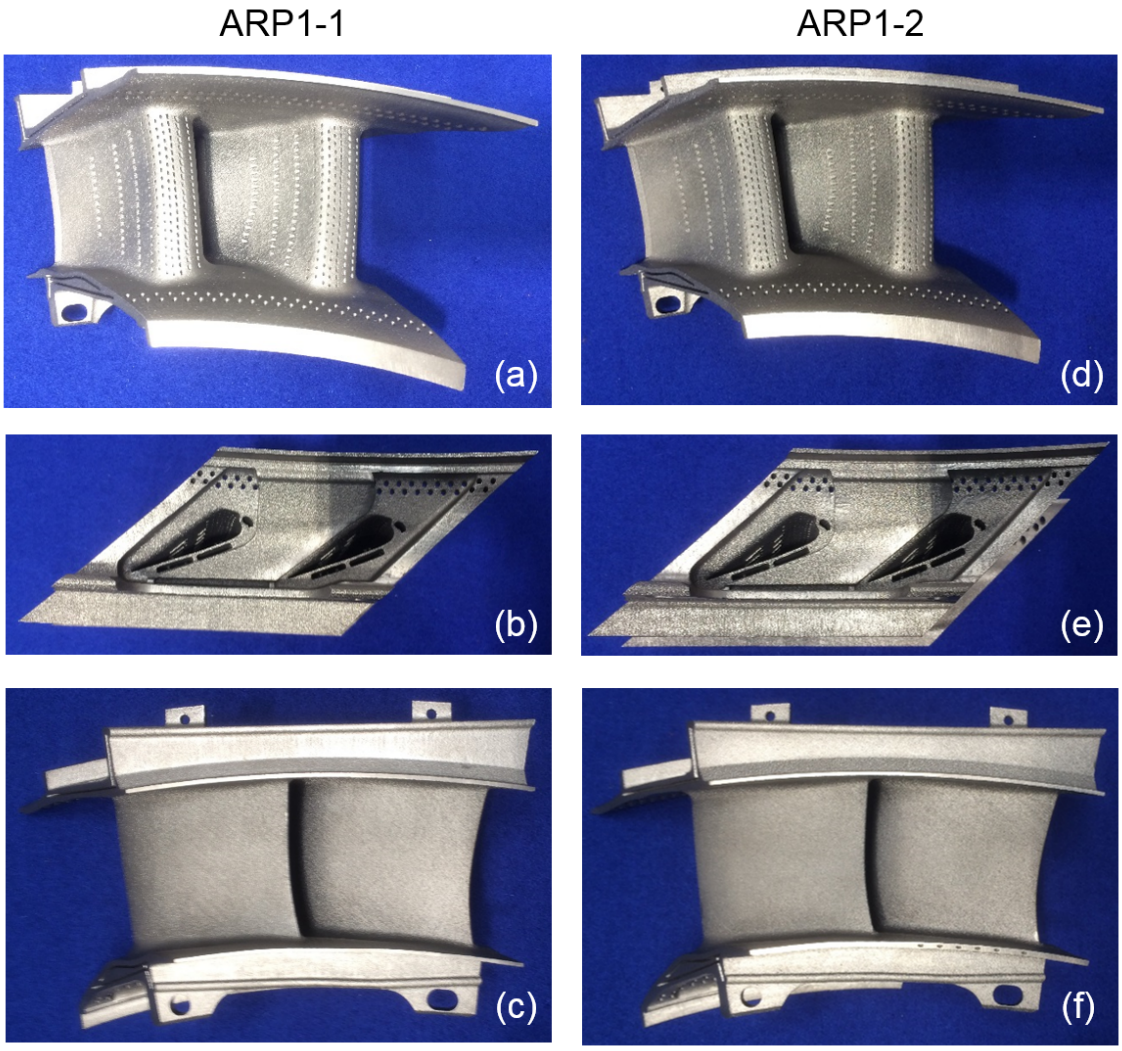


Figure 5.15: ARP1-1 and ARP1-2 as laser sintered. ARP1-1:(a) leading edge view, (b) hub platform view, and (c) trailing edge view. ARP1-2: (d) leading edge view, (e) hub platform view, and (f) trailing edge view.

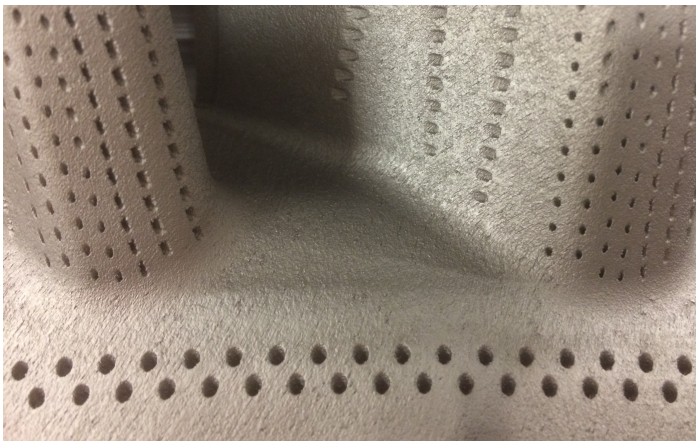


Figure 5.16: Laser-sintered vane: detail of the hub platform holes (RIDN).

The laser-sintering process was carefully analyzed in collaboration with the manufacturer (3T RPD UK) in all its steps to define the best practice for the building of the parts (e.g. orientation of extrusion, supports design, etc.). The strategy gave initial confidence that a tolerance of 0.5 mm could be achieved over the entire build, and 0.4 mm on the vane TE. However, 3D scans of the DMLS parts reported that some of the areas fell outside the specified tolerances, as depicted in Figure 5.17. This was due to the complexity of the parts, and mainly related to the internal vane cooling system (i.e. internal decorations). A maximum deviation from model specifications of +0.5 mm was registered at approximately 70% span of the vane PS, and on the hub PS filled. The manufactured parts were sufficiently close to the CAD specifications and no major issues were registered with both vane internal and platform cooling systems.

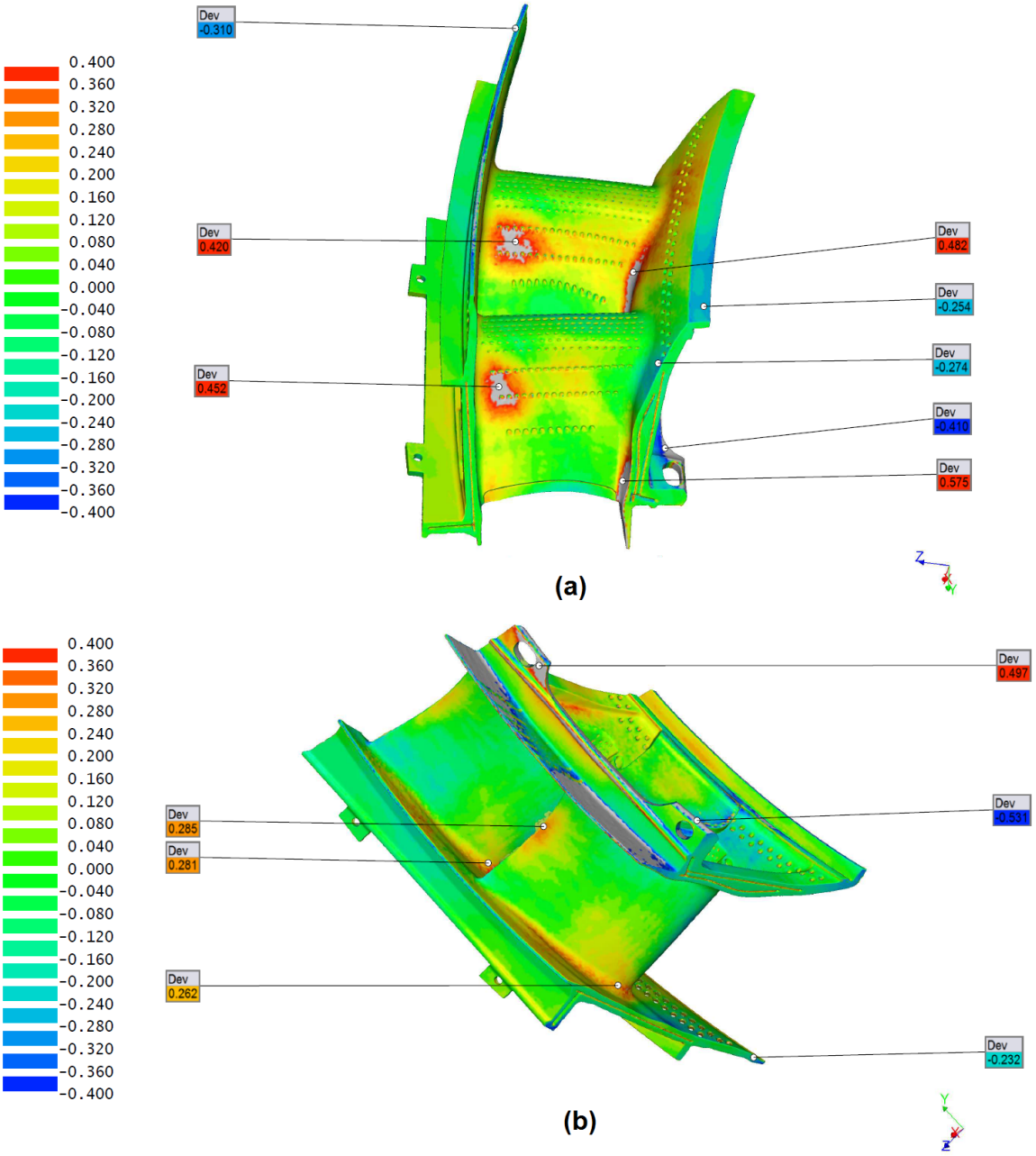


Figure 5.17: 3D scan of Ti6Al4V ARP1-1 vane. (a) Pressure side view and(b) suction side view. Values represent the deviation in mm.

5.9 Conclusions

In this chapter, the design of HP-NGV vane reverse-pass platforms has been carried out. A bespoke conjugate aero-thermal network was developed to predict aero-

dynamic loss and temperature distribution of a NGV hub endwall from a modern jet-engine. The design approach was based on the counter-current arrangement of mainstream and coolant, in which the coolant flows in the opposite direction to the mainstream gas before being discharged through a number of film cooling holes in the platform. Two designs—one including a reverse-pass channel extending up to the vane platform support rail (ARP1-1), and a second one including an additional set of rim holes through the trailing platform (ARP1-2)—were thermally investigated and results compared to the baseline configuration. Results showed that both designs perform with a temperature reduction of approximately 100 K in the front region of the platform. This corresponds to a decrease in non-dimensional temperature ϕ of 0.11. This was mainly due to an increase in internal heat transfer coefficient generated by improved guidance of the coolant flow and the presence of internal decorations. The design ARP1-2 was also shown to perform with approximately 200 K reduction in metal temperature in the trailing region (corresponding to a decrease in ϕ = 0.22), attributed to a substantial enhancement of the internal HTC allowed by the rim holes. CFD evaluations show that the reverse-pass designs can perform with increased adiabatic film effectiveness. This was due to reduced momentum flux ratio (with corresponding better attached cooling jets—see Chapter 3) determined by an increase in pressure loss through the reverse-pass system.

Three designs (ARP1-1, ARP1-2, and engine baseline) were manufactured by laser-sintering using titanium alloy. 3D scans of the DMLS parts were performed to measure maximum deviations from the CAD specifications. The parts presented a maximum deviation of +0.5 mm in localized areas and were therefore suitable for aero-thermal tests at high-speed conditions.

Chapter 6

Experimental Investigation of High-Pressure Reverse-Pass Vane Platforms

6.1 Introduction

This chapter describes an experimental work to assess the thermal performance of the reverse-pass HP-NGV platforms designed in the previous chapter. Tests are performed at the Engine Capacity Aerothermal (ECAT) Facility of the University of Oxford. The ECAT Facility allows for overall effectiveness studies at matched Reynolds number, Mach number, Biot number, and coolant-to-mainstream pressure ratio with accurate flow capacity measurements (Povey 2004). The aim of this chapter is to experimentally demonstrate the benefit coming from the implementation of a reverse-pass system for NGVs platform cooling. The comparison is performed back-to-back with the baseline engine system at different coolant-to-mainstream pressure ratios. The structure of the chapter is reported in the following text.

After a brief introduction on the ECAT Facility and its operation, the attention is focussed on the design and implementation of major modifications to allow for measuring platform surface temperature using an existing infra-red system. The design (based on reflective infra-red mirrors) is described in detail. Three sections covering infra-red calibration, measurement uncertainty, and test plan are also reported.

Aero-thermal results are presented and discussed thoroughly in the last section of this chapter.

6.2 The Oxford ECAT facility

This section describes a recently commissioned engine-parts facility at the University of Oxford. The facility was designed for high technology-readiness-level research, new technology demonstration, and for engine component validation. Detailed information about the ECAT facility can be found in Kirollos et al. (2017).

The Engine Component AeroThermal (ECAT) facility has a modular working section which houses a full annulus of engine components. The current working section is designed to operate with high-pressure nozzle guide vanes from a modern large civil jet-engine. Current HP-NGVs are film-cooled, platform cooled, and internally cooled. The facility allows for high degree of engine similarity by matching Mach number, Reynolds number, and coolant-to-mainstream pressure ratio. The facility also allows for studies on combustor-turbine interaction, with a combustor simulator module which is capable of both rich-burn and lean-burn combined swirl, temperature, and turbulence profiles. Two operating modes are possible: *blowdown* mode for full capacity characteristics; and *regulated* mode for aerodynamic loss and overall cooling effectiveness measurements at a single steady-state condition. Very accurate capacity measurement (with a precision error of $\pm 0.02\%$) can be performed. Such a small precision error allows for accurate estimation of capacity characteristics when real engine parts are blowing. It also allows for fundamental research on a number of aerodynamic topics (trailing edge, design and performance, cooling mixing loss, coolant migration, shock control).

Overall cooling effectiveness can be measured allowing rainbow tests to be performed and the back-to-back comparison of different cooling designs. The results

can be used for validation of conjugate CFD, high fidelity modelling of novel cooling schemes, and for extracting engine-realistic boundary conditions for optimization research.

In addition to capacity and overall cooling effectiveness measurements, aerodynamic performance measurements are possible, enabling the ranking of designs under highly representative conditions of Mach number, Reynolds number, cooling flow, turbulence intensity, temperature distortion factor (OTDF), and swirl profile.

6.2.1 Operation of the Oxford ECAT facility

Inheriting many of the aspects of the Oxford Capacity facility (Povey 2004), the Oxford ECAT facility is an engine-scale, semi-transient blow-down facility in which air from a storage tank at 27.6 bar is discharged at approximately 2.5 bar through the annular test section. The latter is composed by HP NGVs from real engine parts, completed with internal cooling geometry, RIDN (hub) and RODN (case) platform flows. The facility operates at high levels of engine similarity as possible to match the engine Mach number, Reynolds number, and coolant-to-mainstream pressure ratio. These quantities are scaled to account for the flow temperature difference between ECAT and engine conditions. The methodology to perform the scaling is described by Povey (2004).

6.2.2 Facility layout and principles of operation

The principal components of the ECAT facility are shown in Figure 6.1 (schematic) and Figure 6.2 (photo). Dry air is stored at 27.6 bar (400 psi) in two pressure vessels of 60 m^3. One mode of operation of the ECAT facility allows airflow from the pressure tank through an adjustable area limiter (labelled A1 in Figure 6.1) bypassing the pressure regulator (blow-down mode operation). The second operation mode consists of the air flowing through the area limiter and then through the Oxford Flow Inline

High Flow (IHF) regulator (regulated mode operation). These two modes allow for the running of the tests at different conditions, for different research purposes.

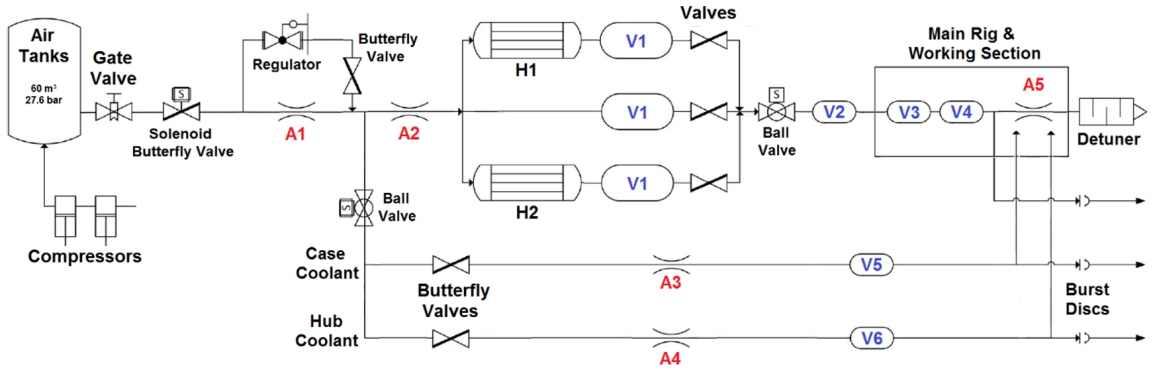


Figure 6.1: Flow-path schematic of the Oxford ECAT Facility.

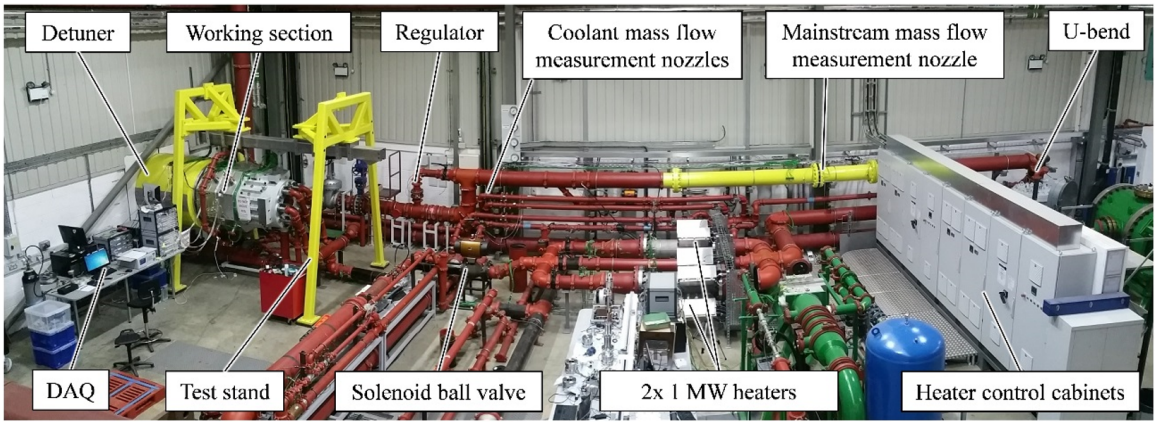


Figure 6.2: The main components of the Oxford ECAT Facility.

Downstream of the pressure regulator, the main flow is divided into the mainstream line and independent casing and hub stream, each having a variable area choked nozzle. The choked nozzle on the manistream line (A2 in Figure 6.1) is a sonic venturi with a diameter of 76.2 mm. This nozzle was installed in accordance with the ISO-9300 standard and calibrated to a National Institute of Standards and Technology (NIST). The uncertainty in the discharge coefficient of the nozzle is ± 0.5%, which leads to a bias uncertainty of ± 0.5% and a precision uncertainty of ± 0.02% in measured capacity (Povey 2004). Independent mass flow measuring systems are present on both case and hub streams.

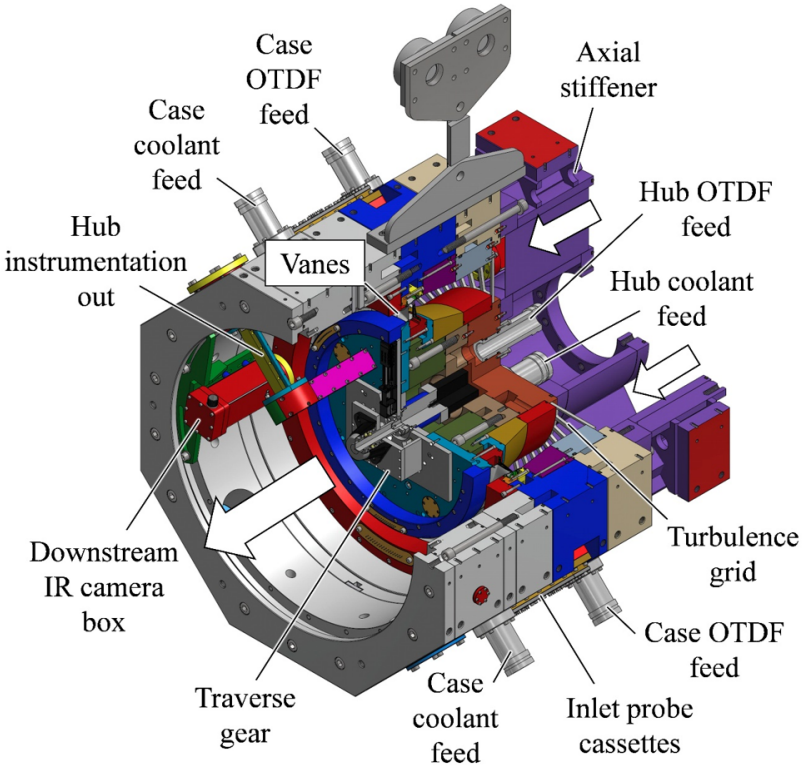


Figure 6.3: The working section of the Oxford Capacity Facility.

Two 2 MW heaters (labelled H1 and H2 in Figure 6.1) are installed downstream the main nozzle. The heaters are rated to raise the mainstream temperature by 60 K at the nominal vane pressure ratio. The mainstream flow enters the rig through the manifold (Figure 6.3) and then into the settling chamber. It then flows through a distribution plate into the axial stiffener. Flow then encounters a turbulence grid before passing through the combustor cavity into the NGV cascade. The annulus line of the combustor-NGV section is closely matched to that of the engine. Recent builds of the facility include swirler section and temperature distortion feeds to allow for the testing at conditions representative of lean-burn combustors.

A test run is initiated by opening the air-actuated solenoid ball valves located on the 8 inch (203.2 mm) diameter main feed line and on the 4 inch (101.6 mm) diameter auxiliary feed line upstream of the working section, followed by the opening of the actuated butterfly valve to give a steady, controlled and repeatable start to the run.

The run is typically terminated by closing the two ball valves.

6.3 Facility commissioning for platform tests

In order to ensure a complete view of both upstream and downstream portions of the hub endwall, a number of modifications were implemented on the original test section of the ECAT facility. These modifications consisted mainly of the installation of gold-coated infra-red mirrors. The design of the mirror system for both front and rear platform views is described in the next section.

6.3.1 Front and rear platform view design

A number of components of the ECAT facility were modified from the original build to obtain a view of the upstream and downstream portion of the hub endwall for infra-red measurements. The original infra-red camera locations and hardware (previously designed for PS and SS views), were kept the same as the original build. The metal boxes containing the cameras (and the supporting brackets) were also kept the same as the original ECAT build. This choice was made to perform an easy integration of the endwall view system and be able to quickly replace the hardware between vane PS/SS tests and endwalls tests.

Both front and rear views of the endwall were designed by using camera CAD tools in SolidWorks. Camera lens specifications were set in Solidworks to simulate the camera view by using the global assembly of the facility (Figure 6.4). In this way, it was possible to obtain a realistic prediction of the image reflected into the mirror and therefore adjust the design to match the desired view. This process allowed a substantial reduction in design time.

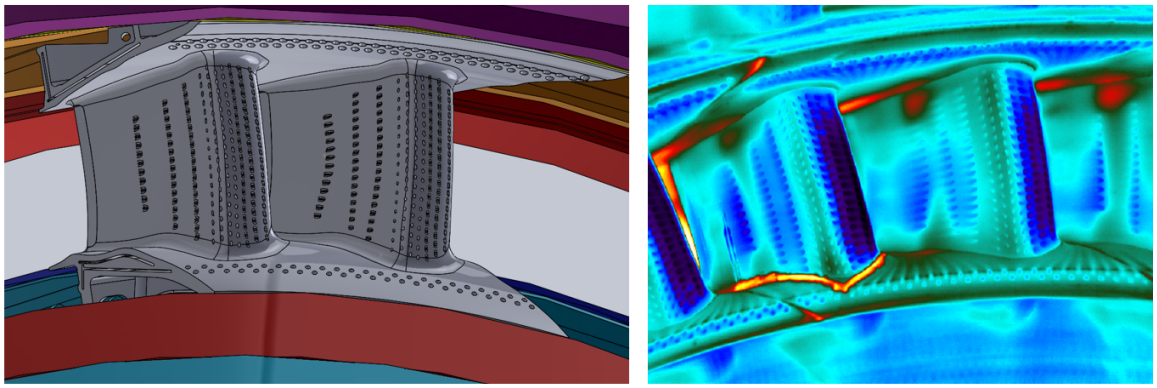


Figure 6.4: Camera view obtained from the CAD model (a), and view from the IR camera acquired during a test (b).

The IR mirrors were manufactured by LBP Optics from aluminium (Al6082 T6 grade) and coated with a gold layer to obtain a highly reflective surface in the infra-red wavelength range.

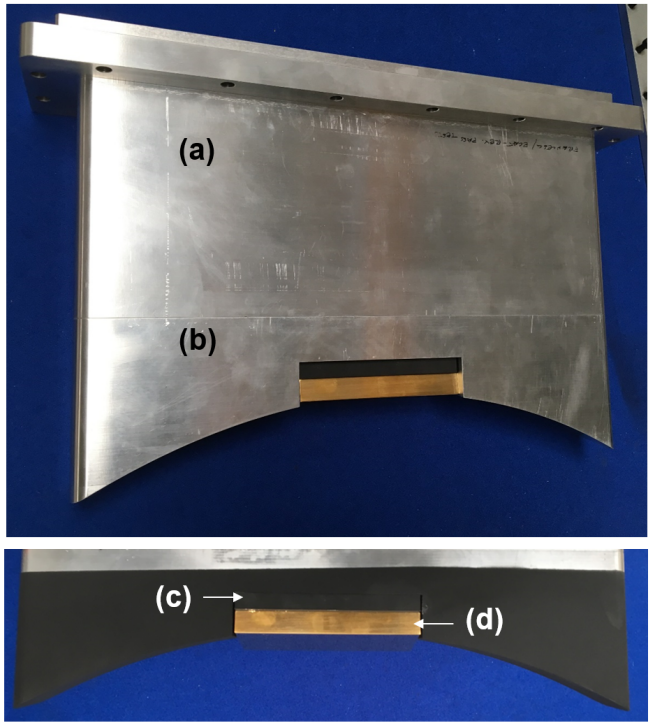


Figure 6.5: Photo of upstream cassette with IR mirror. Top cassette body (a), bottom cassette body (b), angled support bracket (c), and gold-coated IR mirror (d).

Figure 6.5 depicts the front-view system. A slot was machined on the bottom face

of the upstream instrumentation cassette (a) to allow for housing a gold-coated mirror (d) by using an aluminium angled bracket (c) and adjust the mirror orientation to the desired angle.

Figure 6.6 depicts the downstream mirror system. The IR mirror (a) was mounted onto an angled support bracket (b), and fixed to the top face of a slot machined on the exit case ring (c).

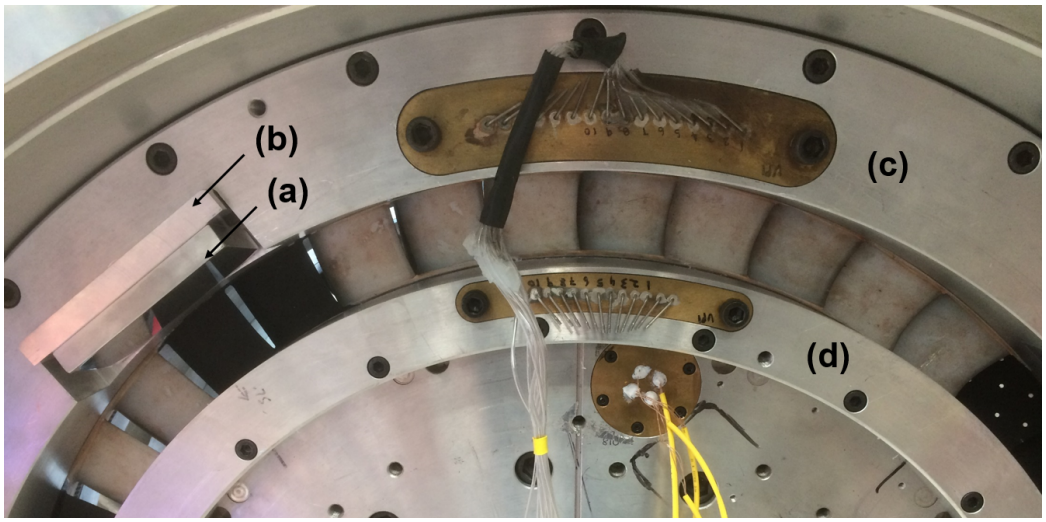


Figure 6.6: Photo of the vane test section (viewed from downstream); (a) IR mirror, (b) angled support bracket, (c) vane casing ring, and (d) vane hub ring.

Both mirrors had a thickness of 15 mm in order to ensure minimum deformation during mounting and therefore minimum distortion of the reflected infra-red signal.

6.4 Infra-Red thermography

Infra-Red thermography allows reliable, non-intrusive, full-coverage temperature measurements. In this technique, the resistance of microbolometers is a function of temperature, which is a function of incident electromagnetic radiation. In turbomachinery research, the use of infra-red thermography has attracted more and more users over the last few years as it represents a robust, versatile, non-intrusive technique with full-coverage temperature capability—a particularly important characteristic in turbine

film cooling research. However, infra-red measurements are not trivial and require knowledge of emissivity of the object, transmissivity of the atmosphere, transmissivity of the optical system, and surrounding radiance. The knowledge of these quantities is not straightforward and, in some cases, requires specific *in-situ* calibrations.

In general, the conversion from radiometric value to temperature requires a black-body calibration, in which the camera hardware must be known, and a grey-body calibration, in which information of the object and its surrounding is required.

6.4.1 Infra-Red thermography theory

Two FLIR A655sc cameras with 13 mm (45 deg) and 21.4 mm (25 deg) lenses were used for infra-red measurements. The cameras have a focal plane array (FPA) of 640 $\times$ 480 microbolometers to convert the incident infra-red radiation (in the wavelength range 7.5–14.0 μm) from the voltage across the detectors. The electrical resistance of microbolometers is a function of temperature which, in turn, is a function of the incident electromagnetic radiation. The camera software performs offset compensation, 16 bit A/D conversion, gain compensation, and non-uniformity correction (NUC) by normalizing the voltage readings across the FPA to compensate for variation in pixel characteristic (FLIR 2014). Ambient drift compensation (ADC) is also performed by the camera processor by continuously monitoring the internal temperature to correct for spurious radiation influences.

The resultant pixel raw digital count $R(x)$ (where x is the pixel location) is approximately linear with the incident infra-red radiation ($q_{cam}(x)$) in the spectral band 7.5–14.0 μm. The latter has the following form:

$$q_{cam}(x) = \sigma T_{bb}^4(x) = aR(x) + b, \tag{6.1}$$

where a and b are constants, specific to a given camera and T_{bb} is the equivalent

black-body temperature. That is, the temperature of an ideal black-body to generate the same incident infra-red radiation.

Assuming that the emissivity of the object is independent of wavelength and direction, no radiation is transmitted through the object (e.g. a grey, opaque object with a diffuse surface), the absorptivity α is then equal to the emissivity of the surface ε (see Kirchhoff's law). The assumption of grey, opaque surface holds in the spectral range 7.5–14.0 μm and for painted metallic objects. The assumption that the emissivity is the same in all directions (diffuse surface) does not hold for large viewing angles. Taking the Kirchhoff's Law and the Stefan-Boltzmann Law (total radiated energy from a black body), the temperature of the object can be deducted from the black-body measurement by using the following equation:

$$T_{bb}^4(x) = \varepsilon\tau T_w^4(x) + (1-\varepsilon)\tau T_R^4(x) + (1-\tau)T_{atm}^4(x), \tag{6.2}$$

where T_R is the effective temperature of the object's surroundings (assuming an emissivity of the surrounding equal to unity), τ is the atmospheric transmittance, and T_{atm} is the atmospheric temperature.

Black-body calibration cannot be used to estimate the grey-body parameters because Equation 6.2 is independent of grey-body parameters in the case of isothermal conditions (i.e. $T_{bb} = T_w = T_R$). In general, black-body calibration allows for the estimation of the temperature of a black-body from the camera radiance measurement. However, the vane of interest at ECAT running conditions cannot be modelled as a black-body because the emissivity is less than unity *and* the temperature of the surroundings is not equal to the temperature of the vane of interest. In addition, the transmittance of the protective Zinc-Selenide window is not unity *and* the temperature of the surroundings is not equal to the temperature of the vane of interest. Therefore, in order to determine the value of ε, τ, and T_R an *in-situ* grey-body

calibration must be performed.

6.4.2 Grey-body calibration theory

At the ECAT conditions, the test section cannot be modelled as a black-body because the emissivity of the object is not unity *and* the temperature of the object and its surroundings are not the same. At these conditions, grey-body parameters must be known to account for the contribution to overall radiance received by the camera due to surroundings and external optics.

During a thermal test at the ECAT conditions, the total radiance received by the IR camera $q_{cam}(x,t)$ is the sum of the following contributions: the incident radiance from the vane of interest (after reflection from the infra-red mirror) $q''_w(x,t)$, the radiation due to surroundings reflected off the vane of interest $q'''_R(x,t)$, and the radiance due to the temperature of the external optics (i.e. ZnSe window) $q_{opt}(t)$:

$$q_{cam}(x,t) = q''_w(x,t) + q'''_R(x,t) + q_{opt}(t). \tag{6.3}$$

The transmittance of air at nominal humidity over small distances (i.e. the distance between the IR cameras and the vane of interest in the ECAT facility) is approximately unity (FLIR 2012). Therefore, absorption or emission from the test gas can be ignored.

$q_{cam}(x,t)$ is the total radiance received by the camera and can be linked to the equivalent black body temperature by using the Stefan-Boltzmann equation:

$$q_{cam}(x,t) \equiv \sigma T^4_{bb}(x,t), \tag{6.4}$$

where σ is the Stefan-Boltzmann constant. The camera performs the conversion from the radiometric value to the equivalent black-body temperature by means of a factory black-body calibration. The later has the following form (for a cavity-type black-body

calibration):

$$\sigma T_{bb}^4 = \sigma T_w^4 = aR(x) + b, \tag{6.5}$$

which is independent of grey-body parameters (i.e. emissivity, transmittance etc.) for a perfectly isothermal system. In Equation 6.5, $R(x)$ is the radiometric value (function of space), and a and b are constants obtained by regression during the calibration for a given camera hardware.

A sketch of ray traces for the rear and front portions of the hub endwall are depicted in Figure 6.7a and 6.7b, respectively. The total incident radiation received by the camera due to the temperature of the platform (region of interest in the figure) can be cast as:

$$q''_w(x,t) = \tau q'_w(x,t) = \tau\rho q_w(x,t) = \tau\rho\varepsilon(x,\theta)\sigma T_w^4(x,t), \tag{6.6}$$

where τ is the transmittance of the window, ρ is the reflectivity of the gold-coated mirror, $\varepsilon(x,\theta)$ is the emissivity of the object, and σ is the Stefan-Boltzmann constant. ε is function of view angle θ. It is assumed that the transmittance is constant over the area of the window. $q'_w(x,t)$ is the radiance before the Zn-Se window due to the temperature of the platform. The reflectivity of the gold-coated mirror is high (~ 0.99 in the range 7.5μm–14.0μm, EdmundOptics (2018)), and therefore it can be assumed that $q'_w(x,t) \sim q_w(x,t)$. $T_w(x,t)$ is the temperature of interest and is used for overall cooling effectiveness scaling in this chapter.

The camera-incident radiance due to the temperature of the surrounding walls $q''_R(x,t)$ reflecting off the vane surface is related to an equivalent surrounding temperature $T_R(x,t)$ using the vane emissivity and window transmittance:

$$q'''_R(x,t) = \tau q''_R(x,t) = \tau\rho q'_R(x,t) = \tau\rho(1-\varepsilon(x,\theta))q_R(x,t) = \tau\rho(1-\varepsilon(x,\theta))\sigma T_R^4(x,t), \tag{6.7}$$

where $q''_R(x,t)$ is the radiance before the Zn-Se window and $q'_R(x,t)$ is the radiance after reflection from the vane of interest. Given that the reflectivity of the gold-coated mirror is high, it can be assumed that $q''_R(x,t) \sim q'_R(x,t)$. $T_R(x,t)$ is the temperature integrated over all surroundings. It is rather difficult to calculate $T_R(x,t)$ and specific measurements are required to estimate its value.

The radiance received by the camera due to external optics (Zn-Se window) is related to the temperature $T_{opt}(t)$ and the transmittance of the window τ by:

$$q_{opt}(t) = \sigma(1-\tau)T^4_{opt}. \tag{6.8}$$

Substituting Equations 6.4–6.8 into Equation 6.3, we can write:

$$T^4_{bb}(x,t) = \varepsilon(x,\theta)\tau T^4_w(x,t) + (1-\varepsilon(x,\theta))\,\tau T^4_R(x,t) + (1-\tau)T^4_{opt}(t). \tag{6.9}$$

$T_{bb}(x,t)$ is the equivalent black-body temperature measured by the camera, and $T_w(x,t)$ is the temperature of the region of interest. $T_R(x,t)$, $\varepsilon(x,\theta)$, τ, and $T_{opt}(t)$ are unknown. Kirollos (2016) defined a *surrounding radiance* term q^*, which is dependent on surface location, viewing angle, and time:

$$q^*(x,\theta,t) \equiv \frac{\sigma\left(\tau\,(1-\varepsilon(x,\theta))\,T^4_R(x,t) + (1-\tau)T^4_{opt}(t)\right)}{1-\tau\varepsilon(x,\theta)}. \tag{6.10}$$

q^* has a physical meaning as it incorporates all extraneous radiation sources other than the object of interest. The surrounding radiance term is used to correct the camera measurement, and the temperature of the wall is calculated as:

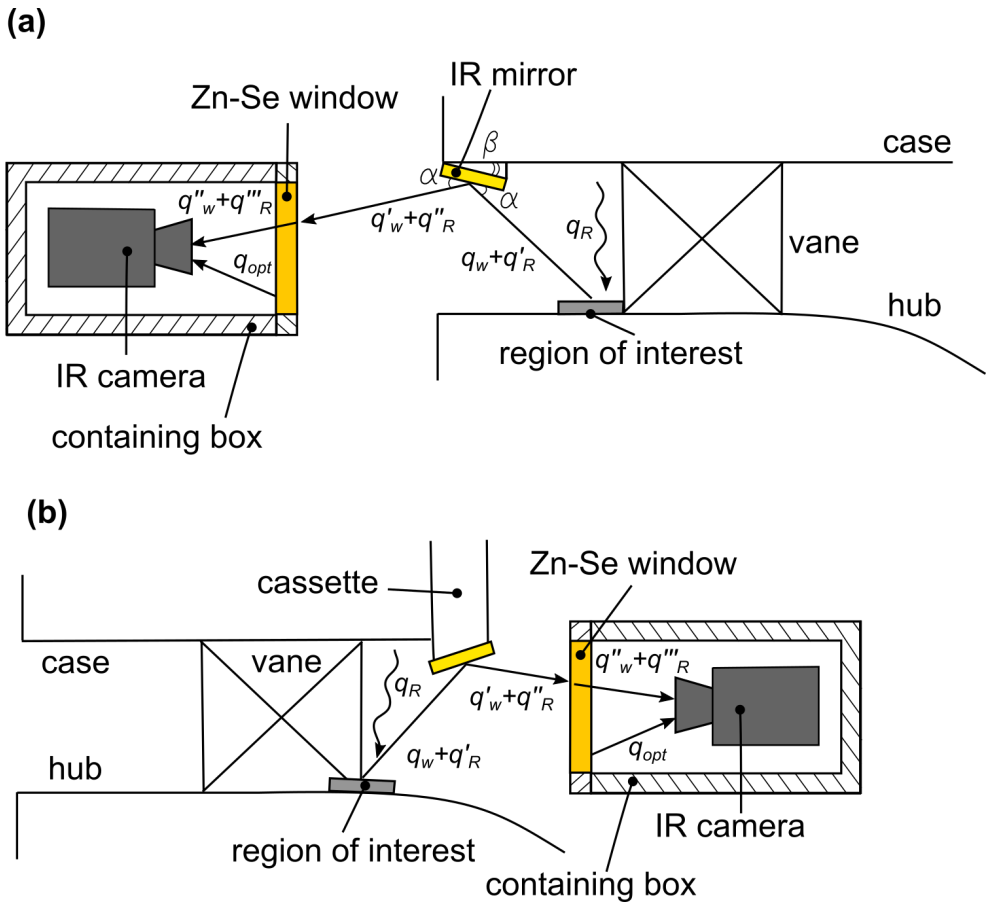


Figure 6.7: Sketch of ray traces for (a) rear view and (b) front view during nominal operation.

$$T_w(x,t) = \sqrt[4]{\frac{\sigma T_{bb}^4(x,t) - (1-\tau\varepsilon(x,\theta))q^*(x,\theta,t)}{\sigma\tau\varepsilon(x,\theta)}}. \tag{6.11}$$

In the work of Kirollos (2016), q^* was measured per run using a surrogate radiation correction vane. In the present work, q^* is determined by performing a bespoke *in-situ* experiment for both front and rear endwall views.

6.4.3 Surrounding radiance correction

During the surrounding radiance experiment, the surface temperature at a point on both upstream and downstream endwalls $T_w(x_{TC},t)$ is measured using surface thermocouples. The equivalent black-body temperature at a point next to each ther-

mocouple $T_{bb}(x_{TC}, t)$ is measured using the IR cameras. The thermocouple and IR temperature histories, transmittance and emissivity values are then used to estimate the surrounding radiance:

$$q^*(t) = \frac{\sigma T_{bb}^4(x_{TC}, t) - \sigma\tau\varepsilon T_w^4(x_{TC}, t)}{1 - \tau\varepsilon}. \tag{6.12}$$

In Equation 6.12, we introduce the following assumptions; firstly, we assume that the emissivity is constant over the platform surface (i.e. $\varepsilon(x, \theta) \sim \varepsilon(\theta)$). This assumption is seen as reasonable for both front and rear endwall regions since they were uniformly spray-painted. Secondly, it is assumed that the emissivity is independent of the viewing angle:

$$\varepsilon(\theta) \sim \varepsilon. \tag{6.13}$$

This assumption is seen as reasonable since the angle variation over both front and rear endwall profiles—within the region of interest—is small. A constant value—different for both front and rear views—is estimated for an averaged viewing angle by using the correlation presented in Kirollos and Povey (2017) for black paint. Finally, the surrounding radiance is assumed to be constant over the endwall surface and independent of camera viewing angle, though different for front and rear endwalls:

$$q^*(x, \theta, t) \sim q^*(t). \tag{6.14}$$

The effect of considering uniform q^* over the field-of-view is unknown. However, this assumption was seen as acceptable for the comparative purposes of this study. More information about the spatial variation of surrounding radiance would come in the form of more calibration points over the endwall, though introducing higher complexity in the experiments.

An accurate measurement of q^* would require the acquisition of the black-body

temperature from a pixel next to the thermocouple location. To do this, a sufficiently isothermal region around the thermocouple junction must be ensured, in order to reduce the dependency on the pixel location. In addition, the thermocouple must correctly measure the surface temperature. This may be affected by the thermal resistance of the adhesive layer used to place the thermocouple on the surface—in fact, there is heat flux through the vane metal surface. A thermally insulating layer would therefore represent an ideal condition in which both thermocouple and IR camera would measure the correct surface temperature. To this end, bespoke *in-situ* calibration systems for both rear and front endwalls were designed and manufactured.

The rear endwall calibration system included a 3 mm thick rectangular Rohacell layer (thermal conductivity $k = 0.02$ W m^{-1} K^{-1}) in which a 4 mm diameter, 0.5 mm thick copper disk was pressed and glued. A surface thermocouple was then placed on the surface of the copper disk by using thermally conductive paste and the entire surface was uniformly painted black. The purpose of the copper disk was to enhance the temperature uniformity around the thermocouple junction. Figure 6.8 shows the downstream endwall calibration system.

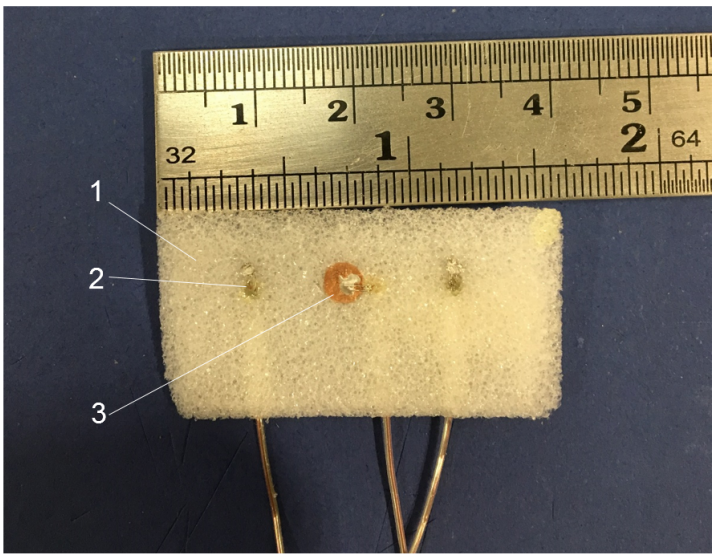


Figure 6.8: Picture of *in-situ* downstream endwall calibration system. (1) Rohacell layer, (2) surface thermocouple, and (3) thin copper disk.

The black-body temperature field for the downstream calibration system is presented in Figure 6.9. The calibration patch (visible on the top part of Figures 6.9a and 6.9b) was flush mounted against the platform trailing edge to reduce potential flow separations. At hot conditions (Figure 6.9b), the region of the copper disk shows a uniform temperature.

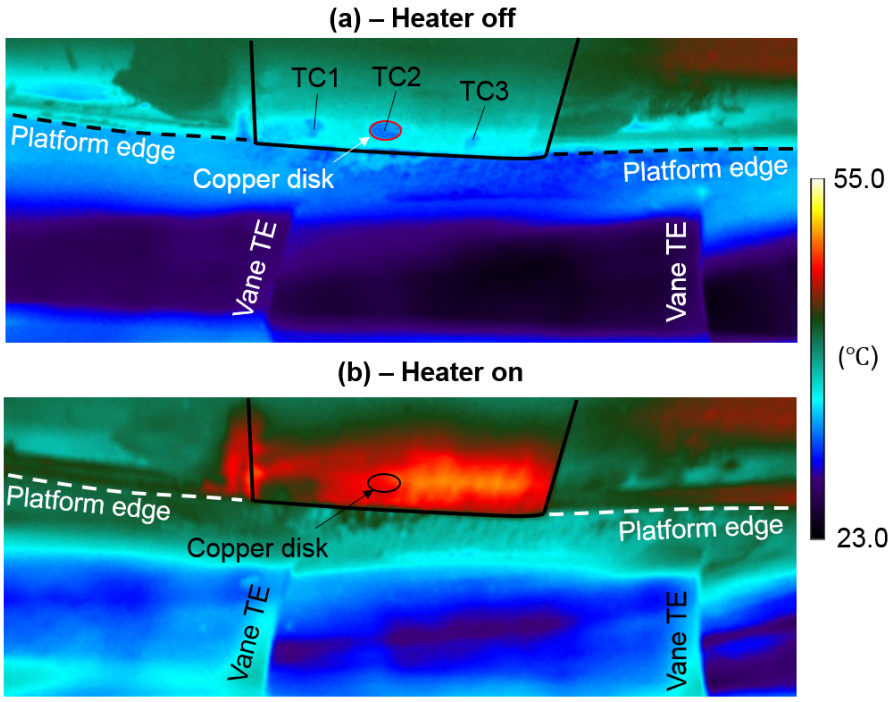


Figure 6.9: Equivalent black-body temperature field on downstream calibration region after heater mesh cut-off (a), and during heater on (b).

Due to space constraints and limited physical access to the upstream endwall, the front calibration system was integrated into the existing instrumentation cassette. The cassette was machined to house a 12 mm diameter cylindrical support with a 3 mm thick Rohacell layer (Figure 6.10). The external temperature of the Rohacell layer was measured by a surface thermocouple. As depicted in Figure 6.9b, the Rohacell region was highly isothermal due to the upstream temperature profile being approximately uniform. It is assumed the surrounding radiance measured with the system of Figure 6.10 is representative of the surrounding radiance reflected off the

upstream endwall. This assumption is seen as reasonable as both upstream hub and case annuli have similar geometry (i.e. similar view factor with respect to hub and case endwalls) and reach similar temperature levels during running conditions.

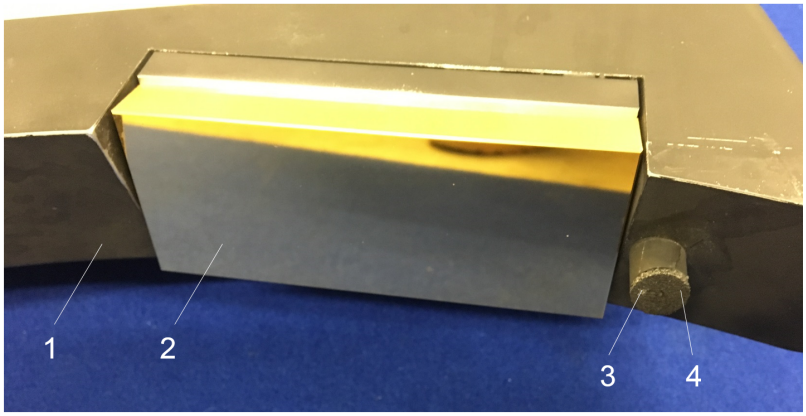


Figure 6.10: Picture of *in-situ* front platform calibration system. (1) instrumentation cassette, (2) gold-coated mirror, (3) Rohacell layer, and (4) surface thermocouple.

Results of surrounding radiance correction function are shown in Figure 6.11 for a high powered run. Surrounding radiance follows a mainstream-like temperature and it is sensitive enough to capture the temperature rise of the facility during heater mesh on, the facility cooling during heater mesh off, and residual heat after air-off. The thermocouple and IR data are manually aligned in time by applying a constant time shift. The low spikes in Figure 6.11 are due to camera refocus during the run.

Surrounding radiance results as a function of $(T_{0m} - T_{0m,0})$ (where $T_{0m,0}$ is the mainstream temperature at initial conditions) for the rear endwall are presented in Figure 6.12 for 70% and 80% of the maximum heater power. Surrounding radiance follows a second order polynomial function with the mainstream temperature. A data correlation is performed to estimate the value of the surrounding radiance for the rear endwall view, based on the mainstream temperature measured at each run (data fitting in Figure 6.12). Separate correlations are used for 70% and 80% heater power.

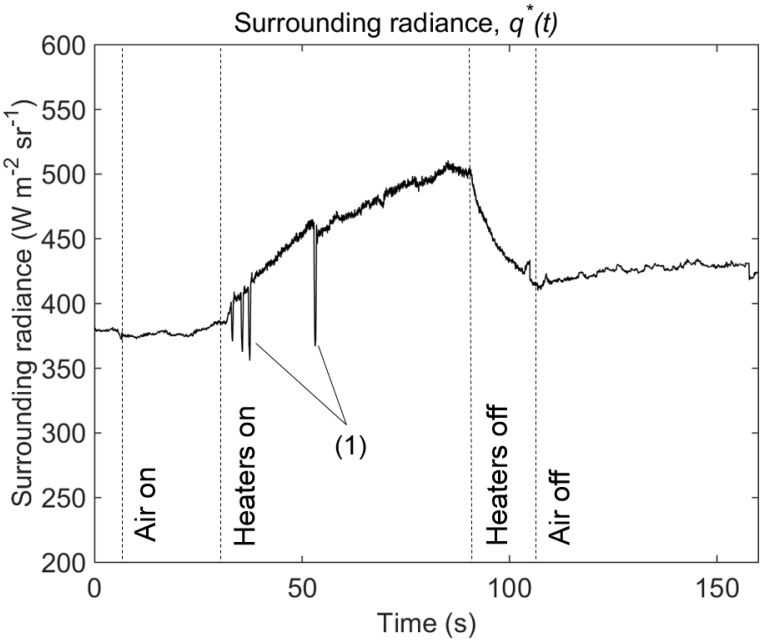


Figure 6.11: Surrounding radiance for a high-powered run (80% heater power settings). (1) camera refocus.

Surrounding radiance results as a function of $(T_{0m} - T_{0m,0})$ for the front endwall are presented in Figure 6.13 for 70% and 80% of the maximum heater power. Similar to the rear endwall, the surrounding radiance measured on the front endwall follows a second order polynomial function with mainstream temperature. Similar procedure involving the data fitting in Figure 6.13, is used to estimate the surrounding radiance based on the mainstream temperature measured at each run. Separate functions are used for 70% and 80% heater power runs.

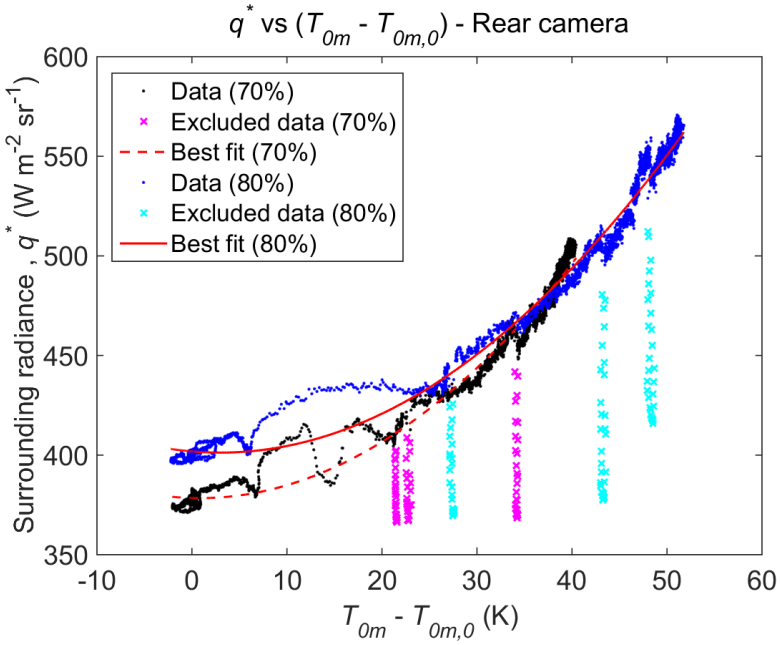


Figure 6.12: Surrounding radiance as a function of mainstream temperature measured on rear endwall, for 70% and 80% heater power runs. Cyan and magenta points are due to camera refocus and therefore excluded from the fitting.

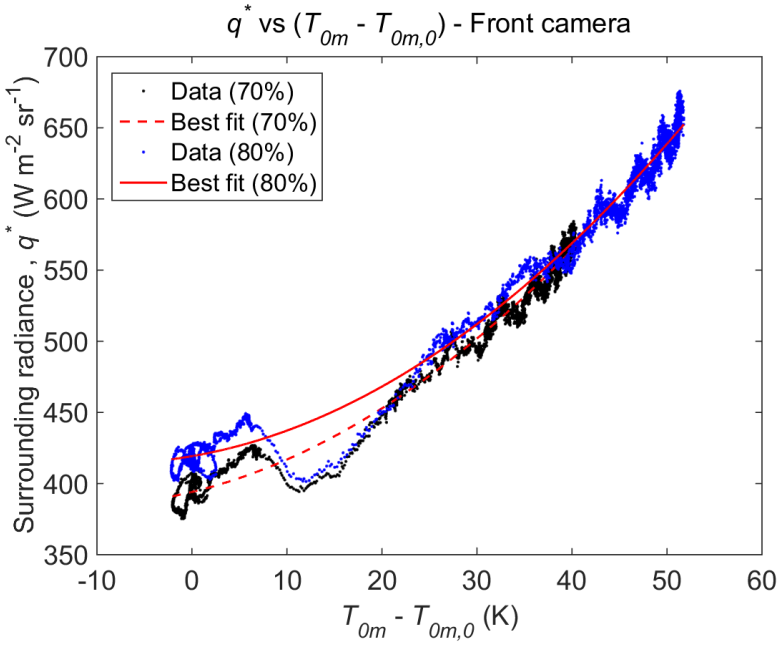


Figure 6.13: Surrounding radiance as a function of mainstream temperature measured on front endwall, for 70% and 80% heater power runs.

6.4.4 Infra-Red hardware

The temperature of the platform was measured by by two FLIR A655sc IR cameras which were situated within the main pressure vessel. Each camera was placed within a protective, pressure-rated box (Figure 6.14), connected to atmosphere via a vent line. The box had a coated Zinc-Selenide window for optical access. The nominal transmittance of the window was 0.97 in the spectral band 7.5–14.0 μm (measured by the manufacturer). The IR cameras were located far upstream of the vanes in order to avoid any potential effect on the aero-thermal performance of the vanes within the field-of-view. The two cameras can be rotated to any circumferential location around the rig annulus.

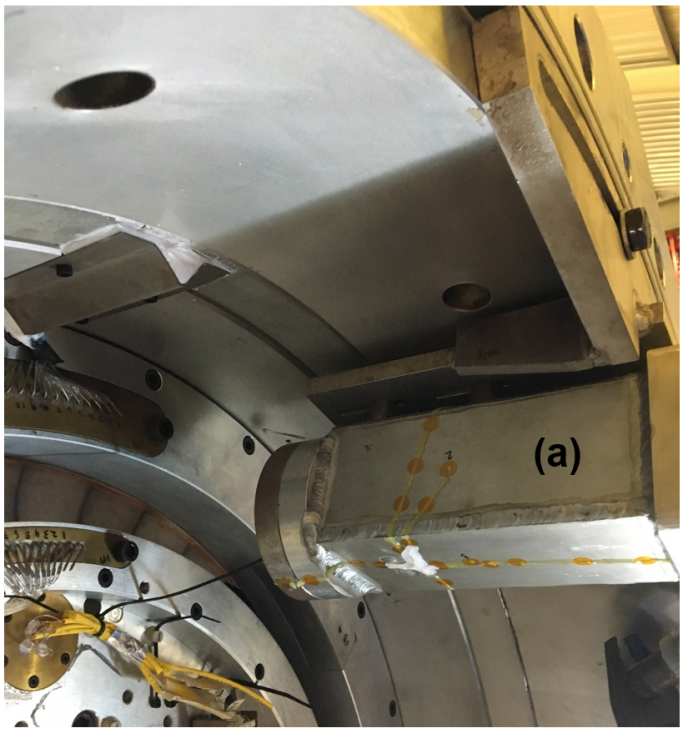


Figure 6.14: Photo of metal box containing the IR camera (a) for vane SS view.

IR raw data were acquired simultaneously from both cameras using FLIR ResearchIR Max software, at a frequency of 50 Hz. The software was also used to set focus position, ambient drift compensation and trigger settings. LabVIEW was used

to simultaneously acquire the signal from pressure and temperature sensors, and to trigger the IR cameras via virtual COM ports.

6.5 Experimental uncertainty

An uncertainty analysis for the measurements of overall cooling effectiveness is now presented. Based on the theory proposed by Moffat (1988), the individual contribution of each measurement to the overall error in the measurement chain is discussed. The overall cooling effectiveness is defined as:

$$\theta \equiv \frac{cT_{0m} - T_w}{T_{0m} - T_{0c}} = \frac{A}{B}, \tag{6.15}$$

where A and B represent the numerator and denominator of Equation 6.15, respectively. T_{0m} is the mainstream total temperature, T_{0c} is the coolant total temperature and T_w is the wall temperature (calculated using Equation 6.11). c is the recovery ratio, defined as:

$$c \equiv \frac{T_r}{T_{0m}}, \tag{6.16}$$

where T_r is the recovery temperature. c is estimated by using data from two runs at the same pressure ratio. This procedure is described later in the text.

In Equation 6.15 we identify two sources of uncertainty: the uncertainty in $B = T_{0m} - T_{0c}$, u_B, and the uncertainty in $A = cT_{0m} - T_w$, u_A. The first one can be estimated by assuming that the uncertainties in the thermocouples measuring T_{0m} and T_{0c} are uncorrelated (i.e. the thermocouples do not come from the same batch of wire). In this case, the bias uncertainty on B is represented by the offset between the two thermocouples readings at isothermal conditions (0.5 K), and the precision uncertainty is represented by the standard deviation on the mean. The latter can be assumed to be small compared to the bias uncertainty when a large number of

samples are averaged.

The second source of uncertainty is determined by the error on both T_{0m} and T_w. The uncertainty on T_w can be estimated by applying the uncertainty propagation theory to Equation 6.11:

$$u_{T_w} = \sqrt{\left(\frac{\partial T_w}{\partial q^*} u_{q^*}\right)^2 + \left(\frac{\partial T_w}{\partial T_{bb}} u_{T_{bb}}\right)^2 + \left(\frac{\partial T_w}{\partial \varepsilon} u_\varepsilon\right)^2}. \tag{6.17}$$

It is therefore necessary to estimate the uncertainty on the measurements of q^*, T_{bb}, and ε. The uncertainty on T_{bb} is estimated by knowing the uncertainty on the black-body calibration (1 K), whereas the uncertainty due to ε is assumed to be small as the emissivity value was estimated in-situ. The uncertainty in q^* can be estimated by performing an error propagation analysis considering Equation 6.12:

$$u_{q^*} = \sqrt{\left(\frac{\partial q^*}{\partial T_{bb,TC}} u_{T_{bb,TC}}\right)^2 + \left(\frac{\partial q^*}{\partial T_{w,TC}} u_{T_{w,TC}}\right)^2 + \left(\frac{\partial q^*}{\partial \varepsilon} u_\varepsilon\right)^2}. \tag{6.18}$$

To solve Equation 6.18, knowledge of the uncertainties due to the black-body temperature measurement at the calibration point $T_{bb}(x_{TC})$, the emissivity ε estimation, and the thermocouple measurement at the calibration point $T_w(x_{TC})$ are required. The first uncertainty can be estimated from the black-body calibration (1 K), the second uncertainty can be assumed to be small, and the third source of uncertainty is the thermocouple uncertainty (1 K). It is therefore possible to perform an error propagation analysis using equation 6.12 and estimate the overall uncertainty in surrounding radiance u_{q^*}.

Finally, knowing the uncertainty in q^* (u_{q^*}) and in T_w (u_{Tw}), the uncertainty in θ (u_θ) can be estimated by performing an error propagation analysis using Equation

6.15:

$$u_\theta = \sqrt{\left(\frac{\partial\theta}{\partial A}\right)^2 u_A^2 + \left(\frac{\partial\theta}{\partial B}\right)^2 u_B^2} = \sqrt{\left(\frac{1}{B}\right)^2 u_A^2 + \left(-\frac{1}{B^2}\right)^2 u_B^2}. \tag{6.19}$$

Results of absolute uncertainty in overall cooling effectiveness are shown in Figure 6.15 as a function of the temperature ratio T_{0m}/T_{0c} and overall cooling effectiveness. The uncertainty in overall effectiveness u_θ is around 0.035 for the nominal temperature ratio, and approximately insensitive to the value of θ.

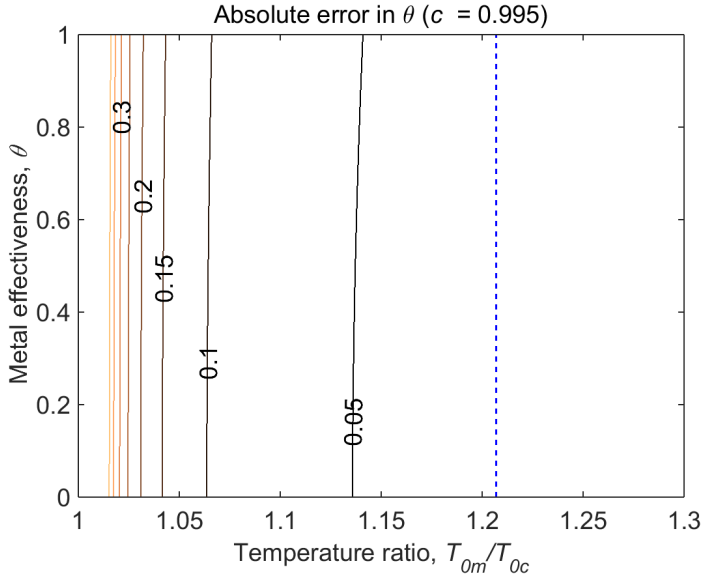


Figure 6.15: Uncertainty in overall cooling effectiveness u_θ as a function of temperature ratio and θ, for a recovery ratio $c = 0.995$.

6.6 Experimental test matrix

Surface temperature data for both upstream and downstream endwalls were acquired at three pressure ratios, for three designs (baseline vane, ARP1-1, and ARP1-2 design). Each run was repeated for two values of the mainstream heater power (70% and 80% of the maximum heater power) to determine the overall cooling effectiveness with the procedure described in later in the text. This involved a total number of 18 useful runs for completing the entire experimental campaign. Table 6.1 reports the

experimental test matrix for the platform cooling tests of this chapter.

Design	**RUN**	**Heater Power (%)**	**Pressure ratio**	**Field-of-view**
ARP1-1	1	70	1.01	Hub front+rear
	2	80		
	3	70	1.02	
	4	80		
	5	70	1.03	
	6	80		
ARP1-2	7	70	1.01	Hub front+rear
	8	80		
	9	70	1.02	
	10	80		
	11	70	1.03	
	12	80		
Baseline	13	70	1.01	Hub front+rear
	14	80		
	15	70	1.02	
	16	80		
	17	70	1.03	
	18	80		

Table 6.1: Experimental test matrix.

6.7 Coolant capacity test results

A coolant capacity leak test or *dynamic leak test* was performed to evaluate the coolant discharge characteristic for both hub and case systems. A blow-down test was run by charging both hub and case lines and blowing air though the vane cooling system. This allowed to obtain a large variation of the coolant-to-mainstream pressure ratio and characterize hub and case coolant capacities.

Results of the dynamic leak test were compared to a previous build to understand the changes introduced by the implementation of the new vane test section. Figure 6.16 depicts the results of the dynamic leak test for two builds: a previous build commissioned in 2016, and the new build (commissioned in 2018). The latter differs from

the 2016 build only in that three vane pairs are replaced by the laser-sintered vanes designed in the previous chapter. It is worth mentioning that the 2016 build includes a number perforated plates to restrict the flow issued through the vane case. These plates are not included in the three laser-sintered vanes of the new build, and hub and case plena communicates via a larger through-hole area. The effect of the absence of perforated plates can be observed in Figure 6.16. In particular, we observe that the case capacity curve is shifted downwards and the hub capacity curve is shifted upwards for the present build. This can be explained by the fact that the larger through-flow area leads to a rebalance of the total pressure across hub and case cavities. This effect is also observed in Figure 6.17, where the pressure difference between hub and case cavities is plotted as a function of coolant-to-mainstream pressure ratio. The latter is presented as $(p_{0h} + p_{0h})/2p_{0m}$, where m refers to mainstream conditions. Two runs from the previous build (red and black lines) show higher pressure difference across case and hub cavities compared to the new build (blue line), indicating that the there is a total pressure rebalancing across the plena. In summary—for given coolant mass flow rates—a larger through-flow area leads to increased total pressure in the case cavity and decreased total pressure in the hub cavity, and therefore to an increase in hub coolant capacity and a decrease in case coolant capacity.

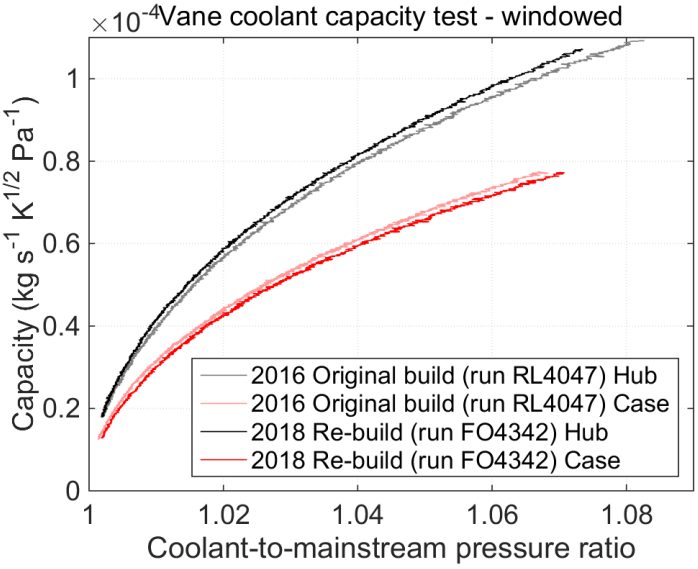


Figure 6.16: Dynamic leak test results for previous build (red and black lines) and new build (blue line).

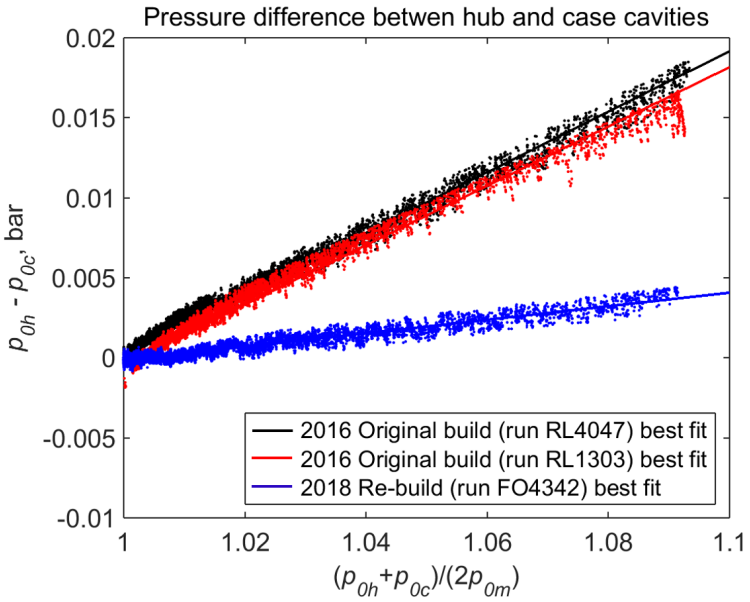


Figure 6.17: Comparison of hub and casing plena pressure difference between the previous build (red and black lines) and the new build (blue line).

6.8 Test conditions

Typical test conditions are presented in Figure 6.18, where vane exit Mach number and vane coolant-to-mainstream pressure ratios are plotted as a function of time during a run. The vane exit Mach number can be set to match the engine value ($M_2 \sim 0.92$) over a specific time window during the run by adjusting the upstream total pressure through the pressure regulator located on the main feed line. Coolant-to-mainstream pressure ratio can be adjusted to the desired value by selecting the correct chocked nozzles on both hub and casing coolant lines. Figure 6.18 shows the time-varying ratio between hub coolant total pressure and mainstream pressure ($p_{0c,hub}/p_{0m}$), case coolant total pressure and mainstream pressure ($p_{0c,case}/p_{0m}$), and the average between these two values ($p_{0c,ave}/p_{0m}$).

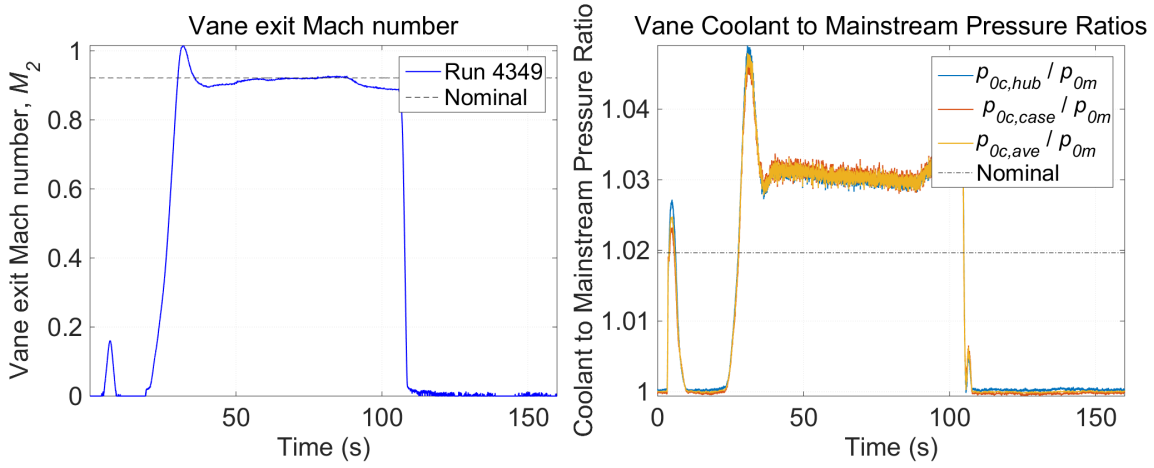


Figure 6.18: Example of ECAT test conditions for a typical run.

6.9 Description of the field-of-view

The vane pressure side view—referred in this chapter as *front* or *upstream* platform view—is depicted in Figure 6.19. A number of regions are marked in the figure to aid interpretation of the overall effectiveness results reported later: (1) hub film cooling holes; (2) leading vane leading edge; (3) trailing vane leading edge; (4) infra-red mirror

boundaries; (5) trailing vane PS fillet; (6) leading vane PS fillet; (7) pressure side thermocouple; (8) trailing vane of neighbouring vane pair; (9) pressure side platform junction; (10) suction side platform junction.

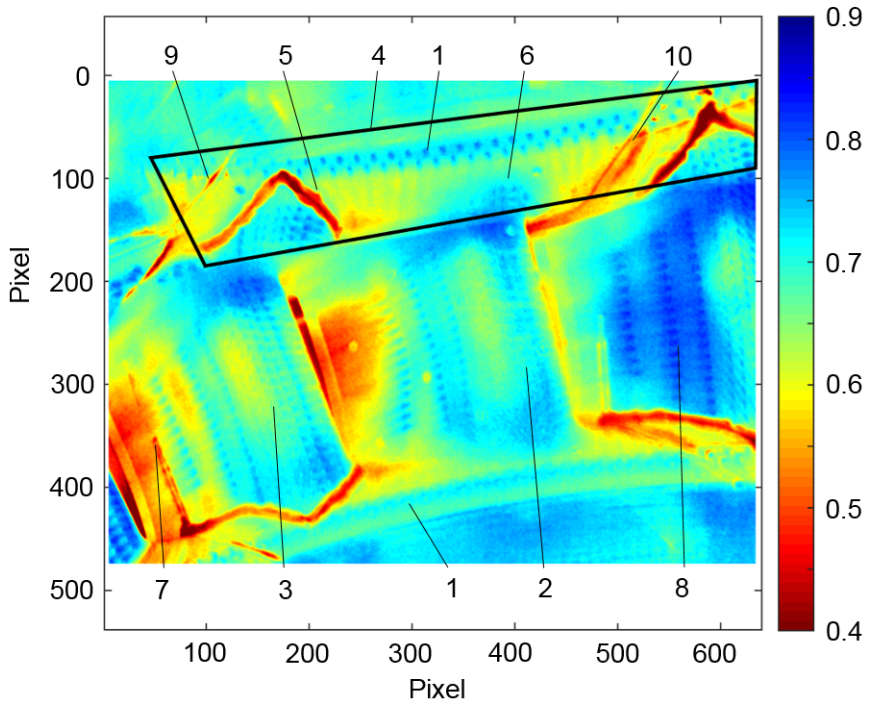


Figure 6.19: Front platform field-of-view (upstream IR camera).

The vane suction side view—referred in this chapter as *rear* or *downstream* platform view—is depicted in Figure 6.20. A number of regions is marked in the figure to aid interpretation of the overall effectiveness results reported later: (1) hub platform edge; (2) leading vane trailing edge; (3) trailing vane trailing edge; (4) leading vane SS fillet; (5) trailing vane SS fillet; (6) suction side thermocouple; (7) infra-red mirror boundaries.

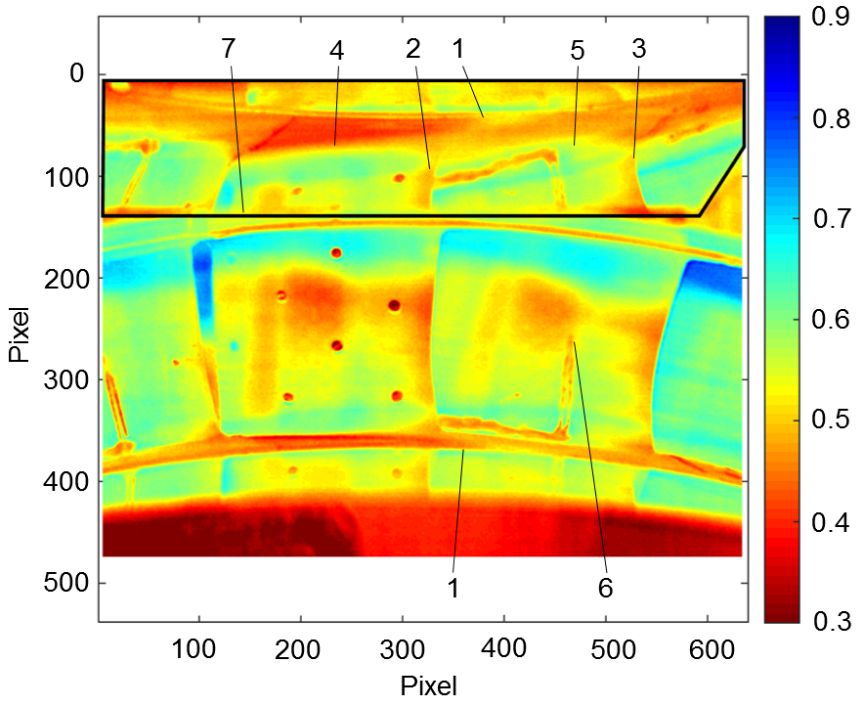


Figure 6.20: Rear platform field-of-view (downstream IR camera).

6.10 Overall cooling effectiveness results

In this section, the impact of coolant-to-mainstream pressure ratio and platform cooling arrangement on the overall cooling effectiveness is presented and discussed in detail.

The external temperature of the endwall is non-dimensionalized in terms of overall cooling effectiveness θ. The latter is defined as:

$$\theta \equiv \frac{cT_{0m} - T_w}{T_{0m} - T_{0c}}, \tag{6.20}$$

where T_{0m} is the mainstream total temperature, T_{0c} is the coolant total temperature, T_w is the external wall temperature measured by infra-red thermography, and c is the recovery ratio. The latter is defined as: $c = T_r/T_{0m}$, where T_r is the recovery temperature. T_r is lower than the mainstream total temperature for Prandtl numbers

$Pr < 1$ because the wall-normal heat conduction is higher than viscous heating within the thermal boundary layer for high Mach number flows. The recovery temperature is a function of the mainstream Mach number and a recovery factor r:

$$T_r = T_{0m} \frac{1 + r\frac{\gamma-1}{2}M^2}{1 + \frac{\gamma-1}{2}M^2}, \tag{6.21}$$

where r is commonly defined equal to $r = Pr^{1/2}$ for laminar flows and $r = Pr^{1/3}$ for turbulent flows.

The mainstream temperature recovery ratio $c = T_r/T_{0m}$ is matched between engine and rig because the external Mach number distribution, recovery factor and ratio of specific heats are approximately matched at engine and rig conditions. c is independent of the temperature and mainly dependent on the external aerodynamic boundary layer (Kirollos 2016). Therefore, the recovery ratio is influenced by the film cooling injection and function of the coolant-to-mainstream pressure ratio p_{0c}/p_{0m}.

We can therefore assume that the recovery ratio is only function of the pressure ratio; as a result, for a test i:

$$c_i \left(\frac{T_{0m,i}}{T_{r,i}} \right) + \theta_i \left(\frac{T_{0c,i} - T_{0m,i}}{T_{w,i}} \right) = 1. \tag{6.22}$$

It is not possible to estimate both c and θ from a single run. However, their value can be obtained by running two tests with similar pressure ratio, though at different mainstream temperature. In this way, Equation 6.22 becomes a system of two equations in two unknowns and can be solved for c and θ.

6.10.1 Effect of coolant-to-mainstream pressure ratio

We now compare results of overall cooling effectiveness as a function of coolant-to-mainstream pressure ratio for the baseline case, ARP1-1 design, and ARP1-2 design. The impact of different cooling arrangements is also discussed. The attention is drawn

to the endwall temperature field and endwall flows. Discussion of results concerning vane pressure side and suction side is outside the scope of this thesis and will be not reported for brevity.

6.10.1.1 Baseline design

Figure 6.21a shows the overall cooling effectiveness field for pressure side and upstream hub endwall view for a pressure ratio of 1.01. The overall IR camera field of view is presented in the figure, including the mirror outline marked with a black line. The view in the mirror includes approximately 2.0 passages from the LE fillet of the trailing vane belonging to the central vane pair to the LE fillet of the neighbouring vane pair. There is trace of the thermocouple wires wrapping around the vane LE on the left hand side of the figure (see Figure 6.19 to aid interpretation). We focus the attention on the central vane passage (called *closed passage*). To aid interpretation of the results, we define the right hand side vane on the closed passage as *leading vane*, and the left hand side vane as *trailing vane* (see Figures 6.19 and 6.20). Film traces are visible downstream the hub (RIDN) holes and characterized by a relatively high value of overall effectiveness. The overall effectiveness rapidly decays along the vane axial coordinate due to mixing with the mainstream flow. There is no evidence of jet lift-off. In fact, this is expected for a low-momentum flux case (i.e. low coolant-to-mainstream pressure ratio), in which the jets do not carry enough momentum to penetrate into the mainstream. We also observe a relatively low overall effectiveness ($\theta = 0.6$) region around the mid portion of the endwall close to the trailing vane suction side. Here, the films are pushed towards the vane SS by the mainstream flow due to the cross-passage pressure gradients. However, this effect is rather weak and the upstream endwall is generally well cooled even for this low value of pressure ratio. This result is in line with some of previous unpublished work carried at ECAT for the same engine hardware, in which effects of secondary flows and subsequent film

disruption were observed only at pressure ratios below 1.00.

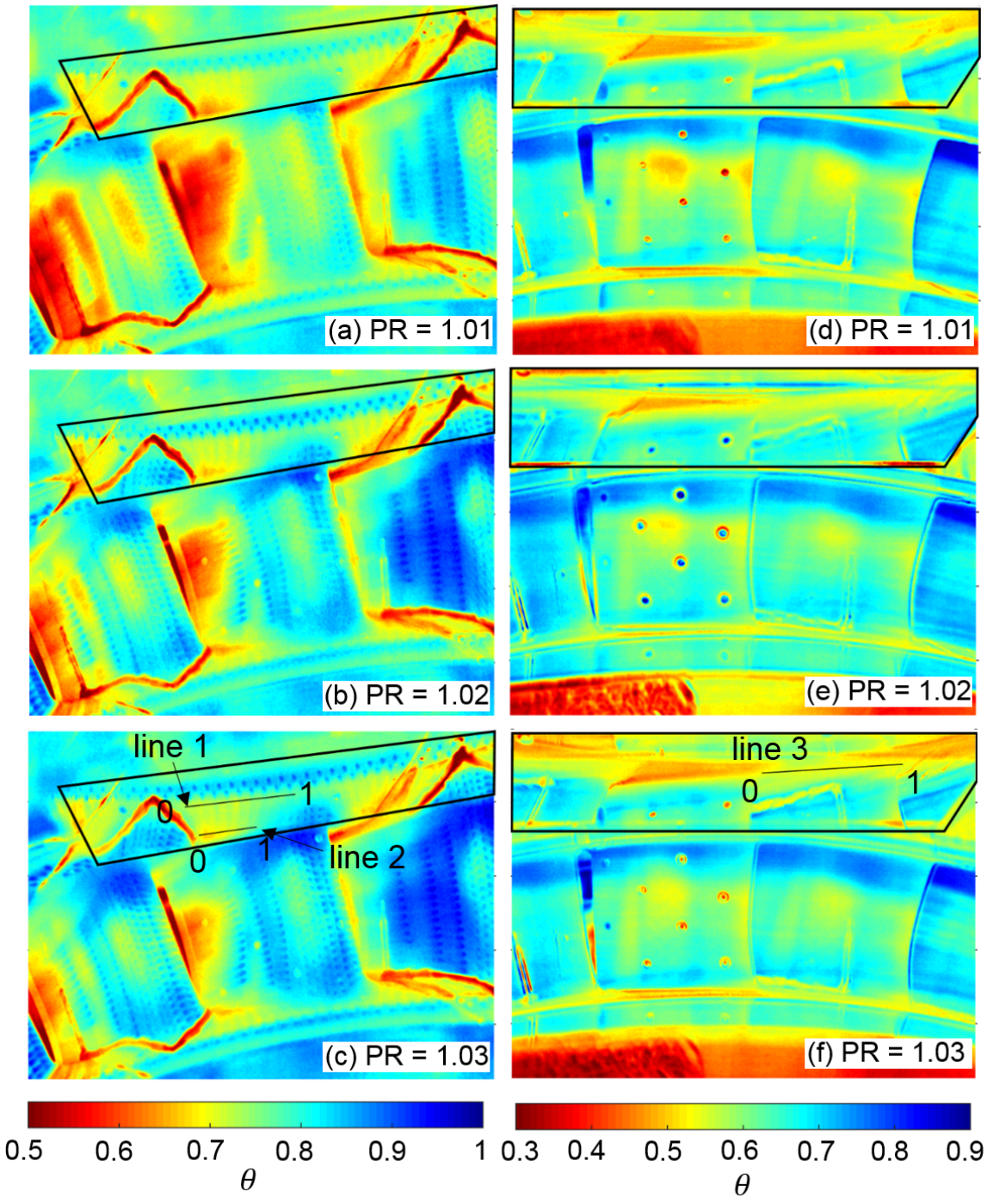


Figure 6.21: Overall cooling effectiveness distribution on upstream endwall (a–c), and downstream endwall (d–f) at various pressure ratios for the baseline design.

Figure 6.21b shows the overall cooling effectiveness field for PR = 1.02. At this

PR, we observe an increase in overall effectiveness in the region close to the hub holes. The region immediately downstream the holes shows an improved coverage and higher overall effectiveness compared to the the case with PR = 1.01. In addition, the hot region taking place approximately at mid-passage is now reduced. This is explained by considering the nature of ballistic cooling, in which the jets issued from the endwall holes aim to cool the platform further downstream by following a long trajectory before impinging the endwall. Improved overall effectiveness is also observed on the vane LE region due to increased pressure ratio and therefore increased blowing ratio.

Figure 6.21c depicts the overall cooling effectiveness distribution for PR = 1.03. Lines 1 and 2 used for data post-processing are also indicated in the figure. Line 1 is located just downstream the second row of holes and runs from the LE suction side (where the normalized coordinate is equal to 0) to the LE pressure side (where the normalized coordinate is equal to 1). Line 2 is located approximately on the mid-platform region and runs from the LE suction side (0) to the LE pressure side (1). For this value of PR (i.e. PR = 1.03), we observe further improved overall cooling effectiveness on both downstream of the cooling holes (where now the overall effectiveness is above 0.7) and the mid-platform region. In fact, at this PR, the hot spot is substantially reduced. Interestingly, there is no evidence of dramatic jet-lift off downstream the second row of holes and the overall cooling effectiveness seems to follow a monotonic trend within the tested range of pressure ratio.

In summary, the overall effectiveness on the front platform, increases monotonically with increasing pressure ratio. In addition, there is no clear evidence of jet lift-off for the tested pressure ratio range.

Figure 6.21d shows the overall cooling effectiveness field for suction side and downstream endwall views for a pressure ratio of 1.01. The overall IR camera field of view is presented in the figure, including the mirror outline marked with a black line. The view in the mirror includes approximately 2.0 passages from the SS fillet of the neigh-

bouring left hand side vane pair to the SS fillet of the neighbouring right hand side vane pair. There is evidence of the thermocouple wire on the trailing vane SS. The region of interest is the central vane passage (called *closed passage*).

At a pressure ratio of 1.01, we observe a rather uniform overall cooling distribution on the exit region, with a slightly lower overall effectiveness observed on the leading vane SS fillet. This hot region may be due to film disruption and consequent flow separation downstream of the step in between two platforms. The region downstream the central vane shows an approximately uniform overall effectiveness distribution of around 0.55.

At higher coolant-to-mainstream pressure ratios (PR = 1.02 and 1.03), depicted in Figures 6.21e and 6.21f, the overall effectiveness is not improved further, showing similar distributions to the case with PR = 1.01. The overall cooling effectiveness is rather insensitive to variations in pressure ratio in the rear portion of the endwall primary due to the local flowfield being highly mixed in this region.

To aid interpretation of results of Figures 6.21a–f, the mirror views for both upstream and downstream endwalls are isolated in Figures 6.22a–c (front endwall), and Figures 6.22d–f (rear endwall). All the regions lying outside the mirror boundaries are also reported in gray-scale for the same purpose.

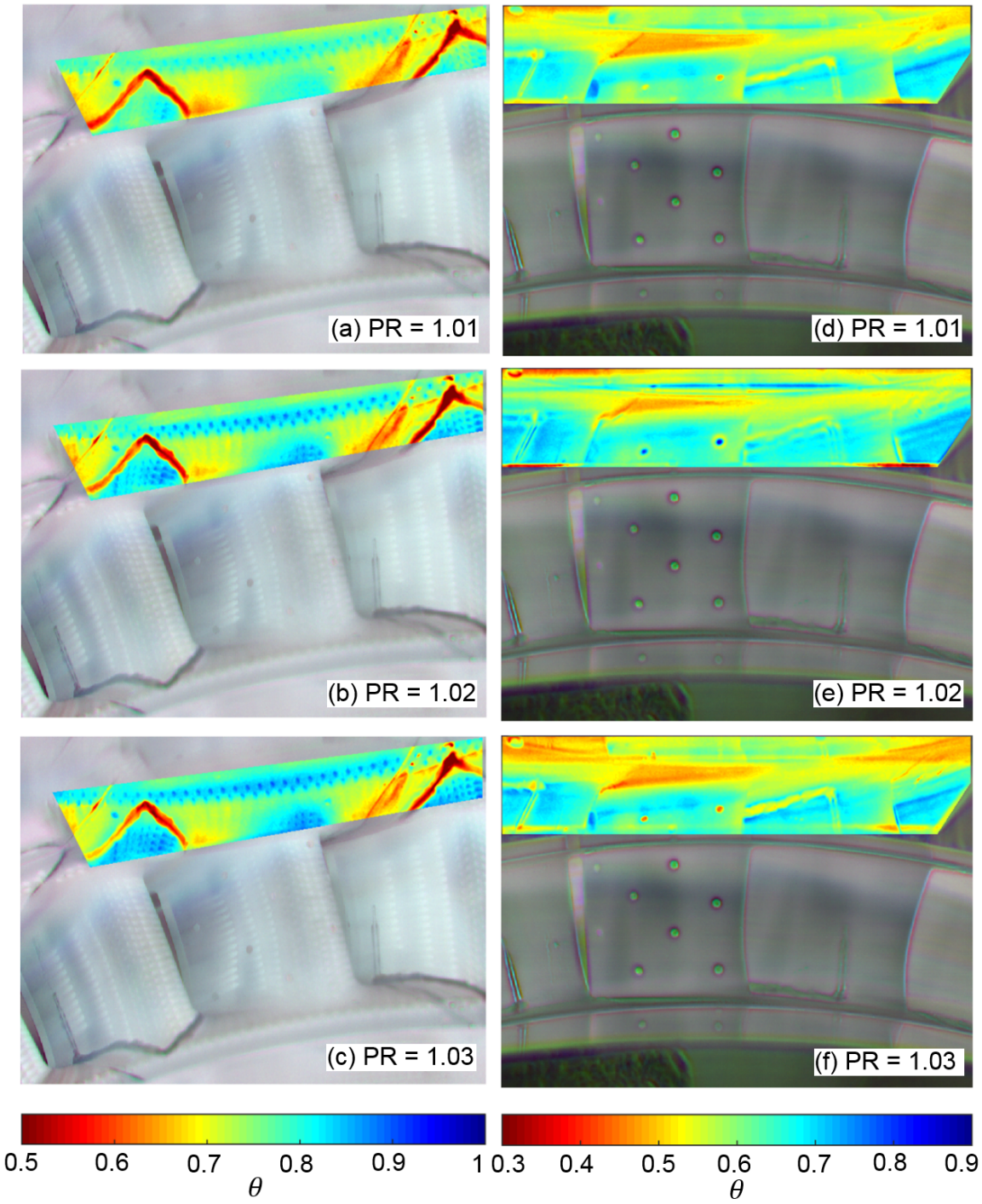


Figure 6.22: Overall cooling effectiveness distribution on upstream endwall (a–c), and downstream endwall (d–f) at various pressure ratios for the baseline design.

Figure 6.23a depicts the overall effectiveness distribution on line 1 (i.e. downstream the second row of cooling holes) for the baseline case, and for three coolant-

to-mainstream pressure ratios (PR = 1.01, 1.02, and 1.03).

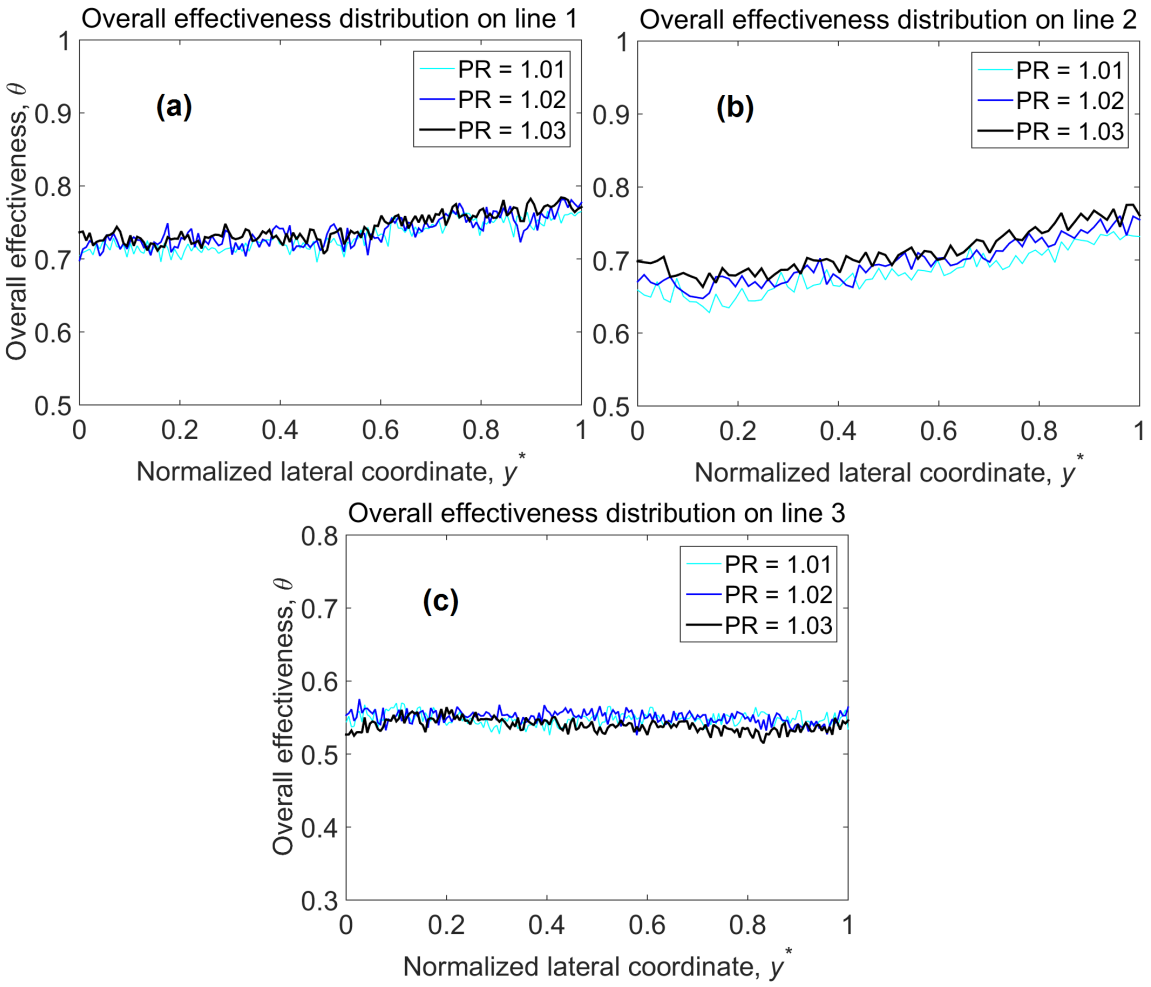


Figure 6.23: Overall effectiveness distribution (baseline design) on lines 1, 2, and 3 for PR = 1.01, 1.02, and 1.03.

On this line, the lateral distribution of overall effectiveness is rather uniform, with values between $\theta = 0.7$ (on the vane LE SS of the central passage) and $\theta = 0.77$ (on the vane LE PS of the central passage). The coolant-to-mainstream pressure ratio has a small impact in this region, though the overall effectiveness takes slightly higher values for increasing PR. As observed in Figure 6.21a–c, there is almost no evidence of jet lift-off for these values of the pressure ratio.

On line 2 (Figure 6.23b), the effect of PR is more evident, with improved overall effectiveness distribution for increasing pressure ratio. The case with lowest pressure

ratio (PR = 1.01) takes a value of approximately $\theta = 0.65$ on the vane LE SS and a value of approximately $\theta = 0.75$ on the vane LE PS. The case with highest PR (PR = 1.03) takes a value of approximately $\theta = 0.70$ on the vane LE SS and $\theta = 0.77$ on the vane LE PS. The cooling effectiveness increases monotonically with PR in at this line because the jets become more effective further downstream into the platform for higher momentum fluxes—in fact, the jets reattach around 30% of the vane axial chord—leading to improved cooling effectiveness in this region (see Figure 6.22a–c).

Results on line 3 (i.e. at the vane exit) are depicted in Figure 6.23c. Here, we observe relatively small influence of PR on the overall effectiveness (see also results of Figure 6.21a–c). This can be attributed to the flowfield at the vane exit being fully mixed and hence less sensitive to the coolant-to-mainstream pressure ratio (and therefore to the bulk momentum flux ratio).

6.10.1.2 Reverse-passed ARP1-1 design

Figure 6.24a depicts the PS and upstream endwall views for the ARP1-1 design for a pressure ratio PR = 1.01. In the figure, the mirror boundaries are marked with a black line. The field of view includes approximately 2.0 passages, from the left hand side *open passage*—i.e. the passage where two platforms are linked together—to the right hand side open passage. There is trace of the thermocouple leads running on the PS of the trailing vane belonging to the central vane pair. At PR = 1.01, the front region of the endwall shows a uniform overall effectiveness distribution, with good film coverage. In fact, the hot region registered for the baseline case at the same pressure ratio is now completely suppressed. This result is achieved by the combination of two factors: the improved guidance of the internal flow due to the reverse-pass channel—and therefore enhanced internal HTC—and the reduced jet momentum flux due to increased internal pressure loss. These effects jointly contribute to (i) improved film coverage and (ii) enhanced coolant heat pick-up through the platform.

For pressure ratios of PR = 1.02 and PR = 1.03 (Figure 6.24b and c), the overall effectiveness is further improved on the front endwall, with increased level of uniformity. Here, θ is higher than 0.7 for PR = 1.02 and 0.75 for PR = 1.03. The overall effectiveness increases monotonically with increasing pressure ratio on the upstream endwall. No jet lift-off is observed even at high momentum flux ratios. This result is perhaps expected as design ARP1-1 operates at higher pressure loss introduced by the internal cooling system with consequent reduced total pressure at the cooling hole inlet.

Figure 6.24d shows the overall effectiveness distribution on the downstream endwall for the design ARP1-1 at PR = 1.01. The overall IR camera field of view is presented in the figure, including the mirror outline marked with a black line. The view in the mirror includes approximately 2.5 passages, from the SS fillet of the neighbouring left hand side open passage to the SS fillet of the neighbouring right hand side open passage. We focus the attention to the exit region of the central passage (called *closed passage*). Compared to Figure 6.24d (downstream platform view for baseline design at PR = 1.01), we observe a slightly reduced overall effectiveness downstream of the central vane passage (i.e. the reverse-passed vane passage). This result may be explained by a change in mass flow rate between the baseline case and the reverse-pass design. In fact, internal pressure loss and change in the local discharge coefficient might have caused a reduction of the coolant mass flow rate, leading to the worsening of the overall effectiveness in the platform exit region. Although there is some reasonableness in this argument, it is not fully supported by all of the evidence. This effect is believed to require further investigation.

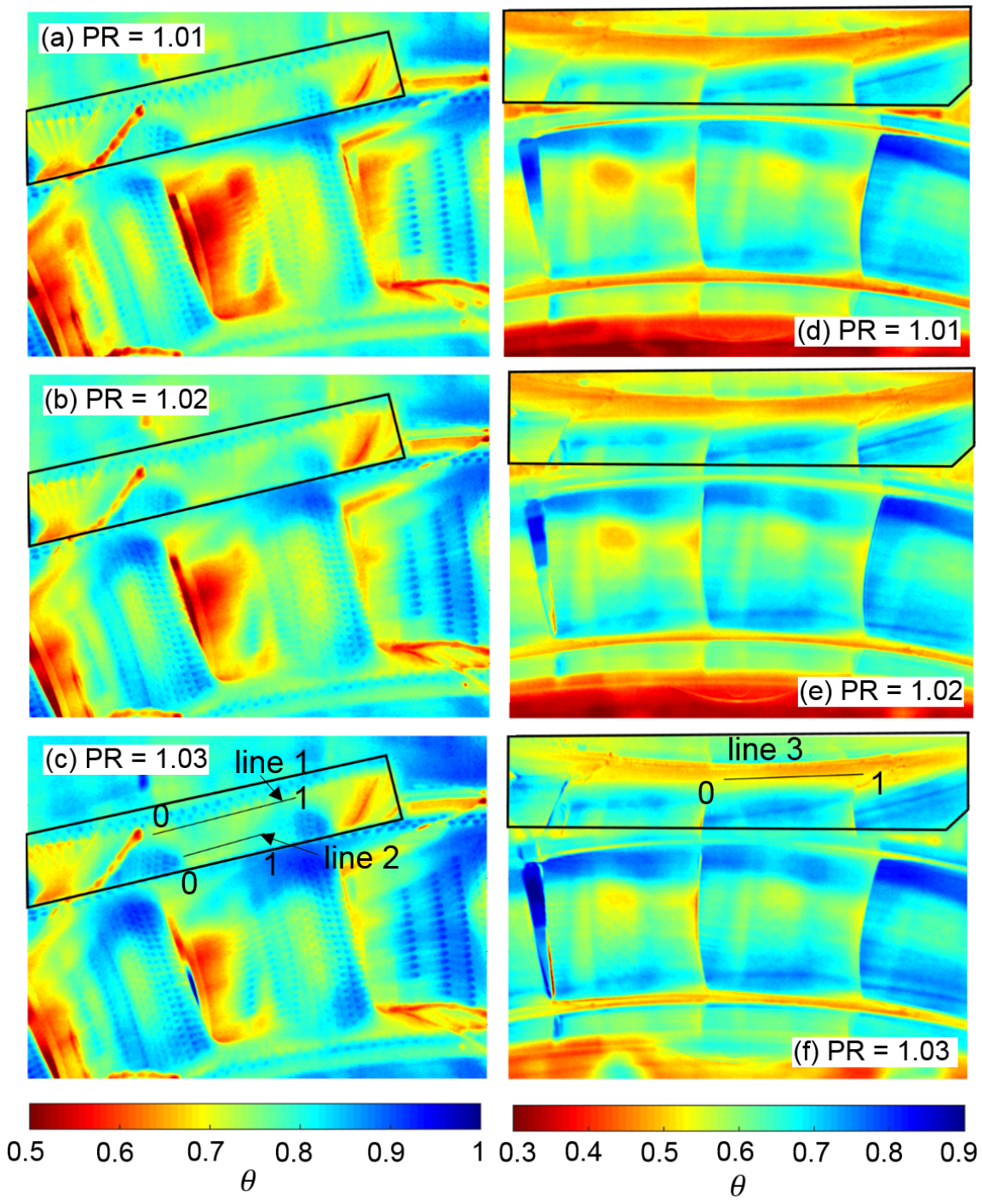


Figure 6.24: Overall cooling effectiveness distribution on upstream endwall (a–c), and downstream endwall (d–f) at various pressure ratios for the ARP1-1 design.

For the cases with PR = 1.02 and 1.03 (Figures 6.24e and 6.24f), the overall effectiveness at the vane exit increases monotonically with pressure ratio. In fact,

the improved cooling performance observed on the upstream endwall for increasing pressure ratios consequently leads to an improved film coverage at the vane exit. This effect may be due to the fact that the *ballistic* nature of the jets is affected by the internal cooling system, which now operates at a lower coolant-to-mainstream momentum flux ratio. The latter directly affects the trajectory of the jets with consequent early reattachment point.

In summary, for the ARP1-1 design (which includes a reverse-pass platform arrangement on the central vane passage), we observe a monotonic increase in overall effectiveness with pressure ratio for both front and rear endwall regions. We also register a reduction in overall effectiveness on the downstream endwall when compared to the baseline design for similar pressure ratios.

To aid interpretation of results of Figures 6.24a–f, the mirror views for both front and rear endwalls are isolated in Figures 6.25a–c (upstream endwall), and Figures 6.25d–f (downstream endwall). All the regions lying outside the mirror boundaries are also reported in grey-scale for the same purpose.

Figure 6.26a depicts the overall effectiveness distribution on line 1 (marked in Figure 6.24c) for the ARP1-1 design. Line 1 is located downstream the second row of cooling holes and runs from the trailing vane LE SS (where the local normalized lateral coordinate is $y^* = 0$) to the leading vane LE PS (where $y^* = 1$). At this line, the pressure ratio has a small effect on the distribution of θ, with minimum $\theta = 0.7$. Maximum overall effectiveness value of $\theta = 0.8$ is observed at $y^* = 0.2$. For the pressure ratio range PR = 1.01–1.03, there is no evidence of jet lift-off. This result is in agreement with the argument that—for a reverse-passed design—the jets are expected to lift-off at higher values of the feed coolant pressure due to pressure loss through the endwall cooling system.

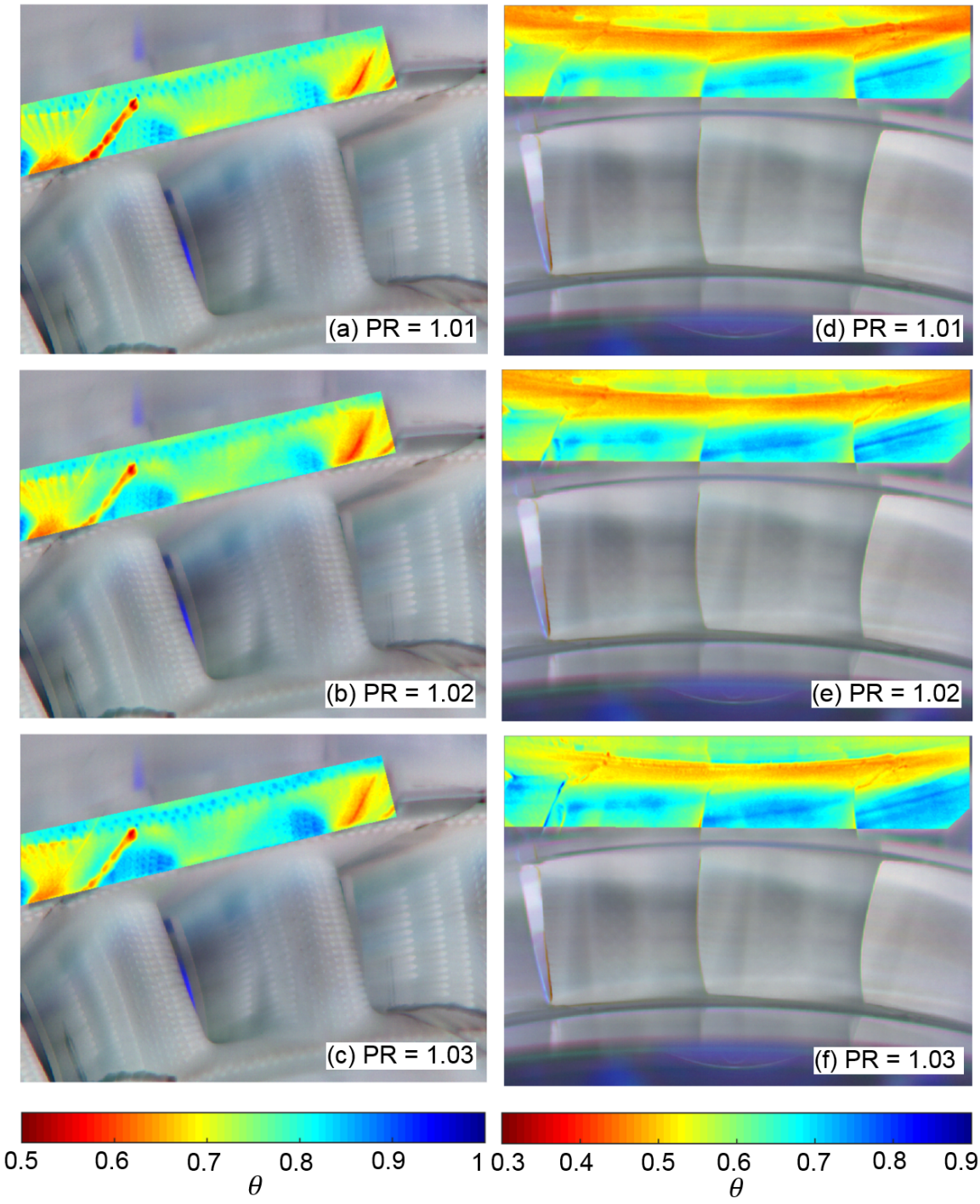


Figure 6.25: Overall cooling effectiveness distribution on upstream endwall (a–c), and downstream endwall (d–f) at various pressure ratios for ARP1-1 design.

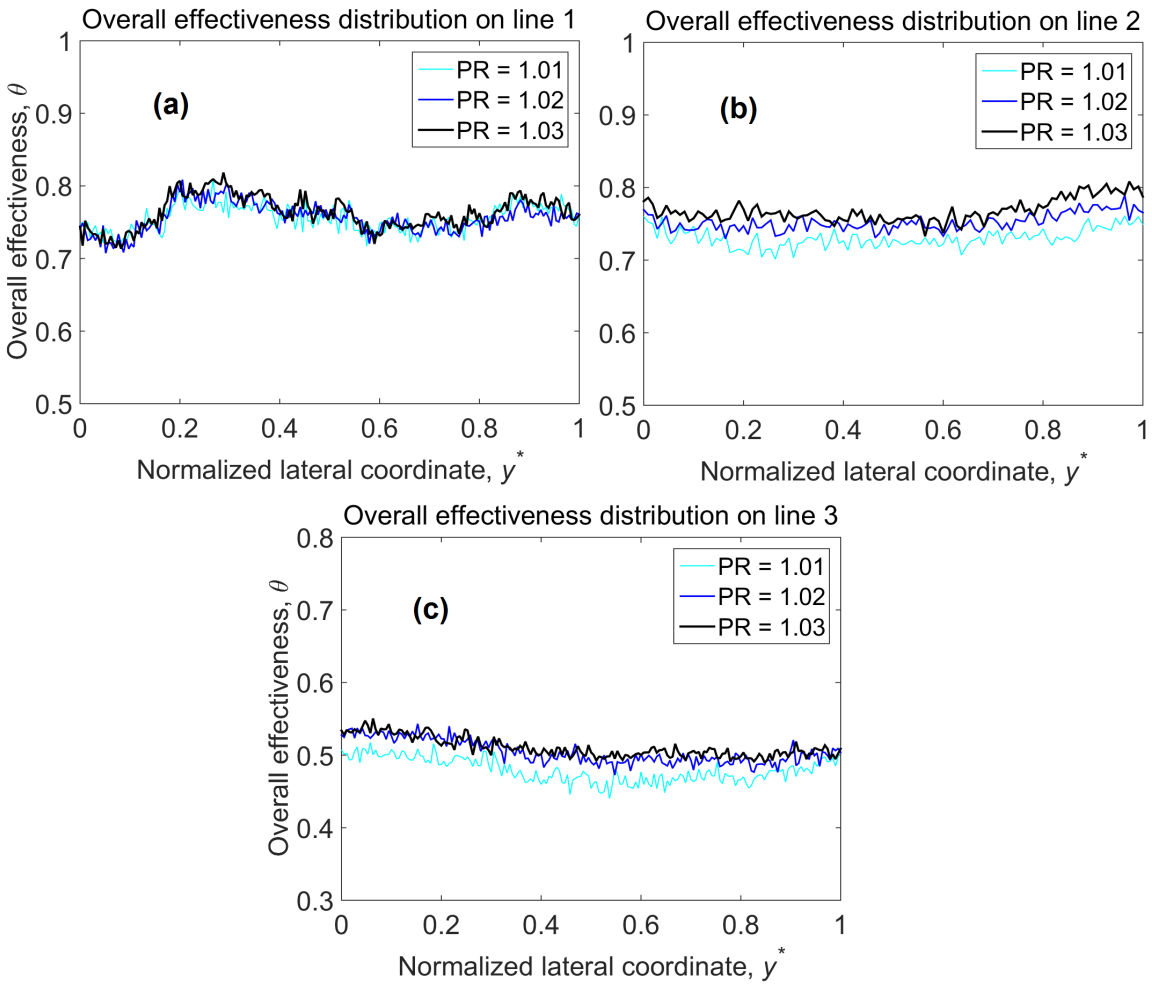


Figure 6.26: Overall effectiveness distribution (ARP1-1 design) on lines 1, 2, and 3 for PR = 1.01, 1.02, and 1.03.

Figure 6.26b depicts the overall effectiveness distribution on line 2 (marked in Figure 6.24c) for the ARP1-1 design. Line 2 is located at approximately mid-chord and runs from the trailing vane SS (where the local normalized lateral coordinate is y^* = 0) to the leading vane PS (where y^* = 1). At this line, we observe a dependency of overall effectiveness on pressure ratio, with higher cooling performance registered for increasing PR. The lateral distribution is rather uniform for all PRs, and uniformly increases by $\Delta\theta = 0.07$ from PR = 1.01 to PR = 1.03. Similar behaviour is observed on the baseline case (see Figure 6.23b) and will be discussed in the context of different cooling arrangements later in the text.

Figure 6.26c depicts the overall effectiveness distribution on line 3 (marked in Figure 6.24e) for the ARP1-1 design. Line 3 runs from the leading vane TE (where the local normalized coordinate is $y^* = 0$) to the trailing vane TE (where $y^* = 1$). The overall effectiveness values are below $\theta = 0.5$ for a pressure ratio PR = 1.01. Overall effectiveness increases for increasing pressure ratio and reaches an approximately uniform value around $\theta = 0.55$ for PR = 1.03.

In general, the ARP1-1 shows relatively high cooling performance on both line 1 and line 2, where θ is above 0.7 along the entire normalized lateral coordinate. On line 2, there is strong dependency of θ on pressure ratio due to improved cooling coverage and jet behaviour in this region. At the vane exit line, we observe a dependency of θ on pressure ratio, with improved cooling performance for increasing PR.

6.10.1.3 Reverse-passed ARP1-2 design

This section reports the results for the ARP1-2 design. The latter includes a number of film holes through the vane platform trailing edge.

Figure 6.27a depicts the PS and front view for the ARP1-2 design at a pressure ratio PR = 1.01. In the figure, the mirror boundaries are marked with a black line. The field of view includes approximately 2.0 passages, from the left hand side *open passage*—i.e. the passage where two platforms are linked together—to the right hand side open passage. At PR = 1.01, a low effectiveness region is observed on the upstream platform, close to the vane LE-PS region. Local geometrical defects within the internal channel might have caused increased total pressure loss and therefore poor cooling effectiveness at low PR. Hole starvation is in fact observed for the cooling holes close to the LE pressure side, where there is no trace of the films, and the local overall effectiveness is around $\theta = 0.6$.

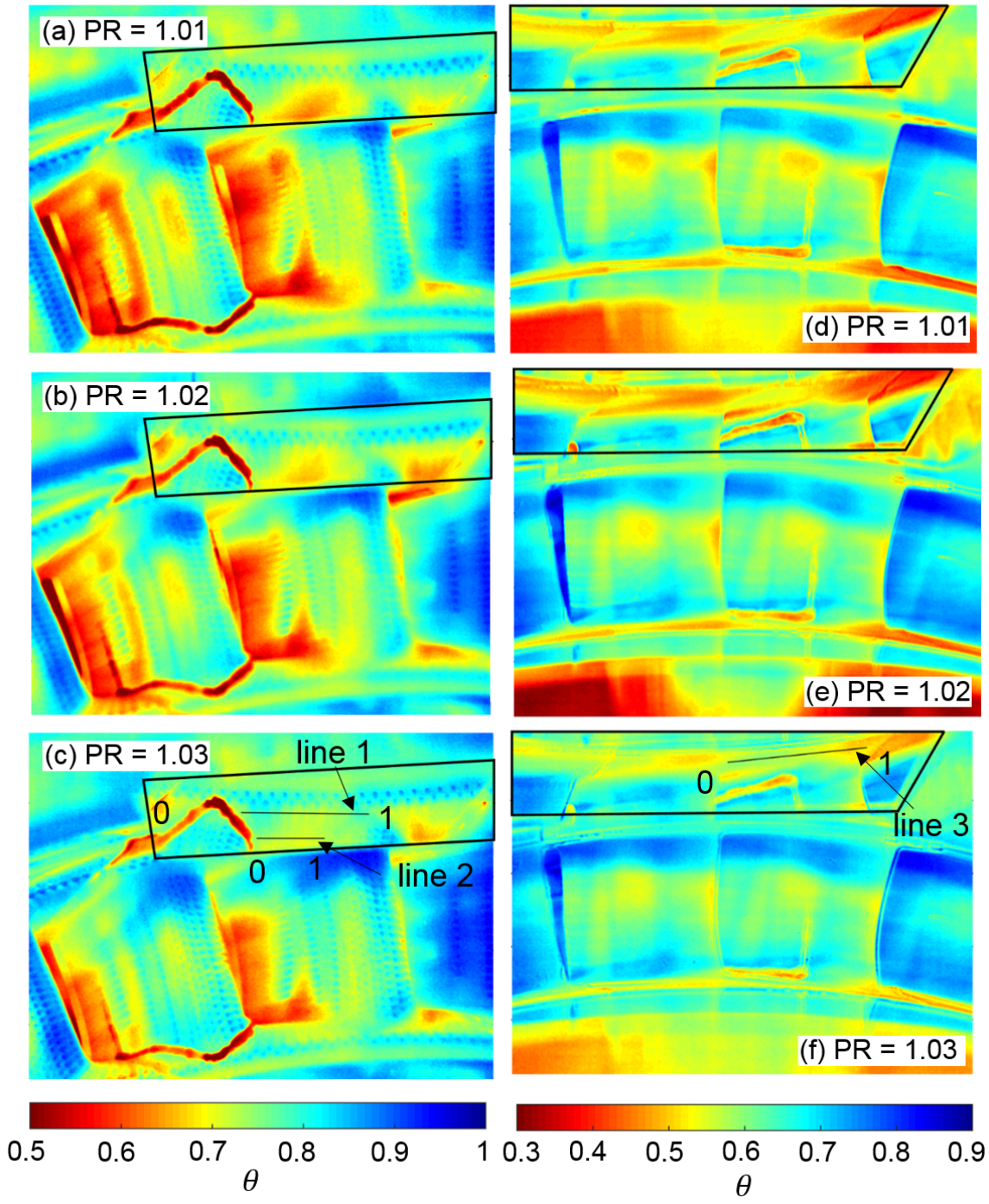


Figure 6.27: Overall cooling effectiveness distribution on upstream endwall (a–c), and downstream endwall (d–f) at various pressure ratios for ARP1-2 design.

Figure 6.27b shows the overall effectiveness contour map for PR = 1.02. At PR = 1.02, the overall effectiveness is improved due to the total pressure excess available

at the cooling hole exit. The hot region is ameliorated, though traces of mainstream gas ingestion are still observed.

Figure 6.27c depicts the overall effectiveness map for PR = 1.03. Lines 1 and 2 used for data post-processing are also indicated in the figure. Line 1 is located just downstream the second row of hub holes and runs from LE suction side (where its normalized coordinate is equal to 0) to LE pressure side (where its normalized coordinate is equal to 1). Line 2 is located at approximately the mid-platform and runs from LE suction side (0) to LE pressure side (1). At PR = 1.03, the total pressure excess is large enough to counterbalance the increased total pressure loss and the entire front platform region appears uniformly cooled for this value of the pressure ratio. Here, θ is in the range $0.7 < \theta < 0.8$.

In summary, the front platform of the ARP1-2 design shows monotonically increasing overall effectiveness with increasing pressure ratio. Relatively poor cooling performance are registered for PR = 1.01 and PR = 1.02, which lead to the generation of a hot region in proximity of the LE-PS of the trailing vane of the closed passage.

Figure 6.27d shows the overall cooling effectiveness field for suction side and downstream hub endwall view for a pressure ratio of 1.01. The overall IR camera field of view is presented in the figure, including the mirror outline marked with a black line. The view in the mirror includes approximately 2.5 passages from the SS fillet of the neighbouring left hand side vane to the SS fillet of the neighbouring right hand side vane. There is trace of a thermocouple lead on the trailing vane SS. We focus the attention on the exit region of the central passage. At a pressure ratio of 1.01, we observe a relatively good coverage downstream the central passage. There is also trace of a low overall effectiveness region on the SS fillet of the leading vane. The latter is most likely due to the influence of the SS horseshoe vortex which, at this axial location, is merged to the PS horseshoe vortex from the adjacent vane—the latter in fact migrates from PS to SS under the effect of the vane pressure gradients. There is

also evidence of a low overall effectiveness region across the platform junction on the neighbouring right hand side vane passage. This is most likely due to flow separation occurring downstream the slash-face gap in between the two platforms.

The overall effectiveness picture on the downstream endwall is rather complex, and at a PR = 1.02 (Figure 6.27e) we observe slightly worsened θ. We find that the effect of secondary flows is strengthened at this pressure ratio, with slightly lower overall effectiveness on both leading vane SS fillet and downstream the slash-face gap. However, the region downstream the closed passage performs with similar overall effectiveness compared to PR = 1.01, indicating that the rim holes are contributing to improve the cooling performance in this region.

At PR = 1.03 (Figure 6.27f), we observe good overall cooling performance, with increased overall cooling effectiveness over the entire downstream platform.

In summary, we observe relatively high overall effectiveness on the downstream endwall of design ARP1-2 (central passage), with increased cooling performance for PR = 1.03. On the other hand, two regions at relatively poor overall effectiveness are observed on both SS fillet of the leading vane and downstream of the slash-face gap between the central vane platform and the right hand side neighbouring vane platform.

To aid interpretation of results of Figures 6.27a–f, the mirror views for both front and rear endwalls are isolated in Figures 6.28a–c (front endwall), and Figures 6.28d–f (rear endwall). All the regions lying outside the mirror boundaries are also reported in grey-scale for the same purpose.

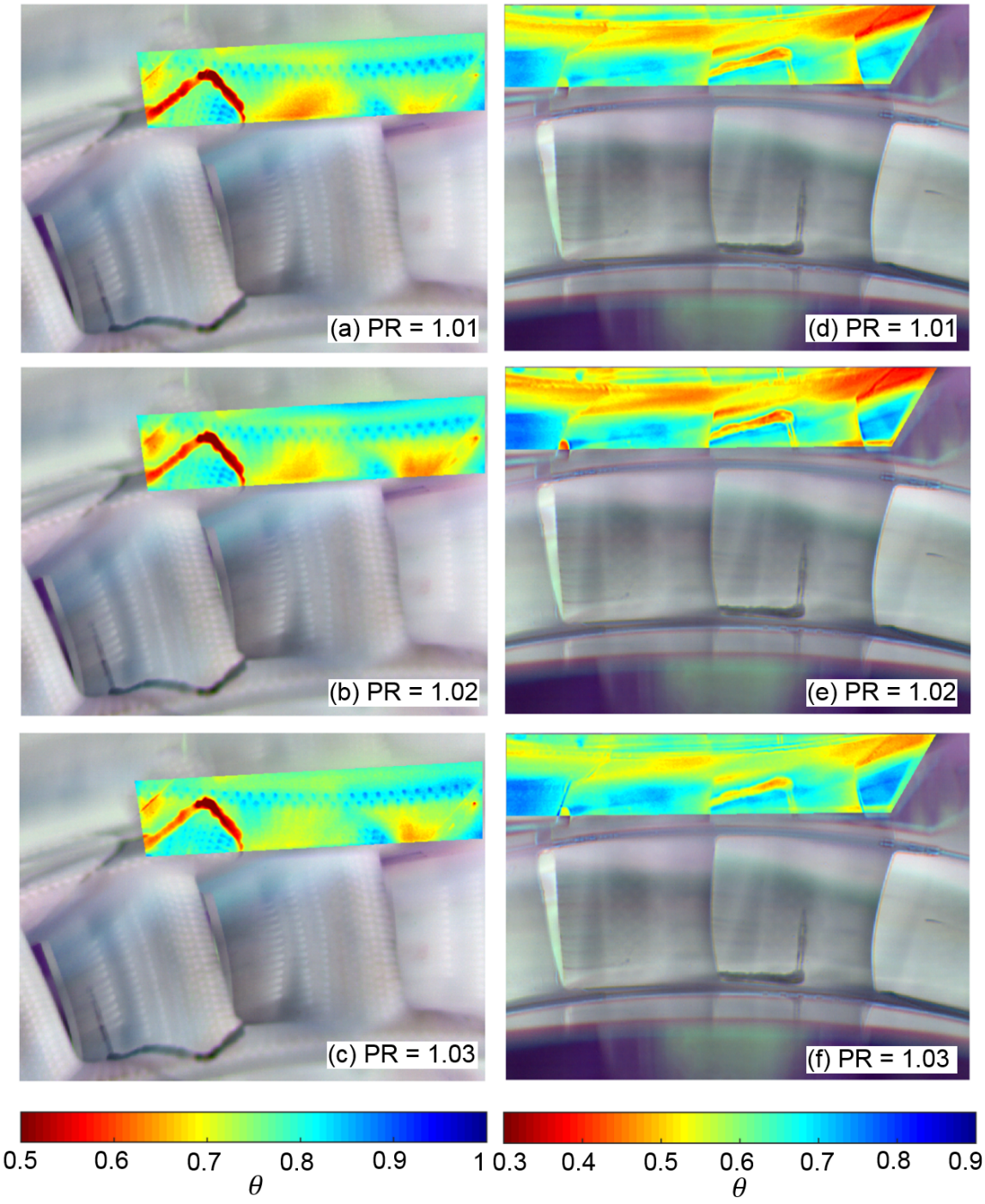


Figure 6.28: Overall cooling effectiveness distribution on upstream endwall (a–c), and downstream endwall (d–f) at various pressure ratios for the ARP1-1 design.

Figure 6.29a depicts the overall effectiveness distribution on line 1 (marked in Figure 6.27c) for the ARP1-2 design. Line 1 is located downstream the second row of

cooling holes and runs from the trailing vane LE (where the local normalized lateral coordinate is $y^* = 0$) to the leading vane LE (where $y^* = 1$). At this line, the overall effectiveness is found to be above $\theta = 0.7$ along the entire lateral coordinate y^*, and reach its maximum value at approximately $y^* = 0.2$. There is a weak dependence on PR on the region $y^* > 0.5$, in which the overall effectiveness is increased for increasing PR.

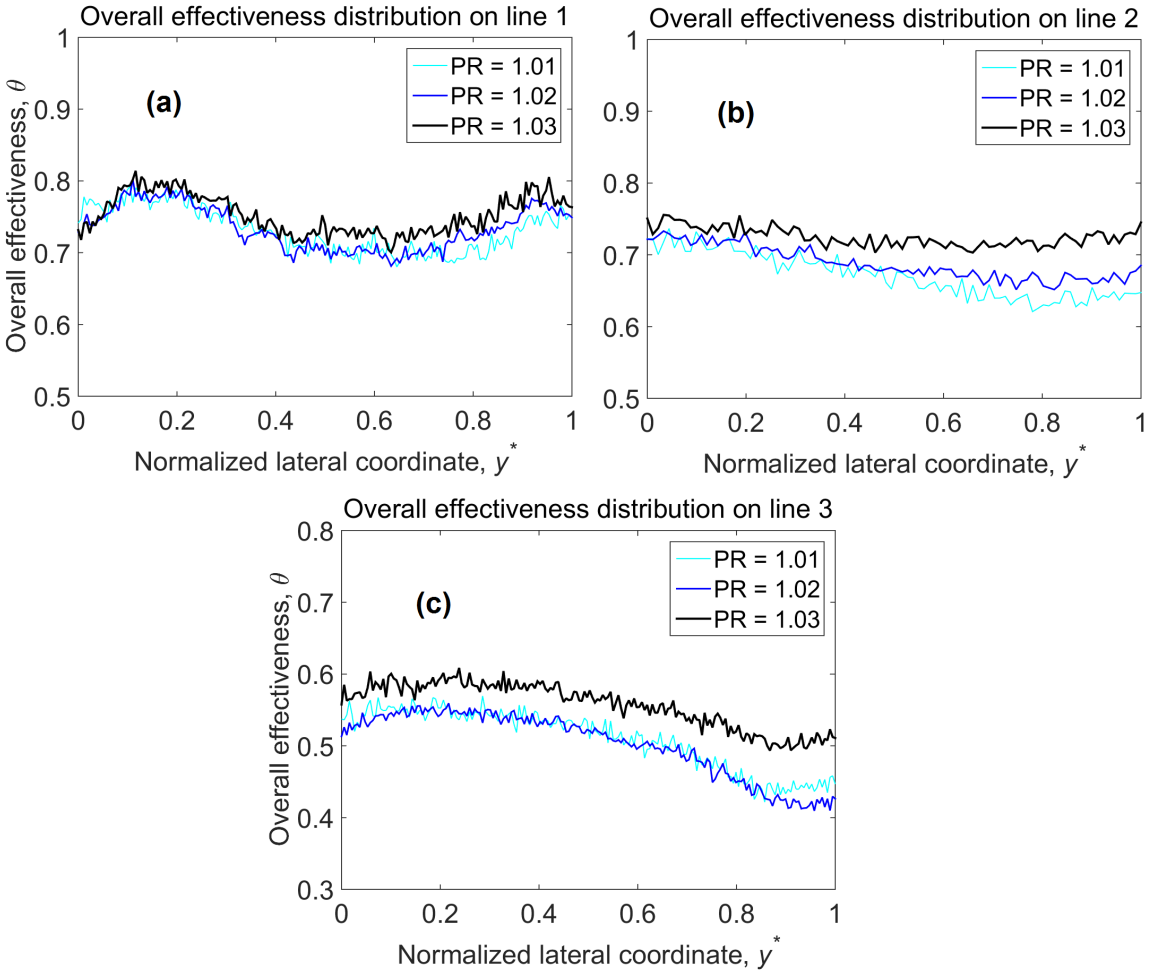


Figure 6.29: Overall effectiveness distribution (ARP1-2 design) on lines 1, 2, and 3 for PR = 1.01, 1.02, and 1.03.

Figure 6.29b depicts the overall effectiveness distribution on line 2 (marked in Figure 6.27c) for the ARP1-2 design. Line 2 is located at approximately mid-chord and runs from the trailing vane SS (where the local normalized lateral coordinate is

$y^* = 0$) to the leading vane PS (where $y^* = 1$). Here, we observe a low effectiveness in the region $y^* > 0.5$ at a low pressure ratio (PR = 1.01). Possible geometrical defects in the internal passage due to the complex manufacturing of the part might have caused internal flow separation, with internal total pressure loss increase. This could be the reason for substantially reduced overall performance when compared to ARP1-1 for similar pressure ratios. The cooling performance are ameliorated with increasing PR, and reach an approximately uniform value as high as $\theta = 0.75$ for PR = 1.03.

Figure 6.29c depicts the overall effectiveness distribution on line 3 (marked in Figure 6.27f) for the ARP1-1 design. Line 3 runs from the leading vane TE (where the local normalized coordinate is $y^* = 0$) to the trailing vane TE (where $y^* = 1$). The overall effectiveness picture on the downstream wall of ARP1-2 is complex. In general, it is insensitive to PR in the range PR = 1.01–1.02, but shows a substantially improved levels for PR = 1.03.

6.10.2 Impact of cooling arrangement

The impact of cooling arrangement is now assessed by comparing back-to-back overall cooling effectiveness profiles at three axial locations on the platform.

Figure 6.30 depicts the overall effectiveness distribution along line 1 (downstream the second row of cooling holes) for the three designs tested and PR = 1.02. Compared to the baseline case, design ARP1-1 performs with improved overall effectiveness, with approximately uniform overall effectiveness distribution (the average value is around $\theta = 0.75$). Compared to the baseline design, there is a maximum reduction of $\Delta\theta = 0.08$, which corresponds to a drop in temperature of approximately 73 K at scaled engine conditions. This result is in line with the improvement predicted by the conjugate network on the front region of the platform, presented in Chapter 5. Design ARP1-2 performs with higher θ in the region $0.0 < y^* < 0.4$, and slightly

reduced θ for $y^* > 0.4$.

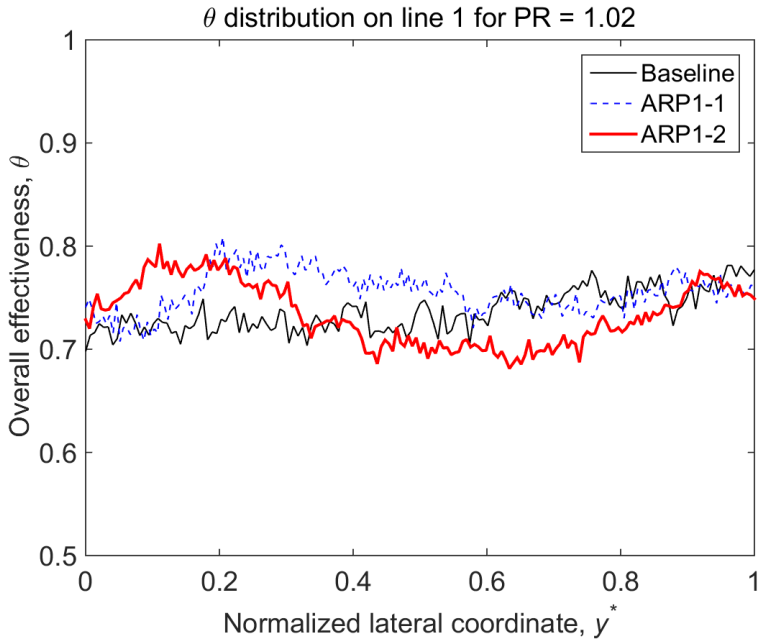


Figure 6.30: Overall cooling effectiveness distribution on line 1 for PR = 1.02 for all designs tested.

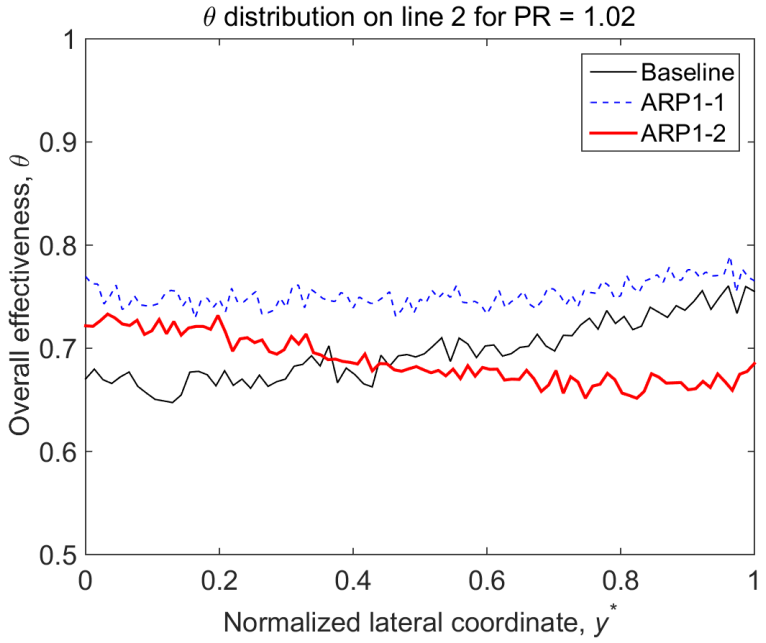


Figure 6.31: Overall cooling effectiveness distribution on line 2 for PR = 1.02 for all designs tested.

Figure 6.31 depicts the overall effectiveness distribution along line 2 (at approxi-

mately 40% of the axial location) for the three designs and PR = 1.02. At this line, design ARP1-1 shows improved cooling performance with respect to both baseline case and ARP1-2 design. ARP1-1 performs with very uniform distribution and averaged value around $\theta = 0.78$. As observed on line 1, design ARP1-2 performs with higher θ than the baseline for $y^* < 0.4$, and reduced θ for $y^* > 0.4$. Compared to the baseline design, there is a maximum reduction of $\Delta\theta = 0.10$, which corresponds to a drop in temperature of approximately 90 K at scaled engine conditions. This result is in line with the improvement predicted by the conjugate network on the mid-chord region of the platform, presented in Chapter 5

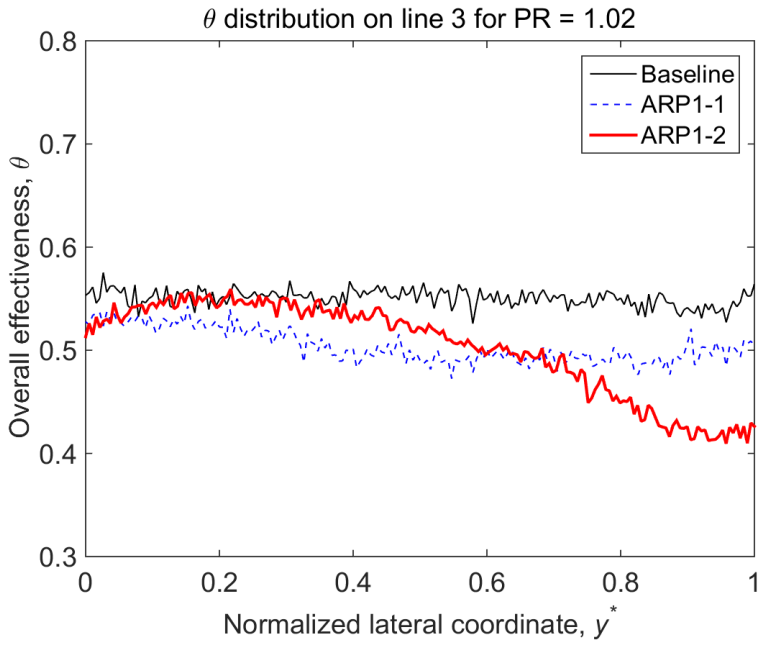


Figure 6.32: Overall cooling effectiveness distribution on line 3 for PR = 1.02 for all designs tested.

Figure 6.32 depicts the overall effectiveness distribution along line 3 (at the vane exit) for the three designs and PR = 1.02. At the vane exit, we observe reduced cooling performance for both ARP1-1 and ARP1-2. In fact at this line, the baseline case shows higher overall effectiveness with high degree of uniformity. The presence of the rim holes of design ARP1-2 helps improve the overall effectiveness in the region

$0.0 < y^* < 0.4$ for this pressure ratio. The trough in the region $y^* > 0.6$ is likely due to the flow separation—with consequent disruption of the film layer and reduced cooling performance—as observed in Figure 6.28.

6.11 Conclusions

In this chapter, an experimental investigation of internal platform cooling systems based on the reverse-pass scheme was carried out by using infra-red thermography. Tests were performed back-to-back over a range of engine representative coolant-to-mainstream pressure ratios. A new build was commissioned for the ECAT facility to include a number of DMLS parts to be tested at high speed conditions. Existing hardware was modified to allow to perform full-coverage temperature measurement by means of infra-red thermography. A system based on infra-red mirrors was developed to perform measurements of overall cooling effectiveness on both upstream and downstream endwalls. A bespoke in-situ correction technique was also developed to correct for the camera incident radiation due to the surroundings.

Results were compared back-to-back in terms of overall cooling effectiveness surface distributions and lateral profiles at various axial locations as a function of the coolant-to-mainstream pressure ratio. Results show that the reverse-pass design performs with substantially improved overall effectiveness on the front endwall due to the contribution of two effects; first, the internal heat transfer coefficient is enhanced thanks to a better guidance of the internal cooling flow and the presence of the pedestal bank at the channel inlet. Second, the total pressure loss introduced by the internal system contributes to a reduction in the coolant-to-mainstream momentum flux ratio, leading to better attached jets and improved both lateral and streamwise film coverage. On the other hand, with reduced momentum flux ratio, the jets reattach earlier in the platform and most of the coolant potential is used on the front

endwall. Internal pressure loss and a change in the local discharge coefficient might have caused a reduction of the coolant mass flow rate, leading to the worsening of the overall effectiveness in the platform exit region. This effect is ameliorated by the presence of the rim holes which enable to increase the heat pick up in the platform trailing edge region.

The ARP1-2 design was found to perform with reduced cooling performance on the upstream endwall compared to ARP1-1, for the same coolant-to-mainstream pressure ratio. This is attributed to unexpected internal pressure loss increase due to possible manufacturing defects within the reverse-pass channel of the ARP1-2 design. However, overall effectiveness of ARP1-2 is improved for higher pressure ratios, and hot regions completely suppressed for PR = 1.03.

In general, the reverse-pass design surpasses in performance the baseline arrangement on the upstream endwall and shows some potential of enhancing the overall cooling effectiveness on the downstream endwall by means of the rim holes.

Results of this chapter are hoped to be useful to researcher and turbine designers in understanding endwall flows and heat transfer and designing effective platform cooling systems. In particular, insights are given into the endwall aero-thermal field of real engine hardware at engine representative conditions.

Chapter 7

Conclusions

In this thesis, a combined analytical, numerical, and experimental work has been conducted to improve the design and understanding of high-pressure nozzle guide vane endwall cooling systems. A combination of fundamental research and high TRL (Techonlogy Readiness Level) studies have been carried out to address the main aerodynamic and heat transfer aspects of endwall flows. The present chapter is structured in such a way that the main contribution of the thesis is divided across four principal research areas.

It is hoped that the contribution of this thesis will be useful to turbine designers and researchers in understanding and designing improved HP-NGV endwall cooling systems.

7.1 Non-dimensional groups in film cooling studies

By conducting a dimensional analysis of a flow field with a mixing coolant film, it has been shown that the situation is governed by twelve non-dimensional groups. Making film effectiveness the subject, we can show that seven of the remaining eleven groups can be regarded as boundary conditions for the main flow path—and must be matched for complete similarity—and the remaining four relate specifically to the introduction of film cooling. It is argued that the film effectiveness is a strong function

of the following groups:

(i) the momentum flux ratio, $I \equiv (\rho_2 u_2^2) \,/\, (\rho_1 u_1^2)$;

(ii) the blowing ratio, BR$\equiv (\rho_2 u_2) \,/\, (\rho_1 u_1)$;

(iii) the heat capacity flux ratio, $E \equiv (\rho_2 u_2 c_{p2}) \,/\, (\rho_1 u_1 c_{p1})$;

(iv) the temperature ratio, TR$\equiv T_{02}/T_{01}$.

With the aid of extensive RANS and LES predictions, each of these four groups are varied whilst keeping the remaining groups constant. This enabled the independent effect of each group to be studied.

An important observation that departs from previous literature is that we see strong *region dependence* of the sensitivity of the film effectiveness to each of these four parameters. We define three regions for analysis: a *binary region* in which the films are essentially unmixed; an *intermediate region* in which the films are partially mixed; and a *mixed-out region* in which the films are well mixed. The key results of these four studies (one per controlling non-dimensional group) are now summarized in turn.

Momentum flux ratio. In the binary region we find the film effectiveness distribution has a strong dependence on the momentum flux ratio, because this controls the aerodynamic state of the jets i.e. the coolant trajectory and shape of the jet. This result is consistent with a large body of literature. In the intermediate region there is still significant dependence of the film effectiveness distribution on momentum flux ratio. This is beyond the reattachment point of the jets, so the sensitivity is likely associated with changes in mixing caused by different initial coolant trajectories. We find that in the mixed out region, the film effectiveness is insensitive of the momentum flux ratio.

Blowing ratio. This is a commonly-used parameter in turbomachinery literature primarily because it relates to the input controls in many experiments, or the cycle

cost (aerodynamic and thermodynamic) in engine applications. It is found, however, that the relatively subtle physical processes this parameter controls are not those discussed in existing literature, and further observe that the sensitivity of film cooling to blowing ratio (when varied on its own) is much lower than to other non-dimensional parameters. Indeed, in much of the literature, changes in film effectiveness which should correctly be attributed to energy flux ratios changes are incorrectly attributed to blowing ratio changes. Although there is less sensitivity of film cooling to blowing ratio than to other parameters, we have shown that blowing ratio is responsible for describing the initial *volume flow rate ratio* or *velocity ratio* of the cooling jet with respect to the mainstream flow (when coolant is expanded to the local static pressure at the hole exit).

Heat capacity flux ratio. The heat capacity flux ratio is a measure of the relative (with respect to the mainstream) potential of the coolant stream to store heat. In the binary region, where the flow is essentially unmixed, the balance of specific heat capacity flux is unimportant, because it has little effect on the approximately binary values the film effectiveness takes (here it is only the structure of the flow that is important). In the intermediate and mixed-out regions where the flow is relatively well mixed, the relative heat storage capacity of the coolant and mainstream flows is extremely important, and there is an approximately linear relationship between the laterally averaged film effectiveness and the heat capacity flux ratio. In these regions, the film effectiveness is more sensitive to this parameter than any other.

Temperature ratio. A change in in temperature ratio alone does not cause a change in density (or density ratio) of the coolant film at the point of issuing from the hole, but, interestingly, does cause a change in the density of a *partially mixed* layer of coolant. A key result is the density of such a layer decreases (from a maximum at TR = 1) for temperature ratios *either side of unity.* There are two consequences of this effect: firstly, the kinematic viscosity increases *either side of a TR of unity*

leading to higher momentum diffusivity and greater mixing within the near wall region; secondly, there is a volume dilation effect during the mixing process (of coolant gas with entrained mainstream).

7.2 Effect of momentum flux ratio on HP-NGV endwall cooling systems

For this branch of work, experiments were carried out on a linear, low-speed cascade with engine-realistic combustor simulator from a modern engine geometry. The tested range of momentum flux ratio was designed to span the typical engine range for HP-NGV endwall cooling systems. Results show a strong dependency of the thermal field and flow structures on the bulk momentum flux ratio. In particular, suppression of secondary flows is observed for relatively low values of momentum flux ratio. For higher momentum flux ratios (i.e. mid-portion of the typical engine range), a substantial vane up-wash is also observed, with relative inefficient use of coolant. This indicates that engine systems operating at high coolant mass flow rates can benefit from the introduction of internal pressure loss (for example a reverse-pass systems with internal heat transfer enhancement devices) to reduce the momentum flux ratio and optimize the coolant usage.

7.3 Film cooling optimization based on the scalar tracking method

An optimization strategy based on the scalar tracking method was developed to isolate the contribution to each film cooling hole to the overall effectiveness. Linear superposition techniques were used to construct a proxy model for the CFD to predict adiabatic film cooling effectiveness. The proxy model was then used in a rapid

optimization loop based on genetic algorithms. In this way, CFD could be used for model recalibration only and the number of total CFD runs substantially reduced when compared to other optimization works presented in the literature. Results have suggested that the method can only be suitable for certain classes of problems, where the influence of *global* and *local* flow regime shifts is small (e.g. changes in flow structures due to change in the cooling hole mass flow rate). An optimization test case was developed following a strategy that aimed to limit the errors due to flow changes. Results showed that the method is suitable for cases where the momentum flux ratio is fixed during the optimization and both lateral and streamwise hole spacing are larger than $3d$ and $25d$, respectively. With the aim of minimizing the difference from a target film effectiveness distribution *and* minimizing mixing loss introduced by film cooling, an optimization test case was performed for a flat plate with 60 holes. The optimization was stopped after 5 CFD runs because the improvement between two subsequent *outer* iterations was smaller than 3%. The optimized configuration operated with 10% improved life and 29% reduced loss. The optimization method presented in this thesis has been critically analyzed and its validity discussed in relation to its potential applicability to film cooling systems. The aim of this branch of work was mainly to understand the major limitations of the use of linear superposition for film cooling systems. In summary, some concerns exist regarding the applicability of the method in case of complex flowfields and in cases where holes are clustered (e.g. NGV platforms). However, it is believed that the method could be used for simpler cases, such as film cooling of combustor liners or afterburners.

7.4 Design and assessment of HP-NGV reverse-pass platforms

This section describes an experimental study of reverse-pass platform designs at high speed conditions. Tests were carried out at the Engine Component Aero-Thermal (ECAT) facility at the University of Oxford. The aim of this work is to characterize the aero-thermal field of novel platform designs based on reverse-pass cooling schemes at engine-matched Reynolds number, Mach number, Biot number, and coolant-to-mainstream pressure ratio. Detailed overall cooling effectiveness distributions are measured by means of infra-red thermography on both upstream and downstream regions of the vane hub endwall. The proposed designs are compared back-to-back to the baseline engine platform cooling system at various coolant-to-mainstream pressure ratios.

Results show that the reverse-pass designs perform with substantially improved overall effectiveness on the front endwall due to the contribution of two effects; first, the internal heat transfer coefficient is enhanced as a result of improved guidance of the internal cooling flow and the presence of the internal heat transfer enhancement devices. Second, the total pressure loss introduced by the internal system contributes to reduce the coolant-to-mainstream momentum flux ratio, and leads to better attached jets and improved both lateral and streamwise film coverage. On the other hand, with reduced momentum flux ratio, the jets reattach earlier in the platform and most of the coolant potential is used on the front endwall. In the vane exit region, the increased turbulence and mixing lead to reduced overall effectiveness compared to the baseline case. This effect is ameliorated by the presence of the rim holes which allow to reduce the heat load in the platform trailing edge region.

7.5 Application of the research and future work

The content of this thesis is structured to include miscellaneous aspects of high pressure nozzle guide vane endwall cooling. A number of insights can be gained at various levels, from a fundamental aspect to a more applied point of view. In this way, it is possible to extract information of—for instance—film cooling flow physics and scaling theory, gain insights into the main challenges in the designs and optimization of external/internal endwall systems, and understand aero-thermal field of real engine hardware at engine representative conditions.

Both experimental and numerical techniques presented in this thesis were developed to satisfy strict requirements of accuracy, and therefore were in line with the current state-of-the-art (i.e. bespoke in situ IR calibration, LES simulations, etc.). However, it is believed that some additional work would be beneficial to further improve the analysis presented. A summary of suggested future work is reported below with reference to the relevant chapter.

Chapter 4. The effect of varying the inlet conditions on the optimization results was not investigated. It is expected that the results of the combined MOGA-scalar tracking network would be dependent on the inlet conditions, and in particular on the number of *global* runs required to reach an optimum design.

Chapter 6. It is suggested that the field of view (for both upstream and downstream endwalls) is mapped onto a CAD model (or photograph of the real geometry) to aid interpretation of the overall effectiveness results presented.

Chapter 6. A flow check for the platform holes of all DMLS parts is suggested to correlate the results obtained from the IR tests to geometrical changes in the internal cooling system. This tests will also give an estimate for the averaged platform discharge coefficient.

Chapter 6. It is suggested that an uncertainty analysis is performed including the uncertainty deriving from the recovery ratio (c). The latter was used to calculate

the overall cooling effectiveness via a two-tests procedure in which both c and θ were estimated from two tests at different power settings. In this regard, it is suggested that the accuracy on determining c is assessed in relation to the difference in temperature allowed by the mainstream heaters for the two tests.

Appendix A

Demonstration that VR and VFRR are Inversely Proportional to BR when Varying BR Alone

In this section, we demonstrate the slightly counter-intuitive result that for fixed momentum flux ratio, fixed specific heat capacity flux ratio, and fixed temperature ratio, and in experiments in which the inlet total pressure and external aerodynamics are fixed (see text relating to Equation 2.2), the velocity ratio and volume flow rate ratio are inversely proportional to blowing ratio.

Consider Equation B.3 , repeated here for convenience:

$$BR \equiv \frac{\rho_2 u_2}{\rho_1 u_1} = \left(I \frac{\rho_2}{\rho_1} \right)^{\frac{1}{2}} = \left(\frac{p_{02}}{p_{01}} \frac{T_{01}}{T_{02}} \frac{cp_1}{cp_2} \frac{\gamma_2}{\gamma_1} \frac{\gamma_1 - 1}{\gamma_2 - 1} \frac{p_{02} - p}{p_{01} - p} \right)^{\frac{1}{2}} = \pi_2.$$

Constant temperature ratio by definition means the term $(T_{02}/T_{01}))$ is constant. As we have noted, for incompressible flow, constant momentum flux ratio implies constant $(p_{02} - p)((p_{01} - p)$. In our CFD experiments, we arbitrarily fix p_{01} and the domain exit static pressure (note that this leave sufficient freedom to adjust our non-dimensional groups as required). The domain geometry is fixed, and therefore this leads to fixed local static pressure, p, at the cooling hole exit. These boundary conditions are the same as many real experiments with fixed external aerodynamics. Constant $(p_{02} - p)/(p_{01} - p)$, constant p_{01}, and constant p necessarily imply constant p_{02} and therefore constant p_{02}/p_{01}.

Let us now return to Equation B.3. For the constraints we have specified, there are two remaining degrees of freedom

$$\frac{\gamma_2}{\gamma_1} \frac{\gamma_1 - 1}{\gamma_2 - 1}, \tag{A.1}$$

$$\frac{c_{p1}}{c_{p2}}. \tag{A.2}$$

Recalling Equation 2.7, $E = BR(c_{p2}/c_{p1})$, fixed specific heat capacity flux ratio implies a proportional relationship between c_{p1}/c_{p2} and BR. Noting the square root on all terms on the right hand side of Equation B.3, noting the result $c_{p1}/c_{p2} \propto BR$, and noting there are only two degrees of freedom with the specified constraints (terms A.1, A.2), we see that the term A.1 must also be proportional to BR. That is

$$\gamma_2/\gamma_1(\gamma_1 - 1)(\gamma_2 - 1) \propto c_{p1}/c_{p2} \propto BR. \tag{A.3}$$

Using Meyer's relation

$$\gamma_2/\gamma_1(\gamma_1 - 1)(\gamma_2 - 1) = (c_{p1}/c_{p2}) = R_1/R_2, \tag{A.4}$$

therefore

$$R_1/R_2 \propto BR^2. \tag{A.5}$$

Taking the ideal gas law, $p/\rho = RT$, noting that for incompressible flow $p_0 \approx p$ and $T_0 \approx T$, recalling that in all of the studies in this paper we arbitrarily fixed T_{01} (see text related to equation 2.15), and that in this study in particular (varying blowing ratio alone) we have fixed T_{01}/T_{02}, we obtain, for this study

$$\rho \propto 1/R. \tag{A.6}$$

Combining A.5 and A.6

$$BR^2 \propto \rho_2/\rho_1. \tag{A.7}$$

Therefore as BR increases, ρ_2/ρ_1 will increase as the square of BR. For fixed I, recalling Equation 2.4 ($I = \rho_2 u_2^2/\rho_1 u_1^2$), the ratio u_2^2/u_1^2 will be inversely proportional to BR. That is, $u_2/u_1 \propto 1/BR$. *The velocity ratio and volume flow rate ratio are inversely proportional to blowing ratio.*

Appendix B

Demonstration that for TR Either Side of Unity there is a Reduction in Density in the Mixing Layer

In this section, we demonstrate the result that for fixed momentum flux ratio, fixed blowing ratio, and fixed specific heat capacity flux ratio, and in experiments in which the inlet total pressure and external aerodynamics are fixed, that for coolant-to-mainstream temperature ratios *either side* of unity, there is a decrease in the density ratio of the flow in a partially mixed out film, and an associated increase both in kinematic viscosity, and in the volume of the mixing layer.

Consider the form of the non-dimensional groups we intend to keep constant, I, E and BR.

$$I \equiv \frac{\rho_2 u_2^2}{\rho_1 u_1^2} = \frac{p_{02} - p}{p_{01} - p}, \tag{B.1}$$

$$E \equiv \frac{\rho_2 u_2 c_{p2}}{\rho_1 u_1 c_{p1}} = BR \frac{c_{p2}}{c_{p1}}, \tag{B.2}$$

$$BR \equiv \frac{\rho_2 u_2}{\rho_1 u_1} = \left(\left(\frac{p_{02}}{p_{01}} \right) \left(\frac{T_{01}}{T_{02}} \right) \left(\frac{cp_1}{cp_2} \right) \left(\frac{\gamma_2}{\gamma_1} \frac{\gamma_1 - 1}{\gamma_2 - 1} \right) \left(\frac{p_{02} - p}{p_{01} - p} \right) \right)^{\frac{1}{2}}. \tag{B.3}$$

To keep I constant (Equation B.1), we required fixed inlet total pressure (p_{01}) and external aerodynamics (p), and additionally fixed coolant total pressure, p_{02}. To keep E constant (Equation B.2), noting that BR must also be kept constant in this study, we required constant c_{p1}/c_{p2} . Finally, to keep BR constant (Equation B.3), and noting that first, third, and fifth terms in the right hand parentheses are constant (required for constant I and E), and further noting that we are varying term two (by definition, as variation of temperature ratio—alone—is the purpose of this study), we observe that the fourth term, $\gamma_2/\gamma_1(\gamma_1 - 1)/(\gamma_2 - 1)$, is inversely proportional to T_{01}/T_{02}. It is possible to show that $(c_{p1}/c_{p2})(\gamma_2/\gamma_1)(\gamma_1 - 1)/(\gamma_2 - 1) = R_1/R_2$. Thus,

for constant c_{p1}, c_{p2} and R_1 (constraints that meet our requirements in this study) we see that $T_{01}/T_{02} \propto 1/(R_1/R_2)$ or $R_2 \propto 1/(T_{02}/T_{01}) \equiv 1/TR$). This result is plotted in Figure B.1. A consequence of the inverse proportionality of R_2 and T_{02} is that ρ_2 is constant (for incompressible flow) with varying T_{02} or TR. This is also shown in Figure B.1.

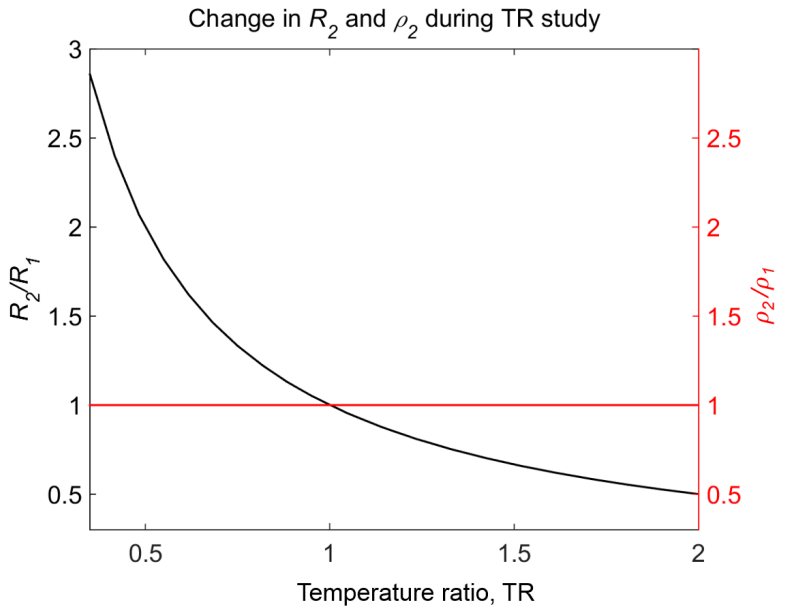


Figure B.1: Variation of coolant gas constant R_2 (normalized by R_1, which is constant with TR), and coolant gas density ρ_2 (normalized by ρ_1, which is constant with TR) as a function of temperature ratio.

Figure B.1 shows the required variation in R_2 (normalized by R_1, which is constant with TR) to maintain constant values of I, E and BR whilst varying TR. We now consider the impact of this variation in R_2 on the behaviour of partially mixed coolant film. Consider the control volume of Figure B.2, which we will use to examine the behaviour of a partially mixed film.

We want to consider the changes in behaviour with TR within the mixing film, and to do this we arbitrarily pick a mixing ratio $\dot{m}_1/\dot{m}_2 = 1$). We define a bounding streamline as the line that contains these two streams of equal mass flux. We define the boundary conditions for the mixing process as follows:

(i) Constant static pressure along the bounding streamline;

(ii) No heat transfer across the bounding streamline.

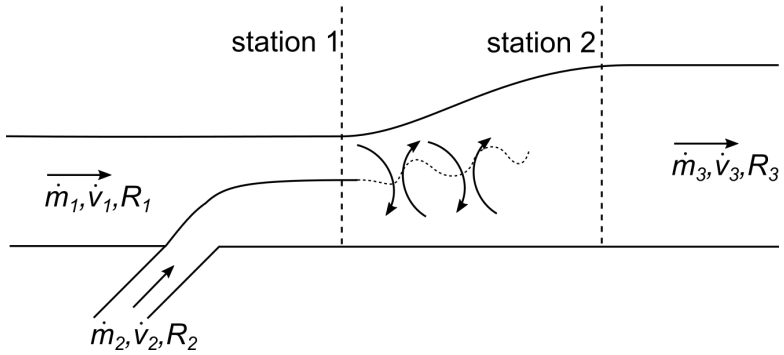


Figure B.2: Control volume for a partially mixed coolant film.

At the inlet state, station 1, the two flows are entirely unmixed. At the outlet state, station 2, the two flows are fully mixed. We note that the (mass) continuity condition and constraint that $c_{p1} = c_{p2}$ means that at station 2 the equivalent adiabatic film effectiveness is 0.5.

It is worth noting that for constant BR (in our varying TR study), and for the same flow structure (dictated by I in the region close to the hole) the mass flow rate (per unit domain width) distributions with wall-normal distance through station 1 do no vary with TR. That is, the position of the hypothetical bounding streamline that preserves the condition $\dot{m}_1/\dot{m}_2 = 1$ does not change with TR. Likewise, for constant I, the distribution with wall-normal distance of *volume flow rate per unit domain width* is unchanged with varying TR. In fact, for all values of TR, the nominal values BR $= 1$ and $I = 1$ imply $\dot{V}_1/\dot{V}_2 = 1$, for our arbitrarily selected $\dot{m}_1/\dot{m}_2 = 1$. In summary, the mass flow rates and volume flow rates into the control volume at station 1 are unchanged with changing TR.

We now consider what happens in the process of fully mixing the flows between station 1 and station 2. The mixed out total temperature T_{03}, is determined by the energy and (mass) continuity equations

$$\dot{m}_1 c_{p1} T_{01} + \dot{m}_2 c_{p2} T_{02} = \dot{m}_3 c_{p3} T_{03}, \tag{B.4}$$

$$\dot{m}_1 + \dot{m}_2 = \dot{m}_3, \tag{B.5}$$

where we note in general that $c_{p3}\dot{m}_3 = c_{p1}\dot{m}_1 + c_{p2}\dot{m}_2$, but in our special case $c_{p1} = c_{p2} = c_{p3}$. For our special case, the mixed-out temperature at station 2 is given by

$$T_{03} = (T_{01}\dot{m}_1 + T_{02}\dot{m}_2)/\dot{m}_3. \tag{B.6}$$

Likewise, the mixed-out specific gas constant at station 2 is

$$R_3 = (R_1\dot{m}_1 + R_2\dot{m}_2)/\dot{m}_3. \tag{B.7}$$

For constant T_{01} and R_1, the resulting variations in T_{03} and R_3 (normalized by T_{01} and R_1) with TR are presented in Figure B.3. The mixed out temperature T_{03} increases linearly with T_{02} (and therefore TR). The mixed out specific gas constant R_3 is quasi-inversely-proportional to T_{02} (and therefore TR). This is explained (via equation B.7) by the constant value of R_1, the precisely-inverse relationship between R_2 and TR (Figure B.1) and the fixed ratio $\dot{m}_1/\dot{m}_2 = 1$.

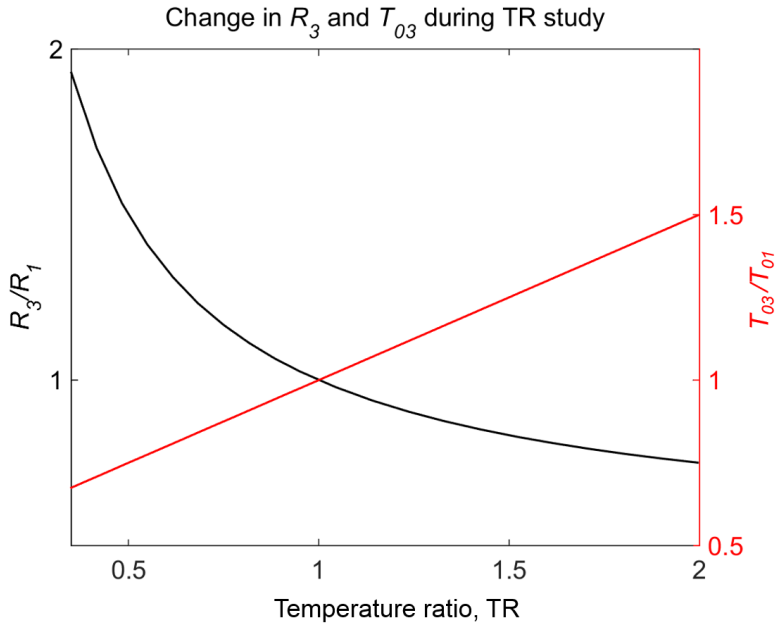


Figure B.3: Variation of R_3 (normalized by R_1, which is constant with TR) and T_{03} (normalized by T_{01}, which is constant with TR) as a function of TR.

We now consider the consequences of the trends $T_{03} = f(\text{TR})$ and $R_3 = f(\text{TR})$ for the mixed out density, ρ_3, and the corresponding volumetric flow rate out of the control volume, $\dot{V}_3$.

The mixed out density obeys the ideal gas law, $\rho_3 = p_3/R_3T_3$, and noting both that the mixing process occurs at constant static pressure ($p_1 = p_2 = p_3$) and that the flow is to a good approximation incompressible ($T_3 \approx T_{03}$ and $\rho_3 \approx \rho_{03}$), the function that ρ_3 takes with TR, $\rho_3(\text{TR})$, is dictated by the trends $T_{03}(\text{TR})$ and $R_3(\text{TR})$ in Figure B.3 (these are presented normalized by the constant values T_{01} and R_1). These trends are such that the resulting mixed out density decreases for temperature ratios either side of unity. The trend is shown in Figure B.4. The important result is perhaps

surprising, and has interesting implications that are discussed in the main body of this paper. The most significant of these results is that kinematic viscosity increases either side of a temperature ratio of unity, or equivalently there is higher momentum diffusivity in the mixing layer either side of unity (note that the dynamic viscosity, which is a fluid property, is constant). The variation with temperature ratio of the kinematic viscosity of the partially mixed layer (normalized by the kinematic viscosity of the coolant at the point of injection, ν_2) is shown in Figure B.4. Results are shown for mixing ratios m $\dot{m}_1/\dot{m}_2 = 0.5$, 1.0, and 2.0.

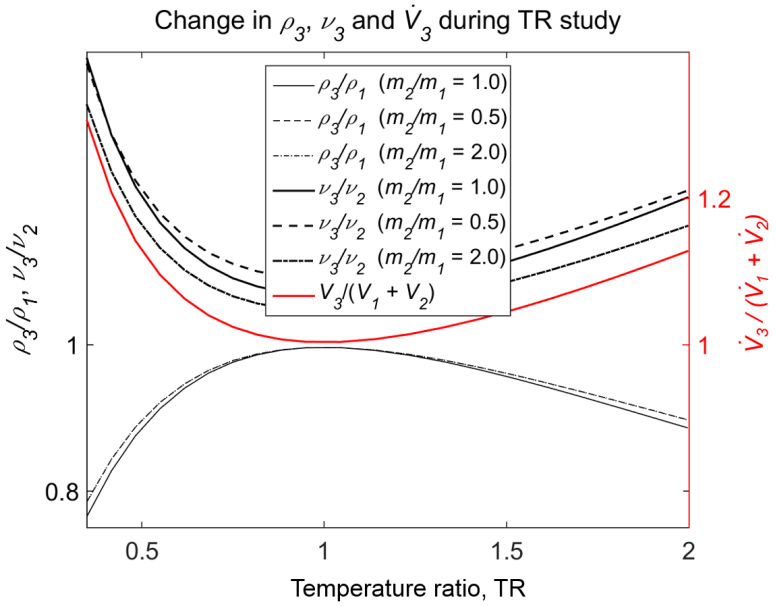


Figure B.4: Variation with TR of: density ratio of the partially mixed layer ρ_3/ρ_1; volume flow rate ratio of the partially mixed layer $\dot{V}_3/(\dot{V}_1 + \dot{V}_2)$; kinematic viscosity ratio of the partially mixed layer ν_3/ν_2.

Now we ask what happens to the volume flow rate ratio $\dot{V}_3/(\dot{V}_1 + \dot{V}_2)$ across the domain (i.e. between unmixed station 1, and fully mixed station 2). We recall that the inlet mass flow rates are equal to each other, and constant with varying TR, and that inlet volume flow rates, $\dot{V}_1$ and $\dot{V}_2$, are equal to each other and constant with varying TR. It follows that the output mass flow rate is constant with varying TR. The output density varies as shown in Figure B.4, however. The result is that the volume flow rate ratio increases either side of a TR of unity (see Figure B.4). This is equivalent to volume dilation in the mixing layer, which pushes flow structures—including turbulent structures—further into the main-flow than would be the case for TR = 1. This second significant result is discussed in the main body of the paper.

Bibliography

Adams, B. M., Ebeida, M. S., Eldred, M. S., Kakeman, J. D., Swirler, P. S., Stephens, J. A., Vigil, D. M. and Wildey, T. M. (2015), *Dakota, A Multilevel Parallel Object-Oriented Framework for Design Optimization, Parameter Estimation, Uncertainty Quantification, and Sensitivity Analysis: Version 6.2: User's Manual*, Sandia National Laboratories. SAND2014-4633.

Armstrong, J. and Winstanley, D. (1988), 'A Review of Staggered Array Pin Fin Heat Transfer for Turbine Cooling Applications', *ASME J. Turbomach.* **110**(1), 94–103.

Ayoub, C. E. (2014), Three-Dimensional Aero-Thermal Optimization of Film Cooling in a High Pressure Turbine, PhD thesis, Concordia University, Motreal, Quebec, Canada.

Bagshaw, D. A. (2009), Passage Shaping in Axial Flow Turbines, PhD thesis, University of Duram.

Barigozzi, G., Franchini, G., Perdichizzi, A. and Quattrore, M. (2010), 'Endwall Film Cooling Effects on Secondary Flows in a Contoured Endwall Nozzle Vane', *ASME. J. Turbomach.* **132**(4), 041005–041005–9.

Bogard, D. G. and Thole, K. A. (2006), 'Gas Turbine Film Cooling', *Journal of Propulsion and Power* **22**(2), 249– 270.

Cresci, I., Ireland, P., Bacic, M., Tibbott, I. and Rawlinson, A. (2015), 'Velocity and Turbulence Intensity Profiles Downstream of a Long Reach Endwall Double Row of Film Cooling Holes in a Gas Turbine Combustor Representative Environment', *ASME paper* **GT2015-42307**.

Day, C. R., Oldfield, M. L. G. and Lock, G. D. (2000), 'Aerodynamic Performance of an Annular Cascade of Film Cooled Nozzle Guide Vanes Under Engine Representative Conditions', *Experiments in Fluids* **29**, 117–129.

Dittus, F. W. and Boelter, L. M. K. (1930), 'Heat Transfer in Automobile Radiator of the Tubular Type', *University of California at Berkley Publ. Eng.* **2**.

Eddy, J. and Lewis, K. (2001), 'Effective Generation of Pareto Sets using Genetic Programming', *ASME paper* **DETC2001/DAC21094**.

EdmundOptics (2018), 'Pmetallic Mirror Coatings'.
URL: *https* : *//www.edmundoptics.com/resources/application* − *notes/optics/metallic* − *mirror* − *coatings/*

Ekkad, S. V., Han, J. C. and Du, H. (1998), 'Detailed Film Cooling Measurements on a Cylindrical Leading Edge Model: Effect of Free-Stream Turbulence and Coolant Density', *J. Turbomach.* **120**(4), 799–807.

FLIR (2012), *The Ultimate Infrared Handbook for R&D Professionals*, FLIR systems Inc., Wilsonville. Publ. no. T559243.

FLIR (2014), 'Flir A655sc data sheet'.
URL: *www.flirmedia.com/MMC/THG/Brochures/RND*_011

Fonseca, C. M. and Fleming, P. J. (1993), Genetic Algorithms for Multiobjective Optimization: Formulation, Discussion and Generalization, *in* 'Genetic Algorithms: Proceedings of the Fifth International Conference'.

Friedrichs, S., Hodson, H. P. and Dawes, W. N. (1999), 'The Design of an Improved Endwall Film-Cooling Configuration', *ASME. J. Turbomach.* **121**(4), 772–780.

Gao, Z., Narzary, D. and Han, J. C. (2009), 'Turbine Blade Platform Film Cooling With Typical Stator-Rotor Purge Flow and Discrete-Hole Film Cooling', *ASME. J. Turbomach.* **131**(4), 041004–041004–11.

Giel, P. W., Thurman, D. R., Fossen, G. J. V., Hippensteele, S. A. and Boyle, R. J. (1998), 'Endwall Heat Transfer Measurements in a Transonic Turbine Cascade', *ASME. J. Turbomach.* **120**(2), 305–313.

Greiner, N. J., Rutledge, J. L. and Polanka, M. D. (2014), 'Scaling of Film Cooling Performance From Ambient to Engine Temperatures', *ASME J. Turbomach.* **137**(7), 071007–1–10.

Haas, W., Rodi, W. and Shonung, B. (1991), 'The Influence of Density Difference Between Hot and Coolant Gas on Film Cooling by a Row of Holes: Predictions and Experiments', *ASME J. Turbomach.* **114**(4), 747–755.

Han, S. J. and Golstein, R. J. (2005), 'Influence of Blade Leading Edge Geometry on Turbine Endwall Heat (Mass) Transfer', *ASME J. Turbomach.* **128**(4), 798–813.

Harasgama, S. P. and Burton, C. D. (1992), 'Film Cooling Reasearch on the Endwall of a Turbine Nozzle Guide Vane in a Short Duration Annular Cascade: Part 1–Experimental Technique and Results', *ASME. J. Turbomach.* **114**(4), 734–740.

Hippensteele, S. A. (1974), Pressure-loss and Flow Coefficient Inside a Chordwise-Finned, Impingement, Convection, and Film Air-Cooled Turbine Vane, Technical Report TM X-3028, NASA.

Horlock, J. H., Watson, D. T. and Jones, T. V. (2001), 'Limitations on Gas Turbine Performance Imposed by Large Turbine Cooling Flows', *ASME. J. Eng. Gas Turbines Power* **123**(3), 487–494.

Ingram, J. L. (2003), Endwall Profiling for the Reduction of Secondary Flow in Turbines, PhD thesis, University of Duram.

Jiang, Y., Lin, H., Yue, G., Zheng, Q. and Xu, X. (2017), 'Aero-Thermal Optimization on Multi-Rows Film Cooling of a Realistic Marine High Pressure Turbine Vane', *Applied Thermal Engineering* **111**, 537–549.

Johnson, J. J., King, P. I., Clark, J. P. and Ooten, M. K. (2014), 'Genetic Algorithm Optimization of a High-Pressure Turbine Vane Pressure Side Film Cooling Array', *J. Turbomach.* **136**(1), 011011–011011–11.

Kirollos, B. (2016), Aerothermal Optimisation of Novel Cooling Schemes for High Pressure Components Using Combined Theoretical, Numerical and Experimental Techniques, PhD thesis, University of Oxford.

Kirollos, B., Lubbock, R., Beard, P., Goenaga, F., Rawlinson, A., Janke, E. and Povey, T. (2017), 'ECAT: an Engine Component Aerothermal Facility at the University of Oxford', *ASME paper* **GT2017-64736**.

Kirollos, B. and Povey, T. (2014), 'Reverse-Pass Cooling Systems for Improved Performance', *ASME J. Turbomach.* **136**(11), 111004–1–10.

Kirollos, B. and Povey, T. (2015), 'An Energy-Based Method for Predicting the Additive Effect of Multiple Film Cooling Rows"', *J. Eng. Gas Turbines Power* **137**(12), 122607–1–8.

Kirollos, B. and Povey, T. (2017), 'High-accuracy infra-red thermography method using reflective marker arrays', *Meas. Sci. Technol.* **25**, 095405 12pp.

Kollen, O. and Koschel, W. (1985), Effect of Film Cooling on the Aerodynamic Performance of a Turbine Cascade, Technical Report CP 390, NATO AGARD.

Langston, L. S., Nice, M. L. and Hopper, R. M. (1977), 'Three-Dimensional Flow Within a Turbine Cascade Passage', *ASME J. Eng. Power* **99**(1), 21–28.

Lin, X. C., Liu, J. J. and An, B. (2015), 'Calculation of Film-Cooling Effectiveness and Aerodynamic Losses Using DES/SAS and RANS Methods and Compared with Experimental Results', *ASME paper* **GT2016-89477**.

Lyall, M. (2006), Heat Transfer From Low Aspect Ratio Pin Fins, Master's thesis, Virginia Polytechnic Institute and State University.

Mazzoni, C., Luque, S. and Rosic, B. (2015), 'Capabilities of Thermal Wall Function to Predict Heat Transfer on the NGVs of a Gas Turbine with Multiple Can Combustors', *ASME paper* **GT2015-43515**.

Metzger, D. E., Berry, R. A. and Bronson, J. P. (1982), 'Developing Heat Transfer in Rectangular Ducts With Staggered Arrays of Short Pin Fins', *J. Heat Transfer* **104**(4), 700–706.

Moffat, R. J. (1988), 'Describing the Uncertainties in Experimental Results', *Experimental Thermal and Fluid Science* **1**, 3–17.

Nemdili, F., Theodorodis, G. and Jubran, B. A. (2008), 'Reynolds Stress Transport Modeling of Film Cooling at the Leading Edge of a Symmetrical Turbine Blade Model', *Heat Transfer Engineering* **29**(11), 950–960.

Nicoud, F. and Ducros, F. (2014), 'Subgrid-Scale Stress Modelling Based on the Square of the Velocity Gradient Tensor', *Flow, Turbulence, and Combustion* **62**, 183–200.

Ornano, F. and Povey, T. (2017*a*), 'Experimental and Computational Study of the Effect of Momentum-flux Ratio on High Pressure NGV Endwall Cooling Systems', *ASME paper* **GT2017-64229**.

Ornano, F. and Povey, T. (2017*b*), 'Experimental and Computational Study of the Effect of Momentum-flux Ratio on High Pressure NGV Endwall Cooling Systems', *ASME J. Turbomach.* **139**(12), 121002–16.

Ornano, F. and Povey, T. (2018), 'Theory of Non-dimensional Groups in Film Effectiveness Studies', *Submitted to Int. J. of Thermal Science* .

Pedersen, D. R., Eckert, E. and Golstein, R. (1977), 'Film Cooling with Large Density Differences Between the Maistream and the Secondary Fluid Measured by the Heat-Mass Transfer Analogy', *J. Heat Transfer* **99**(4), 620–627.

Povey, T. (2004), Transient Mass Flow Rate Measurement Facility, Technical report, University of Oxford.

Prost, J. W. and Acharya, S. (1991), 'The Role of Density Ratio and Blowing Ratio on Film Cooling in a Vane Passage', *ASME paper* **GT2010-23680**.

Pullan, G. and Harvey, N. W. (2008), 'The Influence of Sweep on Axial Flow Turbine Aerodynamics in the Endwall Region', *J. Turbomach.* **041011**, 1–11.

Qureshi, I., Beretta, A. and Povey, T. (2011), 'Effect of Simulated Combustor Temperature Nonuniformity on HP Vane and End Wall Heat Transfer: an Experimental and Computational Investigation', *ASME. J. Eng. Gas Turbines Power* **133**(3), 031901–11.

Qureshi, I., Smith, D. A. and Povey, T. (2012), 'HP Vane Aerodynamics and Heat Transfer in the Presence of Aggressive Inlet Swirl', *ASME. J. Turbomach.* **135**(2), 021040–13.

Roach, P. E. (2016), 'The Generation of Nearly Isotropic Turbulence by Means of Grids', *Int. Journal of Heat and Fluid Flow* **8**, 82–92.

Rutledge, J. L. and Polanka, M. D. (2014), 'Computational Fluid Dynamics Evaluations of Unconventional Film Cooling Scaling Parameters on a Simulated Turbine Blade Leading Edge', *ASME J. Turbomach.* **136**(10), 101006–1–10.

Salvadori, S., Montomoli, F., Martelli, F., Chana, K. S., Quireshi, I. and Povey, T. (2011), 'Analysis on the Effect of a Nonuniform Inlet Profile on Heat Transfer and Fluid Flow in Turbine Stages', *ASME. J. Turbomach.* **134**(1), 011012–011012–14.

Sellers, J. P. (1963), 'Gaseous Film Cooling With Multiple Injection', *AIAA J.* **1**(9).

Shalash, K. M., El-Gabry, L. A. and El-Azm, M. M. A. (2013), 'Numerical Modelling of Slot Film Cooling Using a Wall Function', *ASME paper* **GT2013-94127**.

Sharma, O. P. and Butler, T. L. (1987), 'Prediction of Endwall Losses and Secondary Flows in Axial Flow Turbine Cascades', *ASME J. Turbomach.* **129**(2), 229–236.

Shiau, C. C., Chen, F. C., Han, J. C., Azad, S. and Lee, C. P. (2016), 'Full-Scale Turbine Vane Endwall Film Cooling Effectiveness Distribution Using Pressure-Sensitive Paint Technique', *J. Turbomach.* **138**(5), 051002–1–10.

Sieverding, C. H. (1985), 'Recent Progress in the Understanding of Basics Aspects of Secondary Flows in Turbine Blade Passages', *ASME J. Eng. Gas Turbines Power* **107**(2), 248–257.

Sinha, A. K., Bogard, D. G. and Crawford, M. E. (1992), 'Film Cooling Effectiveness Downstream of a Single Row of Holes With Variable Density Ratio', *J. Turbomach.* **113**(4), 442–449.

Thole, K. A. and Knost, D. G. (2005), 'Heat Transfer and Film-Cooling for the Endwall of a First Stage Turbine Vane', *Int. J. of Heat and Mass Transfer* **48**, 5255–5269.

Thole, K. A., Sinha, A. K. and Bogard, D. G. (1990), 'Mean Temperature Measurements of Jets with a Crossflow for Gas Turbine Film Cooling', *Proceeding of the Third International Symposium on Transport Phenomena and Dynamics of Rotating Machinery (ISROMAC-3)* .

Thomas, M. (2014), Optimization of Endwall Film-Cooling in Axial Turbines, PhD thesis, University of Oxford.

Thomas, M., Kirollos, B., Jackson, D. and Povey, T. (2013), 'Experimental and CFD Studies of NGV Endwall Cooling', *ASME paper* **GT-2013-95639**.

Thomas, M. and Povey, T. (2016), 'Improving Turbine Endwall Cooling Uniformity by Controlling Near-Wall Secondary Flows', *Proceedings of the Institution of Mechanical Engineers, Part G, Journal of Aerospace* .

Tyacke, J. C. and Tucker, P. G. (2015), 'Future Use of Large Eddy Simulations in Aero-Engines', *ASME J. Turbomach.* **137**(8), 0810051–16.

Vinton, K. R., Watson, T. B., Wright, L. M., Crites, D. C., Morris, M. C. and Riahi, A. (2017), 'Combined Effect of Freestream Pressure Gradient and Density Ratio on the Film Cooling Effectiveness of Round and Shaped Holes on a Flat Plate', *ASME J. Turbomach.* **139**(4), 041003–1–10.

Wang, D., Ornano, F., Sheng, L. Y., Wells, R., Hjalmarsson, C., Hedlund, L. and T.Povey (2017), 'FLOvane: a New Approach for High-Pressure Vane Design', *ASME J. Turbomach.* **139**(6), 061002–14.

Wang, H. P., Olson, S. J., J., R., Goldstein and Eckert, E. R. G. (1997), 'Flow Visualization in a Linear Turbine Cascade of High Performance Turbine Blades', *ASME J. Turbomach.* **119**(1), 1–8.

Zess, G. and Thole, K. (2005), 'Computational Design and Experimental Evaluation of Using a Leading Edge Fillet on a Gas Turbine Vane', *ASME J. Turbomach.* **124**(2), 167–175.

Zhang, Y., Li, Y. and Yuan, X. (2017), 'Effects of Inlet Swirl on Endwall Film Cooling in Neighbouring Vane Passages', *ASME paper* **GT2017-64397**.